

Felix Keiderling

Direct Noise Computation of High Reynolds Number Subsonic Jet Flow using LES



Dissertation ETH No. 17955

Visualization taken from a large-eddy simulation (LES) of a Mach 0.9 jet at a Reynolds number of $Re = 4.5 \cdot 10^5$. Vortical structures of the jet shear layers are shown by contours of $|\boldsymbol{\omega}|$. The directly computed acoustic near-field is visualized by pressure fluctuations.

A digital version of this thesis can be downloaded from ETH e-collection:
<http://e-collection.ethbib.ethz.ch/>

This thesis was typeset using the pdfL^AT_EX and the `hyperref` package.

Diss. ETH No. 17955

Direct Noise Computation of High Reynolds Number Subsonic Jet Flow Using LES

A dissertation submitted to
ETH ZURICH

for the degree of
Doctor of Technical Sciences

presented by

Felix Keiderling

Dipl.-Ing. Luft- und Raumfahrttechnik, Universität Stuttgart
M.Sc. Aerospace Engineering, University of Arizona
born on July 8, 1975
citizen of Germany

accepted on the recommendation of

Prof. Dr. L. Kleiser
Dr. habil. (HDR) C. Bogey (EC Lyon)

2008

Abstract

The effect of nonlinear interaction of instability eigenmodes on jet flow transition and its noise for a round jet at a Mach number of $Ma = 0.9$ and a Reynolds number of $Re = 4.5 \cdot 10^5$ based on jet exit conditions is investigated by large-eddy simulations. At the inflow, helical perturbations determined from linear stability theory are superimposed on a laminar base flow in order to initiate transition to turbulence. Two different ranges of azimuthal wavenumbers n are excited. The first type of simulations excites modes $|n| = 1, \dots, 8$ while the second excludes $|n| \leq 3$ from the inflow forcing. For both modal compositions we investigate the effect of the disturbance amplitude and vary it in the range from 1.5%, 3.0% to 4.5% of the jet inlet velocity. Thereby, we aim to characterize sources of noise generation and, in particular, underlying mode interactions.

For the first type of excitation the changes in forcing amplitude mostly affect the streamwise position of the transition process which is shifted upstream for larger excitation levels. The transition process is similar for the three amplitudes and is characterized by strong vortex pairings that directly place an imprint on the emitted noise. The simulation results are in fair agreement with experimental and numerical reference data.

For the second type of excitation we observe changes in the transition of the jet with increasing forcing amplitude. As the shear layer roll up, pronounced vortex pairings are more and more weakened and vortex rings are distorted to form three-dimensional structures. This change in transitional behavior affects the acoustic near field which exhibits features of both, natural and tonally-excited jets. In particular for high forcing amplitudes, a tonal component outside the initially excited frequency range is observed. This tone can be linked to fluid-dynamic events in the early transitional region as well as at the end of the potential core. Furthermore, its frequency can be explained by a weakly nonlinear interaction of initially excited eigenmodes.

To substantiate the soundness of the predictions, insensitivity against the choice of certain numerical parameters is demonstrated. The relaxation-term coefficient of the ADM subgrid-scale model is reduced and effects are found to be small. Subgrid-scale model effects are further investigated by simulating a baseline configuration using approximately deconvolved information. Finally, we address the effect of the azimuthal resolution on our simulation results.

Kurzfassung

Die vorliegende Dissertation befasst sich mit dem Einfluss der nichtlinearen Interaktion von Instabilitätsmoden auf den laminar-turbulenten Übergang eines runden Freistrahls bei einer Machzahl von 0.9 und einer Reynoldszahl von $Re = 4.5 \cdot 10^5$ gebildet mit Grössen am Eintritt des Freistrahls. Hierzu wird eine Reihe von Grobstruktursimulationen (LES) durchgeführt. Am Einströmrand des numerisch Rechengebietes werden dreidimensionale Störungen gemäss linearer Stabilitätstheorie mit einer laminaren Grundströmung überlagert, um den Umschlag einzuleiten. Hierbei werden zwei unterschiedliche Zusammensetzungen der Einströmstörungen untersucht: Beim ersten Typ werden Umfangswellenzahlen $|n| = 1, \dots, 8$ angeregt, im zweiten nur Wellenzahlen $4 \leq |n| \leq 8$. Für die jeweiligen Zusammensetzungen der modalen Anregung wird der Einfluss der Stör-Amplitude im Bereich von 1.5% bis 4.5% (bezogen auf die Eintrittsgeschwindigkeit des Freistrahls) untersucht.

Bei der Anregung der Eigenmoden $|n| = 1, \dots, 8$ beschränkt sich der Einfluss der Stör-Amplitude hauptsächlich auf den Ort des Umschlags. Das Transitionsverhalten für unterschiedliche Amplituden ist relativ ähnlich und geprägt von Wirbelpaarungen, die auch den direkt berechneten Schall dominieren. Strömungs- wie auch Schallergebnisse stimmen qualitativ mit Referenzdaten überein und sind deutlich vom Transitionsverhalten geprägt.

Für den zweiten Typ der Anregung wird bei Vergrösserung der Stör-Amplitude eine Veränderung des Transitionsverhaltens festgestellt, welches von gelegentlich auftretenden Wirbelpaarungen zu einem Umschlag mit dreidimensionalen Wirbelstrukturen wechselt. Diese Veränderung im Transitions-geschehen beeinflusst das dadurch generierte akustische Nahfeld. Die Ergebnisse im Strömungsbereich sind in sehr guter Übereinstimmung mit experimentellen und anderen numerischen Resultaten. Das direkt berechnete akustische Nahfeld hat Eigenschaften von sowohl natürlichen als auch tonal angeregten Freistrahlen, die zum einen mit Vorgängen im Transitionsbereich der Scherschicht und zum anderen mit Ereignissen am Ende des Potentialströmungskerns in Zusammenhang gebracht werden können. Die besonders für grosse Stör-Amplituden auftretende tonale Komponente, welche ausserhalb des angeregten Frequenzbandes liegt, lässt sich mit Hilfe schwach nichtlinearer Theorie als Interaktion angeregter Moden erklären.

Um die Sensitivität des Simulationsverfahrens zu untersuchen, und somit auch die Zuverlässigkeit der Vorhersagen zu demonstrieren, werden

bestimmte numerische Parameter verändert. Zuerst wird der Relaxationskoeffizient des Feinstrukturmodells verändert, dessen Einfluss auf die Ergebnisse sich als gering erweist. Der Einfluss des gewählten Feinstrukturmodells wird anhand einer Simulation untersucht, die approximativ entfilterte Feldgrößen verwendet. Abschliessend wird der Einfluss der numerischen Auflösung in Umfangsrichtung untersucht.

Acknowledgements

I would like to thank Prof. Leonhard Kleiser for supervising my research in this PhD project at the Institute of Fluid Dynamics (IFD). I would like to express my gratitude for his constant support and to allow me great latitude in the alignment and execution of research – whilst maintaining the confidence and interest in my work.

I am in particular indebted to Christophe Bogey (CB2) not only for numerous fruitful and at times truly illuminating discussion during my stay at Centre Acoustique (Ecole Centrale de Lyon) but also for continuously showing interest in my work. He shared his experience unconditionally with no expectation of return, provided insight and encouragement which was constant support during the difficult times of this project. Dr. habil. (HDR) Christophe Bogey also acted as co-examiner of my dissertation.

I would also like to take the chance and thank Prof. Christophe Bailly (CB1) for giving me the opportunity to come to Lyon as visiting researcher. Also, I would like to thank Prof. Hermann F. Fasel who introduced me to the beauty of research in CFD.

My thanks also go to the members of IFD. In particular I thank Drs. S. B. Müller, A. Jocksch and D. Obrist for discussions at IFD and Dr. T. Bosse for introducing me to Zurich. Also, I would like to thank all my former colleagues and long-lasting friends from Lahr, Stuttgart, Tucson, Zurich, Lyon and many other places.

I owe my family for their support and encouragement along my way. Last but not least, I pay tribute to Grit for not forcing me to strain at the leash when office hours seemed not to end. Her support was extremely valuable during the ups and downs of this journey. I also thank our little girl Annabelle for her lovely smile.

Zürich, March 2009

Felix Keiderling

Contents

Nomenclature	V
1 Introduction	1
1.1 Motivation	1
1.2 Background	2
1.3 Classification of noise prediction approaches	5
1.4 Numerical methods for noise prediction	6
1.5 Objectives and outline	10
2 Mathematical model and numerical methods	13
2.1 Governing equations for compressible LES	14
2.2 SGS closure: ADM and regularization based model	17
2.3 Description of employed filter	20
2.4 Simulation method	21
2.4.1 Cylindrical coordinate singularity treatment	22
2.4.2 Spatial discretization	25
2.4.3 Temporal discretization	28
2.5 Boundary treatment	30
2.5.1 Nonreflecting boundary conditions	31
2.5.2 Sponge-layer technique	32
2.5.3 Inflow treatment	33
2.5.4 Linear stability investigation	33
2.5.5 Inflow disturbance seeding	36
2.6 Computational grid	37
2.7 Validation	39
2.8 Initial conditions and statistical analysis	42
2.9 Spectral signal processing of time series	44
3 LES results for flow and acoustic field	47
3.1 Introduction	47
3.1.1 Parametrization	47
3.2 Influence of the disturbance amplitude	50
3.2.1 Instantaneous data	50
3.2.2 Mean flow and turbulence results	55
3.2.3 Acoustic results	67

3.2.4	Relevant noise generation mechanism: Vortex pairing noise	73
3.3	Influence of the modal composition of disturbances	74
3.3.1	Instantaneous data	75
3.3.2	Mean flow and turbulence results	80
3.3.3	Acoustic results	92
3.3.4	Relevant noise generation mechanism: “Cut-and-connect” process and weakly nonlinear theory	100
3.4	Direct comparison of modal composition effects	104
3.4.1	Flow results	104
3.4.2	Acoustic results	110
3.5	Influence of the relaxation coefficient χ	113
3.5.1	Effect on the flow field	113
3.5.2	Effect on the acoustic field	118
3.5.3	Summary on the effects of the relaxation coefficient	118
3.6	Effect of the deconvolution operator	120
3.6.1	Effect on the flow field	120
3.6.2	Effect on the acoustic field	124
3.6.3	Summary on the effects of the deconvolution approach	127
3.7	Resolution effects on the simulation results	127
3.7.1	Resolution effect on the flow field	131
3.7.2	Effect on the acoustic field	138
3.7.3	Summary of azimuthal resolution effects	141
4	Summary, conclusions and recommendations	143
4.1	Summary and conclusions	143
4.1.1	Effect of physical parameters	145
4.1.2	Effect of numerical parameters	147
4.2	Recommendations	149
A	Linear stability theory	151
A.1	Linearized governing equations	151
A.1.1	Compressible Navier-Stokes equations in cylindrical coordinates	151
A.1.2	Linearization	154
A.1.3	Wave ansatz for disturbances	160
A.1.4	Boundary conditions	165
A.1.5	Matrix notation of equations	166

A.2	Discretization on Gauss-Lobatto and Gauss points	168
A.3	Disturbances in conservative variables	170
B	Implementation details of sponge technique	173
B.1	Inflow sponge	173
B.2	Ambient sponge and outflow damping	176
C	Phase-speed and grid anisotropy effects	179
	Bibliography	183
	Curriculum vitae	

Nomenclature

Roman symbols

$a_i^g, f_i^g, r_i^g, d_i^g$	axial grid stretching parameters with $i = 1, 2$
$A_{\text{total,LST}}$	total disturbance amplitude
A	amplitude
$\mathbf{A}, \mathbf{B}, \mathbf{C}, \mathbf{E}$	coefficient matrices in linear stability problem
D_j	jet diameter
\mathbf{D}	differential operator matrix
E	total energy
$E(n)$	turbulent kinetic energy (TKE) of wavenumber n
f'	first derivative of f in section 2.4.2
f_s	sampling rate
f_N	Nyquist frequency
G	filter operator
I	identity operator
J	Jacobian matrix
k	thermal conductivity
L	computational domain length
Ma	Mach number
n	azimuthal wavenumber
$ n = \pm n$	right- and left-turning wavenumber n
N_r, N_θ, N_z	grid points in radial, azimuthal and axial direction
N_θ^r	number of retained modes in context of mode-clipping outlined in section 2.4.2
\mathcal{O}	order
p	pressure
Pr	Prandtl number
q_i	molecular heat flux vector
\mathbf{Q}	vector of conservative variables
Q_N	deconvolution operator
\tilde{r}	mapped radial coordinate in section 2.4.1
r_0	jet radius ($r_0 = D_j/2$)
$r_{1/2}$	jet half-width
rnd_i	random number with $i = 1, 2$
(r, θ, z)	cylindrical coordinates
(R, θ, ϕ)	spherical polar coordinates
R	specific gas constant

\mathcal{R}	auto-correlation coefficient in azimuthal direction
Re	Reynolds number
S	Sutherland constant
S_{ij}	strain rate tensor
St	Strouhal number based on jet diameter $St = \omega D_j / (2\pi U_j)$
St^g	Strouhal number representable on grid
St_N	Strouhal number based on Nyquist frequency f_N
St_θ	Strouhal number based on initial momentum thickness $St_\theta = \omega \theta_0 / (2\pi U_j)$
t	time
T	temperature
T_{sim}	simulation time
u_1, u_2, u_3	Cartesian velocities corresponding to \mathbf{X}
u, v, w	cylindrical velocities in radial, azimuthal and axial direction
U_j	jet exit velocity
w_c	mean axial velocity on jet centerline
$\mathbf{X} = (x_1, x_2, x_3)^T$	Cartesian coordinates in physical space
z_0	virtual origin
z_c	length of potential core

Greek symbols

α	subgrid-scale terms in the total resolved energy equation (2.7c)
$\alpha = \alpha_r + i\alpha_i$	complex axial wavenumber
α_i	coefficients of the discrete filter in section 2.3
α^g, β^g	radial grid stretching parameters
β	subgrid-scale terms in the filtered momentum equations (2.7b)
γ	ratio of specific heats
ε	relative error
δ_{ij}	Kronecker symbol
δ_ω	vorticity thickness
Δ	general grid spacing, filter width or difference
Δt	time step
$\Delta r, \Delta \theta, \Delta z$	grid spacing in physical space
$\xi = (\xi, \eta, \zeta)^T$	generalized coordinates in computational space

θ_0	initial momentum thickness
λ	second coefficient of viscosity
λ_2	vortex identification criterion following Jeong & Hussain (1995)
μ	dynamic viscosity
ρ	density
σ	sponge function
τ_{ij}	viscous stress tensor
ϕ	polar angle/phase angle
Φ	dissipation
χ	relaxation coefficient
ω	wavenumber, circular frequency
ω_c	cutoff wavenumber
ω_N	resolved Nyquist wavenumber
$\tilde{\omega}$	modified wavenumber
$ \boldsymbol{\omega} $	magnitude of vorticity vector

Other symbols

*	convolution operator
$\langle \rangle$	time- and azimuthal-averaged quantity
div	divergence operator
i	imaginary unit $i = \sqrt{-1}$
$\Re(\cdot), \Im(\cdot)$	real, imaginary part

Subscripts

amb	ambient
b	base flow quantity
c	centerline quantity
infl	inflow
j	jet exit condition
out	outflow
r	radial direction
ref	reference state
spg	sponge quantity
∞	ambient or reference condition
E, S	Euler, Stokes

N	Nyquist
z	axial/streamwise direction

Superscripts

*	dimensional quantity
—	filtered or large-scale quantity
~	mass-weighted filtered or Favre quantity
'	fluctuation
''	Favre fluctuation
~	infinitesimal fluctuation in context of LST
˘	in appendix A.1.2
˘	resolved quantity based on filtered variables
*	deconvolved quantity
^	complex quantity
*	complex conjugate
t, s	temporal or spatial stability problem
T	transpose

Abbreviations

ADM	approximate deconvolution model
ADM-RT	ADM relaxation-term based model
CAA	computational aeroacoustics
CFD	computational fluid dynamics
CFL	Courant-Friedrichs-Lewy number
DNC	direct noise computation
DNS	direct numerical simulation
LES	large-eddy simulation
LST	linear stability theory
NSE	Navier-Stokes equations
OASPL	overall sound pressure level
RANS	Reynolds-averaged Navier-Stokes
RMS	root-mean-square
SGS	subgrid-scale
SPL	sound pressure level

Chapter 1

Introduction

1.1 Motivation

The noise produced by air flows is an issue in a wide range of technical applications in our everyday life, ranging from trains, automobiles and the cooling fans of electronic devices to aircraft jet exhausts. Over the past years, the sensitivity to noise and its effects on human health has been rising steadily. As a consequence, for instance, airlines face severe noise regulations by the authorities and also noise-dependent airport landing fees, which prompted an increased interest of the aircraft industry in research on jet-noise reduction. In particular for aircraft-associated noise the expected development of the airliner market adds fuel to the problem: In the period 2007 to 2026 a leading aircraft manufacturer expects an increase in world passenger traffic of approximately 4.9% per annum (p.a.) and a growth in freight traffic of 5.8% p.a. (see Global Market Forecast, Airbus S.A.S., 2007). In the context of this expected growth, the acceptance – especially in the vicinity of residential areas – will be tied inevitably to noise reduction.

Prediction tools that can *a priori* determine the acoustic emission of a particular design are therefore needed by the industry. In addition, insight into the underlying mechanisms of sound generation has to be gained in order to influence the flow and hopefully achieve a reduction of perceived noise. The field of computational aeroacoustics (CAA) is a promising approach that can significantly contribute toward the goal of noise prediction and noise reduction as it closes the gap between well-established methods of computational fluid dynamics (CFD) and aeroacoustics. Because of the very high Reynolds numbers of realistic jet engines (on the order of 10^7 based on the nozzle diameter and centerline velocity) the flow in the jet plume is considered fully turbulent. This requires numerical simulations which feature a reliable modeling of turbulence. Since the inherent source of sound is the unsteadiness of the flow, it is widely agreed upon that time-dependent simulation methods are to be used in aeroacoustic research.

The motivation of this study is to enhance the understanding of jet noise generation mechanisms in the high subsonic regime. Because of

the high Reynolds number of practical configurations our numerical approach relies on large-eddy simulations (LES). The sound together with its fluid dynamic source field is computed in a single domain by solving the compressible Navier-Stokes equations. Thereby, we intend also to contribute to research in the field of direct noise computation (DNC) and to assess the predictive quality of LES for high Reynolds number jet-noise problems.

1.2 Background

Since the beginning of the jet engine age more than 60 years ago, drastic reductions in jet noise have been accomplished. The beginning of jet-noise research is intrinsically tied to Sir James Lighthill and his two-part publication entitled “On sound generated aerodynamically” (Lighthill, 1952, 1954). In order to advance the understanding of noise generation mechanisms it was most natural to search for sources of sound contained in the flow field. Through his acoustic analogy, which is based on the rearrangement of the full compressible conservation equations into wave-equation form, the flow is separated into a wave propagation part (wave equation in a homogeneous medium at rest) and an inhomogeneous source consisting of the remaining terms. One important finding is that in the subsonic regime the emitted sound power scales with the eighth power of the jet exit velocity. Therefore, these jet-noise reductions were mostly achieved by increasing the by-pass ratio of the turbofan engines which reduces the jet exit velocity and shields the high-speed core of the jet. There is, however, a technical upper limit for the by-pass ratio, and it has become clear that further progress can only be achieved by more subtle modifications of the jet flow.

In subsequent years modifications to the acoustic analogy were proposed in order to take into account effects that were already pointed out by Lighthill such as source convection (and thus a directivity pattern with dominance in the downstream direction and a Doppler shift of the radiated frequencies (Ffowcs Williams, 1963)) as well as mean flow refraction effects (Lilley, 1974). Nevertheless, the ambiguity of the separation between acoustics and the interaction of acoustic waves with the generating flow field remains unresolved in these approaches. Important theoretical contributions by Powell, Howe and Möhring that rely on a vorticity formulation of the source term of the wave equation are not further addressed here; rather we refer to the review articles by Goldstein

(1984), Lilley (1995), Tam (1998) and Jordan & Gervais (2007).

Turbulence research and thereby also aeroacoustic research noticed the importance of scale separation when Crow & Champagne (1971) provided experimental evidence for the existence of large coherent structures within turbulent flow fields and, more importantly, in the noise producing region of the investigated jet. They showed that surging excitation of the jet raises the latent order of large coherent structures above background turbulence and linked it to instability waves. About the same time, several researchers suggested that instability waves might be the major source of sound in the supersonic regime. Because of very prominent radiation patterns emitted from supersonic jet flows (see Fig. 1.1), a lot of work was devoted to clarify this and a successful theory of noise generated by instability waves was proposed by Tam (1971). As the

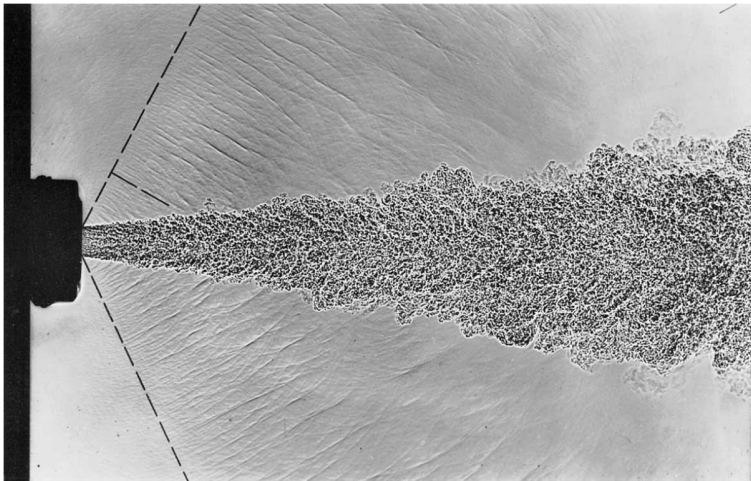


Figure 1.1: Directional sound waves radiated from the shear layers of a supersonic jet of helium. This photograph is copyright Cambridge University Press, Tam (J. Fluid Mech. 1971), plate 1. Reprinted with permission.

present work focuses on subsonic jet noise we refer to the review articles by Tam (1995*a,b*) for further details concerning the characteristics of supersonic jet noise (such as turbulent mixing noise, broadband shock-associated noise and screech tones) and the developed theories.

The work of Winant & Browand (1974) showed that the vortex pair-

ing in a mixing layer is initiated by instability waves (either naturally occurring or mechanically excited). They also pointed out the strong similarities to the dynamics of the coherent structures in the round jet experiments by Crow & Champagne (1971). Because of these similarities Winant & Browand proposed to consider vortex pairing as an important source of sound even for high Reynolds number jet flow. Brown & Roshko (1974) experimentally demonstrated the presence of such coherent structures in a high Reynolds numbers ($Re = 0.5 \cdot 10^6$) mixing layer and found the Reynolds number effect to be restricted to the range and size of the small scales. The large-scale picture exhibited virtually no influence. Against the background of supersonic jet noise and with respect to these experimental findings, a theory similar to the supersonic regime was sought which could uniquely explain the underlying noise generation mechanisms. As the efficiency of Mach wave radiation is significantly reduced for subsonic jets the question remains whether its noise is dominated by large coherent structures or small and more isotropic eddies. Also, the effect of large-scale structures on the subsonic jet noise remains unclear as for example pointed out in the review articles by Goldstein (1984) and Tam (1995*b*).

Very early, the effect of modifications of the jet – either upstream or right at its exit – on the emitted noise was investigated by various experimental groups. Bechert & Pfizenmaier (1975), for example, found an amplification of broad band noise in a subsonic cold jet by pure tonal excitation. In contrast to this, other investigators, such as Kibens, noticed a reduced broadband response, as pointed out in the comprehensive review article by Crighton (1981). According to him these opposing observations were related to the difference in Reynolds number of the experiments: There seemed to exist a critical Reynolds number of $Re \approx 10^5$ below and above which excitation resulted in a reduction and amplification of turbulence and broadband emitted noise. Zaman & Hussain (1981) investigated the turbulence suppression effect for a variety of excitations. Subsequently Hussain & Hasan (1985) demonstrated that this could effectively reduce the far-field jet noise. These experiments did not only confirm the Reynolds number barrier proposed by Crighton but also render comparisons between low-Reynolds number jets and practical jets questionable at least to some extent. Hussain & Hasan (1985) identified an additional constraint for the noise suppression/amplification: the state of the oncoming boundary layer within the nozzle. For noise reduction the boundary layer needs to be initially lam-

inar, which was subsequently verified in experiments by Zaman (1985).

Motivated by these experimental findings modifications to the nozzle of jet engines have shown that altering the flow at the nozzle exit (e.g., by chevrons, tabs, air injection) can reduce the noise by enhanced mixing of the high- and low-speed streams (we refer to Castelain (2006) for an overview of noise reduction approaches). However, research on effective noise reduction methods has largely been based on trial-and-error experiments. Without exception the proposed measures result in a reduced engine efficiency and loss of thrust and, therefore, are not attractive for the industry. The application of micro-jets to alter the jet flow with a relatively small mass-flux are hence attractive and are investigated by Arakeri *et al.* (2003) and Castelain (2006). Nevertheless, the underlying noise generation mechanisms (in the subsonic regime prevalent during aircraft take-off) are not yet understood and no predictive tool for the design process is available for complex jet nozzle modifications. Therefore, it is strongly desirable to further enhance our understanding of the noise generation mechanisms by examining the connection between flow features and the radiated noise.

Full-scale engine tests are infeasible because of the enormous complexity of the underlying problem. Regardless of the chosen approach (analytical, experimental or numerical) to tackle this problem, several approximations and simplifications have to be made. In the field of jet-noise research a model problem is set up which focuses solely on the noise generated by the turbulent jet exhaust plume, which represents the major noise source during take-off of a civil airplane. Of course this is only a crude model compared to flow behind a jet engine. However, as long as the major mechanisms are captured, this idealized model can serve as test-bed to shed light on fundamental physics of jet-noise generation.

1.3 Classification of noise prediction approaches

The prediction methods employed in the field of computational aeroacoustics can be grouped into so-called “hybrid” and “direct” methods. When taking the hybrid approach the domain is divided into a noise generating region associated with the turbulent sources and a region in which the generated noise propagates into the far field. In contrast, when performing a direct noise computation the discretized domain is extended and the compressible Navier-Stokes equations are solved in the fluid dynamic region as well as in the contiguous acoustic field. Thereby,

this approach circumvents the problem of truncating and coupling two domains and also the problem that the definition of the acoustic source terms is not unique. In particular in the case of high subsonic Mach numbers, the lack of a clear scale separation mentioned above makes the distinction between source terms and propagating medium (employed in hybrid approaches) ambiguous and remains a subject of ongoing discussions (Wang *et al.*, 2006; Jordan & Gervais, 2007). On the other hand, the direct computation approach is computationally more expensive because of the continuous discretization into the acoustic field. Therefore, DNC contain only a part of the acoustic field, which is referred to as the acoustic near field. Clearly, the advantage is that all possible interaction effects between sound waves and the fluid flow are inherently captured by this approach. Thus, as long as the employed numerical methods establish the correct physical model, the directly calculated acoustic field is *a priori* exact.

1.4 Numerical methods for noise prediction

No matter whether a hybrid or a direct noise computation approach is taken, there is an ultimate requirement for accurate numerical techniques because of the huge disparity of length and time scales between the hydrodynamic region and the acoustic field. Only a minute fraction of the flow's kinetic energy transfers to sound waves which then propagate over large distances without significant viscous damping. It is important to point out that we focus on a high subsonic jet in which scales cannot be clearly separated. This poses additional problems that will be addressed below. The review article by Colonius & Lele (2004) gives a detailed introduction to the field of computational aeroacoustics and also addresses issues concerning appropriate numerical methods.

For the hybrid approach various methods have been used successfully in the literature to propagate the sound to the acoustic far field. The methods that exist range from acoustic analogies and Kirchhoff surface-methods (Lighthill, 1952; Ffowcs Williams & Hawkings, 1969) to solving the linearized Euler equations. These approaches are not addressed. Instead, we refer to the reviews by Lele (1997) and Wang *et al.* (2006) and note that noise prediction methods used in today's industrial design process of jet engine nozzles largely rely on the Reynolds-averaged Navier-Stokes equations (RANS) combined with acoustic analogies. These methods are well established for specific geometries, however, they re-

main at best semi-empirical and need tuning of coefficients to particular cases in order to obtain reliable turbulence predictions and, hence, its noise.

In contrast to this, current aeroacoustic research focuses on time-dependent simulation methods since the flow unsteadiness is the inherent source of sound. Direct Numerical Simulations (DNS) were used for relatively low Reynolds number flows such as the investigation of the sound generation in a two-dimensional low Mach number mixing layer by Colonius *et al.* (1997). In an overlap-region results of the DNS were compared to predictions using the previously mentioned modified acoustic analogy of Lilley (1974) and it was found that the vortex-pairing dominated noise was not accurately described. Freund (2001) successfully performed a DNS of compressible high subsonic jet flow at a Reynolds number of $Re = 3.6 \cdot 10^3$ (based on the jet diameter). He found very good agreement with the experimental results of a jet at the same jet operating conditions reported by Stromberg *et al.* (1980). Far-reaching conclusions can be drawn from such simulations concerning, for example, mechanisms of sound generation and the structure of noise sources. They also demonstrated the applicability of DNC, i.e. calculating directly the aerodynamically generated sound together with the flow in a unified approach using highly accurate numerical schemes (such as the compact schemes presented by Lele, 1992). However, because of the high computational cost, DNS is restricted to flows in the low Reynolds number regime.

At higher Reynolds numbers, as in the present work, LES can be employed in which only the large scales are fully resolved while the effects of subgrid-scales (SGS) are modeled. The first LES providing parts of the acoustic near-field was presented by Boersma & Lele (1999), however, no details of the emitted acoustic field or near-field pressure spectra were reported. Subsequently, Bogey, Bailly & Juvé (2003) provided the first extensive results on the directly computed acoustic near-field of a Mach 0.9 round jet at an intermediate Reynolds number of $Re = 65 \cdot 10^3$. In the following years, a lot of effort was devoted to this field and investigations focused on different aspects such as the influence of inflow forcing parameters, heating of the jet flow, viscous effects, SGS-model effect and the turbulent energy budget. The works of Bodony & Lele (2004, 2005), Uzun *et al.* (2004), Andersson *et al.* (2005*b*) and Bogey & Bailly (2006*c*, 2007), among others, demonstrated that it is possible to directly compute the generated noise using LES and helped to obtain a more detailed

picture of the underlying physics. These very active years of research contributed to a change of the current understanding of the subsonic jet noise generating mechanism in favor of early experimental findings of Mollo-Christensen *et al.* (1964). They explained the observed spectral characteristics as a combination of two different sources of sound: Large-scale structures dominating the downstream region (including effects of convection and refraction and thus a low-frequency dominance) and a more isotropic broad-banded noise with similar characteristics for all observer positions associated with turbulence generated noise. Tam *et al.* (2003, 2005) refer to this explanation in the context of their self-similar pressure spectra. The experiments by Viswanathan (2004*a,b*) also support this explanation for even more complex nozzle geometries. Similarly, the LES results by Bogey & Bailly (2006*b*) assist in explaining the observed near-field noise of a subsonic jet as the result of two different coexistent noise generating mechanisms.

All flow computation approaches share the problem of suitable boundary conditions at the edges of the computational domain. In the context of aeroacoustics this becomes even more important: as in all transitional/turbulent numerical flow simulations either turbulent inflow conditions are to be prescribed or disturbances have to be introduced to a laminar flow to initiate transition to turbulence. In the first case, the definition of a turbulent inflow often relies on a precursor simulation, which becomes computationally expensive for higher Reynolds numbers, or on the inclusion of parts of the jet nozzle in the simulation domain (see e.g. Shur *et al.*, 2006; Barré *et al.*, 2006). In the latter case, care has to be taken when transition is triggered artificially as this numerical noise may overwhelm the physical one. The disturbances can be either artificial or, as in the present work, based on eigenmodes of some underlying base-flow jet profile.

The pronounced sensitivity of jets to variations of the inflow condition has been demonstrated experimentally (Brown, 2005; Zaman, 1985) as well as numerically (Stanley & Sarkar, 2000; Bogey & Bailly, 2005*b*). Hence, investigating the sensitivity of the simulations to changes in disturbance amplitudes seems appropriate. As pointed out by Wang *et al.* (2006) it is tempting to target the development of computational methods toward the aeroacoustic prediction of realistic systems. However, fundamental studies of generic problems can help in highlighting the physics of the sound generation and bring technical issues forward that must be addressed to achieve satisfactory modeling and prediction of the

mechanisms.

The particularity of the present work lies in the nature of the disturbances introduced at the inflow. The nonlinear development of eigenmodes is believed to play an important role in the sound generation process of forced jets (Laufer & Yen, 1983). For example, Sandham *et al.* (2006) found qualitative agreement for a model consisting of nonlinear mode interaction of a convected vortex packet with full Navier-Stokes simulation data. They reason that the wavenumber difference of disturbances and their nonlinear interaction dominate the subsonic sound radiation from eigenmodes. In contrast, Cheung and coworkers (Cheung *et al.*, 2007; Cheung & Lele, 2007) focus on nonlinear parabolized stability equations (PSE) and demonstrate that this approach accurately captures the acoustic near field of subsonic jet flow (and when combined with an acoustic analogy also the far-field noise). Only recently, Sandham & Salgado (2008) investigated nonlinear mode-by-mode interactions using linear PSE. Employing these modes to drive a source term of an acoustic analogy they found good agreement with experimental reference data. The latter two approaches may remain restricted to lower Reynolds numbers because the rapid amplitude growth of modes may result in convergence problems or even divergence as well as in an axially fast developing flow, which contradicts the underlying assumption in the derivation of the PSE (Cheung & Lele, 2007). The findings of Sandham & Salgado and Cheung *et al.*, regardless of the relatively low Reynolds number, are however important as there is experimental evidence by Suzuki & Colonius (2006) that instability waves are present in fully turbulent jets at high Reynolds number. In the present study we therefore investigate inflow conditions based on linearly unstable eigenmodes. We attempt to clarify effects of the inflow forcing amplitude and the modal composition of the imposed disturbances on the transitional behavior of the jet. From changes in transition and resulting variations of the aerodynamic properties we aim at inferring the dominant modes and structures in the breakdown process of the jet. Possibly, in the combination with the directly computed acoustic near-field noise, conclusions might be drawn about the underlying mechanisms of noise generation focusing, in particular, on the early nonlinear mode interactions. The quality of the predictions and the system stability of the computational setup is assessed by demonstrating insensitivity against changes of important numerical parameters.

1.5 Objectives and outline

In the present work, the nonlinear development of linearly unstable eigenmodes of a high subsonic jet flow at high Reynolds number is investigated. The effects of the nonlinear disturbance development on the jet flow and its emitted noise is analyzed using large-eddy simulations that provide the full spatio-temporal information. This information serves as a data base to investigate the spectral properties of the directly computed near-field noise. Important inflow conditions of the jet flow are modified and subsequently their effect on the flow and on its noise is to be investigated. In order to accomplish this goal the following objectives need to be achieved:

- Development of a highly accurate and efficient solver of the time-dependent three-dimensional compressible Navier-Stokes equations expressed in cylindrical coordinates allowing for the direct noise computation of high Reynolds number high Mach number jet flow in a simplified model configuration using LES.
- Development of a numerical code that accurately solves the eigenvalue problem established by the linearized viscous disturbance equations of the cylindrical Navier-Stokes equations.
- Investigation of the spatial stability properties of an analytically defined base-flow profile.
- Investigation of the nonlinear interaction of the previously determined unstable eigenmodes using the developed LES code.
- Identification and explanation of noise generation mechanisms excited by the forcing of instability waves.
- Assessment of the predictive capabilities and investigation of the sensitivity of the setup to changes in numerical parameters.

The thesis is organized as follows: In chapter 2 the governing equations together with the employed numerical methods are given. This chapter also comprises the description of the SGS closure, boundary conditions, inflow treatment and the spatial stability investigation of the inflow profile. The results for the flow field and the generated noise are reported in chapter 3 which starts with the specification of the parameters of the eleven investigated cases. First, the effect of physical

parameters (disturbance amplitude and modal composition of excitation) is investigated. Thereafter, computational parameters (SGS coefficient, SGS model, resolution) are discussed. Each LES result section is grouped into a representation of instantaneous data, mean flow and turbulence results and the directly computed jet noise. Characteristics of the acoustic near-field are linked subsequently to events in the fluid dynamic region. Finally, the findings are summarized and conclusions are drawn in chapter 4.

Chapter 2

Mathematical model and numerical methods

The mathematical model of fluid dynamics is given by the set of conservation equations of mass, momentum and energy, put forth independently by Navier and Stokes in the early 1800's (Darrigol, 2002). The momentum equations are often referred to as Navier-Stokes equations, whereas conservation of mass is also called the continuity equation. In the field of computational fluid dynamics, however, the whole set of non-linear, coupled, partial differential equations is commonly referred to as Navier-Stokes equations (NSE) (Tannehill *et al.*, 1997) and this nomenclature will be employed in the following.

The numerical solution of the unsteady Navier-Stokes equations requires that all relevant scales in space and time are resolved sufficiently. For turbulent flows where scales may span several orders of magnitude this resolution requirement becomes computationally very expensive. This scale disparity is even increased when computing the aerodynamically generated noise by means of direct noise computations and, as mentioned before, the time-dependence inherently ties these noise computations to turbulent flow simulations. To handle the huge scale disparity in space and time large-eddy simulation is the appropriate approach for high Reynolds number flows. The underlying basis for LES is the separation of spatial scales with respect to some reference length, typically related to the grid spacing Δ , i.e. the assumption that scales in the flow can be separated into large-scale eddies and small-scale turbulence. By using this length scale Δ the structures in the flow are divided into resolved ones which have spatial extent larger than Δ and unresolved ones. The unresolved small scales are often referred to as subgrid-scales. The large, energy containing structures are usually characterized by anisotropy whereas the smaller scales are generally more homogeneous and isotropic and thus are suitable to *a priori* modeling approaches. The scale separation for the Navier-Stokes equations is done by performing a low-pass filtering in wavenumber space. It will be described in more detail in the derivation of the governing equations.

2.1 Governing equations for compressible LES

The governing equations for the current LES code are the filtered compressible Navier-Stokes equations in nondimensional, conservative form for a generalized coordinate system. In order to arrive at the nondimensionalized form, dimensional reference scales are introduced which results in the following dimensionless parameters

$$Re = \frac{\rho_\infty^* u_\infty^* L_\infty^*}{\mu_\infty^*} \quad (2.1a)$$

$$Ma = \frac{u_\infty^*}{a_\infty^*} \quad (2.1b)$$

$$Pr = \frac{c_p^* \mu_\infty^*}{k_\infty^*}, \quad (2.1c)$$

known as the Reynolds, Mach and Prandtl number, respectively. For a more detailed description of the reference scales we refer to appendix A. Here, we note only that the governing equations are nondimensionalized by the jet radius $r_0 = D_j/2$, jet exit velocity U_j , jet density ρ_j , the dynamic viscosity μ_j and jet temperature T_j (all taken at the nozzle exit on the jet centerline). The Prandtl number is set to $Pr = 0.71$. To close the system of equations the fluid is assumed to be a perfect gas, $p = \rho T / (\gamma Ma^2)$.

For the derivation of the governing equations we introduce a spatial low-pass filtering operation for any flow quantity f that separates scales into a filtered or large-scale part \bar{f} and a small-scale part f' , i.e., $f = \bar{f} + f'$. The filtered part of f is obtained according to the convolution of G and f

$$\bar{f}(\mathbf{x}, t) = G * f = \int_{\Omega} G(\mathbf{x} - \mathbf{x}', t - t') f(\mathbf{x}', t') dt' d\mathbf{x}', \quad (2.2)$$

where G is the filter kernel and Ω denotes the computational domain. The mass-weighted Favre filtering procedure

$$\tilde{f} = \frac{\rho f}{\bar{\rho}} \quad (2.3)$$

is beneficial in the compressible regime due to the resulting compactness of the governing equations. The Favre fluctuations are given by

$f'' = f - \tilde{f}$ and this decomposition is employed for the velocity components and the temperature. Applying the filtering procedure (equations (2.2) and (2.3)) to the conservation laws a similar form of the governing equations to those given by Vreman (1995) is obtained. Here, we employ generalized coordinates $\boldsymbol{\xi} = (\xi, \eta, \zeta)^T$ and perform the filtering in the equidistant computational space. The generalized coordinates of the computational space are given by a cube of unit side length and are related to the physical coordinates $\mathbf{X} = (x_1, x_2, x_3)^T$ through the mapping relations

$$x_1 = x_1(\xi, \zeta) \quad (2.4a)$$

$$x_2 = x_2(\eta) \quad (2.4b)$$

$$x_3 = x_3(\xi, \zeta). \quad (2.4c)$$

The Cartesian velocities corresponding to \mathbf{X} are given by u_1, u_2, u_3 . As will become evident below we have to distinguish strictly between the Cartesian velocities and the cylindrical ones to be introduced later. Because the Cartesian coordinate x_2 depends only on η the Jacobian of the coordinate transformation simplifies to

$$J = \det \left(\frac{\partial \xi_i}{\partial X_i} \right) = \frac{\partial \xi}{\partial x_1} \frac{\partial \zeta}{\partial x_3} - \frac{\partial \xi}{\partial x_3} \frac{\partial \zeta}{\partial x_1}. \quad (2.5)$$

As pointed out before, the filter function G is independent of the equidistant computational coordinate $\boldsymbol{\xi}$ and prevents additional errors from appearing (errors that would be due to a variable filter width in computational space). Using this outlined approach we obtain equations for the resolved conservative variables $\mathbf{Q} = (\bar{\rho}, \bar{\rho}\tilde{u}_1, \bar{\rho}\tilde{u}_2, \bar{\rho}\tilde{u}_3, \tilde{E})^T$, where $\tilde{\cdot}$ denotes a resolved quantity that is computed using filtered variables, e.g., the total resolved energy

$$\tilde{E} = \frac{\bar{p}}{\gamma - 1} + \frac{1}{2} \frac{\overline{\rho u_i} \overline{\rho u_i}}{\bar{\rho}}. \quad (2.6)$$

Using the Einstein summation convention ($i = 1, 2, 3$) and ∂_q as a shorthand for a partial derivative with respect to q we arrive at

$$J^{-1} \partial_t (\bar{\rho}) + \partial_{\xi_i} (J^{-1} \xi_{i,j} \bar{\rho} \tilde{u}_j) = 0 \quad (2.7a)$$

$$\begin{aligned} \partial_t (J^{-1} \bar{\rho} \tilde{u}_i) + \partial_{\xi_k} (J^{-1} \xi_{k,j} (\bar{\rho} \tilde{u}_i \tilde{u}_j + \bar{p} \delta_{ij})) \\ - \partial_{\xi_k} (J^{-1} \xi_{k,j} \tilde{\tau}_{ij}) = -\partial_{\xi_k} (J^{-1} \xi_{k,j} \bar{\rho} \sigma_{ij}) + \beta_i \end{aligned} \quad (2.7b)$$

$$\partial_t (J^{-1} \tilde{E}) + \partial_{\xi_k} (J^{-1} \xi_{k,j} ((\tilde{E} + \bar{p}) \tilde{u}_j - \tilde{\tau}_{ij} \tilde{u}_i + \tilde{q}_j)) = -\alpha, \quad (2.7c)$$

where the metric coefficients are abbreviated by $\xi_{i,j} \equiv \partial\xi_i/\partial x_j$ and δ_{ij} denotes the Kronecker delta. In the following, this notation is also employed for the velocity gradients in the computational space, i.e., $\tilde{u}_{i,j} \equiv \partial\tilde{u}_i/\partial\xi_j$. Note that the index j of the summation convention is not to be mistaken with the subscript for jet exit quantities. On the right-hand side of the governing equations, we find only subgrid-scale terms that need modeling. Commutation errors between filtering and differentiation operation are neglected (Stolz, 2000). The viscous stress tensor in equation (2.7b) is given by

$$\tilde{\tau}_{ij} = \frac{\check{\mu}(\check{T})}{Re} \check{S}_{ij}, \quad (2.8)$$

with the strain rate tensor

$$\check{S}_{ij} = \xi_{k,j}\tilde{u}_{i,k} + \xi_{k,i}\tilde{u}_{j,k} - 2/3 \xi_{k,l}\tilde{u}_{l,k}\delta_{ij}, \quad (2.9)$$

and the temperature-dependent viscosity $\check{\mu}$ determined according to Sutherland's law (Schlichting, 1979)

$$\check{\mu}(\check{T}) = \check{T}^{3/2} + \frac{1+S}{\check{T}+S} \quad (2.10)$$

with the Sutherland constant set to $S = 0.404$ for air. The subgrid-scale terms of the momentum equations (2.7b) are the subgrid-scale stress tensor σ_{ij}

$$\bar{\rho}\sigma_{ij} = \bar{\rho}(\widetilde{u_i u_j} - \tilde{u}_i \tilde{u}_j) \quad (2.11)$$

which originates from the nonlinearity in the convective terms. Additional contributions β_i in equation (2.7b) are of the form

$$\beta_i = \partial_{\xi_k} (J^{-1}(\bar{\tau}_{ij} - \tilde{\tau}_{ij})\xi_{k,j}) \quad (2.12)$$

and arise from the nonlinearity of the viscous stress tensor due to the temperature-dependent viscosity. The resolved heat flux vector within the filtered energy equation (2.7c) is given by

$$\check{q}_j = \frac{\check{\mu}(\check{T})}{(\gamma - 1)RePrMa^2} \xi_{k,j} \frac{\partial \check{T}}{\partial x_j}. \quad (2.13)$$

In equation (2.7c) the variable α combines six additional subgrid-scale terms which are neglected. Their physical interpretation can be found

in the work of Vreman (1995) or Stolz (2000). For details concerning the decomposition of the subgrid-scale tensor (in the so-called Leonard tensor, the cross-stress tensor and the Reynolds subgrid tensor) we refer to Sagaut (2001). In the remainder, we will restrict ourselves to simulations for which no *a priori* analysis of different subgrid-scale terms is possible. Therefore, in the following section we will focus on the modeling approach for the unknown subgrid-stress tensor σ_{ij} (as introduced in equation (2.11)).

2.2 Subgrid-scale closure: ADM and regularization based model

The approximate deconvolution model (ADM) as proposed by Stolz *et al.* (see, e.g. Stolz & Adams, 1999; Stolz *et al.*, 2001*a,b*), is based on the ansatz that closure for the unknown nonlinear subgrid-scale terms can be obtained using an approximation of the unfiltered field. These deconvolved quantities are obtained by repeated application of a filter. Following the established nomenclature a regularized inverse operator Q_N can be obtained by truncating an infinite geometric series at some arbitrarily chosen N , obtaining a regularized approximation of G^{-1} , i.e.,

$$Q_N = \sum_{\nu=0}^N (I - G)^\nu \approx G^{-1}, \quad (2.14)$$

where I is the identity operator. The approximately deconvolved quantity is determined by convolution of the operator Q_N with the filtered quantity \bar{f}

$$f^* = Q_N * \bar{f}. \quad (2.15)$$

Using this deconvolution approach alleviates the closure problem and has the advantage that no physical model is necessary. Nevertheless, the effect of non-represented scales on the accurately resolved scales of the discretized governing equations needs to be accounted for. In order to model the energy transfer to the non-represented scales, a relaxation term is subtracted from the right-hand side of the governing equations (2.7a)–(2.7c) which acts only on a band of the smallest resolved scales. Following the nomenclature of Stolz *et al.* (2001*b*) the deconvolution operator Q_N applied to the primary filter G describes the form of this explicit secondary filter. In Fig. 2.1 the transfer functions of

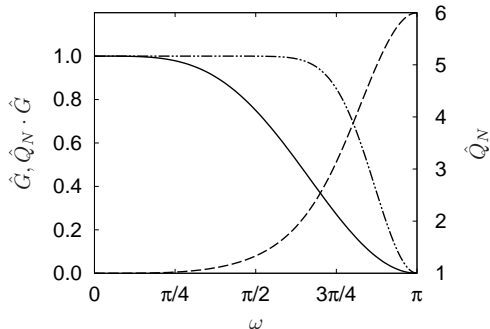


Figure 2.1: Transfer functions: — explicit primary filter \hat{G} , --- approximate inverse \hat{Q}_N , -·-·- secondary filter $\hat{Q}_N \cdot \hat{G}$ for $N = 5$. The filter transfer function \hat{G} corresponds to equation (2.20).

the primary and secondary filter, \hat{G} and $\hat{Q}_N \cdot \hat{G}$, are shown along with the transfer function of the approximate inverse \hat{Q}_N for the deconvolution order of $N = 5$ employed throughout the present work.

In the present investigation two subgrid-scale modeling approaches are taken. In order to reduce the computational cost all but one simulation are performed without relying on deconvolved quantities, i.e. the effect of unresolved scales is modeled using only the previously described relaxation term. The influence of the original ADM formulation is addressed separately (see section 3.6). As has been pointed out by Stolz (2000) the relaxation term can also be interpreted as applying a secondary filter to \bar{f} every $1/(\chi\Delta t)$ time steps where Δt is the computational time step and χ is the relaxation coefficient to be determined. Note that the transfer function of the relaxation term is similar to the one of an explicit filter employed in a series of investigations by Bailly & Bogey (2006) and Bogey & Bailly (2006c, 2007) which will serve as reference data. Thus, the first approach can be interpreted as taking the primary filtered quantities \bar{f} as grid-filtered quantities. The deconvolution operator Q_N is employed only in order to determine the functional form of the relaxation term, however, no deconvolved quantities are used. This approach has successfully been applied to incompressible channel flow (Schlatter *et al.*, 2004). We will refer to this model as ADM-RT since only the relaxation term of ADM is employed. The set of governing

equations for ADM-RT thus simplifies to

$$J^{-1} \partial_t (\rho) + \partial_{\xi_i} (J^{-1} \xi_{i,j} \rho u_j) = -\chi_C (I - Q_N * G) * \rho \quad (2.16a)$$

$$\begin{aligned} \partial_t (J^{-1} \rho u_i) + \partial_{\xi_k} (J^{-1} \xi_{k,j} (\rho u_i u_j + p \delta_{ij} - \tau_{ij})) \\ = -\chi_M (I - Q_N * G) * \rho u_i \end{aligned} \quad (2.16b)$$

$$\begin{aligned} \partial_t (J^{-1} E) + \partial_{\xi_k} (J^{-1} \xi_{k,j} ((E + p) u_j - \tau_{ij} u_i + q_j)) \\ = -\chi_E (I - Q_N * G) * E. \end{aligned} \quad (2.16c)$$

Here, the Favre-filtered velocities (as defined by equation (2.3)) are not denoted by a tilde for clarity. When the deconvolution of the convective terms is employed, a similar system of governing equations for ADM as given by Stolz (2000) is obtained. This set of equations is repeated here for completeness:

$$J^{-1} \partial_t (\bar{\rho}) + \overline{\partial_{\xi_i} (J^{-1} \xi_{i,j} (\rho u_j)^*)} = -\chi_C (I - Q_N * G) * \bar{\rho} \quad (2.17a)$$

$$\begin{aligned} \partial_t (J^{-1} \overline{\rho u_i}) + \overline{\partial_{\xi_k} (J^{-1} \xi_{k,j} ((\rho u_i)^* (\rho u_j)^* / \rho^* + \check{p}^* \delta_{ij} - \check{\tau}_{ij}^*))} \\ = -\chi_M (I - Q_N * G) * \overline{\rho u_i} \end{aligned} \quad (2.17b)$$

$$\begin{aligned} \partial_t (J^{-1} \overline{E}) + \\ \overline{\partial_{\xi_k} (J^{-1} \xi_{k,j} ((E^* + \check{p}^*) (\rho u_j)^* / \rho^* - \check{\tau}_{ij}^* (\rho u_i)^* / \rho^* + \check{q}_j^*))} \\ = -\chi_E (I - Q_N * G) * \overline{E}. \end{aligned} \quad (2.17c)$$

What remains is a specification of the relaxation coefficients χ_i , where the index $i = C, M, E$ denotes the coefficients for the continuity, momentum and energy equations, respectively. Stolz *et al.* (2001b) describe a procedure how to determine the relaxation coefficient dynamically depending on the amount of kinetic energy contained in the wavenumber range above the filter cutoff. To further reduce the number of computational operations and thereby the computational cost, the relaxation coefficient is set equal to a constant value in the present work. This procedure has shown to give reliable results for high Reynolds number jet flow and its directly computed aeroacoustic noise (Keiderling & Kleiser, 2007) using the originally proposed upper bound of $\chi = \chi_C = \chi_M = \chi_E = 1/\Delta t$ (Δt is again the computational time step). These findings are supported by results of Müller (2007) who compared LES data using ADM for different but constant values χ to DNS data. For a swirling jet flow he found only minor changes in the vicinity of the

centerline when changing χ . In the following, we refer to the vector of resolved conservative variables as \mathbf{Q} for both SGS modeling approaches, i.e., $\mathbf{Q} = (\rho, \rho u_1, \rho u_2, \rho u_3, E)^T$ in the case of the relaxation term model is used equivalently to $\mathbf{Q} = (\bar{\rho}, \bar{\rho}\tilde{u}_1, \bar{\rho}\tilde{u}_2, \bar{\rho}\tilde{u}_3, \bar{E})^T$ in the case of ADM.

The focus of this work is not on modeling approaches for the SGS terms. However, we note that the chosen SGS closure may have an effect not only on the flow field but also on the aerodynamically generated acoustic field. This effect was investigated, for example, by Seror *et al.* (2001) for forced isotropic turbulence or by Andersson *et al.* (2005a) and Bogey & Bailly (2005a) for subsonic jet noise.

2.3 Description of employed filter

The functional form of the employed filter G as introduced in equation (2.2) is now specified. The three-dimensional filtering operation is realized by the successive application of one-dimensional filter operations in each spatial direction. For details concerning its construction as well as a comparison to various other approaches reported in literature we refer to the work of Stolz (2000). In particular the determination of the filter coefficients α_j and the treatment of near-boundary grid points by asymmetric stencils is reported in his appendix B and not repeated here. We only give the one-dimensional filter employed in the interior of the domain.

As will be shown shortly, the most appropriate coordinate system are cylindrical coordinates. This choice results in two inhomogeneous coordinate directions, the radial (r) and the streamwise or axial (z) direction, and the homogeneous azimuthal direction (θ). In the interior of the domain, the inhomogeneous axial and radial direction are filtered using an explicit five-point stencil. The discrete filtered function values are thus given by

$$\bar{f}_i = (G * f)|_i = \sum_{j=-2}^2 \alpha_j f_{i+j}. \quad (2.18)$$

Its transfer function follows as

$$\hat{G}(\omega) = \sum_{j=-2}^2 \alpha_j \exp(i \omega j). \quad (2.19)$$

The filter coefficients α_j can be determined for non-equidistant grids along curved lines without loss of generality using the constraints outlined in Stolz (2000). For an equidistant grid equation (2.19) is real and given by

$$\hat{G}(\omega) = \frac{5}{8} + \frac{1}{2} \cos(\omega) - \frac{1}{8} \cos(2\omega), \quad (2.20)$$

which is also employed in Fig. 2.1. We note that as a result of the construction procedure the cutoff wavenumber ω_c of the explicit filter \hat{G} is approximately $\omega_c \approx 0.63\pi$. Here, the cutoff wavenumber ω_c separates resolved wavenumbers $\omega \leq \omega_c$ from inaccurately represented wavenumber $\omega_c < \omega \leq \omega_N$, where ω_N is the Nyquist wavenumber $\omega_N = \pi$ (with a wavelength twice the constant grid spacing in the computational space).

In the homogeneous azimuthal direction θ the filtering is performed directly in wavenumber space by multiplying each Fourier coefficient by \hat{G} .

2.4 Simulation method

Following the method of lines, the system of time-dependent partial differential equations is treated separately, i.e., the spatial problem is solved independently of the temporal problem. As pointed out before, the most natural choice for a coordinate system to simulate round jet flow is a cylindrical coordinate system established by the spatial coordinates (r, θ, z) . This leads to two inhomogeneous coordinate directions (r and z) and the homogeneous azimuthal direction (θ). In addition, simply because of the transformation from Cartesian to cylindrical coordinates (i) the inverse of the radial coordinate r appears in the governing equations which thus become singular at $r = 0$ and (ii) additional force terms arise (centrifugal and Coriolis force) which necessitate a specific numerical treatment. The first problem is dealt with in the next section, whereas the latter can be avoided by using the previously introduced generalized coordinates ξ .

In order to solve the governing equations expressed in generalized coordinates (ξ, η, ζ) an appropriate mapping is used which connects the two coordinate systems. Anderson *et al.* (1968) and Vinokur (1974) present a conservative formulation of the Navier-Stokes equations in cylindrical

coordinates by defining the generalized coordinates $\xi = (\xi, \eta, \zeta)^T$ as

$$\xi = \theta/(2\pi) = \arctan(x_3/x_1)/(2\pi) \quad (2.21a)$$

$$\eta = z/L_z = x_2/L_z \quad (2.21b)$$

$$\zeta = r/L_r = \sqrt{x_1^2 + x_3^2}/L_r, \quad (2.21c)$$

where parameters L_r and L_z are the length of the computational domain in radial and streamwise direction. Figure 2.2 shows a sketch of the relation between the cylindrical grid represented by Cartesian coordinates (x_1, x_2, x_3) and the cylindrical coordinates (r, θ, z) . Also the corresponding generalized computational space coordinates (ξ, η, ζ) are illustrated. On the right-hand side of equations (2.21a)–(2.21c) the relation between cylindrical coordinates and Cartesian coordinates (as introduced in equations (2.4a)–(2.4c)) is given. The velocity components in the cylindrical coordinates system are denoted by (u, v, w) and correspond to the radial, azimuthal and axial velocity. These velocity components can be determined from the Cartesian velocity components $((u_1, u_2, u_3))$ as employed in the numerical code) using the rotation matrix

$$\begin{bmatrix} u \\ v \\ w \end{bmatrix} = \begin{bmatrix} \cos \theta & 0 & -\sin \theta \\ -\sin \theta & 0 & -\cos \theta \\ 0 & 1 & 0 \end{bmatrix} \begin{bmatrix} u_1 \\ u_2 \\ u_3 \end{bmatrix}. \quad (2.22)$$

Before we turn to the description of the discretization schemes in space and time the treatment of the singular line $r = 0$ of the cylindrical coordinate system is addressed.

2.4.1 Cylindrical coordinate singularity treatment

Various methods dealing with the cylindrical coordinate singularity have been proposed in literature and were successfully employed for sub- as well as supersonic jet flow investigation. For a concise overview of different approaches we refer to Freund *et al.* (1997). In their work derivatives at $r = 0$ are determined in a Cartesian coordinate system and the radial and azimuthal velocities are transformed into Cartesian velocities. They note that it is possible to construct a finite difference grid with no grid point at $r = 0$ and to employ difference stencils that span the centerline without evaluations at the pole. However, because of smoothness requirements for the grid stretching and the cost of coordinate transforms for the flux evaluations they render this approach undesirable. On the

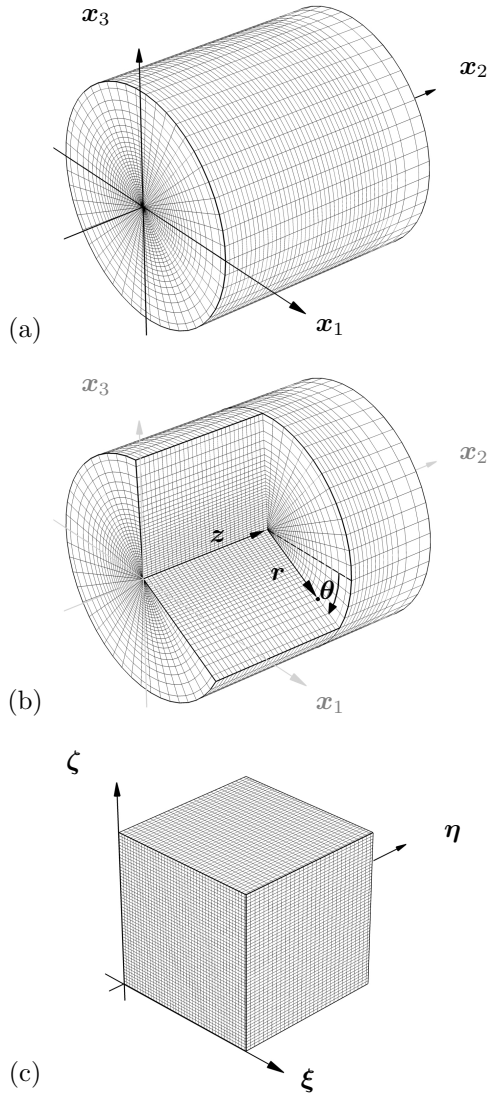


Figure 2.2: Sketch of (a) cylindrical grid in Cartesian coordinate system (x_1, x_2, x_3) (b) partial view of cylindrical grid with cylindrical coordinates (r, θ, z) and (c) computational space in generalized coordinates (ξ, η, ζ) .

other hand, Mohseni & Colonius (2000) employ exactly this approach by using a shifted grid in the radial direction and thereby avoid a change of the numerical scheme or the application of boundary schemes in the vicinity of the pole. More recently, Constantinescu & Lele (2003) proposed a set of governing equations valid at the pole based on a series expansion near $r = 0$.

In order to retain the conservative formulation of the governing equations, the approach of Mohseni & Colonius (2000) is followed here. In their approach, the radial coordinate is mapped from r to \tilde{r} as indicated by the arrow, yielding the domain $[0, R] \times [0, 2\pi] \mapsto [-R, R] \times [0, \pi]$. Figure 2.3 shows a sketch of the domain in the $r - \theta$ as well as in the mapped $\tilde{r} - \theta$ plane. It should be pointed out that radial derivatives

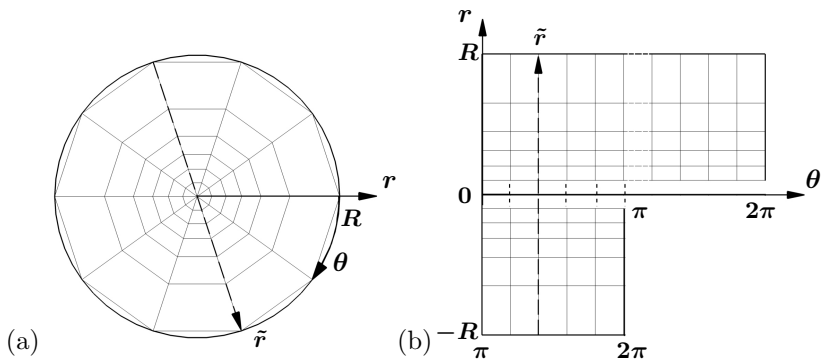


Figure 2.3: Sketch of (a) physical domain in $r-\theta$ -plane and (b) mapped computational domain during evaluation of radial derivatives.

are evaluated with respect to the mapped coordinate \tilde{r} , which avoids a boundary scheme close to the pole. Thereby, a change of the numerical scheme is alleviated within the region of interest and differentiation can be performed across the centerline without any boundary scheme. This approach restricts the choice of the azimuthal resolution N_θ to be even. Note that in the discrete computational space the mapped domains are defined as $(0, R] \times [0, 2\pi] \mapsto [-R, R] \setminus \{0\} \times [0, \pi)$.

Barré (2006) compares the approaches by Mohseni & Colonius (2000) and Constantinescu & Lele (2003). Because of the more stringent time-step restriction in the latter approach (the first radial grid cell is of size $\Delta r/2$ and thus the azimuthal stencil size $r_k \Delta \theta$ is smaller) he prefers the

first one. For computational schemes which discretize the homogeneous direction by using a Fourier spectral method, this restriction can be easily alleviated by artificially reducing the number of retained modes as done by Freund *et al.* (1997) and also documented by Canuto *et al.* (1988). The mode reduction employed here is described below in the context of the discretization in the azimuthal direction.

2.4.2 Spatial discretization

First, the discretization scheme for the radial and streamwise direction will be described followed by the description of the schemes employed in the periodic azimuthal direction. For completeness we point out that the governing equations are discretized as described in section 2.2, i.e., we evaluate the convective and the diffusive terms and then determine the corresponding flux derivatives by successive application of first-derivative operators.

Radial and axial discretization

To achieve a high order of convergence and not having to use overly wide stencils that would cause problems at the computational boundaries the discrete differential operators are approximated by compact finite differences of tenth order (Lele, 1992). On equidistant grid points with spacing Δ in the computational space the first derivative of a function f at grid point j , denoted in this section by f'_j , can be implicitly approximated by

$$\begin{aligned} \frac{1}{20}f'_{j-2} + \frac{1}{2}f'_{j-1} + f'_j + \frac{1}{2}f'_{j+1} + \frac{1}{20}f'_{j+2} = \\ \frac{17}{24} \frac{f_{j+1} - f_{j-1}}{\Delta} + \frac{101}{600} \frac{f_{j+2} - f_{j-2}}{\Delta} + \frac{1}{600} \frac{f_{j+3} - f_{j-3}}{\Delta}. \end{aligned} \quad (2.23)$$

For the treatment of the inhomogeneous boundaries the explicit seven-point difference stencil requires the closure at three boundary nodes. For brevity, we report only the order of employed approximations: the schemes at the boundaries ($j = 1, N$) and at the next-to-boundary nodes ($j = 2, N - 1$) are third-order and fifth-order accurate, both being compact and asymmetric. At the second next-to-boundary nodes the scheme is of sixth order, compact and symmetric. For details concerning the coefficients of the respective schemes and the choice of boundary closure we refer to Lele (1992). The approximation of the first derivative of the

employed schemes is illustrated in Fig. 2.4 where the modified wavenumber $\tilde{\omega}$ is plotted versus the wavenumber ω . The solid line corresponds to exact differentiation. For the tenth-order differentiation scheme employed in the present LES the modified wavenumber $\tilde{\omega}$ is close to the exact wavenumber for $\omega \lesssim 3\pi/4$. Equation (2.23) results in a band-

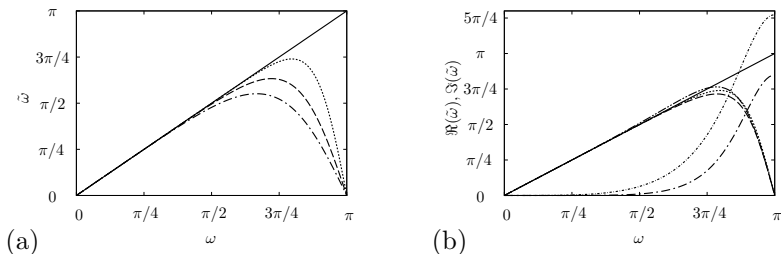


Figure 2.4: (a) Modified wavenumber $\tilde{\omega}$ vs. wavenumber ω for central schemes of different order: \cdots 10; $---$ 6; $- \cdot -$ 4. (b) Real and imaginary part of modified wavenumber $\tilde{\omega}$ vs. wavenumber ω for asymmetric boundary schemes of order 5 (\Re $---$, \Im $- \cdot -$) and 3 (\Re $- \cdot -$, $-\Im$ $---$). For comparison the modified wavenumber $\tilde{\omega}$ of the central scheme of tenth order is replotted (\cdots).

structured matrix with an implicit stencil width of five points and an explicit side of width seven. This penta-diagonal system is solved by performing one LU-decomposition of the constant coefficient matrices and storing the results. Subsequently, forward-backward substitution is employed to calculate the derivatives (Adams, 1993).

The tenth-order compact scheme in the interior is favored over other, say lower order schemes or schemes optimized with respect to their dispersion properties, for two reasons: First, a highly efficient implementation of solvers for penta- as well as tri-diagonal band-structured matrices is at our disposal and therefore the increase in order of accuracy does only insignificantly increase the computational cost. Second, the compact schemes are well established and tested, whereas the question if optimized schemes (in combination with explicit time-integration schemes used in practice) maintain their order in applications with artificial boundary conditions and large wave-propagation distances is subject of ongoing discussions (Pirozzoli & Bernardini, 2007).

Azimuthal discretization

The derivatives in the homogeneous azimuthal direction are computed using a Fourier pseudo-spectral method. For evaluation of the derivatives the physical space quantities are transformed into wavenumber space. The discrete Fourier transform for the Fourier coefficient \hat{f} for azimuthal wavenumber n is given by

$$\hat{f}_n = \frac{1}{N_\theta} \sum_{j=0}^{N_\theta-1} f_j e^{-i(n\theta_j)}, \quad (2.24)$$

where N_θ is the number of azimuthal grid points, n is given by $-N_\theta/2 + 1 \leq n \leq N_\theta/2 - 1$, $f_j = f(\theta_j)$ is the function value at grid point j and $\theta_j = 2\pi j/N_\theta$ with $j = 0, \dots, N_\theta - 1$. The inverse transform is

$$f_j = \sum_{n=-N_\theta/2+1}^{N_\theta/2-1} \hat{f}_n e^{i(n\theta_j)}. \quad (2.25)$$

Differentiation can be performed in Fourier space by multiplying each Fourier coefficient by the imaginary unit times the corresponding wavenumber according to

$$f'_j = \sum_{n=-N_\theta/2+1}^{N_\theta/2-1} in \hat{f}_n e^{i(n\theta_j)}. \quad (2.26)$$

Note that in the present implementation an additional factor of 2π appears due to the transformation from computational space of length one to physical space coordinate θ with a 2π -periodicity. As pointed out previously (section 2.4.1) steps are taken to alleviate the time-step restriction which stems from the azimuthal grid spacing becoming excessively fine as $r \rightarrow 0$. A simple yet effective method is to artificially reduce the number of retained Fourier modes as described by Freund *et al.* (1997). We truncate the summation in equation (2.26) as a function of radial location, i.e., the number of modes N_θ is replaced by a number of retained modes N_θ^r

$$f'_j = \sum_{n=-N_\theta^r/2+1}^{N_\theta^r/2-1} in \hat{f}_n e^{i(n\theta_j)} \quad (2.27)$$

with

$$N_\theta^r = N_\theta^T(r_k) = \min(2 + 4 \cdot k, N_\theta), \quad (2.28)$$

$k = 1$ at the first radial grid line and $k = N_r$ at the outer radial boundary. The radial dependence of the number of retained Fourier modes is visualized in Fig. 2.5.

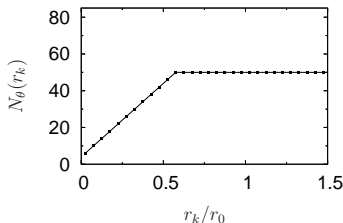


Figure 2.5: Visualization of linear dependence (in the interior) of the number of retained Fourier modes N_θ^r on the discrete radial coordinate r_k marked by

2.4.3 Temporal discretization

In CFD, commonly used integration schemes are explicit third- and fourth-order accurate Runge-Kutta methods because of their relatively large stability regions. To reduce the size of memory that needs to be addressed the integration steps are often rearranged to allow for a low-storage formulation as described by Williamson (1980) which requires only two additional memory arrays per variable. In computational aeroacoustics the choice of time-integration scheme is not purely driven by the formal order of accuracy but also by the fact that wave propagation needs to be time-accurate for relatively long integration times. Therefore, Hu *et al.* (1996) propose to employ multi-stage schemes but to optimize the dispersion and dissipation properties at a certain order rather than obtaining the maximum possible formal order of accuracy. Based on accuracy test performed by Müller (2007) we choose to use a recently proposed explicit low-storage fourth-order accurate Runge-Kutta method by Berland *et al.* (2006). It is based on a six-stage scheme where two coefficients are employed to optimize the scheme's dispersion and dissipation properties. Note that Müller (2007) compared several integration schemes and found that this scheme offers very good stability properties. More importantly, it maintains the order of accuracy for non-autonomous problems, i.e., a time-dependent integrand, which is essential for the kind of inflow forcing we employ. For details concerning

convergence tests and implementation details such as the coefficients of the particular scheme we refer to the literature (Berland *et al.*, 2006) and the work of Müller.

In order to determine an estimate for the admissible time-step a model equation containing advection and diffusion properties is solved (Adams, 1993; Müller, 2007). This time-step limit depends on the combination of spatial and temporal discretization and their respective stability limits at each grid point. Following the derivation given by Müller (2007) the following CFL condition is obtained

$$\Delta t < \frac{\text{CFL}}{A}, \quad (2.29)$$

with A given by

$$\begin{aligned} A = \pi \left(\frac{|u| + \sqrt{T}/Ma}{\Delta r} + \frac{(|v| + \sqrt{T}/Ma)N_{\theta}^r(r_k)}{N_{\theta}r\Delta\theta} \right. \\ \left. + \frac{|w| + \sqrt{T}/Ma}{\Delta z} \right. \\ \left. + \pi d_{\max} \left(\frac{1}{\Delta r^2} + \frac{(N_{\theta}^r(r_k))^2}{N_{\theta}^2 r^2 \Delta\theta^2} + \frac{1}{\Delta z^2} \right) \right), \end{aligned} \quad (2.30)$$

and

$$d_{\max} = \max \left(\frac{\mu}{\rho Re}, \frac{\mu}{\rho(\gamma - 1)Ma^2 Pr Re} \right). \quad (2.31)$$

As introduced in the context of mode-clipping in the azimuthal direction (see section 2.4.2), N_{θ}^r denotes the number of retained Fourier modes and r_k the discrete radial coordinate r at radial grid line with index k . In equation (2.29) CFL is given by the convective and diffusive stability limits of the time-integration scheme. As can be seen from the denominator of d_{\max} the heat conduction and viscous effect will not restrict the time-step due to the high Reynolds number of the current jet flow. We can expect the stability of the time integration to depend on the convective term. For purely convective problems the CFL number of the employed scheme is $\text{CFL} \approx 3.8$. Recall that the CFL number defined in equation (2.30) is formulated in wavenumber space and thus is larger by a factor of π for the convective limit compared to the effective CFL number (for details such as the stability diagrams for the employed low-dispersion and dissipation scheme we again refer to Müller (2007) and Berland *et al.* (2006)).

As mentioned before the employed grid, in particular in the azimuthal direction, is very fine and thus necessitates very small time steps. This small time step in combination with the long integration times (necessary to converge low-frequency near-field noise) rendered such simulations infeasible from a computational cost point of view. Therefore, we decided to only monitor the above criterion and determine empirically a time step that yielded stable time integration. Partially this approach is motivated by the SGS model which positively influences the stability properties but is not accounted for in the model equation determining the admissible time step. Using equation (2.29) as time-step criterion yields a CFL number of $\text{CFL} \approx 6.5$ at the first radial grid line and $\text{CFL} \approx 5.0$ at the second radial grid line. At the radial position of $r(k = 12)$, where the mode-clipping is inactive, we find $\text{CFL} \approx 4.5$. Within the shear-layer, i.e. at the radial location with $k = 19$ the criterion further relaxes to $\text{CFL} \approx 4.0$ and has proven to yield stable long-time simulations.

2.5 Boundary treatment

As pointed out before, the definition of suitable boundary conditions is crucial, particularly in the context of aeroacoustics. Even minute discrepancies with Navier-Stokes dynamics result in the generation of artificial fluctuations that can overwhelm the physical noise. The physical modeling of a – at least theoretically – infinite domain poses additional problems for the simulation of free jet flows. In contrast to flows which have a well-defined co-flow the entrainment velocities cannot be known in advance. The surrounding fluid is entrained by the vortex interaction within the jet shear layer and the resulting velocity field is thereby merely a consequence of it. Experimental investigations that could provide data for the definition of suitable boundary conditions are rare and often the three-dimensional velocity field is determined by measuring two velocity components and analytically calculating the third one. In the literature, various approaches have been proposed to mimic numerically the infinite domain. These range from characteristics-based boundary conditions (so-called nonreflecting boundary conditions) to damping zones (so-called sponge-layers, buffer-domains or fringe-regions) or a combination of both. For a review see the article by Colonius (2004).

Initial tests relied on a combination of Dirichlet inflow boundary conditions supplemented by an inflow sponge to prevent spurious oscillations generated by upstream-traveling sound waves hitting the fixed

inflow boundary. This approach did not yield satisfactory results: First, the inflow sponge region had to be relatively large to allow the sound waves to decrease sufficiently in amplitude. Second, the strongly imposed Dirichlet boundary condition (with zero velocity on the side of the jet) prevented the physically correct entrainment of fluid from upstream. Therefore, we take a similar approach as Bogey & Bailly (2006a) consisting of only weakly enforced boundary conditions and nonreflecting boundary conditions. Figure 2.6 shows a sketch of the computational domain and the imposed boundary conditions. The respective details are described briefly in the following subsections.

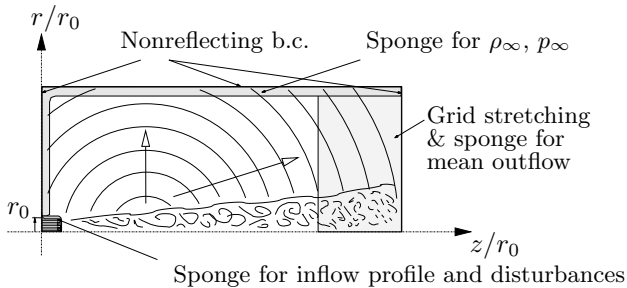


Figure 2.6: Sketch of computational domain, boundary conditions and simulation set-up. Shaded areas mark sponge layers and the grid-stretching area/sponge layer in the outflow region.

2.5.1 Nonreflecting boundary conditions

As illustrated in Fig. 2.6 all boundaries of the computational domain employ nonreflecting boundary conditions (Thompson, 1987). It proved necessary to take the conservative formulation expressed in curvilinear coordinates at the radial boundary into account by adapting the characteristics. Otherwise disturbances were generated at the outer boundary that eventually led to numerical instability. For brevity, we do not outline the derivation of the characteristic variables and their adaptation but refer to the work of Kim & Lee (2000).

2.5.2 Sponge-layer technique

As described before, the nonreflecting boundary conditions are supplemented by sponge layers (Israeli & Orszag, 1981; Bodony, 2006) which define the inflow condition and the lateral and outflow boundary conditions of the computational domain. In this sponge zone an artificial term is added to the right-hand side of the Navier-Stokes equations according to the general form

$$\frac{\partial \mathbf{Q}}{\partial t} = \mathcal{RHS}(\mathbf{Q}) - \sigma(\mathbf{Q} - \mathbf{Q}_{\text{ref}}). \quad (2.32)$$

Here, \mathbf{Q} denotes again the unknown conservative state vector, \mathcal{RHS} represents all flux terms of the Navier-Stokes equations written on the right-hand side and \mathbf{Q}_{ref} denotes a reference state to be defined. If the sponge coefficient σ (that may vary in space) is greater than zero in equation (2.32), the vector \mathbf{Q} is driven to the known vector \mathbf{Q}_{ref} .

In the present work, the sponge regions shown in Fig. 2.6 are treated as follows. In the *inflow-sponge* region, disturbances equivalent to amplified eigenmodes predicted by linear stability theory (LST) are superimposed on a hyperbolic-tangent inflow profile in a similar fashion as done by Lui & Lele (2003) and Bodony & Lele (2004). For an example of instability-wave excitation in jet-noise investigations we refer to the work of Bodony & Lele (2005) and Bodony (2006), where, in particular, the latter addresses technical issues of the sponge technique in this context. Implementation details of the disturbance triggering can be found in appendix B.

Close to the jet inflow a sponge surrounding the computational domain in the radial and upstream directions is employed to prevent a mean pressure drift reported for example by Colonius *et al.* (1997). This thin sponge layer exclusively acts on density and pressure, i.e. $\mathbf{Q}_{\text{ref}} = (\rho_{\infty}, 0, 0, 0, ((\gamma - 1)\gamma Ma^2)^{-1})^T$, which maintains their ambient-state values. With this approach no reference solution needs to be imposed, such as results of a precursor Reynolds-averaged Navier-Stokes simulation as done, for example, by Bodony & Lele (2004, 2005). In the following, we refer to this sponge region as the *ambient sponge* described in more detail in appendix B.2.

At the outflow, the instantaneous flow field is relaxed to a spatially varying axisymmetric mean flow to prevent spurious acoustic reflections generated by passing vortices that violate the 1D nonreflecting boundary

conditions. This *outflow sponge* reference solution is based on a separate three-dimensional simulation using the same set-up averaged over 25 flow-through times L_z/U_j and in the azimuthal direction, however without an outflow sponge. The same outflow reference solution is employed for all simulations. Further details can be found in section 2.8 and in appendix B.2.

2.5.3 Inflow treatment

The treatment of the inflow boundary and thereby the definition of the inflow condition is very important. Gutmark & Ho (1983) for example, tabulated various jet flow experiments and observed a huge variation of self-similar quantities such as the jet spreading rate. They linked this phenomenon to spatially coherent structures inherently present in the various testing facilities to which the jet flow reacted very sensitively. Researchers attempt to exploit this sensitivity in the context of jet-noise suppression (as pointed out in the introductory section 1.2). In particular for numerical simulations this sensitivity becomes an important issue: as pointed out before all jet-noise simulations have in common that either turbulent inflow conditions are to be prescribed or disturbances have to be introduced into an initially laminar flow to initiate transition to turbulence. No matter which approach is favored it is challenging to distinguish between physical effects and numerical artifacts (which stem from the interaction of the natural sensitivity and the artificial inflow definition) unless a parametric study of inflow parameters shows consistent trends. The studies by Stanley & Sarkar (2000) or Bogey & Bailly (2005*b*) are examples for the numerically investigated sensitivity of jets.

2.5.4 Linear stability investigation

As outlined in section 1.4, we intend to investigate the nonlinear interaction of unstable modes and their role in the noise generation mechanism. Therefore, transition to turbulence is triggered by superimposing a number of unstable modes onto the base flow. To determine these modes, a classical wave ansatz for the disturbances is introduced to the linearized compressible Navier-Stokes equations in cylindrical coordinates. The resulting eigenvalue problem is then solved using a Chebyshev collocation method (Müller *et al.*, 2004; Müller & Kleiser, 2008). The detailed derivation of the linearized governing equations as well as the numerical methods for solving them can be found in appendix A. In this subsection,

the results of the linear stability investigation of the base-flow profile are described. At the inflow a hyperbolic-tangent base-flow profile representative for jet flow profiles close to the jet nozzle exit (Michalke, 1984),

$$\frac{w_b}{U_j} = \frac{1}{2} \left[1 + \tanh \left\{ \frac{r_0}{2\theta_0} \left(1 - \frac{r}{r_0} \right) \right\} \right], \quad (2.33)$$

is imposed where the initial momentum thickness is set to $\theta_0/r_0 = 1/20$. This value is chosen such that the steep gradients within the velocity profile can adequately be resolved by the used grid. In numerical studies and in LES, in particular, the choice of the initial momentum thickness is driven by computational cost constraints. Experimentally observed initial momentum thicknesses can be smaller by at least an order of magnitude. Zaman (1985), for example, reports $\theta_0/r_0 \approx 1/250$ for jets at Reynolds numbers of $Re \gtrsim 2.5 \cdot 10^5$. Correspondingly, a jet exit boundary layer with the currently investigated initial momentum thickness would be laminar and at Reynolds numbers below 10^5 , as also supported by the data of Zaman.

The spatial stability properties of the base-flow profile given by equation (2.33) are analyzed using the previously mentioned Chebyshev collocation method. Different azimuthal wavenumbers n are investigated with respect to their linear spatial stability properties. Note that at the inflow plane two length scales are appropriate for the jet flow, the initial momentum thickness θ_0 and the jet diameter D_j . Here, we rely on a scaling of the frequency ω based on the diameter D_j because we are interested in the downstream development where the thickness becomes comparable to D_j and hence, curvature effects become important. For stability investigations of profiles with varying initial momentum thickness the relevant length scale becomes θ_0 , as will be shown below.

The growth rates as well as phase speeds associated with the viscous instabilities of the inflow profile (equation (2.33)) are shown in Fig. 2.7 as a function of the Strouhal number $St = \omega D_j / (2\pi U_j)$. In Fig. 2.7(a) the growth rate is indicated by the imaginary part of the streamwise wavenumber α_i . Figure 2.7(b) shows the phase speed of the disturbances which is the ratio of the angular frequency to the real part of the streamwise wavenumber, ω/α_r . In agreement with results reported by Michalke (1984) we find the axisymmetric or varicose mode $n = 0$ to be least stable reaching maximum amplification around $St = 0.676$. This corresponds to $St_\theta = \omega\theta_0/(2\pi U_j) = 0.0169$ which is in good agreement with the inviscid theoretical value of $St_\theta = 0.0165$ (Michalke, 1984). At

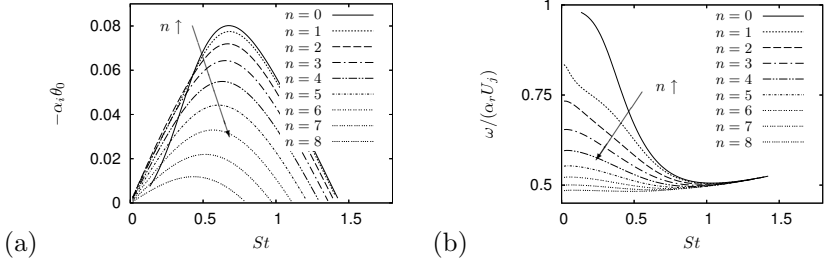


Figure 2.7: a) Growth rate $-\alpha_i$ vs. St and b) phase speed ω/α_r vs. St for different azimuthal wavenumbers n .

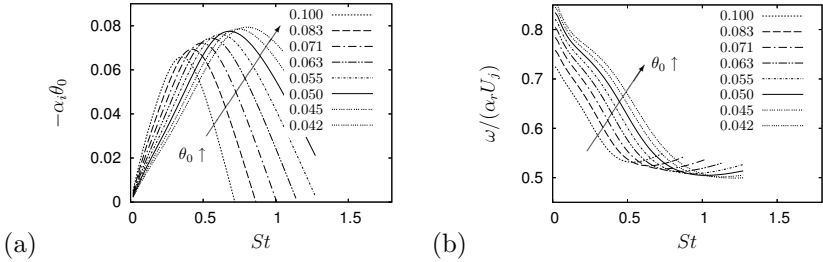


Figure 2.8: (a) Growth rate $-\alpha_i$ vs. St and (b) phase speed ω/α_r vs. St for different values of initial momentum thickness θ_0 .

low frequencies ω , the growth rates $-\alpha_i$ for mode $n = 0$ are no longer dominant and for $St \lesssim 0.42$ the helical mode $n = 1$ is least stable. In Fig. 2.7(b) one finds that all disturbances with $St > 0.8$ propagate with similar phase speed ω/α_r .

The dependence of the stability properties on the initial momentum thickness θ_0 is shown in Fig. 2.8 for the helical mode $n = 1$. On the left of Fig. 2.8 the growth rate is plotted versus the Strouhal number and on the right the corresponding phase speed is given. The solid bold line denotes $\theta_0 = 0.050$ which is employed for the LES inflow profile. With an increase in the initial momentum thickness, i.e., when the steepness of the velocity profile increases, the growth rates increase and the locations of maximum amplification shift to higher Strouhal numbers. Also, for $St \leq 0.5$ the phase velocity increases with larger initial momentum thickness. For higher Strouhal numbers this trend is inverted and profiles with lower θ_0 exhibit higher phase speeds.

The same data is shown again in Fig. 2.9 using the initial momentum

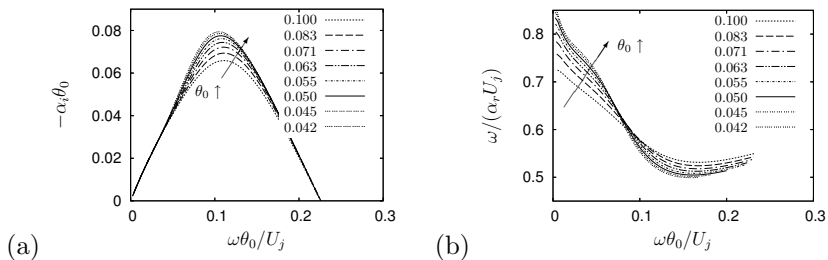


Figure 2.9: (a) Growth rate $-\alpha_i$ vs. ω and (b) phase speed ω/α_r vs. ω for different values of initial momentum thickness θ_0 .

thickness θ_0 as relevant length to scale ω . Now, we observe a perfect alignment of the growth rates $-\alpha_i$ with increasing initial momentum thickness. The locus below and above which the phase speed is increased or decreased for larger θ_0 shifts to $\omega \theta_0 / U_j \lesssim 0.08$ because of the different scaling of the frequency.

2.5.5 Inflow disturbance seeding

As pointed out before, transition is triggered by a collection of flow instabilities that are superimposed onto the base flow. To this end, azimuthal wavenumbers $|n| = n_{\min}, \dots, n_{\max}$ (i.e., right- and left-turning modes $\pm n$) are excited at those frequencies which give the maximum growth rate (fundamental frequencies). The parameter n_{\max} is set to 8 which is the highest unstable azimuthal wavenumber. Depending on the type of modal composition that is investigated n_{\min} is chosen differently: First, we excite all unstable helical modes, i.e., n_{\min} is set to unity. In the second set of LES, we exclude modes $n \leq 3$ and set $n_{\min} = 4$. The motivation for this ad-hoc exclusion of low-order modes $n \leq 3$ from the forcing is twofold: First, Bodony & Lele (2002) report an over-prediction of sound pressure levels (SPL) and link it to the dominant axisymmetric mode when disturbing with LST modes $n = 0, \pm 1, \pm 2$ in their study. Second, Bogey & Bailly (2005b) report a delayed streamwise development of the jet flow and observe a reduction of SPL when excluding modes $n = 0$ through $n = 3$ from their ring-vortex forcing method. Note that the numerical reference data (Bogey & Bailly, 2005b) employs a total of sixteen azimuthal modes $|n| \leq 15$ for the inflow excitation.

The linear superposition of the eigenmodes is given by

$$\mathbf{Q}_{\text{infl}}(r, \theta, z, t) = \mathbf{Q}_b(r) + \sum_{|n|=n_{\text{min}}}^{n_{\text{max}}} \mathbf{Q}'_n(r, \theta, z, t) \quad (2.34)$$

with

$$\sum_{|n|=n_{\text{min}}}^{n_{\text{max}}} \mathbf{Q}'_n = A_{\text{total,LST}} \frac{\sum_{|n|} A_n \Re \left(\hat{\mathbf{Q}}_n(r) e^{i(\alpha_n z + n\theta - \omega_n t + \phi_n)} \right)}{\sum_{|n|} A_n}, \quad (2.35)$$

conservative state vector \mathbf{Q} at the inflow. In equation (2.34) \mathbf{Q}_b denotes the base-flow state. The complex eigenfunction $\hat{\mathbf{Q}}$ in equation (2.35) is normalized by setting $\max |\hat{w}| = 1$. Because the eigenfunctions are determined in primitive variables the conservative variables of $\hat{\mathbf{Q}}$ need to be determined (the derivation is given in appendix A.3). The laminar base flow $\mathbf{Q}_b(r)$ is derived from equation (2.33), employing the Crocco-Busemann relation for an isothermal jet flow (see e.g. Schlichting, 1979) as well as the linearized equation of state. The eigenmodes are modulated in amplitude A_n and phase ϕ_n in a random-walk fashion (see appendix B.1 for details) in order to prevent phase-locking (Bodony & Lele, 2004). The superposition of instability waves is scaled with the sum of amplitudes A_n to obtain the total disturbance amplitude $A_{\text{total,LST}}$ which will be varied parametrically.

The disturbed inflow profile \mathbf{Q}_{infl} is imposed only weakly in order to prevent reflections at the inflow as well as to allow for entrainment of surrounding fluid toward the jet shear layers. The reference state is defined by equation (2.34), i.e. by a spatially and temporally varying superposition of linearly unstable modes onto a laminar velocity profile. The influence of the disturbance amplitude $A_{\text{total,LST}}$ and the effect of exclusion of low azimuthal wavenumbers on the flow field and its associated noise is investigated. Because of the dominant role of eigenmodes in plane mixing-layer flow (see section 1.4), their role in the transition process and the noise generation of a jet is to be assessed. The LST disturbances allow specific effects of the nonlinear development of eigenmodes to be investigated.

2.6 Computational grid

The discretized set of governing equations is solved on a cylindrical grid using $N_r \times N_\theta \times N_z$ grid points. As described in section 2.4.2, we rely

on a Fourier spectral method to evaluate azimuthal derivatives in the homogeneous direction θ and, therefore, use a uniform grid. The grid in the radial and axial directions is stretched in order to adequately resolve regions with steep gradients. For the particular application of the direct jet-noise computation the large disparity of length scales (ranging from small-scale eddies in the turbulent plume of the jet to low-wavenumber waves in the acoustic near-field) necessitate well-tuned grids in the radial and axial directions as also a too rapid grid stretching be a parasitic source of sound (Coloniuss & Lele, 2004).

Radial grid

The mapping between equidistant computational and physical space obeys the symmetry constraint with respect to the pole (see the singularity treatment outlined in section 2.4.1). Therefore, the radial grid stretching is based on a mapping which was originally proposed to enhance the accuracy of pseudo-spectral approximations (Bayliss *et al.*, 1995). Details of the implementation and the evaluation of the corresponding metrics can be found in the work of Müller (2007). Here, we restrict ourselves to document the relevant parameters. The parameter α^g (in Müller's equation (3.99)) which specifies the intensity of the grid refinement is set to $\alpha^g = 2.749$. The location of the grid refinement is controlled by the parameter β^g representing the ratio of the radial position r_c where the grid is refined and the radial extent of the computational domain L_r . The symmetrically located refinements have a strong influence and thus, instead of choosing $\beta^g = 1/20$, it is increased to $\beta^g = 0.2137$ in order to shift the location of increased resolution slightly outwards. The chosen combination of α^g and β^g guarantees the smallest radial grid spacing $\Delta r = 0.05r_0$ right at the jet lip line $r = r_0$.

Axial grid

The axial mapping is based on hyperbolic-tangent functions and follows a formulation that has been employed for LES of various jets and their noise (Bodony, 2004; Bodony & Lele, 2005). This mapping allows to specify two locations where the grid is to be refined or coarsened. Because of the sensitivity of noise computations to rapid changes in the grid, we dispense with a grid refinement in the entrance region of the jet flow and only employ a grid stretching in the outflow region. Moreover, an equidistant grid over the whole physically relevant region of

the computational domain is wanted to minimize the degradation of the truncation error (Colonius & Lele, 2004). For the documentation of the functional form of the mapping we refer to Müller (2007) or Bodony (2004). The employed parameters are a_i^g , f_i^g , r_i^g and d_i^g which control the location and the inverse of the intensity of the grid stretching as well as the minimum and initial grid spacing, respectively. Index $i = 1$ denotes the inflow, $i = 2$ the outflow. The parameters are documented in Tab. 2.1.

Table 2.1: Parameters for axial grid refinement.

	inflow 1	outflow 2
a_i^g	0.0	1.03
f_i^g	10	20
r_i^g	0.05	1.8
d_i^g	1.0	0.02

2.7 Validation

In the course of the development of the numerical code different validation tests have been performed. First, the convergence behavior of the spatial discretization operators were tested and reported by Müller (2007). In his work, a boundary-layer solution for the flow field is employed to analytically evaluate all individual flux terms of the Navier-Stokes equations using the algebraic software MAPLE. The same terms were subsequently determined using the present numerical code and the difference between the exact and the numerically computed values is quantified using the L_2 -norm. The observed convergence rates match the theoretically expected values very well. Second, as documented in the work of Keiderling *et al.* (2004), the temporal evolution and formation of a tripolar vortex has been simulated in two dimensions using both a Cartesian version of the code (Adams, 2000) and the cylindrical version. Very good agreement between the results was found. For details we refer to Keiderling *et al.* (2004). Finally, the temporal growth of flow instabilities were investigated and compared to predictions from linear stability theory. This part of the validation is documented here in more detail.

For the validation two base flows are investigated with respect to their temporal stability, i.e., the previously mentioned solver for the linearized stability problem (see section 2.5.4) is employed to determine eigenvalues and eigenfunctions of disturbances that grow temporally (for details of the solver see appendix A). These linearly unstable eigenmodes are subsequently employed to initialize the Navier-Stokes solver together with the same base flow. The disturbance amplitude is set to 10^{-5} for the superposition onto the base flow and the solver is run without any SGS model contributions. After one time step the growth rate based on the total modal energy is calculated (following Hanifi *et al.* (1996)) and compared with the predicted values. The two base flows are the following: Validation case A is based on an inflow profile that corresponds to the initial mixing region of a jet, whereas the second one has been employed by Freund (2001) in his DNS and corresponds to the developed annular-mixing region (Michalke, 1984). The initial momentum thicknesses of the analytically defined profiles are scaled differently, hence, they are compared best visually, as done in Fig. 2.10. Based on the steepness of

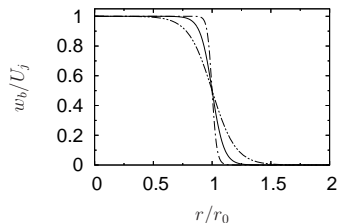


Figure 2.10: Axial velocity component of different base flows: --- validation case A, -.- validation case B, — employed LES base-flow profile (equation (2.33)).

the three velocity profiles shown in Fig. 2.10 we expect validation case B to pose highest resolution requirements for both, the Navier-Stokes code and the eigenvalue solver. As pointed out before, compared to experimental observations the initial momentum thickness employed for the current LES is artificially increased such that the shear layer can be resolved accurately by the grid.

Table 2.2 shows the dimensionless parameters for the validation cases along with the wavenumber of the disturbance in azimuthal and axial direction, n and αr_0 , respectively. The radial grid-mapping parame-

ters of the Chebyshev collocation method are given in Tab. A.1 (see appendix A.2). The grid parameters for the Navier-Stokes code are as follows: The stretching parameters for the radial grid (as defined in section 2.6) are $\alpha^g = 4.0$ and $\beta^g = 0.05$ for case A and $\alpha^g = 8.0$ and $\beta^g = 0.2$ for case B. The streamwise length of the periodic domain contains the fundamental wavelength $2\pi/\alpha$ and is resolved by $N_z = 16$ and $N_z = 64$ grid points for A and B, respectively. For all validation cases the azimuthal direction employs $N_\theta = 4$.

Table 2.2: Base-flow parameters for validation cases A and B.

Validation case	Ma	Pr	Re	n	αr_0
A	0.8	0.7	10^4	1	0.40
B	0.9	0.7	$3.6 \cdot 10^3$	0	9.35

Figure 2.11 shows typical complex eigenfunctions (cylindrical velocities u , v , w , pressure p and temperature T) for validation case A for the azimuthal wavenumber $n = 1$ and the axial wavenumber $\alpha = 0.40/r_0$. Again, all eigenfunctions are normalized by setting $\max|\hat{w}| = 1$. From the eigenfunctions we find that at $r = r_0$ (within the shear layer) very steep gradients occur which need to be resolved by the collocation points. For validation case B these gradients are even higher since the initial momentum thickness of the base-flow profile is significantly smaller than in case A (see Fig. 2.10).

The growth-rate error for various radial resolutions N_r is determined. The details of this validation are presented in Tab. 2.3. With increasing radial grid density we find convergence of the growth rates of the Navier-Stokes code to the values predicted by LST (for which the number of grid points corresponds to the Chebyshev collocation points). Table 2.3 also lists the absolute error $\Delta\omega_i$ and the relative error ε of the predicted growth rates compared to the LST results. Overall, when the steep gradients of the shear layer are adequately resolved the relative errors are on the order of $\varepsilon \approx 10^{-4}$. Note that the determination of the growth rate is difficult as the base-flow profile itself tends to zero just at the outside edge of the shear layer.

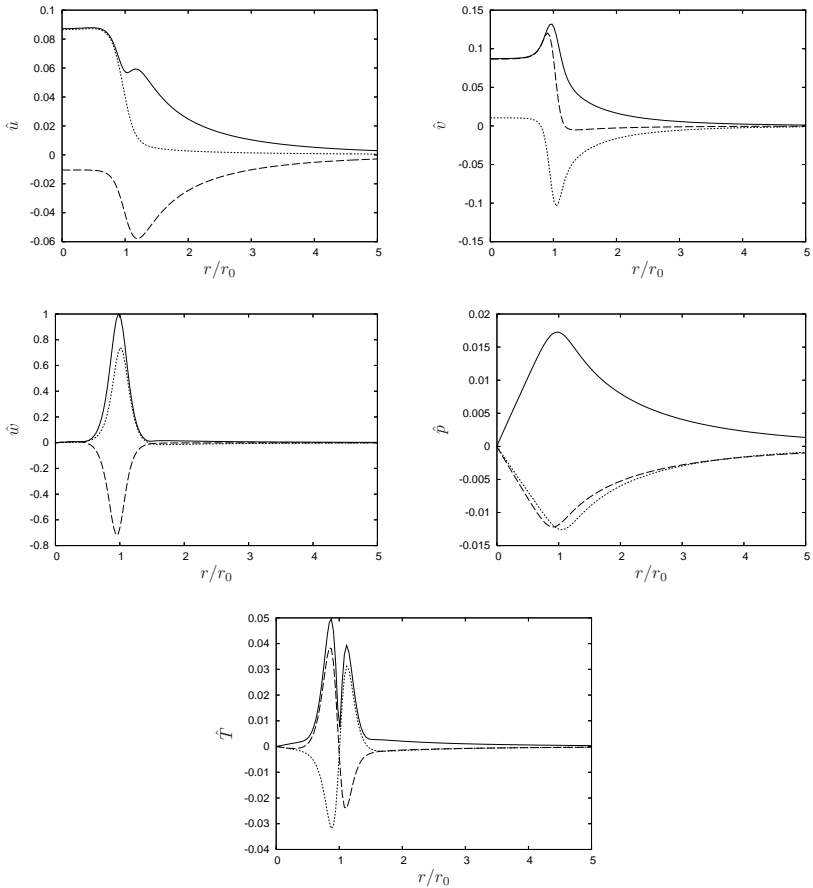


Figure 2.11: Eigenfunctions of validation case A: — magnitude $|\hat{q}|$, - - - - real part $\Re(\hat{q})$ and imaginary part $\Im(\hat{q})$.

2.8 Initial conditions and statistical analysis

All simulations are started from exactly the same initial flow field. Therefore, one simulation is performed to reach this initial state: It starts out with an initial condition based on the analytically defined hyperbolic-tangent profile which is extruded in streamwise direction (for the descrip-

Table 2.3: Convergence of temporal growth rates with radial grid refinement for validation cases A and B. LST denotes growth rate according to linear stability theory. $\Delta\omega_i$ is the absolute error and ε the relative error.

Case	N_r	ω_i	$\Delta\omega_i$	ε
A	40	0.131518	$1.990e-03$	$1.536e-02$
	80	0.129544	$1.627e-05$	$1.256e-04$
	120	0.129526	$-1.322e-06$	$-1.020e-05$
	160	0.129524	$-3.955e-06$	$-3.054e-05$
LST	150	0.129528		
B	40	1.493221	$-1.037e-01$	$-6.497e-02$
	80	1.591635	$-5.338e-03$	$-3.342e-03$
	120	1.595965	$-1.009e-03$	$-6.415e-04$
	160	1.596555	$-4.187e-04$	$-2.622e-04$
	200	1.596688	$-2.853e-04$	$-1.787e-04$
LST	350	1.596974		

tion of the profile see section 2.5.4, equation (2.33)). The forcing parameters correspond to case **Med-m** (to be defined below in section 3.1.1). This set-up is run for $T_{\text{sim}} = 120r_0/U_j$ time units (corresponding to three flow-through times of the domain based on the jet inlet velocity) in order to allow the initial disturbances to leave the computational domain. After this point in time the simulation is run for an additional 25 flow-through times ($T_{\text{sim}} = 1000r_0/U_j$) without imposing an outflow sponge reference solution. Nevertheless, in order to establish a reference solution for the outflow sponge the statistics are collected over this time span and subsequently used as reference field within the outflow sponge region (see section 2.5.2). The final time step of this simulation is employed as the initial condition for all simulations, regardless of the changes in forcing amplitude or modal composition as the initial transient effect due to these changes is considered small compared to the long integration times. We would like to point out that the setup without outflow damping yielded stable simulation results, however, in the animations of the acoustic near-field small spurious acoustic disturbances were visible. This spurious noise could be linked to vortical structures hitting the one-dimensional nonreflecting boundary condition (see section 2.5.1) and is prevented by using this outflow sponge.

The simulation time for all cases presented here is $T_{\text{sim}} = 1000r_0/U_j$

which corresponds to a minimal Strouhal number of $St = D_j / (T_{\text{sim}} U_j) = 2 \times 10^{-3}$. The time step for all simulations is set to $\Delta t = 0.02 r_0 / U_j$. Again, we note that this time step has been determined empirically and violates the CFL criterion of the model problem described in section 2.4.3. Nevertheless, it is not the stability limit of the admissible maximum time step (simulations remained stable up to a time step of $\Delta t = 0.026 r_0 / U_j$). Every fifth time step is analyzed for the flow statistics (10'000 samples) and every tenth step is stored on disk for the acoustic analysis and post-processing (5'000 samples). All mean values, unless stated otherwise, are evaluated using all azimuthal grid points (N_θ) which further increases the sample size.

The initial conditions for cases with coarsened or refined azimuthal resolution are obtained by spectrally interpolating the initial condition with $N_\theta = 50$. All azimuthal data is incorporated in the statistics, i.e., the averages are determined over all azimuthal grid points available and this effect of difference in sample size on the results is considered negligible.

2.9 Spectral signal processing of time series

In the following, we report the details of the digital signal processing employed in the spectral analysis of different time series. All spectra presented in the following are obtained in a post-processing step and are based on 5000 samples acquired over $T_{\text{sim}} = 1000 r_0 / U_j$. The sampling rate of the digitally stored data corresponds to $f_s = 5 r_0 / U_j$. To reduce the variance of the velocity and the pressure spectra the sampling interval is divided into overlapping subintervals and all data in azimuthal direction is employed, i.e., the spectra are averaged over the number of subintervals and the number of azimuthal grid points N_θ . The effects of employing finite-time intervals are reduced by applying a Hann window to each subinterval before performing a discrete Fourier transform in time. Consecutive segments overlap each other by fifty percent. We would like to stress at this point that neither filtering of the time signals nor a spectral smoothing is applied additionally. The interval length for the velocity spectra corresponds to a minimal resolved Strouhal number of $St = 0.04$ (250 samples per segment, 38 segments), whereas we follow Bogey & Bailly (2007) for the pressure spectra and resolve a minimal Strouhal number of $St = 0.1$ (100 samples per segment, 98 segments).

At the higher frequencies, the velocity and the acoustic spectra have

restrictions because of the frequency limit of the underlying data. The limiting factors are the previously mentioned sampling rate and the underlying computational grid which effectively acts as a filter on the propagating waves. The first factor, as described above, is the discrete sampling rate of $f_s = 5r_0/U_j$ with the Nyquist frequency $f_N = f_s/2$ ($St_N = 5$). The second factor is the resolution of the grid in combination with the employed discretization schemes which determines the maximum frequency that can be represented. This frequency, sometimes referred to as grid cutoff frequency or in dimensionless terms as grid Strouhal number St^g (Bodony & Lele, 2005) can be determined approximately for waves that are perfectly aligned with the grid. Let the grid spacing in (r, θ, z) direction at some point P_o be $(\Delta r, r_0\Delta\theta, \Delta_z)$. For perfectly aligned plane waves with wave vector \mathbf{k} pointing in propagation direction we have a wavelength of $\lambda = 2\pi/|\mathbf{k}|$, which now needs to be accurately resolved by the numerical scheme in the respective directions. In the homogeneous azimuthal direction, we find that $N_\theta = 2$ is sufficient to resolve a wave of wavelength λ . From the wavenumber diagram presented in Fig. 2.4 we find that in the interior of the domain wavenumbers up to $3\pi/4$ are accurately resolved in the two inhomogeneous directions. Thus, $N_r = N_z = 3$ is sufficient to resolve an aligned wave correctly. From the relation between the wave vector and the frequency, $|\omega|^2 = |\mathbf{k}|a_\infty^2$, we obtain an estimate for the frequency and thus a Strouhal number which depends on the local grid spacing (and also the azimuthal wavenumber n). In the part of the computational domain where acoustic near-field data will be provided, the current grid cutoff is $St^g \approx 5$ at the downstream observer location for downstream propagating waves and, due to the radially stretched grid, $St^g \approx 3$ for the sideline observer location for radially propagating waves. Note that the effective cutoff depends on the phase speed anisotropy and on the propagation direction due to the grid anisotropy. This aspect is addressed briefly in appendix C.

For the directly computed jet noise it should be verified that hydrodynamic effects are separated from the acoustic regime in the near field. We follow Arndt *et al.* (1997) and choose an ad-hoc threshold for $k \cdot r_s \leq 2$ where r_s is the perpendicular distance from the jet centerline and k the wavenumber given by $k = \omega/a_\infty$. This value has proven to be a reliable estimate (Tinney & Jordan, 2008) and an approximate Strouhal number can readily be determined. The closest and most critical radial location to be analyzed in the following is $r_s = 9r_0$, for which

$St = k \cdot r_s r_0 / (\pi Ma_j r_s) \leq 0.079$. For all radial locations, the estimated Strouhal numbers are therefore below $St = 0.1$ and the near-field pressure signals represent acoustic data.

Chapter 3

LES results for flow and acoustic field

The model problem of jet mixing noise described in section 1.2 is now addressed using the numerical approach outlined in chapter 2. The investigation consists of several simulations focusing on different physical parameters as well as on essential elements of the SGS-modeling approach. The results are grouped according to their respective objectives. First, the influence of the disturbance amplitude employed at the inflow plane is to be investigated for two types of modal excitation in sections 3.2 and 3.3, respectively. In section 3.4, effects of the different types of the modal composition are directly compared. Following these physical inflow parameters the effect of the underlying modeling is studied, first, by attenuating the subgrid-scale relaxation coefficient of ADM-RT (presented in section 3.5), and second, by employing the originally postulated approach of ADM (section 3.6). Finally, we address the effect of the azimuthal resolution on our simulation results. Following the causality principle, the results of each investigation are grouped into the instantaneous data, mean flow and turbulence data in the aerodynamic region and, thereafter, the aerodynamically generated noise as perceived in the near field.

3.1 Introduction

3.1.1 Parametrization

Jet flow parameters

The subject of this study is an isothermal round jet, i.e. the jet-to-ambient temperature ratio is $T_j/T_\infty = 1$. The jet Mach number is $Ma = 0.9$. The Prandtl number is set to $Pr = 0.71$. The governing equations are nondimensionalized using the jet radius $r_0 = D_j/2$, velocity U_j , jet density ρ_j , the dynamic viscosity μ_j and jet temperature T_j (all taken at the nozzle exit on the jet centerline). The Reynolds number of $Re = 4.5 \cdot 10^5$ is between the reference cases at $Re = 1.0 \cdot 10^6$ and $Re = 5.0 \cdot 10^5$ (experiments by Lau *et al.* (1979) and Arakeri *et al.* (2003), respectively) and at $Re = 4.0 \cdot 10^5$ (LES by Bogey & Bailly (2006*c*, 2005*b*)). The differences in the viscous effects associated with the different Reynolds number are here considered

negligible (Viswanathan, 2004a).

Computational grid and simulation parameters

The cylindrical computational domain with dimensions $L_r/r_0 = 20$ and $L_z/r_0 = 40$ is discretized using $N_r \times N_\theta \times N_z = 237 \times 50 \times 349$ ($\approx 4.1 \times 10^6$) grid points. A cut through the computational grid in two planes is shown in Fig. 3.1. In the radial direction the grid is refined in the vicinity of the shear layers and has a minimum radial spacing of $\Delta r/r_0 = 0.05$ at $r/r_0 = 1$. It is then stretched toward the boundary and reaches a maximum spacing of $\Delta r/r_0 = 0.28$ at the radial boundary. The stretching parameters of the radial grid are chosen such that the maximum grid-to-grid stretching ratio is below 3%. In the streamwise direction, the grid spacing is of constant size $\Delta z/r_0 = 0.1$ up to $L_z/r_0 \approx 30$ and continuously increased beyond. The maximum grid spacing $\Delta z/r_0 = 0.6$ is reached at the outflow boundary $L_z/r_0 = 40$. Only a small fraction of the radial domain is covered by the ambient sponge, and because of the low sponge amplitude the physical region of the domain covers $L_r/r_0 = 19.4$ and $L_z/r_0 = 32$.

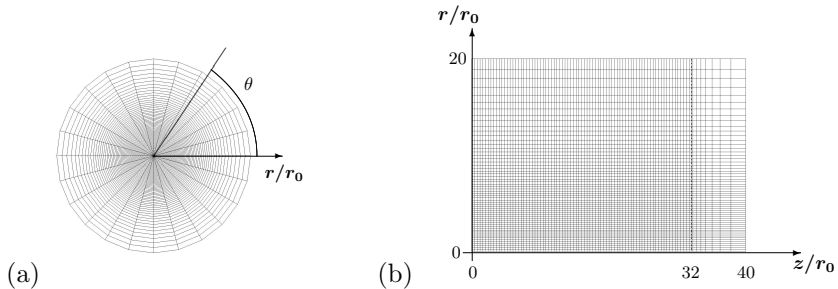


Figure 3.1: Computational grid in (a) the r - θ plane and (b) the r - z half-plane. In the azimuthal direction only every second grid line is shown of a grid corresponding to $N_\theta = 48$ points. Only every fourth grid line is shown in the radial and axial directions. The vertical line (-----) marks the beginning of the outflow sponge zone.

Investigated parameters

The simulations can be grouped in three blocks. The important parameters of all simulations are reported in Tab. 3.1 together with the nomenclature.

First, the effect of a modification of the total disturbance ampli-

Table 3.1: Nomenclature, inflow forcing parameters, SGS-model and azimuthal resolution of investigated simulations.

Case	$A_{\text{total,LST}}$	modes $ n $	SGS-model	χ	N_θ
Low	0.015	1, ..., 8	RT	50	50
Med	0.030	1, ..., 8	RT	50	50
High	0.045	1, ..., 8	RT	50	50
Low-m	0.015	4, ..., 8	RT	50	50
Med-m	0.030	4, ..., 8	RT	50	50
High-m	0.045	4, ..., 8	RT	50	50
L- χ	0.030	4, ..., 8	RT	35.0	50
M- χ	0.030	4, ..., 8	RT	42.5	50
ADM	0.030	4, ..., 8	ADM	50	50
LR	0.030	4, ..., 8	RT	50	32
HR	0.030	4, ..., 8	RT	50	78

tude $A_{\text{total,LST}}$ is investigated. Thereby, the sensitivity of transitional jet simulation results to changes of the inflow condition that has been reported previously (see section 1.4) is to be further clarified. Using disturbances following linear stability theory, the effect of the nonlinear development of eigenmodes and their role in the transition process and the resulting noise can be assessed. Three simulations with forcing amplitudes that range from 1.5% (case **Low**) to 3.0% (case **Med**) to 4.5% (case **High**) of the jet exit velocity U_j are performed where unstable eigenmodes $n = 1, \dots, 8$ are forced. Section 3.3 then deals with the effects of changing the modal composition of disturbances provided to the flow: Azimuthal wavenumbers $|n| \leq 3$ are excluded from the forcing and the excitation amplitude is varied in the same fashion as before (corresponding to cases **Low-m**, **Med-m** and **High-m**) which, in addition, allows to search for consistent effects of the excitation amplitude. In the subsequent section 3.4, a brief overview of the direct comparison of cases **Med** and **Med-m** follows which allows to assess the modal excitation effect more quantitatively.

Among the six investigated jets case **Med-m** is chosen as baseline configuration because of the very good agreement with the reference data. Model effects are assessed from this case by varying the relaxation coefficient. As described in section 2.2, the relaxation coefficient χ is set to the

default value given by the upper bound of the dynamic procedure and successively decreased to $\chi = 0.85/\Delta t$ (case M- χ) and $\chi = 0.7/\Delta t$ (case L- χ). The second part of the investigation of the SGS-model effects focuses on the deconvolution approach described in section 2.2. The same setup with a disturbance level of 3% is used, however, the nonlinear convective terms are now calculated following the deconvolution approach (case ADM).

This study is completed by an investigation of effects of the azimuthal resolution. The computational grid for the baseline configuration contains $N_r \times N_\theta \times N_z = 237 \times 50 \times 349$ points and is compared to simulations with coarse ($N_\theta = 32$, case LR) and fine azimuthal resolution ($N_\theta = 78$, case HR).

3.2 Influence of the disturbance amplitude

In this section, the effect of changes of excitation levels is investigated by changing the disturbance amplitude $A_{\text{total,LST}}$. Eigenmodes from linear stability theory with azimuthal wavenumbers $n = 1$ through $n = 8$ are excited at the inflow. The presentation of the results is grouped into instantaneous data presented in section 3.2.1. Thereafter, the effect of the disturbance amplitude on the statistics of the jet flow is reported followed by the acoustic data in section 3.2.3. Section 3.2.4 addresses possible connections between the hydrodynamic source field and the acoustic near field.

3.2.1 Instantaneous data

Figure 3.2 shows snapshots of the vorticity magnitude $|\omega|$ for the three excitation levels in the developing region of the shear layers. The jet shear layer development is similar for all cases with an asymmetric alignment of structures at opposite sides of the shear layer. The development seems not to be influenced by the increase of forcing amplitude besides the shift in upstream direction. As the shear layers roll up (marked by ①), we observe a large dominant structure. For increased amplitudes (cases Med and High), the developing vortex in the shear layer contains two separate vortex cores marked by a higher concentration of vorticity. For the investigated range of disturbances (1.5%, 3.0% and 4.5%), consecutive structures are spatially separated in the axial direction. Downstream of $z/r_0 \approx 6$, the structures start to merge and interact. As these

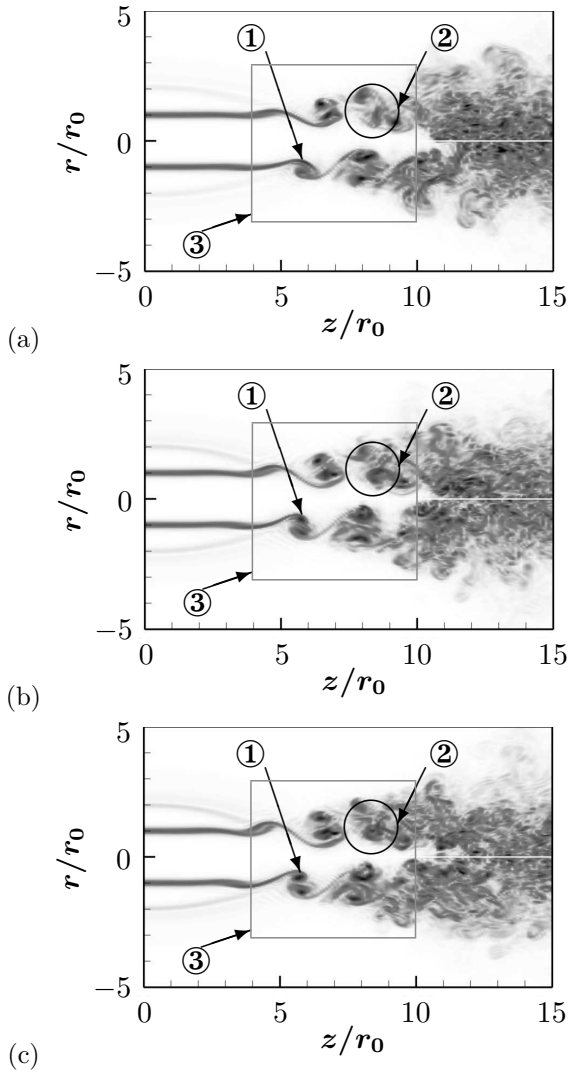


Figure 3.2: Visualization of vortical structures by $|\omega|$ in the $r - z$ plane at $\theta = 0$ for cases (a) Low, (b) Med and (c) High. The gray contour levels from light to dark are within $0 \leq |\omega| \leq 13$. ① dominant structure during roll-up of shear layer; ② interaction of large-scale structures; ③ gray frame is the zoomed region of Fig. 3.3.

stable structures are convected downstream the breakdown proceeds and smaller and smaller scales are generated leading to several vortex cores (see encircled area ②). The spatial extent in which the breakdown into smaller scales takes place is shorter for case **Low** compared to a spatially elongated process for the higher amplitude cases. The gray box in each graph (③) shows the extent of the transitional region (to be focused on in Fig. 3.3). As a side remark we note that the veil that emanates from the inflow region (at the radial position $r/z_0 \approx 2$) is an artifact of the interaction of the two sponge layers that overlap each other there: The inflow sponge relaxes the inflow profile to a fluid at rest whereas entrainment of surrounding fluid is enabled by the ambient sponge. This mild reduction of entrainment results in a spatially confined area of wake-like flow which locally increases the vorticity magnitude in the graphs.

The flow animations help to identify stable large-scale coherent structures. These interactions range from vortex-pairings, over partial pairings to pure tearing of vortices. The roll-up is localized in space regardless of the excitation amplitude, i.e. almost no spatial deviation of the roll-up location can be observed. However, at opposite sides of the shear layer it dominantly occurs in asymmetric (helical) and only rarely in axisymmetric (varicose) fashion. Further downstream, a frequent interaction of a train of vortices can be observed in which leading vortices tend to entrain the trailing vortices. These entrained vortices can also be shed violently through the potential core flow. As just noted, at opposite sides of the shear layer structures seem to order in a spiral manner for all cases. This qualitative observation of helical alignment is to be substantiated in the following by determining the azimuthal one-dimensional turbulent kinetic energy spectrum in the shear layer. In Fig. 3.3, the vortical structures in the transition region of the three jets are visualized using the λ_2 vortex identification criterion (Jeong & Hussain, 1995). Isosurfaces of $\lambda_2 = -1$ are shown in a side view. The streamwise shift of the transition process is well observable by the emergence of the azimuthally coherent two-dimensional structures that dominate the roll-up process. During their interaction subsequent vortices engulf each other in a leap-frog fashion, i.e. the inner part of the trailing vortex is ahead of the outer part of the leading vortex, thereby tearing apart the ring vortices and forming a helically-shaped structure. The differences in spatial extent of the structures becomes more evident using the λ_2 criterion. For case **Low**, large, two-dimensional structures dominate the roll-up and are stable as they are convected downstream. In contrast,

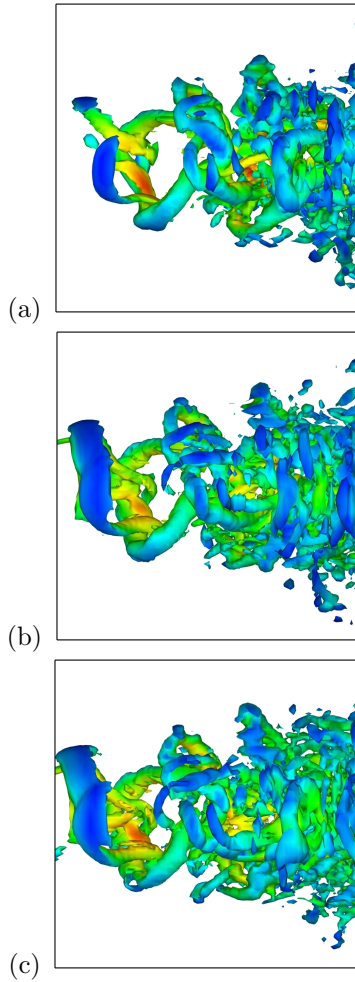



Figure 3.3: Visualization of vortical structures by isosurfaces $\lambda_2 = -1$ in the region $-3 \leq r/r_0 \leq 3$ and $4 \leq z/r_0 \leq 10$ for cases (a) **Low**, (b) **Med** and (c) **High** in a side view. The dimensions of the shown graph corresponds to the gray frame in Fig. 3.2. The isosurface is (color) coded by the local Mach number $0 \leq Ma \leq 1.4$ from dark gray (blue) to light gray (red) .

during the leap-frog interaction of vortices for case *Med* and *High* more three-dimensional and streamwise elongated small vortex filaments are generated which, in addition, tend to distort the purely helical orientation of large structures. The azimuthal correlation of the vortex heads emerging in the radial direction is significantly reduced for increased disturbance levels. Overall, the transitional behavior is similar for all cases, however, initiated at larger distances from the inflow and dominated by stable two-dimensional structures using the low excitation level. For the three forcing amplitudes, we observe that the structures that dominate the early transition process seem to align in an asymmetric fashion with respect to the jet centerline.

In order to obtain an impression of the instantaneous near-field noise of the jet flow, the same data is visualized again in Fig. 3.4 together with the pressure fluctuations p' in the outer part of the domain. We only present case *Med* since the differences in the visualizations of the instantaneous near-field pressure data are minute for the three disturbance amplitudes. For all simulated cases, sound waves are emitted slightly upstream of where the instantaneous shear layers merge. At the radial and upstream boundaries, all pressure waves leave the domain without generating any spurious noise or artificial reflections. This demonstrates

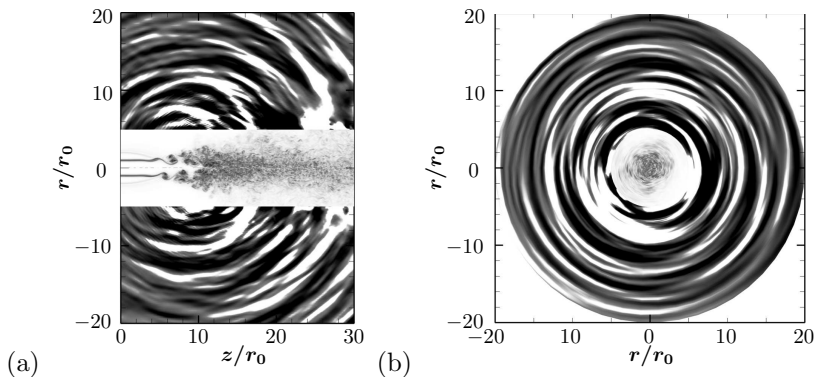


Figure 3.4: Visualization of vortical structures by contours of $|\omega|$ in the near field $r/r_0 < 5$ (gray contour levels from light to dark: within $0 \leq |\omega| \leq 13$) and corresponding pressure fluctuations in the acoustic near field $r/r_0 \geq 5$ (gray contour levels from dark to light within $-5 \cdot 10^{-4} \leq p' \leq 5 \cdot 10^{-4}$) for case *Med*: (a) in the $r - z$ plane at $\theta = 0$ and (b) in the $r - \theta$ plane at $z/r_0 = 12$.

the appropriateness of the chosen combination of nonreflecting boundary conditions supplemented by sponge-layers.

3.2.2 Mean flow and turbulence results

The influence of the forcing amplitudes on the mean flow and on the jet development is now investigated. The axial mean flow and its mean streamlines for case *Med* are visualized in Fig. 3.5. The current setup clearly enables the entrainment of surrounding fluid from the free-stream boundaries. There are no noticeable differences in the streamline patterns for the three excitation levels. The length of the po-

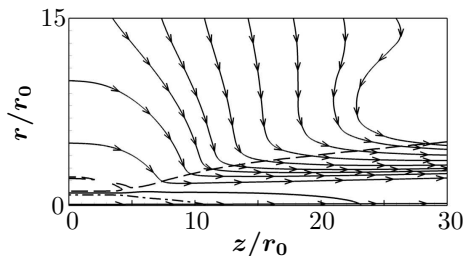


Figure 3.5: Visualization of mean flow streamlines for case *Med*. Lines denote $\cdots \langle w \rangle = 0.95U_j$, $\text{—} \langle w \rangle = 0.5U_j$ and $\text{---} \langle w \rangle = 0.05U_j$.

tential core z_c (here defined by the mean axial velocity on the centerline $w_c(z = z_c) = 0.95U_j$) is $z_c/r_0 \approx 10.84$. The dot-dashed line corresponds to the mean flow value $\langle w \rangle = 0.95U_j$, whereas the dashed line denotes $\langle w \rangle = 0.05U_j$ and exhibits a rather linear spreading of the jet downstream of around five jet diameters. As noted before, we find a region in the vicinity of the jet entrance region where reduced entrainment velocities are found as a side-effect of the interaction of the two overlapping sponge layers. The solid line marks half the jet exit velocity and demonstrates the slow decay of axial momentum which necessitates large computational domains. The potential core lengths z_c vary slightly with forcing amplitude and are listed in Tab. 3.2. With an increased forcing amplitude, we find reduced potential core lengths as expected. In the same table other data characterizing the jet development can be found such as the growth rate of the jet half-width, the virtual origin and the growth rate of the vorticity thickness.

The previously described vortex interaction results in a change of

Table 3.2: Potential core lengths z_c/r_0 , growth rates of the jet half-widths $d(r_{1/2}/r_0)/dz$ (determined by linear fits in the range $15 \leq z/r_0 \leq 30$), virtual origins z_0/r_0 and growth rates of the vorticity thicknesses $d(\delta_\omega/r_0)/dz$ (determined by linear fits in the range $8 \leq z/r_0 \leq 12$) for cases *Low*, *Med* and *High*.

Case	z_c/r_0	$d(r_{1/2}/r_0)/dz$	z_0/r_0	$d(\delta_\omega/r_0)/dz$
Low	11.09	0.085	-1.50	0.247
Med	10.84	0.085	-1.36	0.251
High	10.62	0.072	-4.51	0.252

the mean pressure in a region surrounding the closing of the potential core: Slightly upstream of the closing a region of higher pressure is found, whereas a reduced mean pressure region is established starting in the shear layer and ranging to the collapse of the potential core. This is exemplified by the mean pressure distribution of case *Med* in the transitional region (Fig. 3.6). This low pressure region entrains fluid the

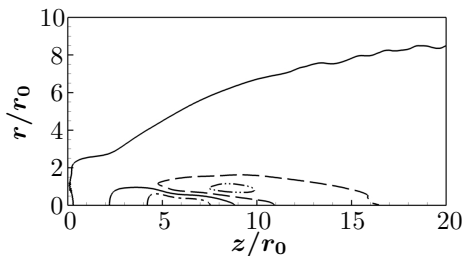


Figure 3.6: Visualization of mean pressure distribution for case *Med*. Lines denote ambient pressure: — $\langle p \rangle = p_\infty$, decreased pressure: --- $\langle p \rangle = 0.98 p_\infty$, -·-· $\langle p \rangle = 0.96 p_\infty$ and increased pressure: ·-·- $\langle p \rangle = 1.01 p_\infty$.

surrounding fluid which is initially at rest. Depending on the magnitude of the pressure gradient, entrained fluid from far downstream is directed upstream, with a velocity magnitude on the order of only one percent of the jet exit velocity. As the fluid approaches the widened jet, it becomes accelerated in the downstream direction again.

The streamwise development of the mean axial velocity at the center-line w_c and the jet half-width $r_{1/2}$ (defined by $\langle w(r = r_{1/2}) \rangle = 0.5w_c$) are

shown in Fig. 3.7. Since the forcing consists of Kelvin-Helmholtz type

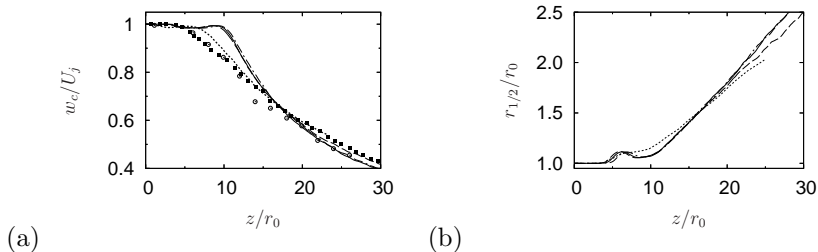


Figure 3.7: (a) Mean axial velocity along the jet centerline w_c and (b) jet half-width $r_{1/2}$: --- Low, — Med, --- High, Bogey & Bailly (2005b), \circ Lau *et al.* (1979), \blacksquare Arakeri *et al.* (2003).

instabilities (that reach their maxima in the shear layer) one can expect that upstream of the potential core collapse the differences along the jet centerline are only small. With increasing forcing amplitude the onset of the decay of the centerline velocity moves slightly upstream. Also a pronounced velocity defect followed by a rebound to values approximately equal to the jet exit velocity can be observed. This velocity distribution along the jet centerline can be explained by the increase in mean pressure with a subsequent pressure drop further downstream (as shown in Fig. 3.6) which first decelerates the fluid and then accelerates it again. The decay itself evolves rather unchanged for all cases, only case High shows a small kink in the mean flow development at late streamwise positions. Compared to the experimental results by Lau *et al.* (1979) and Arakeri *et al.* (2003) we observe a strongly delayed onset of the decay of the centerline velocity. Downstream of $z/r_0 \approx 15$, qualitative agreement with the experimental work of Lau *et al.* is found. The numerical data by Bogey & Bailly (2005b) lies between the results. Note that the LES data of Bogey & Bailly is shifted in axial direction by $z_0/r_0 = -2$ in all graphs to account for the differences in potential core length. We do not collapse all the data at the potential core but rather shift the data to achieve best fit with the mean centerline velocity and higher moments to be looked at later. The experimental data denoted by symbols is shifted as follows: that of Arakeri and coworkers by $z_0/r_0 = -9$, that of Lau *et al.* by $z_0/r_0 = -8$. The relation among the reference data remains constant throughout this work. The computational results share the delayed but stronger decay of the centerline velocity which might be related to the aforementioned artificially increased initial momentum

thicknesses and the difference in oncoming disturbance levels.

The axial profiles for the jet half-width shown in Fig. 3.7(b) do not vary significantly for the range of investigated inflow-forcing amplitudes. After the onset of the jet spreading, we observe a strong lateral contraction of the flow (related to the reduced mean pressure mentioned above) around a streamwise location of $z/r_0 \approx 6$ followed by a fairly linear development. Since the streamwise extent of the computational domain is too short to contain large parts of the self-similar region, the spreading rates of the jet flow have not been determined. Nevertheless, the growth rates of the jet half-width for all simulations (determined by a linear fit in the range $15 \leq z/r_0 \leq 30$) are given in Tab. 3.2. The cases where azimuthal wavenumbers $n = 1$ through $n = 8$ are disturbed have growth rates from $d(r_{1/2}/r_0)/dz \approx 0.072 \dots 0.085$ depending on the disturbance level. The mildly excited flow reaches a value that is close to the experimentally determined value of 0.096 reported by Panchapakesan & Lumley (1993) (which is determined in the self-similar region of the jet). Similar values as ours, i.e. smaller values than in experiments, were found by Bogey & Bailly (2006a), who, when simulating in a box with twice the streamwise extent, observed an increase in the streamwise direction towards asymptotic values in accordance with the literature. This suggests that the growth rates might increase towards the self-similar region which is not captured by our numerical domain.

The root-mean-square (RMS) of the axial and radial velocity fluctuations along the jet centerline $r/r_0 = 0$ are given in Fig. 3.8. Overall, the streamwise evolution of rise and subsequent fall of RMS intensities

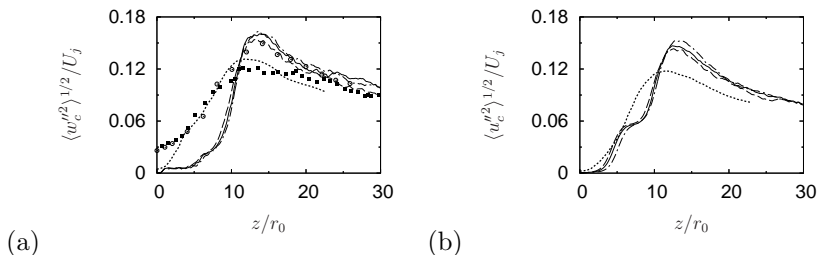


Figure 3.8: RMS of (a) axial velocity fluctuations $\langle w_c'^2 \rangle^{1/2}$ and (b) radial velocity fluctuations $\langle u_c'^2 \rangle^{1/2}$ along the jet centerline: --- Low, — Med, --- High, Bogey & Bailly (2005b), \circ Lau et al. (1979), \blacksquare Arakeri et al. (2003).

is similar for all cases. The axial RMS velocities (Fig. 3.8(a)) saturate close to the inflow at levels of $\langle w_c''^2 \rangle^{1/2} / U_j \approx 0.01$. Six jet-nozzle radii downstream of the inflow the values rise significantly and reach their maxima around the streamwise location of $z/r_0 = 13 \dots 14$. With increasing forcing amplitude $A_{\text{total,LST}}$, the streamwise development is slightly shifted upstream whereas the peaks are reduced in amplitude. After the collapse of the potential core, the three investigated cases agree reasonably well with the experimental data by Lau *et al.* (downstream of $z/r_0 = 10$). In particular, case **High** reaches a similar RMS peak value of $\langle w_c''^2 \rangle^{1/2} / U_j = 0.153$. Note that Lau *et al.* (1979) report the highest experimental RMS fluctuations, however, this is attributed to the analysis procedure and lower values - similar to the Arakeri *et al.* data - were reported in (Lau, 1981). The initial development upstream of the peak location, however, is fundamentally different from the reference data: We observe a minute rise in RMS, whereas the LES data by Bogey & Bailly (2005b) (after a short initial region) exhibits similar growth as observed in the experiments. Their RMS peak value of 0.131 and also the streamwise distribution is in fair agreement with the more recent experiments by Arakeri *et al.* (2003). The RMS distribution with the very rapid increase in RMS substantiates the findings from the instantaneous data that mostly two-dimensional structures dominate the roll-up of the shear layers followed by the sudden emergence of small-scale vortices (see, e.g. the visualization of λ_2 isosurfaces in Fig. 3.3).

In Fig. 3.8(b) the radial RMS velocities along the centerline are shown together with the reference LES. As for the axial fluctuations, considerably higher values are found (25% up to 33%) compared to the data of Bogey & Bailly (2005b). In addition, we observe a localized attenuation in the rise of the RMS around a streamwise location of $z/r_0 \approx 7$. In comparison to the currently employed eigenmode excitation, the ring forcing method used by Bogey & Bailly seems to allow for a smoother transition process with lower RMS peaks along the centerline. Although not shown in Fig. 3.8(b), we would like to point out that the peak level of the radial RMS velocity reported by Bogey *et al.* (2005b) are in fair agreement with the experimental data.

In the following, the effect of changes in forcing amplitude on the early shear layer development is investigated. As mentioned in section 3.2.1, the observations made in the transitional region are to be supported quantitatively by calculating the one-dimensional azimuthal turbulent kinetic energy spectra (Fig. 3.9). We define the spectrum at

location (r, z) as

$$E(n) = \langle \hat{u}_i \hat{u}_i^* \rangle, \quad (3.1)$$

where $E(n)$ is the turbulent kinetic energy (TKE) contained in azimuthal mode n , \hat{u}_i denotes the one-dimensional Fourier transform of velocity component u_i and the asterisk the complex conjugate. Note that we use $\langle \cdot \rangle$ in equation (3.1) to denote a time average only. Five equidistant downstream locations in the transitional region along the nozzle lip-line ($r = r_0$) are evaluated and shown in Fig. 3.9. For clarity, the groups of spectra at the different downstream positions are shifted by one order of magnitude. Also, the most energetic wavenumber $n = 0$ is excluded from the graphs to assess the effects of the forcing amplitude on the excited modes (TKE of $n = 0$ is larger by roughly four order of magnitude). At the inflow we find a difference of more than two orders of magnitude between the turbulent kinetic energy contained in the perturbed modes (i.e. the excited azimuthal wavenumbers $n = 1$ through 8) and the higher wavenumbers. The change in disturbance amplitude is reflected by the different TKE levels. Based on the growth rates predicted by linear theory, one might expect the amount of energy among the wavenumbers to be ordered accordingly. However, this is not exactly the case. The slightly lower energy contained in the wavenumbers $n = 1$

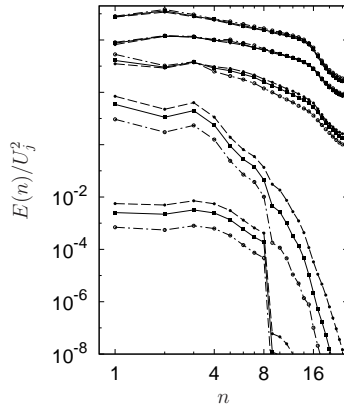


Figure 3.9: One-dimensional turbulence energy spectra E in θ -direction along the nozzle lip line at streamwise positions $z/r_0 = i \cdot 3$ ($i = 0, \dots, 4$, from bottom to top): --- Low, — Med, -.- High. The groups of spectra are shifted by an order of magnitude for clarity.

and $n = 2$ might be related to the linear interaction of the right- and left-turning modes with the initially unexcited varicose mode $n = 0$ as well as an effect of the weakly-enforced inflow condition. At the streamwise position $z/r_0 = 3$, all modes, regardless if initially excited or not, have higher levels of energy. A considerable TKE increase is observed in particular for the wavenumbers $n = 1$ as well as $n = 3$ which dominate the spectra for all forcing amplitudes. Further downstream (at $z/r_0 = 6$) the dominance of the wavenumber $n = 1$ is consolidated. For case **Low** this is the most energetic helical mode which confirms the findings from the instantaneous data of the vorticity magnitude, in particular, the helically shaped dominant structure in Fig. 3.3(a). As a side remark, we note that the TKE increase in the lower wavenumbers is accompanied by a reduction in higher wavenumbers. With increasing distance from the inflow the spectra are almost indistinguishable from each other. At $z/r_0 = 9$, they are characterized by a broad-banded energy distribution. Because of the double-logarithmic representation of the spectra the overall dominance of the even wavenumber $n = 2$ at this location is disguised. It is interesting to note that in the short streamwise distance between these two locations a distinct transfer of turbulent kinetic energy takes place from the asymmetric modes $n = 1$ and $n = 3$ to the symmetric mode $n = 2$ (symmetric and asymmetric here refers to a pointwise symmetry or asymmetry with respect to the pole $r = 0$ and thereby, a symmetry or asymmetry with respect to the downstream axis for all helical modes during their downstream development). Because of the disturbance levels achieved at this streamwise position, linear but also nonlinear interaction of eigenmodes may feed this transfer mechanism. For case **Low**, slightly elevated turbulent kinetic energy is also found in the wavenumber range from five to eight. All excitation levels exhibit a sharp drop-off for $n \geq 16$ of about one order of magnitude, which is related to effects of the relaxation regularization (to be addressed in more detail in sections 3.5.1 and 3.7.1). At the last investigated axial position, we observe a more or less broad-banded energy distribution for modes with $n \leq 15$, but again, we note that the most energetic wavenumber is $n = 2$.

As could be seen from the comparison of the centerline profiles, the effect of the eigenmode-based forcing of modes $|n| = 1, \dots, 8$ on the simulation results seems to be strong compared to the reference data. To better compare the absolute values as well as the streamwise distributions of various quantities, we will not employ an axial shift of the

reference data for the rest of this subsection. In the following, we focus on the development along the nozzle lip line $r/r_0 = 1$ and present the axial and radial velocity fluctuations versus the downstream coordinate (Fig. 3.10). As noted above, the eigenfunctions employed in the forcing reach their maxima in the shear layer of the base-flow profile. Thus, the amplitude effects might be more pronounced in the quantities along the jet nozzle lip line. As expected, the axial RMS velocities greatly

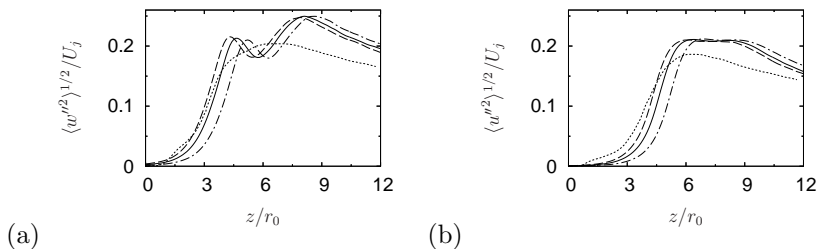


Figure 3.10: RMS of (a) axial velocity fluctuations $\langle w''^2 \rangle^{1/2}$ and (b) radial velocity fluctuations $\langle u''^2 \rangle^{1/2}$ along the nozzle lip line: --- Low, — Med, - · - High, ····· Bogey & Bailly (2005b).

vary for the different excitation levels. First, similar to the centerline distributions, an increase in excitation level shifts the streamwise development upstream, i.e. with an increased forcing amplitude $A_{\text{total,LST}}$ the RMS rises at shorter distances from the inflow. Second, and more strikingly, the streamwise evolution of the RMS exhibits a strong dual-peak shape. Only the very early development is found to behave similarly as reported by Bogey & Bailly (2005b). However, their results show a smoother course of growth, saturation and subsequent decay. For the current simulations we observe that after rising for a downstream distance of approximately four up to five radii the values saturate at $\langle w''^2 \rangle^{1/2} / U_j \approx 0.2$, decay for a short distance and rise again afterwards. Around $z/r_0 \approx 8 \dots 9$, the secondary peaks are reached which are all on the order of 0.25. Most likely, this dual-peak distribution is a result of the very pronounced vortex pairings taking place at this location (see section 3.2.1). The structures that are involved in this vortex interaction are very stable and are initially dominated by odd wavenumbers of low order ($n = 1, 3$). The sudden rise of the even wavenumber $n = 2$ between the streamwise positions $z/r_0 = 6$ and $z/r_0 = 9$ combined with the reduced relevance of $n = 1, 3$ seem to contribute to this stepwise in-

crease of RMS. As the computation of the mean quantities also involves an azimuthal average, a helical alignment tends to smear out gradients whereas an axisymmetric arrangement tends to amplify the dual-peak structure. Since the dominance of the helical mode $n = 1$ is confined to a very short streamwise region, the rise of the double-helical mode $n = 2$ (which in contrast to $n = 1$ is symmetrically aligned to the downstream axis) enhances the dual-peak structure. Similar variations of centerline longitudinal fluctuation intensity can for example be found in the experimental data reported by Crow & Champagne (1971) (their figure 13, p. 564) or in much more detail by Zaman & Hussain (1980) where profiles exhibit strong dual-peak distributions (see their figures 3 (a) and 27, p. 455 and 483). There, vortex pairing in an axisymmetric jet flow under excitation has been investigated. For an excitation frequency corresponding to $St = 0.3$ a similar dual-peak distribution is established characterized by a trough region with reduced fluctuations located at the nozzle lip-line which extends toward the jet centerline.

The evolution of the radial RMS velocities presented in Fig. 3.10(b) is similar to the findings of the axial velocity component. Compared to the results of Bogey & Bailly, we observe a delayed onset even for case **High**, the case for which transition is initiated closest to the inflow. Thus, it seems that the transition is slowed down when triggered by the eigenmode excitation of wavenumbers one through eight is slowed down. In addition, the more abrupt breakdown results in an over-prediction of the RMS by almost 13%. The general distribution, however, is similar to the reference data. From this, we conclude that the effects of the particular excitation mechanism seems to emerge mostly in the early shear layer development and most significantly in the axial velocity fluctuations along the nozzle lip line. Experimental data is not shown, however, we note that the reported values are significantly lower (i.e. on the order of 0.12...0.14) which might be an effect of the artificially increased shear layer thickness (simulation results with comparable inflow profile share this characteristic (Bogey & Bailly, 2005b)).

The effect of the forcing on the development of the vorticity thickness δ_ω , which is determined according to

$$\delta_\omega = \frac{U_j}{\max_r \left| \frac{\partial \langle \omega \rangle}{\partial r} \right|}, \quad (3.2)$$

is now investigated. In Fig. 3.11 the vorticity thickness evolution is shown for the three cases. The development of the initially laminar

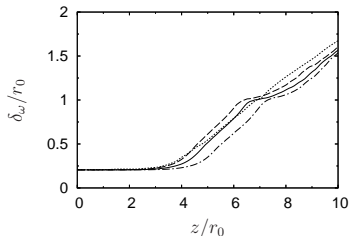


Figure 3.11: Streamwise development of vorticity thickness δ_ω : --- Low, — Med, - - - High, Bogey & Bailly (2005b).

shear layers depends on the amplitude of the disturbances. With increasing forcing amplitude the location where the shear layers thickness is increased moves upstream – which is consistent with our observations for all other quantities so far. The streamwise evolution is almost linear once the spreading started. Yet, at a downstream position of $z/r_0 \approx 6 \dots 7$, the spreading is suddenly strongly diminished and – a little later – increased again. After this second increase the vorticity thickness grows again in a fairly linear fashion. The location matches the position of the dual-peak structure described previously as well as the region where the redistribution of turbulent kinetic energy between $n = 1$ and $n = 2$ is observed (see Figures 3.9 and 3.10(a)). Because of this discontinuous development of the vorticity thickness, the determination of the corresponding growth rates is difficult and ambiguous. Therefore, we decide to determine the growth rates of δ_ω by a linear fit in the range $8 \leq z/r_0 \leq 12$ and report the values in Tab. 3.2. The values of $d(\delta_\omega/r_0)/dz \approx 0.25$ are higher than observed experimentally (see the summary of experiments by Gutmark & Ho (1983) which range from 0.112 to 0.218), but in close agreement with the study by Bogey & Bailly (2005b) (note again that growth rates are determined in the self-similar region not captured by our domain).

The delay of the shear layer development also affects the turbulent stresses. This is exemplified by looking at the radial normal Reynolds stress as well as the shear stress (Fig. 3.12). The profiles are taken at equidistant streamwise locations $z/r_0 = 3, 6$ and 9 and are shifted by the marked amount. Between the first and the second location the values rise rapidly, saturate within this distance and reach their maxima around $z/r_0 \approx 6$. Approaching the potential-core collapse the Reynolds

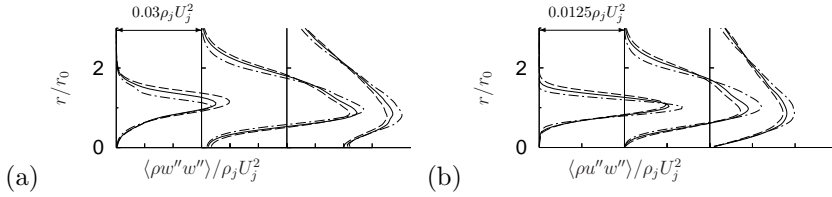


Figure 3.12: Streamwise development of radial Reynolds stress profiles at streamwise positions $z/r_0 = i \cdot 3$ ($i = 1, \dots, 3$ from left to right): (a) $\langle \rho w'' w'' \rangle / \rho_j U_j^2$, (b) $\langle \rho w'' w'' \rangle / \rho_j U_j^2$: --- Low, — Med, - - - High.

stresses decay again. Corresponding to the previously noted upstream shift for higher disturbance amplitudes (see section 3.2.1) we find larger peak values of the axial stress component at $z/r_0 = 3$ for higher forcing amplitudes. For all other measuring points a reversed alignment is found: Case Low (that has the largest delay in streamwise development) reaches largest overall Reynolds stress values and its extent is confined to thinner radial extents. In particular, the very rapid development of $\langle \rho w'' w'' \rangle / \rho_j U_j^2$ in Fig. 3.12(a) for case Low observed between $z/r_0 = 3$ and 6 confirms the impression from the snapshots of instantaneous processes (see Fig. 3.2 and 3.3) that the transition occurs in a spatially more confined area and is more abrupt. It might be the case that this process can be linked to the previously described transfer of energy between the azimuthal modes $n = 1$ and $n = 2$ (see Fig. 3.9) associated with the breakdown of the dominant, azimuthally coherent structure.

This section is concluded by investigating the spectral composition of the axial velocity fluctuations along the jet centerline and the nozzle lip line. For details concerning the post-processing of the recorded velocity signals we refer to section 2.9 and repeat at this point only that the interval length is chosen to resolve a nondimensional frequency of $St = 0.04$. We focus on the transitional region of the jet flow and show the axial velocity spectra at the streamwise positions $z/r_0 = i \cdot 3$ with index i ranging from zero to four (Fig. 3.13). As the disturbances are highest in the shear layer of the inflow profile, one finds more than two orders of magnitude lower peak values along the jet centerline compared to the nozzle lip line (Fig. 3.13(a) vs. Fig. 3.13(b)). The lip-line profiles of the spectral amplitude line up according to the imposed disturbance amplitudes. In agreement with the literature (Huerre & Monkewitz, 1990) the flow is most receptive to disturbances in a Strouhal number range around $St \approx 0.4$, which corresponds to the column mode frequency

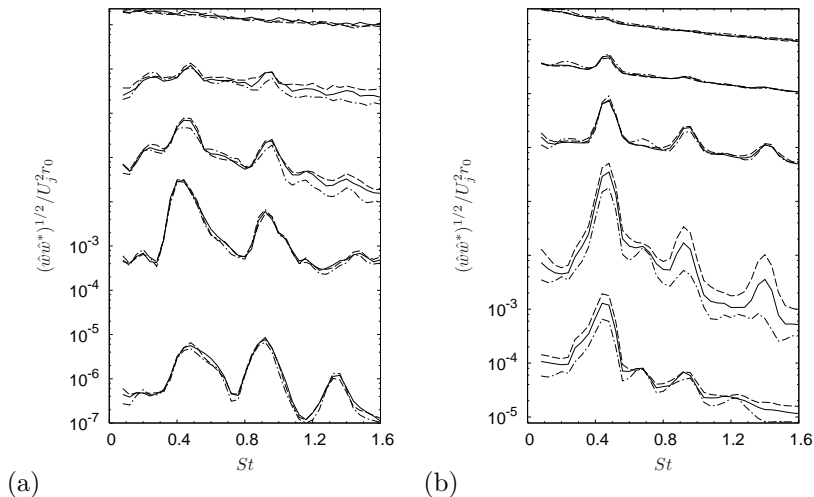


Figure 3.13: Axial velocity spectra at streamwise positions $z/r_0 = i \cdot 3$ ($i = 0, \dots, 4$ from bottom to top) along: (a) jet centerline, (b) jet lip line: --- Low, — Med, -.- High. The groups of spectra are shifted by an order of magnitude for clarity.

(also referred to as preferred mode (Crow & Champagne, 1971; Zaman & Hussain, 1980)) although a broader frequency band is excited at the inflow (recall the disturbed eigenmodes and the nondimensional fundamental frequencies: $(n, St) = (1, 0.68), (2, 0.67), (3, 0.65), (4, 0.63), (5, 0.61), (6, 0.57), (7, 0.51)$ and $(8, 0.43)$). At the second downstream position the velocity spectra are characterized by broad but well-defined peaks. For the lip line we observe three peaks at Strouhal numbers of $St \approx 0.46, 0.92$ and 1.38 , which could correspond to the fundamental frequency and its first and second higher harmonic. Again, the forcing amplitude manifests itself in the intensity of these peaks. In the case of a weakly disturbed flow (case Low) the peak at $St \approx 1.38$ is buried in broad-banded noise, whereas around $St \approx 0.68$, an additional dominant frequency is found. Besides the same dominant Strouhal numbers of $St \approx 0.46$ and $St \approx 0.92$, the centerline spectra show no pronounced effect of the changes in forcing amplitude at the corresponding streamwise position. At $z/r_0 = 6$, the upstream generated triad of frequencies remains dominant along the lip line where the vortex-pairings are ob-

served. The lower frequencies also appear along the centerline as can be seen in Fig. 3.13(a). Also note that in the case of a low forcing amplitude, there is now a pronounced local maximum at $St \approx 0.68$, the frequency that was dominant further upstream. Together with the previously discussed spectrum of turbulent kinetic energy (Fig. 3.9) this could be an effect of the helical mode $n = 1$ emerging at this streamwise location. Further, qualitative support is found by the helical alignment of the vortical structure (see section 3.2.1). This conjecture is in very good agreement with linear stability theory (Michalke, 1984; Michalke & Hermann, 1982), according to which azimuthal wavenumbers $n = 0, 1$ reach their highest growth rates at the fundamental frequency of $St = 0.67$ and $St = 0.68$, respectively. But clearly, this effect is only very weak compared to the dominant harmonics. At the second to last position, i.e. at $z/r_0 = 9$, the persistent and dominant existence of the column mode frequency $St \approx 0.46$ remains unchanged for the lip-line spectra, whereas the centerline spectra maintain peaks at the fundamental frequency and its subharmonic. Again, case **Low** exhibits less pronounced peaks, but a brief streamwise appearance of a frequency corresponding to $St \approx 0.23$ is captured at this location – which could mark the subharmonic of $St \approx 0.46$ and hence randomly occurring vortex-pairings of the column mode. At the location at which the potential core collapses we find no overall dominant frequency in the velocity spectra.

3.2.3 Acoustic results

The DNC approach taken in this work provides the complete time-space information not only in the fluid dynamic region but also in the acoustic near-field. Thereby, the effect on the acoustic emission caused by changes in the forcing amplitudes on various quantities, such as the spectral content of the pressure distribution, the sound pressure levels and azimuthal two-point auto-correlations, can be investigated without any additional modeling approaches or assumptions of far-field analogies. From changes in transition and the resulting variations in the acoustic near-field conclusions might be drawn about the underlying noise generation mechanisms.

First, the pressure spectra for cases **Low**, **Med** and **High** at different observer locations are investigated. The end of the potential core of case **Med** is selected as the origin of a spherical coordinate system (R, θ, ϕ) . The near-field spectra are now investigated with respect to the polar

Table 3.3: Observer locations of spectra measurements and polar distances R and angles ϕ_{exact} for cases *Low*, *Med* and *High*.

ϕ	r/r_0	z/r_0	R/r_0			ϕ_{exact}		
			Low	Med	High	Low	Med	High
30°	9	27	18.3	18.5	18.7	29.5°	29.1°	28.8°
60°	15	21	18.0	18.1	18.2	56.5°	55.9°	55.3°
90°	18	12	18.0	18.0	18.0	87.1°	86.3°	85.6°

angle $0^\circ \leq \phi \leq 180^\circ$ measured from the positive jet axis $r = 0$. The cylindrical coordinates (polar distances R and polar angles ϕ , for each case based on the corresponding potential core length) for all observer locations are reported in Tab. 3.3. Technical details of the post-processing are reported in section 2.9. Recall that no additional filtering or spectral smoothing is applied. The cutoff frequencies of the grid are repeated here: $St^g \approx 5$ at the downstream observer location for downstream propagating waves and, $St^g \approx 3$ for the sideline observer location for radially propagating waves. The data are scaled using standard atmospheric pressure ($p_{\text{atm}} = 982hPa$) and a reference pressure of $p_0 = 2 \times 10^{-5}Pa$ to obtain sound pressure level (SPL, given in dB).

Experimental data (shown by solid square symbols) is taken from a measurement campaign focusing on the spectral properties of noise in the acoustic near field as well as the acoustic far field (Bogey *et al.*, 2007b) of a high-subsonic jet at a Reynolds number of $Re = 7.8 \times 10^5$. Dotted lines represent LES data of Bogey & Bailly (2005b). As tabulated in Table 3.4, the reference data are measured at slightly different polar angles and, more importantly, at different polar distances R from the previously defined origin. Assuming a $1/R$ -decay for the pressure levels, a correction Δ_{SPL} is determined with respect to the common polar distance $R^* = 18r_0$ and accounted for in all graphs. Note that the largest correction is $\Delta_{\text{SPL}} = 1.3dB$ for the reference data and that the small differences in polar distances of cases *Low*, *Med* and *High* are not accounted for. The acoustic data of the following sections 3.3– 3.7 will be provided at the same observer locations, and hence, the corrections are the same for all cases.

The three measurement points with similar polar distances and polar angles that correspond to $\phi \approx 30^\circ$, 60° and 90° are analyzed in Fig. 3.14. The spectra in Fig. 3.14 exhibit a strong dependence on the observation

Table 3.4: Observer locations of spectra measurements and polar distances R and angles ϕ_{exact} for reference data together with polar-distance correction Δ_{SPL} with respect to the common polar distance $R^* = 18r_0$. Reference data: (I): Experiments by Bogey, Barré, Fleury, Bailly & Juvé (2007b); (II): LES by Bogey & Bailly (2006b).

ϕ	Ref.	r/r_0	z/r_0	R/r_0	ϕ_{exact}	R/R^*	Δ_{SPL}/dB
30°	I	15	30	23.3	40.1°	0.74	+1.3
	II	12	29	20.7	35.5°	0.83	+0.7
60°	I	15	20	16.9	62.4°	1.03	-0.1
90°	I	15	10	15.2	98.2°	1.18	-0.7
	II	15	11	15.0	94.5°	1.20	-0.8

angle ϕ , whereas the differences in disturbance amplitude are reflected only in the low frequency band. For small polar angles, as presented in Figures 3.14 (a) and (d), the spectra are dominated by a frequency band below $St = 0.4$. The spectral shape of all cases is in fair agreement with the reference data and we find a strongly enhanced low-frequency band for lower forcing amplitudes. In particular, case **High** follows nicely the reference data and its peak frequency at $St \approx 0.3$, is slightly shifted to higher frequencies compared to the experiments but in very good agreement with the reference LES ($St \approx 0.3$). At higher Strouhal numbers a second local peak is observed for the large-amplitude cases. In Fig. 3.14(d) a peak at $St \approx 0.9$ starts to appear for cases **Med** and **High**. Because of the relatively coarse spectral resolution, the locally dominant Strouhal numbers of $St \approx 0.5$ and 0.9 are most likely related to the dominant frequencies observed in the axial velocity spectra along the jet lip line, i.e. $St \approx 0.46$ and 0.92 , respectively.

For the intermediate observer location the spectra are characterized by a peak at $St = 0.5$. Its strength correlates with the excitation level, as can be seen in the close-up in Fig. 3.14 (e). Under an angle of $\phi \approx 60^\circ$ to the jet axis, only qualitative agreement of the spectral shape with the reference data is found above $St \approx 0.2$. The acoustic noise is over-predicted by more than 5 dB over a broad range of frequencies.

The near-field spectra of the reference data is broad banded for observer locations perpendicular to the jet axis (see Fig. 3.14 (c) and (f)). The LES lack noise contributions of frequencies below $St \approx 0.4$ when

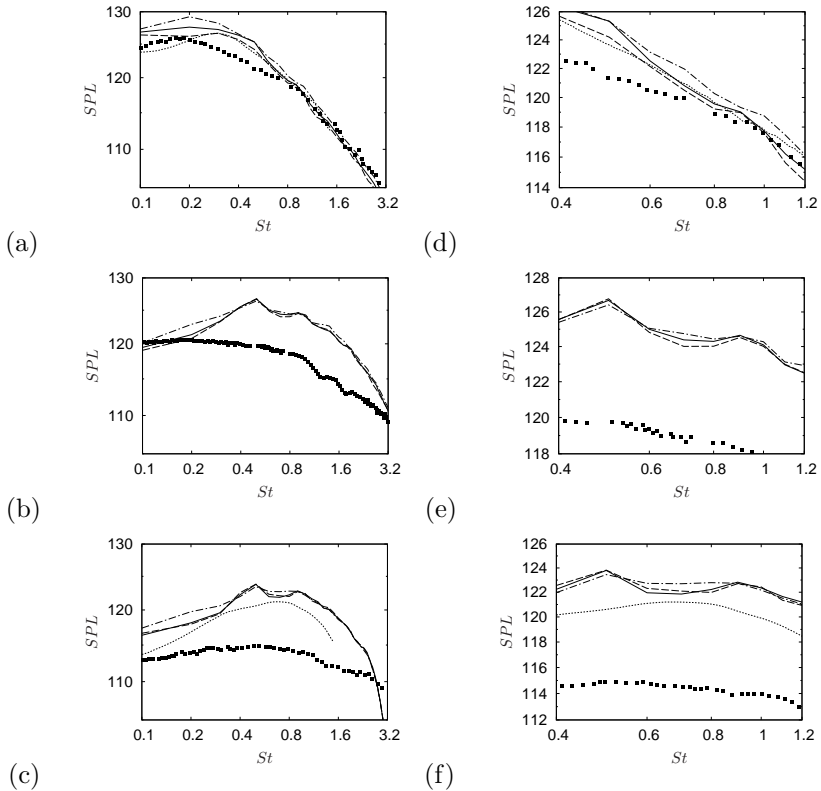


Figure 3.14: Near-field pressure spectra in dB at (a) $\phi = 30^\circ$, (b) $\phi = 60^\circ$ and (c) $\phi = 90^\circ$: --- Low, — Med, - - - High; ■ Bogey et al. (2007b) at (a) $r = 15r_0$, $z = 30r_0$, (b) $r = 15r_0$, $z = 20r_0$, (c) $r = 15r_0$, $z = 10r_0$; Bogey & Bailly (2005b) at (a) $r = 12r_0$, $z = 29r_0$, (c) $r = 15r_0$, $z = 11r_0$. Graphs (d), (e) and (f) show close-up of Strouhal $0.4 \leq St \leq 1.2$.

comparing the spectral shapes only (as also found under intermediate observation angles). We note that experimental studies for various jet flow parameters show a slight decrease of sound pressure for these low frequencies (e.g. Tanna, 1977a,b; Viswanathan, 2004a,b). Nevertheless, the pressure levels are significantly over-predicted by up 9 dB in the sideline direction.

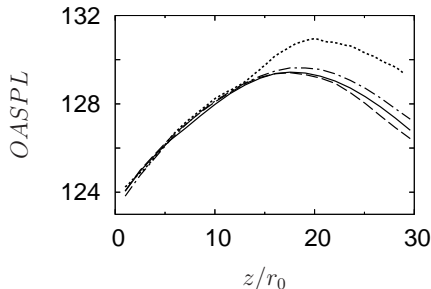


Figure 3.15: Axial distribution of overall sound pressure levels (OASPL in dB) along $r/r_0 = 15$: --- Low, — Med, -.- High, Bogey & Bailly (2006a).

Overall, the main trends of the spectra provided by the simulations are in accordance with the reference data, i.e. the shift of the dominant frequency band from low-frequencies under small angles ϕ to a broad-band character in the sideline direction. However, the eigenmode based forcing changes the transition process and thereby triggers a very stable and strong vortex pairing which contributes to tonal components in the pressure spectra. The frequencies found in the axial velocity spectra (in particular, for medium to high disturbance amplitudes, see Fig. 3.13) correspond very well to the observed tonal components. The sound pressure level around the excited tones is amplified with increased disturbance amplitude while elsewhere a broad-band reduction is found. This effect of turbulence and noise amplification or suppression through excitation is investigated in a series of experiments by Zaman (1985) and Zaman & Hussain (1981, 1980). Quantitatively, the sideline pressure levels are significantly over-predicted and might be related naturally to the increased radial RMS velocities (Bogey & Bailly, 2005b, 2006b; Bodony & Lele, 2008)).

The overall sound pressure levels (OASPL in dB) along the line $r/r_0 = 15$ for the three disturbance amplitudes are shown in Fig. 3.32. Again we compare it to the data presented in the work of Bogey & Bailly (2006a) which is shifted in amplitude to match the level of case Med at $z/r_0 = 0$ (the shift is -4.7 dB). The overall axial distribution of the OASPL is in very good agreement with the reference LES up to a downstream location of $z/r_0 = 17$ from where on the data completely separate: Further downstream, Bogey & Bailly observe approximately 2 dB higher sound pressure levels compared to the eigenmode excited LES

results. The three investigated cases group nicely. Only downstream of $z/r_0 = 21$, we observe a drop of the SPL which is larger for increased disturbance levels. The overall sound pressure levels are reduced in the downstream direction as a result of the induced tonal components. This is again in agreement with the previously mentioned experimental work (Zaman & Hussain, 1981) in which it was speculated that turbulence suppression could result in a overall noise reduction and which has been subsequently demonstrated by Hussain (1986).

This section is concluded by a comparison of the azimuthal (circumferential) correlation properties of recorded pressure signals at two locations corresponding to angles of $\phi = 30^\circ$ and $\phi = 90^\circ$. The coefficient is determined according to

$$\mathcal{R}_{pp}(\Delta\theta) = \frac{\langle p'(r, \theta_0, z, t)p'(r, \theta_0 + \Delta\theta, z, t) \rangle}{\langle p'^2(r, \theta_0, z, t) \rangle^{1/2} \langle p'^2(r, \theta_0 + \Delta\theta, z, t) \rangle^{1/2}}, \quad (3.3)$$

using 5000 samples in time. $\Delta\theta$ denotes the angular separation between the two-point measurements. Under shallow angles to the jet axis, i.e.

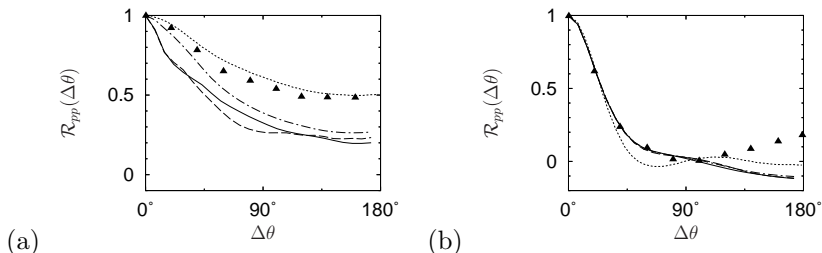


Figure 3.16: Azimuthal correlation coefficient \mathcal{R}_{pp} for pressure signals: (a) at $(r = 12r_0; z = 30r_0)$ and (b) at $(r = 12r_0; z = 12r_0)$. --- Low, — Med, - - - High, Bogey & Bailly (2006b) (taken at (a) $(r = 12r_0; z = 29r_0)$ and (b) $(r = 15r_0; z = 11r_0)$), far-field measurement \blacktriangle Maestrello (1976) ($\phi = 30^\circ$: $Re = 5.2 \cdot 10^4$, $Ma = 0.88$ and $\phi = 90^\circ$: $Re = 4.4 \cdot 10^4$, $Ma = 0.74$).

at $\phi = 30^\circ$ (Fig. 3.16(a)), the correlations of the pressure fluctuations deviate from the reference data even for a very small differences in azimuthal angle $\Delta\theta$. The experiments conducted by Maestrello (1976) are found in very good agreement with the LES results by Bogey & Bailly (2006b). The eigenmodes-based forcing seems to result in azimuthally less correlated pressure at shallow angles. The correlations of cases Med and High decrease even further to $\mathcal{R}_{pp}(180^\circ) \approx 0.20$, values that are

clearly below the reference data. Only for the weakly excited flow (case **Low**), we find a comparable distribution for small separation angles $\Delta\theta$, but also lower correlations (by approximately 50%) at $\Delta\theta = 180^\circ$. The correlation in this sector is enhanced by the dominant emergence of the mode $n = 1$ during the early stage of the transition (see one-dimensional turbulence spectra, Fig. 3.9, for case **Low** compared to cases **Med** and **High**). Overall, the results for $\phi = 30^\circ$ suggest a systematic lack of axisymmetric scales.

Figure 3.16(b) shows the correlation coefficient for the polar angles $\phi = 90^\circ$. There, the correlations are virtually indistinguishable. With increasing angle $\Delta\theta$, the signals quickly loose correlation and for $\Delta \geq 45^\circ$ they are almost uncorrelated, which is in agreement with the LES results by Bogey & Bailly(2006*b*) and with the far-field measurements by Maestrello(1976) (performed at a slightly lower Mach number of $Ma = 0.74$). For exactly opposite azimuthal positions of the microphones, the experiments show a small rebound of correlation whereas the numerical results remain almost uncorrelated. The eigenmode-based inflow forcing strongly breaks symmetrical dominance in the acoustic near-field. This effect is mostly detectable in the downstream direction and seems to be related to the redistribution of modal energy between odd modes $n = 1, 3$ within a relatively short streamwise distance to the even mode $n = 2$. Note that the even wavenumber $n = 2$ (double helix, point symmetric with respect to the downstream axis) cannot contribute to the (varicose) correlation level at $\Delta\theta = 180^\circ$.

3.2.4 Relevant noise generation mechanism: Link between induced vortex pairing and tonal near-field character

In the last part of this section the previously established links between the flow and characteristics of the noise received in the near-field are given. The pressure spectra at small angles show dominant frequencies below $St \approx 0.4$ which is in good agreement with data from the literature. We link this frequency band to the formation of large dominant structures and their subsequent interaction taking place in the early streamwise development of the initially laminar shear layers. The resulting interaction, which is in the form of random vortex pairings and tearings, contributes significantly to the noise emission characteristics. The most significant difference between case **Low** on the one hand and cases **Med** and **High** on the other hand are structures with wavenum-

ber $n = 1$. These structures that are dominant in the one-dimensional turbulent kinetic energy spectra (see Fig. 3.9) and also in the velocity spectra along the nozzle lip line (see Fig. 3.13(b), appearance of fundamental frequency) are generated during the roll-up process upstream of the collapse of the potential core. This formation of structures (note that downstream, at $z/r_0 = 9$ and 12, the velocity spectra of case **Low** reach their maxima in the excited frequency range of $St \approx 0.43$) causes the overall dominance of the low-frequency band in the pressure spectra of case **Low**. The azimuthal correlation coefficient (see Fig. 3.16(a)) supports this, since case **Low** has higher correlations for angles $\Delta\theta = 180^\circ$. This low-azimuthal wavenumber dominance in the downstream direction is in agreement with experimental observations (Michalke & Fuchs, 1975; Maestrello, 1976; Juvé *et al.*, 1979). The stable vortex pairings contribute to the noise observed at $\phi = 60^\circ$ and $\phi = 90^\circ$. Additional tonal contributions emerge which correspond exactly to harmonics detected in the velocity spectra in the jet shear layer. Hence, the perceived near-field noise is a combination of sound emitted by vortex pairings combined with the noise associated with the turbulent mixing process of the jet. The azimuthal auto-correlation coefficients are shown that the mixing noise dominates over the tonal contributions, as the pressure is uncorrelated (see Fig. 3.16). Although the strength of the excited vortex pairings and the resulting tonal components are directly linked to the excitation levels we find the overall sound pressure levels in the downstream direction to be slightly reduced by large amplitude forcing.

3.3 Influence of the modal composition of disturbances

In this section, the effect of changes of the modal composition of the excitation is investigated. Therefore, we exclude lower azimuthal wavenumbers $n = 1$ through 3 from the excitation and disturb only the eigenmodes $n = 4$ through 8 at the inflow. The forcing amplitude $A_{\text{total,LST}}$ is varied again in the same range to assess its effect and look for similarities between the two groups of excited modes. The presentation of the results follows the pattern of the previous section.

3.3.1 Instantaneous data

Figure 3.17 shows snapshots of the vorticity magnitude $|\omega|$ for the three cases **Low-m**, **Med-m** and **High-m** in the developing region of the shear layers. At first sight, the jet shear layer development seems similar for all cases. However, the specific details of the transitional behavior are different. With increasing disturbance amplitude the roll-up process is shifted in the upstream direction. As the shear layers roll up (marked by ①), we observe large dominant structures for case **Low-m**. In contrast, when enforcing larger disturbance amplitudes, as done in cases **Med-m** and **High-m**, the developing shear layer roll up into smaller vortical structures. For low-amplitude forcing consecutive structures are spatially separated and start to interact downstream of $z/r_0 \approx 7$, whereas the structures merge and interact more quickly for larger disturbance amplitude. As these structures are convected downstream, the breakdown process continues and smaller and smaller scales are generated leading to several vortex cores marked by a high concentration of vorticity (see encircled area ②). Clearly, the spatial extent in which the breakdown into smaller scales takes place is much shorter for case **Low-m** compared to a more moderate and spatially elongated process for the higher amplitude cases. As before, the gray box in each graph (③) shows the extent of the transitional region to be looked at in more detail in Fig. 3.18.

The flow animations of these cases also help to identify vortex pairings of the large-scale structures. Compared to a tonally excited jet flow or mixing layer these pairings are less pronounced and occur only occasionally. The occurrence is disguised by the random roll-up process which introduces a variation of the spatial location as well as a jitter of the scales. To some extent, this randomness is reduced by increasing the forcing amplitude, as we can see from the ordering of the vortices: they are ordered in a helical manner at opposite sides of the shear layer for case **Low-m**, whereas the mechanism for case **High-m** seems to be dominated by an axisymmetric component.

As in the previous section vortical structures in the transition region of the three jets are visualized using the λ_2 vortex identification criterion in Fig. 3.18 (isosurfaces of $\lambda_2 = -1$ are shown in a side view). One finds again the shifted transition process. For case **Low-m**, large two-dimensional structures dominate the roll-up, whereas three-dimensional and streamwise elongated small vortex filaments or vortex tubes initiate the breakdown process for higher disturbance levels. As the differences

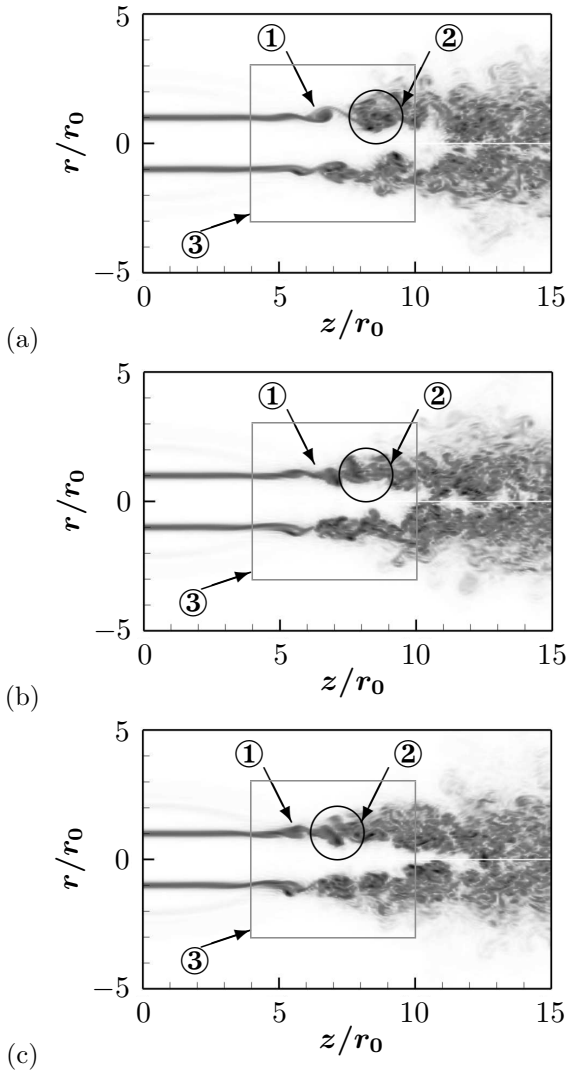


Figure 3.17: Visualization of vortical structures by $|\omega|$ in the $r-z$ plane at $\theta = 0$ for cases (a) Low- m , (b) Med- m and (c) High- m . The gray contour levels from light to dark are within $0 \leq |\omega| \leq 13$. ① dominant structure during roll-up of shear layer; ② interaction of large-scale structures; ③ gray frame is the zoomed region of Fig. 3.18.

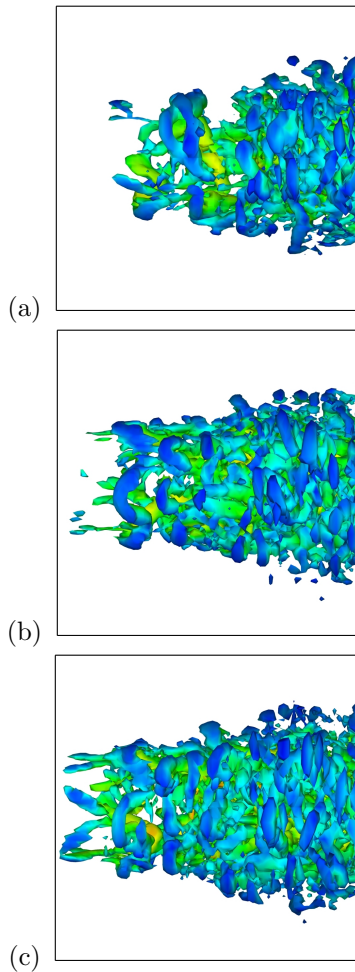



Figure 3.18: Visualization of vortical structures by isosurfaces $\lambda_2 = -1$ in the region $-3 \leq r/r_0 \leq 3$ and $4 \leq z/r_0 \leq 10$ for cases (a) *Low-m*, (b) *Med-m* and (c) *High-m* in a side view. The dimensions of the shown graph corresponds to the gray frame in Fig. 3.17. The isosurface is (color) coded by the local Mach number $0 \leq Ma \leq 1.4$ from dark gray (blue) to light gray (red) .

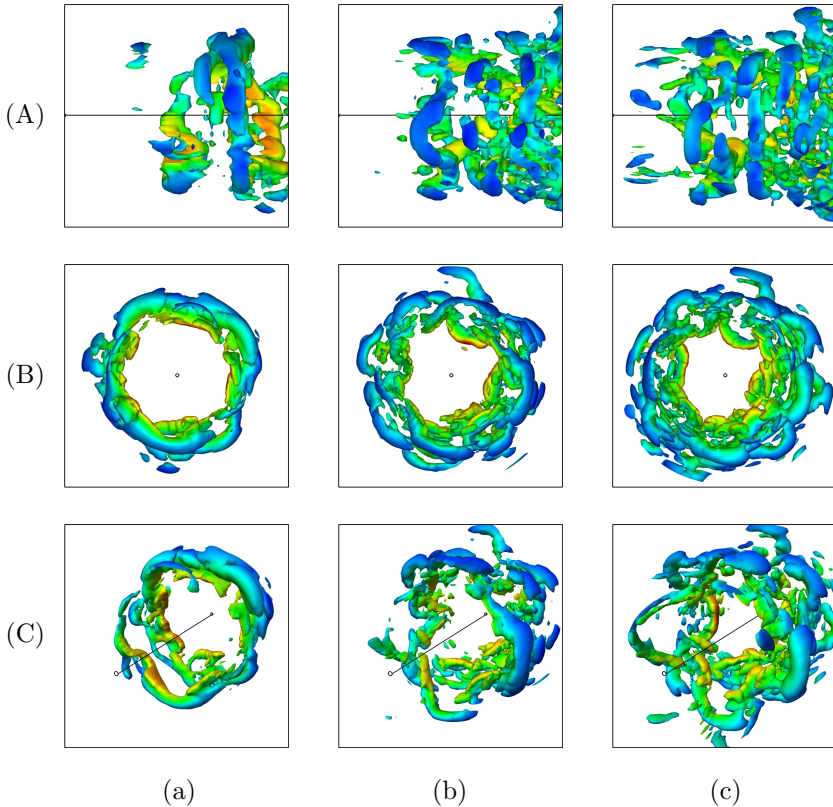



Figure 3.19: Visualization of vortical structures by isosurfaces of $\lambda_2 = -1$ in the region $-1.725 \leq r/r_0 \leq 1.725$ and $4 \leq z/r_0 \leq 7.5$. (a) Low- m , (b) Med- m and (c) High- m in a (A) side view, (B) front view and (C) three-dimensional front-side view. The isosurface is (color) coded by the local Mach number $0 \leq Ma \leq 1.4$ from dark gray (blue) to light gray (red) .

among the three cases are more pronounced compared to the first type of modal excitation we here provide additional graphs in which the quality of the isosurface visualizations is enhanced by spectrally interpolating the data onto $N_\theta = 300$. The isosurfaces $\lambda_2 = -1$ in Fig. 3.19 show the same data, however, the λ_2 criterion is determined on a finer azimuthal mesh.

The differences in spatial extent of the structures become more evident, as can be seen in the side view given in row (A). For case **Low-m**, large azimuthally correlated structures dominate the roll-up whereas three-dimensional and streamwise-elongated small vortex filaments or vortex tubes initiate the breakdown process for higher disturbance levels. The front views in row (B) show that the hairpin vortices emerging in the radial direction have significantly smaller azimuthal spacing but increased radial extent for larger forcing amplitude. In the three-dimensional view presented in row (C) the strong azimuthal coherence and the interaction of the structures for case **Low-m** can be seen, whereas cases **Med-m** and **High-m** show significantly distorted toroidal structures which disintegrate into small structures. In summary, the transitional development is initiated at larger distances from the inflow and is more rapid when using the low excitation level. Thereby, larger, clearly separated structures are generated in the shear layer. However, the position of interacting structures itself is localized with increasing forcing amplitude and occurs in a more axisymmetric fashion. To support these observations quantitatively, the one-dimensional azimuthal turbulent kinetic energy spectra will be investigated in the following section.

In summary, the transitional behavior is initiated at larger distances from the inflow and is more rapid when using the low excitation level. Thereby, larger, clearly separated structures develop in the shear layer. However, the roll-up and downstream positions of subsequent vortex interactions is localized with increase in forcing amplitude and occurs in a more axisymmetric fashion. To quantitatively support these observations, the one-dimensional azimuthal turbulent kinetic energy spectra in the transitional region will be investigated in the following section.

Since the differences in the visualizations of the instantaneous near-field pressure data are minute for the cases with the modified modal composition, we only present case **Med-m** in Fig. 3.20. Very similar to the previously addressed cases, we observe that the sound waves seem to be emitted slightly further upstream of the position where the instantaneous shear layers merge. As pointed out before, the quality of the chosen combination of nonreflecting boundary conditions supplemented by sponge-layers is demonstrated by the waves that leave the computational domain without causing any artificial reflections.

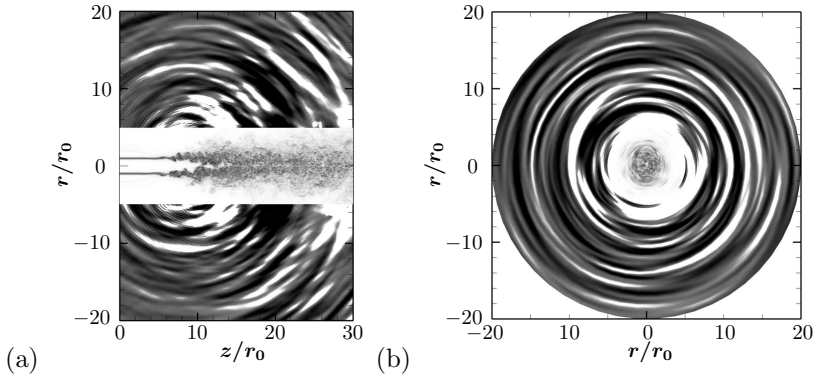


Figure 3.20: Visualization of vortical structures by contours of $|\omega|$ in the near field $r/r_0 < 5$ (gray contour levels from light to dark within $0 \leq |\omega| \leq 13$) and corresponding pressure fluctuations in the acoustic near field $r/r_0 \geq 5$ (gray contour levels from dark to light within $-5 \cdot 10^{-4} \leq p' \leq 5 \cdot 10^{-4}$) for case *Med-m*: (a) in the $r-z$ plane at $\theta = 0$ and (b) in the $r-\theta$ plane at $z/r_0 = 12$.

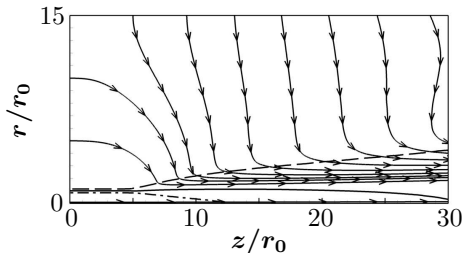


Figure 3.21: Visualization of mean flow streamlines for case *Med-m*. Lines denote $\cdots \langle w \rangle = 0.95U_j$, $\text{—} \langle w \rangle = 0.5U_j$ and $\text{---} \langle w \rangle = 0.05U_j$.

3.3.2 Mean flow and turbulence results

For the modified collection of excited instabilities, we investigate again the influence of the forcing amplitude on the jet mean flow and the turbulence. The entrainment of surrounding fluid can be seen in Fig. 3.21 where the mean flow is visualized. There are no noticeable differences among the streamline patterns of the three different excitation levels. The length of the potential core z_c is $z_c/r_0 \approx 12.17$. The dot-dashed line corresponds to the mean flow value $\langle w \rangle = 0.95U_j$, whereas the dashed

line denotes $\langle w \rangle = 0.05U_j$ and exhibits a rather linear spreading of the jet downstream of around five jet diameters. The solid line marks again 50% of the jet exit velocity and demonstrates the slow decay of axial momentum. Compared to case **Med**, we notice a slightly less pronounced entrainment for case **Med-m**: in the first case, one could see streamlines directed upstream at the end of the domain. The potential core lengths z_c vary slightly with forcing amplitude and are listed in Tab. 3.5. For an increasing forcing amplitude, we find again reduced potential core lengths, as expected. As before, other data characterizing the jet development can be found in the same table (the growth rate of the jet half-width, the virtual origin and the growth rate of the vorticity thickness).

Table 3.5: Potential core lengths z_c/r_0 , growth rates of the jet half-widths $d(r_{1/2}/r_0)/dz$ (determined by linear fits in the range $15 \leq z/r_0 \leq 30$), virtual origins z_0/r_0 and growth rates of the vorticity thicknesses $d(\delta_\omega/r_0)/dz$ (determined by linear fits in the range $6 \leq z/r_0 \leq 10$) for case **Low-m**, **Med-m** and **High-m**.

Case	z_c/r_0	$d(r_{1/2}/r_0)/dz$	z_0/r_0	$d(\delta_\omega/r_0)/dz$
Low-m	12.63	0.062	-5.23	0.249
Med-m	12.17	0.056	-8.00	0.251
High-m	11.99	0.053	-9.78	0.246

The streamwise development of the mean axial velocity at the centerline w_c and the jet half-width $r_{1/2}$ are shown in Fig. 3.22. As said before, we expect the differences along the jet centerline to remain small upstream of the potential core collapse since the forcing excites Kelvin-Helmholtz type instabilities. With increased forcing amplitude, the centerline velocity starts to decay slightly further upstream, while the decay itself remains almost unaffected. The results now compare favorably with the experimental reference data by Lau *et al.* (1979) and Arakeri *et al.* (2003) as well as with numerical data by Bogey & Bailly (2005*b*). Note that in this section the LES data of Bogey & Bailly is shifted in streamwise direction by $z_0/r_0 = 2$ to match the different core lengths. The experimental data (denoted by symbols) is shifted as follows: that of Arakeri and coworkers by $z_0/r_0 = -5$, that of Lau *et al.* by $z_0/r_0 = -4$. The data form two groups: the numerical results exhibit a delayed but in itself a slightly more abrupt onset of velocity decay.

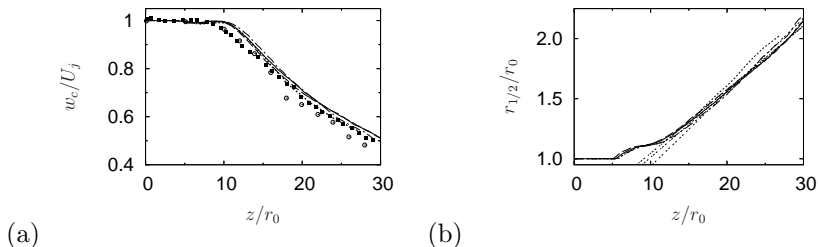


Figure 3.22: (a) Mean axial velocity along the jet centerline w_c and (b) jet half-width $r_{1/2}$: --- *Low-m*, — *Med-m*, - - - *High-m*, *Bogey & Bailly (2005b)*, \circ *Lau et al. (1979)*, \blacksquare *Arakeri et al. (2003)*. --, ---, - - - denote the linear fit to the half-width development for case *Low-m*, *Med-m* and *High-m*.

In the experiments of *Lau et al.*, a faster decay of the mean centerline velocity is observed leading to the lowest mean flow velocities in the investigated domain. Without the axial shift the experimental data show a delayed collapse of the potential core compared to the numerical data. This delayed but more prompt onset of decay for the computational results might again be related to the differences in initial momentum thicknesses and in oncoming disturbance levels and has been similarly reported in other investigations (*Bodony & Lele, 2004; Bogey & Bailly, 2005b; Bodony & Lele, 2008*). This disturbance-level effect, although very small, is best observed for case *Low-m*, where the delayed onset combined with an enhanced decay eventually causes the distribution to cut across the medium-amplitude case.

As before, the jet half-widths (Fig. 3.22(b)) do not vary significantly. Again, the jet spreading sets in around $z/r_0 \approx 5$, but it is not before the end of the potential core that it is significantly increased and the jet widens linearly in the streamwise direction. As explained in the previous section, we determine the growth rates of the jet half-width by a linear fit in the range $15 \leq z/r_0 \leq 30$ (Tab. 3.5). The cases with the modified modal excitation have growth rates from $d(r_{1/2}/r_0)/dz \approx 0.052 \dots 0.062$ and thus are significantly reduced compared to the excitation that triggers all unstable modes. Please recall that similar values are reported by *Bogey & Bailly (2006a)*, who, when doubling the streamwise extent of computational domain observe an increase towards asymptotic values of experiments carried out in the self-similar region (see also section 3.2.2).

The RMS of the axial and radial velocity along the jet centerline

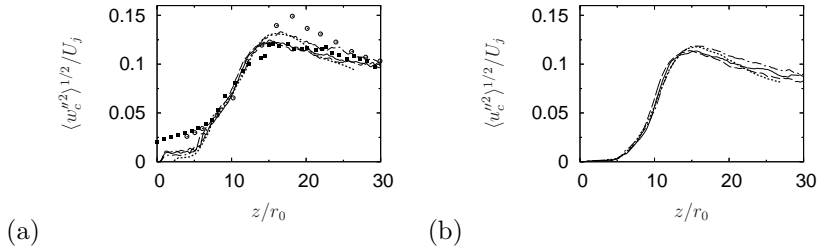


Figure 3.23: RMS of (a) axial velocity fluctuations $\langle w_c''^2 \rangle^{1/2}$ and (b) radial velocity fluctuations $\langle u_c''^2 \rangle^{1/2}$ along the jet centerline: --- Low-m, — Med-m, ··· High-m, ····· Bogey & Bailly (2005b), \circ Lau et al. (1979), \blacksquare Arakeri et al. (2003).

are shown in Fig. 3.23. As for the three previously investigated cases, the axial profiles of the RMS are similar. In particular, cases Med-m and High-m are almost indistinguishable. The axial velocity fluctuations (Fig. 3.23(a)) saturate close to the inflow at levels of $\langle w_c''^2 \rangle^{1/2} / U_j \approx 0.01$. In the transition region the values rise significantly until they reach their maxima around $z/r_0 = 15 \dots 17$. With increasing forcing amplitude, the streamwise development is shifted slightly upstream and the corresponding peaks also occur at shorter distances from the inflow. The agreement between cases Med-m and High-m with the recent experiments of Arakeri *et al.* (2003) is very good with respect to the peak values and the streamwise evolution. Both simulations reach RMS peak values of $\langle w_c''^2 \rangle^{1/2} / U_j = 0.124$. The development of case Low-m is slightly delayed and reaches a peak value of $\langle w_c''^2 \rangle^{1/2} / U_j = 0.133$ which is in good agreement with observations by Bogey & Bailly (2005b). They report a peak value of 0.131, however, they find a slightly faster decay of intensities with streamwise distance. For completeness we repeat that Lau (1981) pointed out that the over-prediction of the RMS of their data (Lau *et al.*, 1979) is attributed to the analysis procedure (see also section 3.2.2).

In Fig. 3.23(b) the radial velocity RMS fluctuations are shown along with the reference LES. For all forcing amplitudes very similar profiles are found. Again, case Low-m reaches highest peak values $\langle u_c''^2 \rangle^{1/2} / U_j = 0.120$ and its evolution up to the peak location is in very good agreement with the results by Bogey & Bailly. In the streamwise direction we observe a less pronounced decay of all RMS distributions compared to their results. Note again that the simulations use fun-

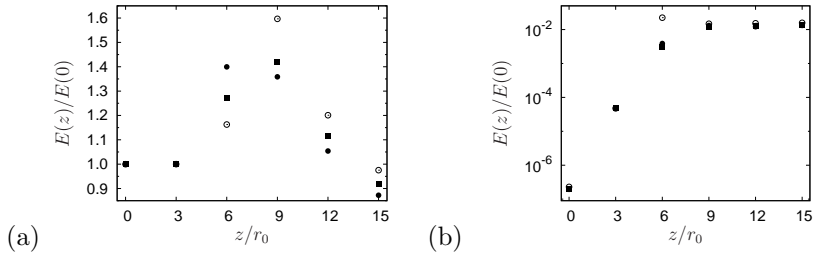


Figure 3.24: One-dimensional turbulence kinetic energy of (a) varicose mode $n = 0$ in linear scales and (b) first helical mode $n = 1$ in logarithmic scales determined along the nozzle lip line at streamwise positions $z/r_0 = i \cdot 3$ ($i = 0, \dots, 5$) normalized by the kinetic energy of case *Med-m* at $z = 0$: $E(n = 0, z = 0) = 3.73 \cdot 10^2 U_j^2$. \circ *Low-m*, \blacksquare *Med-m*, \bullet *High-m*.

damentally different numerical codes, and more importantly, different inflow-forcing methods. From this, one can clearly deduce that the employed collection of instabilities employed in the forcing has a similar effect on the jet development along the centerline as, for example, the ring-vortex method by Bogey & Bailly (2005b).

In the following, the effect of changes in forcing amplitude on the early shear layer development is investigated for this second type of modal composition. Again we analyze the one-dimensional azimuthal turbulent kinetic energy spectra (computed according to equation (3.1)), however, due to the differences in the instantaneous vortical structures for the three forcing amplitudes, the TKE of the axisymmetric mode and the first helical mode are determined at five downstream positions along the nozzle lip line ($r = r_0$) and are shown in Figs. 3.24(a) and (b). The energy is normalized by the energy of case *Med-m* at the jet inflow plane $z = 0$ contained in mode $n = 0$. As could be seen in the instantaneous snapshots, the vortical structures caused by instability waves alter the flow significantly at $z/r_0 \approx 6$. At this location, enhanced TKE levels are observed and the alignment for the three cases follows their initial forcing amplitudes. The modal energy has grown by approximately 16%, 28% and 40% for cases *Low-m*, *Med-m* and *High-m*, respectively. At $z/r_0 = 9$, we find that the roles are inverted: case *Low-m* exhibits the largest amount of energy, which also corresponds to the global maximum for the analyzed positions and all excitation amplitudes. Compared to the inflow level, mode $n = 0$ of case *Low-m* has a 60% TKE

increase. Further downstream, the differences between the three cases are reduced. However, even at $z/r_0 = 15$ the low-amplitude excitation results in higher energy in mode $n = 0$ than the higher amplitude cases.

The helical mode $n = 1$, which seems to dominate the instantaneous roll-up process for case **Low-m**, is analyzed in Fig. 3.24(b). Its downstream evolution is characterized by very small initial amplitudes. A similar inversion of the alignment for the three amplitudes is observed slightly closer to the inflow region compared to $n = 0$. Case **Low-m** has, for instance, a TKE increase of more than four orders of magnitude within a short streamwise distance of three nozzle diameters and exceeds the two other cases. Further downstream, this difference in mode $n = 1$ for the three cases becomes gradually smaller and the results are almost indistinguishable downstream of $z/r_0 = 12$.

We now turn to the downstream development of the higher azimuthal wavenumbers, focusing on the excited modes $n = 4, \dots, 8$. Figure 3.25) shows five equidistant downstream locations along the nozzle lip line. At the inflow, we see the effect of the introduced disturbances, i.e. the

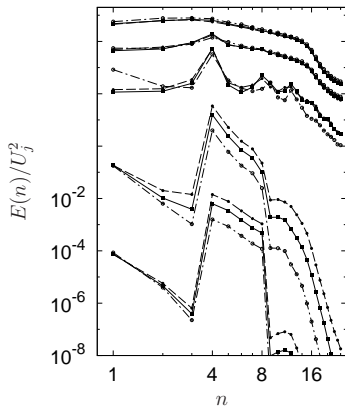


Figure 3.25: One-dimensional turbulence energy spectra E in θ -direction along the nozzle lip line at streamwise positions $z/r_0 = i \cdot 3$ ($i = 0, \dots, 4$ from bottom to top): $-\cdot-$ **Low-m**, $—$ **Med-m**, $---$ **High-m**. The groups of spectra are shifted by a factor of 10 for clarity.

TKE in azimuthal wavenumbers $n = 4$ through 8 is higher, at least by an order of magnitude compared to the unexcited modes. Also, the effect of the amplitude at the inflow is reflected by the different energy

levels of the three cases. Further downstream, the energy increases in all modes, i.e. the initially undisturbed modes also rise. In particular, $n = 4$ outweighs the other excited modes. The other forced modes exhibit less TKE increase and undisturbed modes, e.g. $n = 1$, reach comparable values. At the third streamwise position $z/r_0 = 6$, case **Low-m** exhibits the previously noticed sudden rise of $n = 1$ which substantiates the previously made observation of helical structures during its transition process. As pointed out before, this rise of mode one is accompanied by a downstream-delayed rise of TKE in the all-dominant axisymmetric mode. Significantly enhanced TKE also occurs in the even mode $n = 4$ for all cases and the differences in initial amplitude further diminish. Cases **Med-m** and **High-m** are not only characterized by $n = 4$, but also by higher harmonics thereof. In particular, a pronounced rise in the azimuthal wavenumber $n = 8$ can be observed which seems to allow for further interactions of a weakly developed higher-harmonic $n = 12$. In contrast, case **Low-m** with its prominent increase of mode $n = 1$, exhibits only small changes in the higher wavenumbers $n = 9$ and 12 and, more importantly, no distinct peak at $n = 8$. A redistribution of TKE between the dominant modes might be the reason for the reduction in dominance of $n = 4$ together with the rise of $n = 8$, or the onset of secondary instabilities and nonlinear interactions of modes as appreciable disturbance level are attained at this downstream location. Following Hussain (1986), this interaction could be related to a breakdown process of structures termed ‘*cut-and-connect*’, which describes the connection of two adjoining vortices. The occurrence of vortex heads in circumferential direction visualized by the λ_2 representation in Fig. 3.19 for cases **Med-m** and **High-m** compares favorably with the sketch of an idealized breakdown process (see Hussain, 1986, figure 14, p. 339). Further downstream, the amplitude of the asymmetric mode for case **Low-m** decays and $n = 4$ is found to contain most energy at $z/r_0 = 9$ for all cases. At the last investigated axial position, we observe a broad-banded energy distribution and for wavenumbers $n \geq 16$ a drop-off of about two orders of magnitude.

In the following, we turn to the development along the nozzle lip line. Recall that the amplitude effects are expected to be most pronounced along this line due to the nature of the triggered eigenmodes. The axial and radial velocity fluctuations versus downstream coordinate are given in Fig. 3.26. Consistent with the expectations the axial RMS velocities greatly vary and again exhibit the dual-peak distribution described in

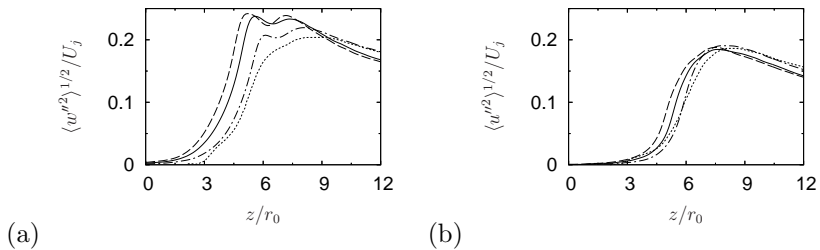


Figure 3.26: RMS of (a) axial velocity fluctuations $\langle w''^2 \rangle^{1/2}$ and (b) radial velocity fluctuations $\langle u''^2 \rangle^{1/2}$ along the nozzle lip line: $-\cdot-$ Low-m, $—$ Med-m, $---$ High-m, \cdots Bogey & Bailly (2005b).

detail in section 3.2.2. Even for a small disturbance amplitude, such as 1.5% in case Low-m, the axial distribution of $\langle w''^2 \rangle^{1/2} / U_j$ starts to rise at the inflow plane and reaches a local maximum three nozzle diameters downstream, before attaining the global maximum at $z/r_0 \approx 8$, i.e. upstream of the end of the potential core. As before, increasing the forcing amplitude shifts the transition process upstream and amplifies the dual-peak structure for which the global maximum now occurs at the first streamwise position. This dual-peak distribution is most likely a result of the localization of vortex pairings (Zaman & Hussain, 1980) at this particular axial position. This assumption is further supported by the following arguments: As could be observed in various quantities so far, an increased forcing amplitude shifts the development of the shear layer upstream but also significantly reduces the streamwise jitter of the shear-layer roll-up. As the computation of the mean quantities also involves an azimuthal average, the dual peaks are more pronounced for cases Med-m and High-m compared to case Low-m. Azimuthal averaging over a helical alignment tends to smear out gradients, whereas an axisymmetric orientation due to the localization tends to amplify the dual-peak structure. The overall streamwise evolution of simulation Low-m is closest to results by Bogey & Bailly (2005b), however, because of the differences in the inflow forcing procedure their result does not exhibit a second peak related to the localized vortex pairings. Note again that similar variations of the centerline longitudinal fluctuation intensity can, for example, be found in the experimental work of Zaman & Hussain (1980) where profiles exhibit strong dual-peak distributions (see, e.g. their figures 3(a) or 27, p. 455 and 483; for further details see also section 3.2.2).

In contrast to the axial velocity, the development of the radial RMS fluctuations remains almost unaffected by the changes of the inflow forcing. This is also in agreement with experimental results (Zaman & Hussain, 1980) which document that radial RMS fluctuations of a jet with controlled vortex pairing exhibit less variation compared to the axial component. Again, a reduction of amplitude seems to slow down the streamwise evolution. Best agreement with the results by Bogey & Bailly is found again for simulation **Low-m**. For completeness, we point out, however, that the axial profiles for the radial velocity RMS are higher than observed experimentally (overestimated by $\sim 40\%$, see Bogey & Bailly (2005b)), which is also related to the artificially increased initial momentum thickness addressed before.

Following the pattern from the previous section, the effect of the forcing on the development of the vorticity thickness is now investigated. Figure 3.27 shows the axial development of the vorticity thickness (as determined by equation (3.2)) for the three cases. The initially laminar

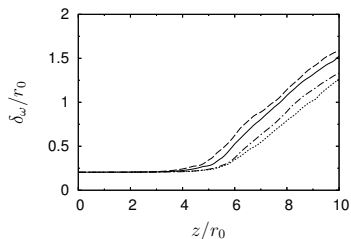


Figure 3.27: Streamwise development of vorticity thickness δ_ω : --- **Low-m**, — **Med-m**, -.- **High-m**, *Bogey & Bailly (2005b)*.

shear layer thicken further upstream when increasing the disturbance amplitude. In contrast to the cases which excite all unstable helical wavenumbers, the streamwise growth is almost linear once the spreading has started. The growth rates of the vorticity thickness given in Table 3.5 have been determined by a linear fit to the data within $6 \leq z/r_0 \leq 10$. The predicted values of $d(\delta_\omega/r_0)/dz \approx 0.25$ are higher than those observed experimentally (see again the summary of experimental values reported by Gutmark & Ho (1983) which are in the range from 0.112 to 0.218), but are again in agreement with the study by Bogey & Bailly (2005b). Also note that case **High-m** has a stepwise increase of the vorticity thickness with a discontinuity around the location where the local

minimum in the dual-peak distribution of the lip line RMS is observed.

The radial Reynolds normal stress and the shear stress are presented in Fig. 3.28. We focus again on the profiles at equidistant streamwise locations $z/r_0 = 3, 6$ and 9 which are shifted by the marked amount.

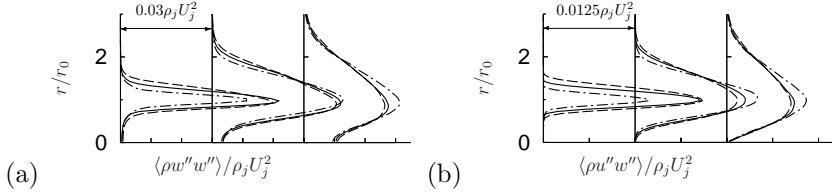


Figure 3.28: Streamwise development of radial Reynolds stress profiles at streamwise positions $z/r_0 = i \cdot 3$ ($i = 1, \dots, 3$ from left to right): (a) $\langle \rho w'' w'' \rangle / \rho_j U_j^2$, (b) $\langle \rho u'' w'' \rangle / \rho_j U_j^2$: --- Low-m, — Med-m, - - - High-m.

Far upstream of the closing of the potential core the values rise rapidly, saturate within a distance of three radii, reach their maxima in the range $z/r_0 \approx 5-6$ and decay in the streamwise direction. Corresponding to the previously noted occurrence of streamwise-elongated vortical structures further upstream for larger disturbance amplitudes (see section 3.3.1), the peaks are higher at corresponding streamwise locations for higher forcing amplitudes. Downstream of $z/r_0 = 6$, which corresponds to the second profile in Fig. 3.28, the orientation changes and we now find case Low-m, whose streamwise development is delayed the strongest, to reach the largest Reynolds stress values. This very rapid development for case Low-m compared to the higher amplitude cases confirms the impression from the snapshots of instantaneous processes (see Fig. 3.17 – Fig. 3.19) that transition occurs in a spatially more confined area and is more rapid. Also, as noted before, the process can be linked to the dominance of azimuthal wavenumbers $n = 0$ and $n = 1$ in this streamwise region as, for example, found in the one-dimensional turbulence kinetic energy spectra presented in Figs. 3.24 and 3.25.

Finally, the axial velocity spectra along the jet centerline and the nozzle lip line in the transition region are investigated. As pointed out before, the interval length during the post-processing is chosen such that the nondimensional frequency $St = 0.04$ is resolved (see section 2.9 for further details). The axial velocity spectra at five streamwise positions $z/r_0 = i \cdot 3$ with $i = 0, \dots, 4$ are shown in Fig. 3.29. The spectra at the inflow plane are as expected, i.e. the peak values along the jet centerline

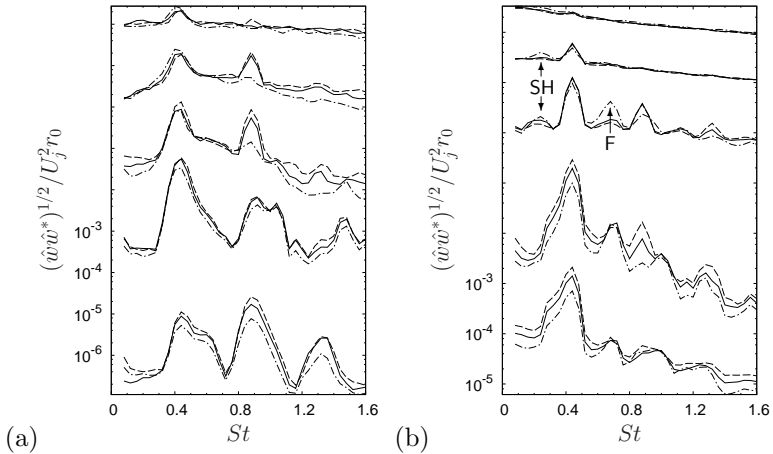


Figure 3.29: Axial velocity spectra at streamwise positions $z/r_0 = i \cdot 3$ ($i = 0, \dots, 4$ from bottom to top) along: (a) jet centerline, (b) jet lip line: --- Low- m , — Med- m , -.- High- m . The groups of spectra are shifted by a factor of 10 for clarity. SH denotes the occurrence of subharmonics. F denotes the advent of the fundamental frequency for case Low- m .

and the nozzle lip differ by two orders of magnitude (Figs. 3.29(a) vs. (b)). Highest peaks occur along the lip line where the magnitude of the axial velocity eigenfunction reaches its maximum and the alignment of the spectral amplitude follows the enforced disturbance amplitudes. As for the first type of modal excitation, the flow is found to be most receptive to disturbances in a Strouhal number range around $St \approx 0.4$, which corresponds to the column mode frequency (Zaman & Hussain, 1980) (also referred to as preferred mode (Crow & Champagne, 1971; Huerre & Monkewitz, 1990)). Overall, we observe a persistent and dominant existence of structures with this Strouhal number that are present along the centerline and the lip line. In combination with the TKE spectra shown in Figs. 3.24 and 3.25, we note that the eigenmode-based forcing does excite modes $n = 4$ through $n = 8$ at the inflow, however, further downstream this interaction results in most-amplified structures with wavenumbers $n = 0$ and $n = 4$ at the frequency of $St = 0.43$. This Strouhal number corresponds to the excitation frequency of the mode $n = 8$. A second dominant frequency, $St \approx 0.88$, emerges at $z/r_0 = 3$

along the lip line presented in Fig. 3.29(b). There, the three cases order according to their excitation amplitude. This frequency persists further downstream and at $z/r_0 = 6$ it appears at the jet centerline at $z/r_0 = 6, 9$. It is important to note that at the centerline this peak at $St \approx 0.88$ is observed only for cases **Med-m** and **High-m** and is not contained in the velocity signals of case **Low-m**.

At $z/r_0 = 6$ a pronounced subharmonic at $St \approx 0.2$ emerges along the lip line, most obviously for the weakly disturbed flow. This subharmonic is marked by the symbol ‘SH’ in Fig. 3.29(b). Its appearance is smeared out because the occurrence of the pairings with the fundamental frequency $St \approx 0.43$ is random as pointed out before. For case **Med-m**, this subharmonic is less pronounced and decays much faster in the stream-wise direction and in case **High-m** it appears only weakly. This supports the previously made observation that low-amplitude forcing results in a random but detectable vortex pairing and a persistent dominance of low frequencies ($St \leq 0.5$) downstream of $z/r_0 = 6$, whereas for case **High-m** a broader range of scales interact.

At $z/r_0 = 6$ case **Low-m** shows a distinct rise of a frequency around $St \approx 0.7$ which is denoted by the symbol ‘F’ in Fig. 3.29(b). This peak corresponds to the fundamental frequency of the asymmetric least stable mode $n = 1$ that plays a dominant role in the transition process although it is initially unexcited (instantaneous data as well as TKE spectra, cf. section 3.3.1). This frequency is in very good agreement with the linear stability theory (Michalke, 1984; Michalke & Hermann, 1982), according to which the azimuthal wavenumbers $n = 0, 1$ reach their highest growth rates at the fundamental frequency of $St = 0.67$ and $St = 0.68$, respectively. Furthermore, with increasing distance from the orifice the ratio of the initial momentum thickness θ_0 to jet radius r_0 increases and, hence, linear theory predicts a dominance of the helical wavenumber $n = 1$ over the axisymmetric mode $n = 0$.

In order to clarify the roles of the axisymmetric and the first helical shear-layer instability modes during the onset of transition of case **Low-m**, the downstream development of the azimuthal Fourier amplitude $\hat{w}(n)$ is determined for two frequencies. The investigated fundamental frequencies of the modes $n = 0$ and $n = 1$ correspond to the Strouhal numbers $St_0^{n=0} = 0.676$ and $St_0^{n=1} = 0.681$. According to LST the growth rates are $-\alpha_i^{n=0}r_0 = 1.60$ and $-\alpha_i^{n=1}r_0 = 1.55$, respectively. As the frequency difference between these two modes is very small the corresponding changes in growth rates are less than two decimal places.

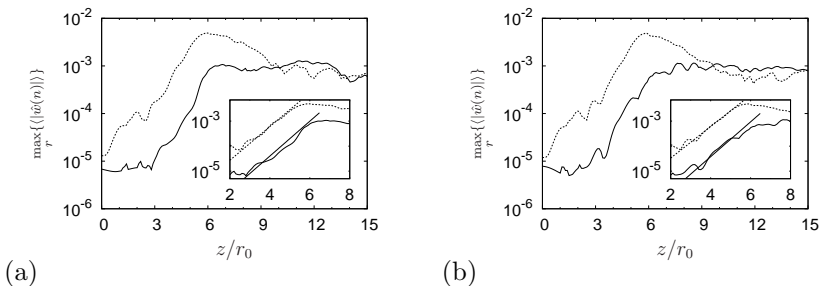


Figure 3.30: Downstream development of Fourier modal amplitude $\hat{w}(n)$ of azimuthal wavenumbers — $n = 0$ and - - - - $n = 1$ for (a) $St_0^{n=0} = 0.676$ and (b) $St_0^{n=1} = 0.681$. Inlay shows zoomed axial region $2 \leq z/r_0 \leq 8$ together with straight lines denoting growth rates according to linear stability theory.

Figure 3.30 shows the downstream development of the modal amplitudes beyond the point of the closing of the potential core. For both frequencies, the modal amplitudes of the helical mode are significantly larger than the amplitude of the axisymmetric mode, in particular around the relevant streamwise position $z/r_0 \approx 6$. Thereby it is substantiated that the occurrence of the fundamental frequency can be linked to the helical azimuthal wavenumber $n = 1$. As a side remark, we note that a very good agreement of the downstream development with the prediction of LST is observed for both modes shortly downstream of the inflow region, as can be seen in the inlays of Figs. 3.30(a) and (b).

3.3.3 Acoustic results

The directly computed near-field information of the three LES (employing the modified modal excitation at the inflow) are now analyzed in the same way as for the first type of excitation presented in section 3.2.3.

In Fig. 3.31, the pressure spectra received under the same observer angles as before are shown. Now, the end of the potential core of case Med-m is selected as the origin of a spherical coordinate system (R, θ, ϕ) which affects the exact coordinates reported in Table 3.6 only minutely (cylindrical and polar coordinates for the three observer locations). Note that the spectra are evaluated at exactly the same fixed computational grid points as before. For details of the post-processing employed in the determination of the spectra, we refer to section 2.9 and repeat here only that neither an additional filtering of the LES time signals nor a spectral

Table 3.6: Observer locations of spectra measurements and polar distances R and angles ϕ_{exact} for cases **Low-m**, **Med-m** and **High-m**.

ϕ	r/r_0	z/r_0	R/r_0			ϕ_{exact}		
			Low	Med	High	Low	Med	High
30°	9	27	17.0	17.3	17.5	32.1°	31.3°	30.9°
60°	15	21	17.2	17.4	17.5	60.8°	59.5°	59.0°
90°	18	12	18.0	18.0	18.0	92.0°	90.5°	90.0°

smoothing is applied. Also note that the difference in polar distances R between the reference data and the current results has been accounted for by assuming a $1/R$ -decay (see Tab. 3.4, page 69).

As for the first type of modal excitation, three measurement points, with similar polar distances R and polar angles $\phi \approx 30^\circ$, 60° and 90° are analyzed in Figs 3.31(a)-(c). A close-up view of the range $0.6 \leq St \leq 1.2$ can be found in graphs (d)-(f). The recent experimental data by Bogey *et al.* (2007b) (high-subsonic jet at a Reynolds number of $Re = 7.8 \times 10^5$) is again shown by solid square symbols. The dotted lines indicate the data from the work of Bogey & Bailly (2005b).

The spectral shapes in Fig. 3.31 exhibit a strong dependence on the observation angle ϕ , whereas the effect of the difference in disturbance amplitude is noticeable most dominantly under intermediate observer angles and for low frequencies. The spectra in Fig. 3.31 exhibit a strong dependence on the observation angle ϕ , whereas the effect of the disturbance amplitude is noticed most dominantly at low frequencies and at intermediate observer angles. For small polar angles (Figs. 3.31(a) and (d)), the spectra are found in very good agreement, i.e. the spectral shape and also the peak of 125 dB is closely reproduced by our results which reach peak values between 124 dB and 127 dB depending on forcing amplitude. Our LES spectra are dominated by a frequency band below $St = 0.4$, which is the peak frequency for all cases. However, the experimentally determined peak of the spectra is around $St \approx 0.2$ and the reference LES peak appears at a slightly higher Strouhal number, $St \approx 0.3$. The spectrum for case **Low-m** exhibits more contributions at lower frequencies compared to the cases with higher excitation amplitudes. This enhanced low frequency band is related to the randomly occurring vortex pairings with helical wavenumber $n = 1$ (see prominent rise of helical mode $n = 1$ in Figs. 3.24, 3.25 and 3.30) whose fundamen-

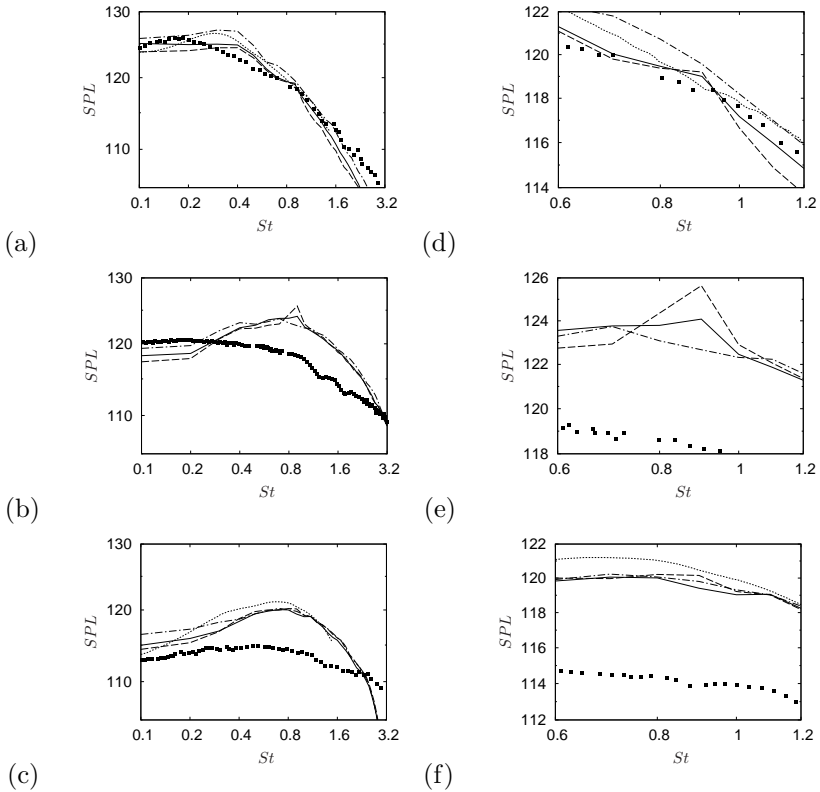


Figure 3.31: Near-field pressure spectra in dB at (a) $\phi = 30^\circ$, (b) $\phi = 60^\circ$ and (c) $\phi = 90^\circ$: $---$ Low- m , $---$ Med- m , $---$ High- m ; \blacksquare Bogey et al. (2007b) at (a) $r = 15r_0$, $z = 30r_0$, (b) $r = 15r_0$, $z = 20r_0$, (c) $r = 15r_0$, $z = 10r_0$; \cdots Bogey & Bailly (2005b) at (a) $r = 12r_0$, $z = 29r_0$, (c) $r = 15r_0$, $z = 11r_0$. Graphs (d), (e) and (f) show close-up of Strouhal $0.6 \leq St \leq 1.2$.

tal frequency is halved to $St \approx 0.35$ during the pairing. This kind of vortex pairings is known to efficiently contribute to noise emissions, in particular, in the downstream directions (Colonius *et al.*, 1997; Mitchell *et al.*, 1999; Bogey *et al.*, 2000). Overall, case Low- m compares favorable with the reference LES. With increasing disturbance amplitude we observe less low-frequency noise, however, a tonal component around

$St \approx 0.9$ starts to appear which is most noticeable in the close-up provided in Fig. 3.31(d). The strength of the tonal peak is tied to less noise in the high-frequency range and, thus, the SPL drop-off sets in at lower frequencies for larger excitation levels.

At an increased observation angle, the overall dominance of the low frequencies is significantly reduced. In Figs. 3.31(b) and (e), at $\phi \approx 60^\circ$, we find generally lower sound pressure levels for frequencies below $St = 0.4$, but again the induced large two-dimensional structures for case **Low-m** result in the highest amplitudes among the three investigated cases. For higher frequencies the experimental data are reproduced only qualitatively up to $St \approx 2$. In the band $0.5 \leq St \leq 2$ a large over-prediction by approximately 5 dB is observed, whereas experiments yield 120 dB . Again, case **Med-m** and **High-m** exhibit a tonal component which is also the global maximum and, as before, its strength is positively correlated to the excitation level. The SPL peak of case **High-m** is very strong, 7 dB larger than the experimentally determined broad-banded spectrum, and still 3 dB larger than case **Low-m**. It is interesting to note that these peaks around $St = 0.9$ are outside of the range of initially excited frequencies but can equally be observed in the axial velocity spectra at the jet centerline and at the nozzle lip line (see Fig. 3.29).

In agreement with experimental as well as LES data, we find that at right angles to the jet axis the emitted noise is characterized by a broad-band spectrum with no dominant frequencies, as can be seen for $\phi = 90^\circ$ in Figs. 3.31(c) and (f). Again, we find significantly over-predicted sound pressure levels, i.e. the current simulations have a peak of 120 dB which is 6 dB higher compared to the experiments (Bogey *et al.*, 2007b). For case **Low-m** a similar spectrum as in the reference LES is found but, as before, with a 2 dB enhancement in the low frequencies $St < 0.3$. All numerical results predict a slight shift of the peaks to higher Strouhal numbers, $St \approx 0.8$ compared to $St \approx 0.6$ in the experiments. As pointed out before, the significantly overestimated pressure levels (in particular in the sideline direction) might be related naturally to the increased radial RMS fluctuations observed before (Bogey & Bailly, 2005b, 2006b; Bodony & Lele, 2008).

Overall, the main trends of the spectra provided by the simulations are in accordance with the reference data with a shift from a dominant low-frequency band at small angles from the jet axis to a broad-band character in the sideline direction. However, the differences in the disturbance amplitude, and the associated changes in the transition process,

generate a tonal peak around a Strouhal number of $St \approx 0.9$ which is outside the band of excited frequencies. Nonlinear interaction of excited and initially unexcited eigenmodes, in connection with the preferred mode, might lead to the dominance of this frequency. This aspect, together with possible explanations, will be addressed in the subsequent section.

The overall sound pressure level (OASPL in dB) level along the line $r/r_0 = 15$ for the three configurations are shown in Fig. 3.32. Again, we compared to the reference data by Bogey & Bailly (2006a) which is shifted to match the levels at $z/r_0 = 0$. The axial distribution with a

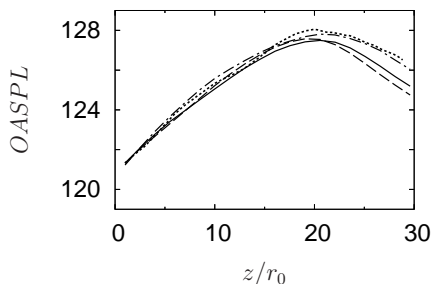


Figure 3.32: Axial distribution of overall sound pressure levels (OASPL in dB) along $r/r_0 = 15$: --- Low-m, — Med-m, -.- High-m, Bogey & Bailly (2006a).

peak around $z/r_0 = 20$ is in good agreement. Again, case Low-m is closet to the results from the literature. Downstream of $z/r_0 = 21$, we find a drop of the SPL for the cases with increased disturbance levels. The overall sound pressure level reductions in the downstream direction are a result of the induced tonal components that were found in the pressure spectra. As given in more detail above, this is in agreement with the experimental work of Zaman & Hussain (1981) (for more details with respect to this noise reduction see section 3.2.3, or the work of Hussain (1986)).

The acoustic section is concluded by comparing the azimuthal correlation of the pressure given by equation (3.3) is investigated at the same locations as before (which correspond to $\phi = 30^\circ$ and $\phi = 90^\circ$). Under small angles to the jet axis, i.e. at $\phi = 30^\circ$ (Fig. 3.33(a)), the pressure fluctuations are correlated similarly for all cases up to $\Delta\theta < 90^\circ$. The agreement with the computation by Bogey & Bailly and the experiments by Maestrello is very good for angular separations $\Delta\theta \leq 60^\circ$. For larger

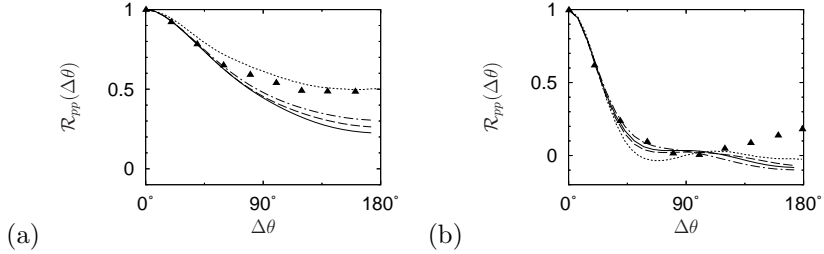


Figure 3.33: Azimuthal correlation coefficient \mathcal{R}_{pp} for pressure signals: (a) at ($r = 12r_0; z = 30r_0$) and (b) at ($r = 12r_0; z = 12r_0$). --- Low-m, — Med-m, - - - High-m, ······ Bogy & Bailly (2006b) (taken at (a) ($r = 12r_0; z = 29r_0$) and (b) ($r = 15r_0; z = 11r_0$)), far-field measurement \blacktriangle Maestrello (1976) ($\phi = 30^\circ$: $Re = 5.2 \cdot 10^4$, $Ma = 0.88$ and $\phi = 90^\circ$: $Re = 4.4 \cdot 10^4$, $Ma = 0.74$).

azimuthal angles $\Delta\theta$, the correlations of cases Med-m and High-m decrease further to $\mathcal{R}_{pp}(180^\circ) \approx 0.2$ and $\mathcal{R}_{pp}(180^\circ) \approx 0.25$, values that are below the reference data (the correlations improved compared to the first type of modal excitation, see section 3.2.3). The correlation in this sector is enhanced when reducing the forcing amplitude in case Low-m leading to correlation levels of 0.3. Overall, the results for $\phi = 30^\circ$ suggest a systematic lack of axisymmetric scales in the signal and that the naturally dominant helical mode occurring during the early stages of transition in case Low-m (see one-dimensional turbulence spectra, Fig. 3.25) contributes significantly to the correlation levels. We also note that the order of the correlation coefficients for the investigated cases corresponds to the amount of turbulent kinetic energy contained in the low azimuthal wavenumbers $n = 1$ and $n = 2$, showing the effectiveness of these structures to contribute to the pressure disturbances in the downstream direction. With respect to the lowered azimuthal coherence we note that Juvé and coworkers (Juvé *et al.*, 1979; Juvé & Sunyach, 1981) report correlation values for unexcited jets that are in very good agreement with ours ($\mathcal{R}_{pp}(180^\circ) = 0.25$). They also observe an increase to values in the range of the reference data when exciting the flow tonally at $St = 0.68$ (jet at $Re = 1.8 \cdot 10^5$, $Ma = 0.4$, $\mathcal{R}_{pp}(180^\circ) \approx 0.54$). The reported data is decomposed into its frequency components and, therefore, not shown for comparison.

The correlations of the pressure fluctuations in the azimuthal direction for polar angles of $\phi = 90^\circ$ are shown in Fig. 3.33(b). At this

location the correlation is similar for all cases. For angles $\Delta\theta \geq 45^\circ$ the signals are almost uncorrelated which is in agreement with the LES results by Bogey & Bailly(2006*b*) and with the far-field measurements by Maestrello(1976). The azimuthal correlations suggest that the eigenmode-based disturbances (which artificially excludes low azimuthal wavenumbers) tend to break the symmetry with respect to the downstream axis, especially at small angles to the jet axis. Note that the dominance of helical wavenumber $n = 4$ exhibits a axisymmetric alignment of structures during the transition process but does not contribute to the correlation level at $\Delta\theta = 180^\circ$. The reason for this loss of azimuthal coherence might be related to transition process which is characterized by the eigenmode interaction and the exclusion of low azimuthal wavenumbers from the inflow forcing while exactly these wavenumbers are believed to constitute major sound sources in the downstream direction (Michalke & Fuchs, 1975; Maestrello, 1976; Juvé *et al.*, 1979; Bogey & Bailly, 2006*b*).

Following Juvé *et al.* (1979) we employ an azimuthal Fourier expansion to obtain a more detailed picture of the different contributions of wavenumbers n to the spatial correlation coefficient \mathcal{R}_{pp} in the form of

$$\mathcal{R}_{pp}(\Delta\theta) = \sum_{n=0}^{N_\theta/2} a_n \cos(n \cdot \Delta\theta) , \quad (3.4)$$

where the sum of the coefficients a_n is normalized to unity. The Fourier components a_n of mode n with a contribution to the acoustic energy of more than one percent are reported in Tab. 3.7 for both observation angles ϕ .

Table 3.7: Contributions to the acoustic field in downstream direction ($\phi = 30^\circ$) and sideline direction ($\phi = 90^\circ$) for case Low-m, Med-m and High-m.

ϕ	Case	$n = 0$	$n = 1$	$n = 2$	$n = 3$	$n = 4$	$n = 5$	$n = 6$	$n = 7$
30°	Low-m	0.56	0.31	0.08	0.03				
	Med-m	0.52	0.35	0.08	0.03				
	High-m	0.53	0.33	0.09	0.03				
90°	Low-m	0.14	0.34	0.18	0.14	0.09	0.05	0.02	0.01
	Med-m	0.15	0.32	0.19	0.16	0.09	0.05	0.02	0.01
	High-m	0.14	0.30	0.20	0.17	0.09	0.05	0.02	0.01

As can be deduced from the presented correlations in the downstream direction, there is a reduced dominance of the axisymmetric mode $n = 0$, but a significantly enhanced contribution from the helical wavenumber $n = 1$ compared to the data reported by Bogey & Bailly (2006*b*) ($n = 0, 1$: $a_n = 0.67, 0.23$). Again, we note that similar values to ours were measured by Juvé & Sunyach (1981) and it is shown there that excitation increases the azimuthal correlation levels and accordingly the Fourier component $n = 0$ at small angles. In the sideline direction, the Fourier coefficients are similarly reported in the literature (again, see the work of Bogey & Bailly: $n = 0, \dots, 3$, : $a_n = 0.15, 0.29, 0.23$ and 0.19). However, the eigenmode forcing and the increased forcing amplitude seem to result in a transfer of energy from modes $n = 2, 3$, which are less energetic, to a broader range of wavenumbers $n \geq 5$.

3.3.4 Relevant noise generation mechanism: Link between “cut-and-connect” process and unexcited tonal component supported by weakly nonlinear theory

In the remaining part, we try to establish possible connections between the directly computed near-field pressure spectra and the flow field. One point is the dominance of a low-frequency band at small angles from the jet axis. Also, an attempt is made to clarify the origin of the tonal contribution in the near-field spectra observed for medium and high forcing amplitudes, in particular, under intermediate observer angles.

The pressure spectra under $\phi = 30^\circ$ show a pronounced frequency band below $St \approx 0.4$. We link this dominance to the formation of structures and subsequent interactions in the form of vortex pairings. The difference between case **Low-m** on the one hand and cases **Med-m** and **High-m** on the other are structures with azimuthal wavenumber $n = 1$. This wavenumber has a pronounced TKE increase (see Fig. 3.25) and evidence for its dominance is found in the velocity spectra along the nozzle lip line (see Fig. 3.29(b), appearance of fundamental frequency) as well as the analysis of the Fourier mode (see Fig. 3.30) at a location where the shear layers roll up. In addition, vortex pairings are indicated by distinct subharmonics that appear in the velocity spectra. The formation of structures causes the overall dominance in the low-frequency range of the pressure spectra for case **Low-m**. This dominance translates into the azimuthal correlation coefficient (see Fig. 3.33(a)) where case **Low-m** has higher correlations for angles $\Delta\theta = 180^\circ$. This dominance of

low-azimuthal wavenumber in downstream direction is, as said before, in agreement with experimental observations (Michalke & Fuchs, 1975; Maestrello, 1976; Juvé *et al.*, 1979).

In the remaining part, a connection between the flow transition and the tonal component observed in the near-field spectra is established. The signal analysis is repeated with an enlarged subinterval length in order to determine the precise frequency of the tonal component to be $St \approx 0.876$. As pointed out before, the strength of the tone increases with disturbance amplitude and at the same time reduces the pressure levels over all other frequencies. This effect of turbulence and noise amplification as well as suppression is similar to effects investigated in a series of experiments by Zaman (1985) and coworkers (Zaman & Hussain, 1981, 1980). The tonal component could result from the breakdown process of structures that develop during the roll-up of the initially laminar shear-layers. The TKE analysis shows that the azimuthal wavenumber $n = 4$ has direct relevance to the roll-up and as this process proceeds its azimuthal higher harmonic $n = 8$ absorbs significant amounts of turbulent kinetic energy. This can indicate a nonlinear interaction of structures described by the ‘*cut-and-connect*’ process. The roles of interacting modes can further be clarified by analyzing their Fourier mode amplitudes $\hat{w}(n)$ at particular frequencies. We investigate the tone frequency $St = 0.876$ and its harmonics. Because of the dominance of $St \approx 0.43$ in the axial velocity spectra we refer to this frequency as the fundamental $St_0^p = 0.438$, and thus its first harmonic frequency, $St_1^p = 2 \cdot St_0^p$, corresponds to the peak in the near-field spectra. For clarity, we restrict the presentation to these two relevant frequencies and the modes that prevail during the transition process, i.e. modes $n = 0, 1, 4$ and 8 . Regardless of the excitation amplitude, shown in rows (a)-(c) of Fig. 3.34 for cases **Low-m**, **Med-m** and **High-m**, similar downstream developments of the modal amplitudes $\hat{w}(n)$ are observed for the fundamental frequency St_0^p shown in column (A) and the first harmonic frequency St_1^p presented in column (B). Overall, the largest Fourier amplitudes occur at the fundamental frequency $St_0^p = 0.438$ for the wavenumber $n = 4$, as can be seen in Figs. 3.34(A). Mode $n = 4$ surmounts the complete transitional region with a peak around $z/r_0 \approx 5$, followed by a slow downstream decay that lasts up to the potential-core collapse. Consistent with our previous observations, the peak location shifts slightly upstream with increasing forcing amplitude. The varicose mode $n = 0$ shortly rises close to the inflow and then saturates at a Fourier amplitude which is lower by one order of magni-

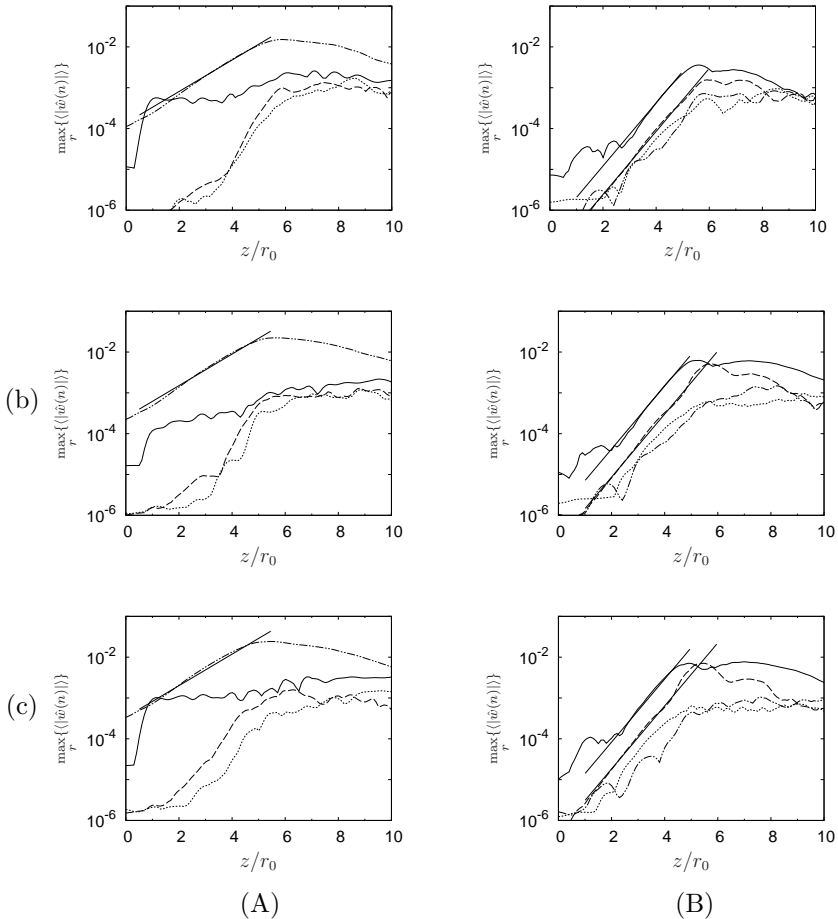


Figure 3.34: Downstream development of Fourier mode amplitude $\hat{w}(n)$ of azimuthal wavenumbers — $n = 0$, $n = 1$, - · - $n = 4$, - - - $n = 8$: (a) Low- m , (b) Med- m and (c) High- m for (A) fundamental frequency St_0^p and (B) peak frequency corresponding to higher harmonic St_1^p . Growth rates denoted by straight lines according to (A) linear theory and (B) weakly nonlinear theory.

tude. As shown in Figs. 3.34(B), the analysis for $St_1^p = 0.876$ indicates that there are two relevant modes, $n = 0$ and $n = 8$, which shape the breakdown process. Their modal amplitudes are lower compared to the fundamental frequency and right from the inflow the axisymmetric mode

plays a prominent role and rises almost linearly downstream of $z/r_0 \approx 2$. Its importance is slightly reduced around $z/r_0 \approx 6$, as can be seen from a small dip in \hat{w} which enlarges with amplitude. This location, where $n = 8$ has reached appreciable amplitude levels, coincides with the position where the dominant mode $n = 4$ at $St_0^p = 0.438$ saturates. Thus, mode $n = 4$ saturates and its azimuthal higher harmonic $n = 8$, together with $n = 0$, rapidly rises at the first harmonic frequency. Exactly at the same downstream location the Reynolds stresses, presented in Fig. 3.28, saturate as well. Particularly for high forcing levels, the modal amplitude $\hat{w}(n = 8)$ at $St_1^p = 0.876$ surpasses the axisymmetric mode at $z/r_0 \approx 5.5$. Further downstream, the amplitude of $n = 8$ is quickly reduced and the axisymmetric mode reassumes its dominance. The other azimuthal wavenumbers are found not to contribute to the overall process in a significant manner and behave similarly as mode $n = 1$, i.e. at the two presented frequencies all other modes rise in a region between $2 \lesssim z/r_0 \lesssim 5$ and then saturate at levels which are almost one order of magnitude below the relevant modes.

The interaction conditions (Cohen & Wygnanski, 1987), according to which waves are prone to subharmonic excitation when similar phase speeds occur, are not satisfied as instability waves $n = 4$ and $n = 8$ have drastically different phase speeds at $St \approx 0.43$ (see Fig. 2.7). However, weakly nonlinear theory, as successfully applied by Sandham & Salgado (2008), can explain this mode interaction. The frequency of the preferred mode seems to be $St \approx 0.43$ in our case, because we force $n = 8$ at exactly this frequency ($n = \pm 8$ are excited at $St = 0.43$). Therefore, mode $n = 4$ that initially is excited at $St = 0.63$ also picks up this particular frequency and grows. According to linear stability theory, mode $n = 4$ has larger growth rates compared to its azimuthal harmonic $n = 8$ which explains the dominance of $n = 4$ at $St_0^p = 0.438$. The nonlinear interaction of two waves with wavenumber $n = 4$ and frequency $St_1^p = 0.438$ generates azimuthal wavenumbers $n = 0$ and $n = 8$ at the tone frequency St_1^p . The growth rate of mode $n = 4$ according to LST is $-\alpha_i^{n=4} r_0 = 0.889$ and the nonlinearly excited modes $n = 0$ and $n = 4$ are found to grow at exactly twice this rate, i.e. $-\alpha_i r_0 \approx 1.778$, which is included in the graphs for comparison. From our analysis of the Fourier modes we conclude that nonlinear interactions of wavenumbers $n = 0, 4$ and $n = 8$ support the ‘*cut-and-connect*’ process of toroidal structures.

The approach by Sandham & Salgado (2008), which showed that driving an acoustic analogy with PSE-based mode-by-mode interactions

can successfully model subsonic jet noise generation mechanisms, has been adapted or simplified to our framework. Here, we apply the concept of weakly nonlinear mode-by-mode interaction to a high Reynolds number jet using eigenmodes determined from linear stability theory. These eigenmodes are determined assuming a parallel base flow and therefore neither the downstream development of the jet nor the interaction of the instabilities with the base flow are taken into account as done in the cases of linear/nonlinear PSE (Sandham & Salgado, 2008; Cheung *et al.*, 2007). Nevertheless, the agreement between the growth rate determined using mode-by-mode interactions and the nonlinear simulation is striking and could help explaining an important subsonic noise generation mechanism observed in high Reynolds number jet flow. Further research in this area is necessary, as in the current study this nonlinear theory is employed only in order to clarify the origin of this tonal component in the near-field pressure spectra of the jet. To gain further insight into the particular transition mechanism and especially into the interaction of eigenmodes in the early nonlinear stages, a more detailed investigation of Fourier amplitudes in combination with PSE might be of interest.

3.4 Direct comparison of modal composition effects

In this section, we only briefly compare some quantities (mean flow and near-field acoustics) for the two cases with different modal compositions. In order to allow a quantitative comparison, we now collapse the data along the jet centerline to account for differences in the potential core lengths. For brevity as well as clarity, we restrict ourselves to cases *Med* and *Med-m*.

3.4.1 Flow results

The streamwise development of the mean axial velocity at the centerline w_c and its RMS are shown in Fig. 3.35. Again, we include the reference data by Lau *et al.* (1979), Arakeri *et al.* (2003) and by Bogey & Bailly (2005*b*) are included. As before, the LES data of Bogey & Bailly is shifted by $z_0/r_0 = 2$. In contrast to the previous section, we use a different shift for the experimental data, i.e. the data of Arakeri and coworkers is shifted by $z_0/r_0 = -3.1$, that of Lau *et al.* by $z_0/r_0 = -2.4$. We find that the exclusion of lower dominant azimuthal modes significantly enhances the overall agreement with the experimental observations. From the point

where the data is matched, we find the centerline velocity of case Med to decay the strongest. This abrupt decay is related to the previously described vortex pairing that is excited by the eigenmode forcing of low azimuthal wavenumbers. Accordingly, the RMS intensities have a delayed onset of growth. However, once appreciable values are attained a very steep and abrupt increase is observed. As said before, the results for case Med-m are found in very good agreement with the reference data. Note that the experimental data has been shifted by $z_0/r_0 = -5.1$ (Arakeri *et al.*) and by $z_0/r_0 = -4.4$ (Lau *et al.*) to allow a better comparison of the streamwise evolution.

The effects of the modal composition on the TKE is shown in Fig. 3.36 for both cases. We provide graphs for the streamwise positions $z/r_0 = 0, 3, 6$ in Figure 3.36(a) and for the positions $z/r_0 = 9, 12$ and 15 in Fig. 3.36(b). At the inflow, we see that the integral disturbance energy of the two cases is kept constant. Case Med which is excited over a broader range of wavenumbers attains lower values of turbulent kinetic energy, whereas case Med-m has increased levels over the excited modes $n = 4$ through $n = 8$. With increasing difference from the inflow plane, the effect of the different eigenmode excitation persists: the triggering of case Med results in a broad-banded distribution of energy of all wavenumbers whereas case Med-m exhibits strong peaks in the dominant axisymmetric mode $n = 4$.

Figure 3.37 shows the relation between the two different types of modal compositions for the lip-line profile of the axial and radial RMS. As described above, the eigenmode based forcing with appreciable amplitudes localizes the roll-up process of the shear layers and subsequent

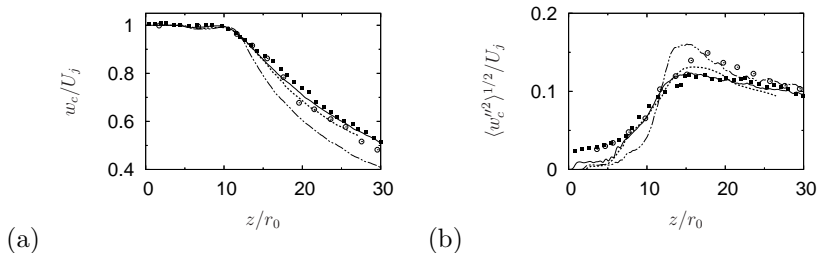


Figure 3.35: (a) Mean axial velocity w_c and (b) RMS of axial velocity fluctuations $\langle w''^2 \rangle^{1/2}$ along the jet centerline: --- Med, — Med-m, Bogey & Bailly (2005b), \circ Lau *et al.* (1979), \blacksquare Arakeri *et al.* (2003).

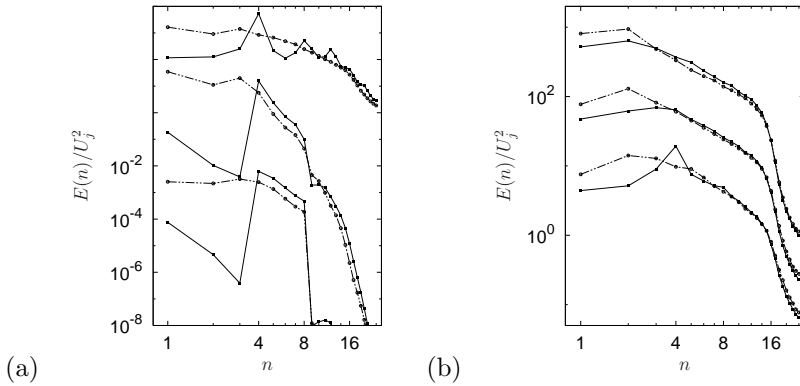


Figure 3.36: One-dimensional turbulence energy spectra E in θ -direction along the nozzle lip line at streamwise positions $z/r_0 = i \cdot 3$ (from bottom to top) (a) $i = 0, 1, 2$, (b) $i = 3, 4, 5$: \cdots Med and — Med-m. The spectra are shifted by a factor of 10 for clarity.

vortex pairings. Because of the strong vortex pairings that occur when exciting also the low azimuthal wavenumbers, the dual-peak structure emerges strongest for case Med, as can be seen in Fig. 3.37(a). The exclusion of the modes results in this noticeable shift of the dominant peak in the upstream direction combined with a pronounced smoothing of the evolution. In addition, the low helical wavenumbers $n = 1, 2, 3$ also seem to enhance significantly the radial RMS shown in Fig. 3.37(b).

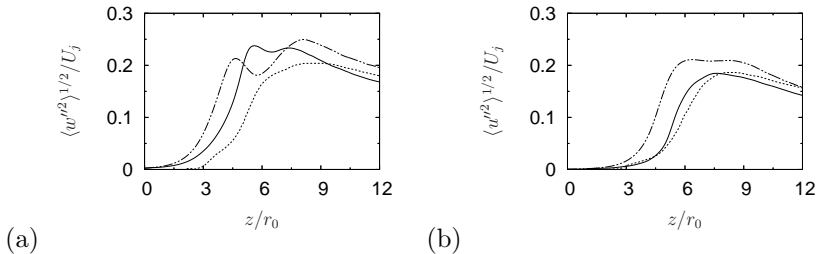


Figure 3.37: RMS of axial velocity fluctuations $\langle w'^2 \rangle^{1/2}$ (a) and of radial velocity fluctuations $\langle u'^2 \rangle^{1/2}$ along the nozzle lip line: \cdots Med, — Med-m and \cdots Bogy & Bailly (2005b).

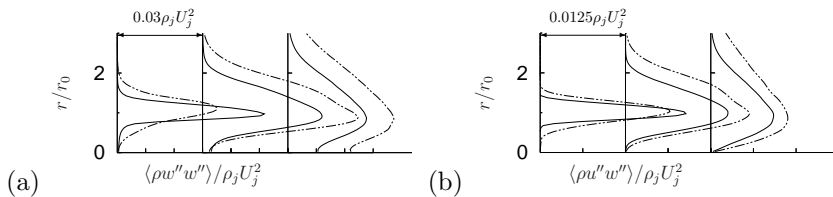


Figure 3.38: Streamwise development of radial Reynolds stress profiles at streamwise positions $z/r_0 = i \cdot 3$ ($i = 1, \dots, 3$ from left to right): (a) $\langle \rho w'' w'' \rangle / \rho_j U_j^2$, (b) $\langle \rho u'' w'' \rangle / \rho_j U_j^2$: - - - Med and — Med-m.

In the following, the effects on the turbulent stresses is addressed. Again, the radial Reynolds normal stress and the shear stress are shown, but in Fig. 3.38 only the two cases are plotted at the equidistant streamwise locations $z/r_0 = 3, 6$ and 9 . In this direct comparison between the different modal compositions, we see the more abrupt transition when exciting low azimuthal wavenumbers in case Med. In particular, the Reynolds normal stress component $\langle \rho w'' w'' \rangle / \rho_j U_j^2$ in Fig. 3.38(a) shows that case Med increases significantly in magnitude between the first and second streamwise position compared to case Med-m. From $z/r_0 = 6$ on downstream, this fast increase results in higher overall values compared to case Med-m in both stress components. In addition, we note that the radial profiles are much wider when exciting the wavenumber $n = 1, 2, 3$ as well.

For completeness, we show in Fig. 3.39 the velocity spectra (along the jet centerline and the lip line) at the same five downstream positions as in Figs. 3.13 and 3.29. As discussed in some detail in sections 3.2.2 and 3.3.2, the exclusion of azimuthal wavenumbers $n = 1, 2, 3$ from the inflow forcing results in velocity spectra that prevent the emergence of higher harmonics of the forcing frequency. This can be seen best in Fig. 3.39(b) (second downstream position) where case Med has well defined higher harmonics of $St \approx 0.5$ and the spectra of case Med-m decays for frequencies higher than $St \approx 0.5$. With increasing downstream distance, we see the different transitional behavior and its effect on the velocity spectra: for case Med-m a tonal component around $St \approx 0.9$ is generated. As explained above, this frequency seems to be tightly coupled to the “cut-and-connect” process and the weakly nonlinear interaction of eigenmodes in a streamwise region $6 \leq z/r_0 \leq 9$.

To shed more light on the differences in the early transition process of

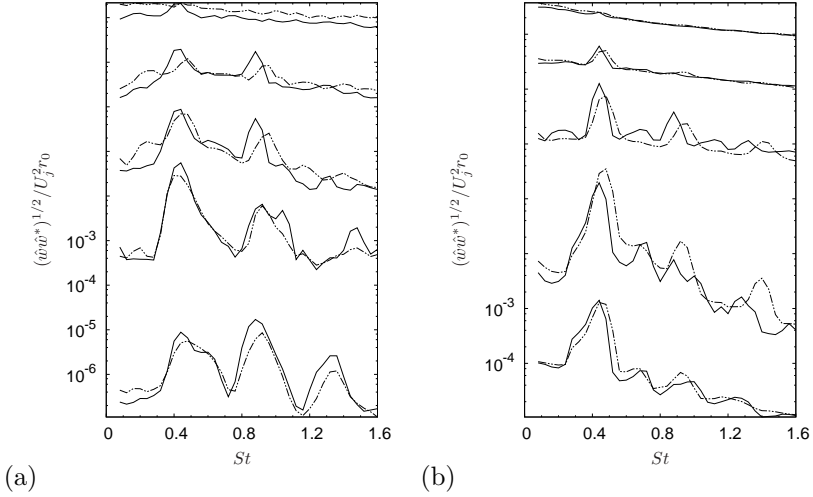


Figure 3.39: Axial velocity spectra at streamwise positions $z/r_0 = i \cdot 3$ ($i = 0, \dots, 4$ from bottom to top) along: (a) jet centerline, (b) jet lip line: --- Med and — Med-m. The spectra are shifted by a factor of 10 for clarity.

the two set-ups, the azimuthal correlation of the radial and axial velocity component are determined and shown in Fig. 3.40. The velocities of case Med (Fig. 3.40(a) and (b)) are weakly correlated at the inflow. With increasing downstream distance, the correlations increase for large angular separations $\Delta\theta \approx 180^\circ$ corresponding to the azimuthal wavenumber $n = 1$. But downstream of the third position, i.e. $z/r_0 \geq 6$, the signals are completely uncorrelated. The axial velocities exhibit less correlation overall. Only at z/r_0 a negative loop between $30^\circ \leq \Delta\theta \leq 120^\circ$ is found.

In contrast to this, we observe a wave-like pattern of azimuthal correlation when the modal composition is changed (case Med-m). This pattern corresponds to the mode $n = 4$ which is also dominant in the TKE spectrum (see section 3.2.2). Both velocity components behave similarly. In accordance with the rising kinetic energy, we also note that the correlations for case Med-m even increase around $z/r_0 = 3$. Further downstream, the strong correlation is gradually lost and for $z/r_0 \geq 9$ the distributions show uncorrelated fluctuations for $\Delta\theta = 30^\circ$. At $z/r_0 = 12$ (see Fig. 3.40(b)), the axial fluctuations of case Med-m are less correlated than case Med with lower levels of \mathcal{R}_{ww} for $\Delta\theta \geq 45^\circ$. This is

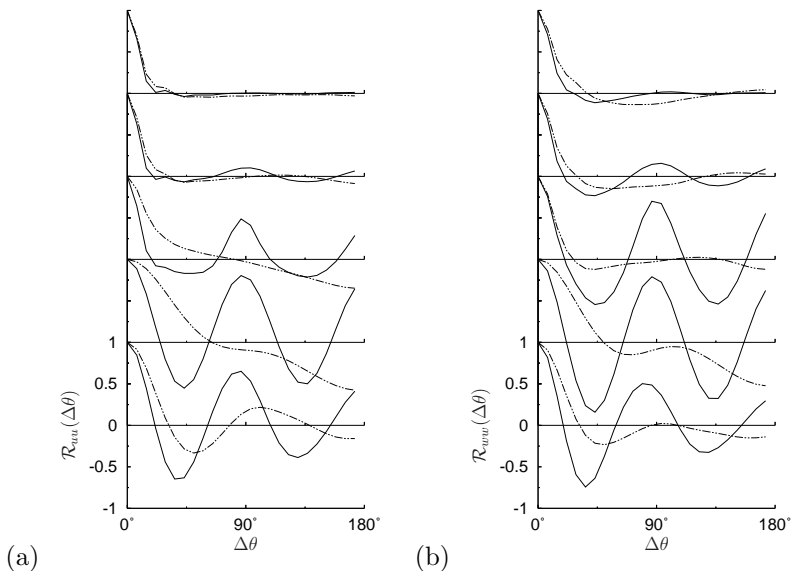


Figure 3.40: Azimuthal correlation coefficient at streamwise positions $z/r_0 = i \cdot 3$ ($i = 0, \dots, 4$ from bottom to top in each figure): (a) for radial velocity \mathcal{R}_{uu} and (b) for axial velocity \mathcal{R}_{ww} along jet lip line $r = r_0$. --- Med and — Med-m.

most likely related to smaller structures which are generated during the breakdown when removing lower wavenumbers from the excitation and which results in azimuthally less correlated signals.

To complete this section, we investigate briefly the azimuthal structure of the pressure in the immediate vicinity of the jet. In a radial region from approximately $r \approx 6r_0$ to $r \approx 10r_0$, the pressure field is most likely a superposition of the hydrodynamic pressure and the acoustic field (see section 2.9 for a separation criteria between hydrodynamic effects and acoustic effects). Figure 3.41 shows the azimuthal correlation coefficient for the pressure signals along two lines of constant radial distance (Fig. 3.41(a) for $r = r_0$ and in Fig. 3.41(b) for $r = 9r_0$). In the vicinity of the jet, the pressure distributions (Fig. 3.41(a)) show the direct influence of the hydrodynamic field. In particular at the streamwise position of $z/r_0 = 6$ where in particular case Med exhibits strong vortex-

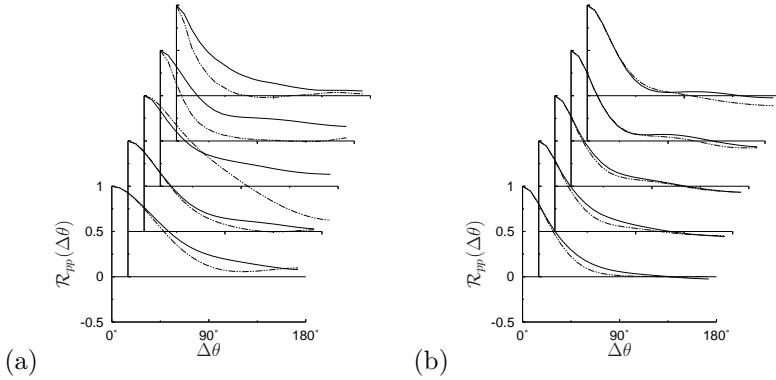


Figure 3.41: Azimuthal correlation coefficient \mathcal{R}_{pp} at streamwise positions $z/r_0 = i \cdot 3$ ($i = 0, \dots, 4$ from bottom to top in each figure): (a) along jet lip line $r = r_0$, (b) along $r/r_0 = 9$. --- *Med* and — *Med-m*.

pairings we find a negative correlation for opposite measuring locations. Approaching the closing of the potential core, the two different excitations result in similar pressure distributions. However, case *Med-m* has clearly enhanced correlation levels and a less pronounced drop-off with increasing angular separation. The pressure distribution for the second radial position (Fig. 3.41(b), corresponding to $r/r_0 = 9$) shows only minor differences in the azimuthal correlation. The modification of the modal excitation strongly alters the transition process and the azimuthal structure of the velocity and pressure fields. Compared to this, the effect on the aerodynamically generated noise seems to be less pronounced in the forward arc compared to the aft arc.

3.4.2 Acoustic results

This subsection compares the data in the acoustic near field for the two different ranges of excited eigenmodes with the medium amplitude (cases *Med* and *Med-m*). For completeness, we point out that the difference in polar distances R between the reference data and the current results has been accounted for in Fig. 3.42 (assuming a $1/R$ -decay; see Tab. 3.4, page 69). Here, we focus only on the differences of the two cases. For details regarding the physical effect, we refer to sections 3.2.3 and 3.3.3. Overall, we find higher sound pressure levels for larger polar angles ϕ

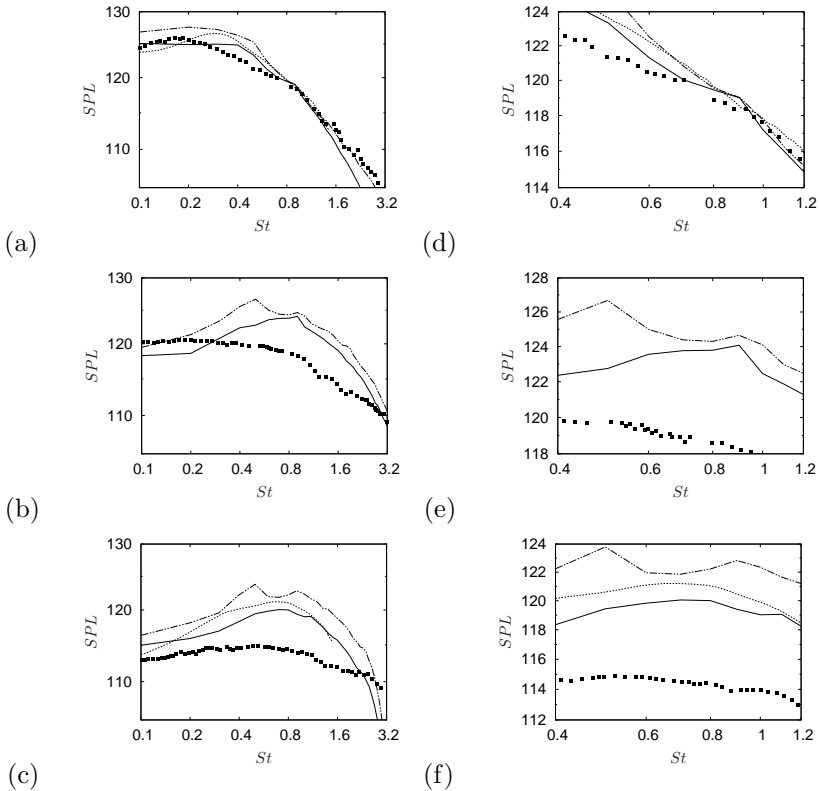


Figure 3.42: Near-field pressure spectra in dB at (a) $\phi = 30^\circ$, (b) $\phi = 60^\circ$ and (c) $\phi = 90^\circ$: --- Med and — Med-m; ■ Bogey et al. (2007b) at (a) $r = 15r_0$, $z = 30r_0$, (b) $r = 15r_0$, $z = 20r_0$, (c) $r = 15r_0$, $z = 10r_0$; Bogey & Bailly (2005b) at (a) $r = 12r_0$, $z = 29r_0$, (c) $r = 15r_0$, $z = 11r_0$. Graphs (d), (e) and (f) show close-up of Strouhal $0.4 \leq St \leq 1.2$.

when disturbing low azimuthal wavenumbers. This could be expected from the generally higher RMS values found, in particular, along the nozzle lip line. For example, as shown in Fig. 3.37(b) case Med has RMS values of the radial velocity fluctuations which are approximately 14% higher than case Med-m due to its strong vortex pairing. These radial velocity fluctuations seem to be directly connected to the sideline noise

(Bogey & Bailly, 2005*b*).

The Fourier coefficients of the azimuthal auto-correlation coefficient $\mathcal{R}_{pp}(\Delta\theta)$ reported before (see section 3.3.3) shows the dominance of low wavenumbers, in particular, in the downstream direction (see section 3.3.3). The corresponding data of Tab. 3.7 is visualized in Fig. 3.43 along with the Fourier coefficients for the cases with the first type of excitation (modes $|n| = 1, \dots, 8$). From these two graphs we find that the

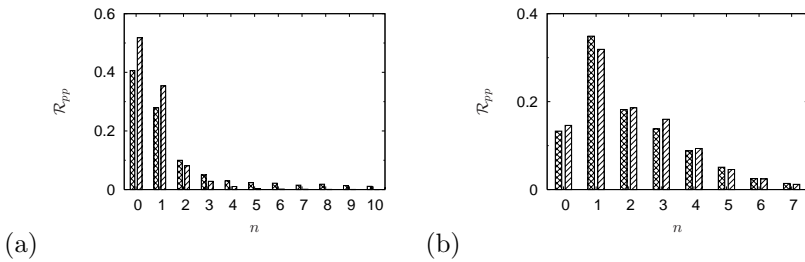


Figure 3.43: Fourier coefficients of correlation coefficient \mathcal{R}_{pp} for pressure signals: (a) at $r = 12r_0, z = 30r_0$ and (b) at $r = 12r_0, z = 12r_0$. Cross-hatched Med, parallel hatching Med-m.

excitation of a larger number of eigenmodes results in a broader range of wavenumbers that contribute to the acoustic field in the downstream direction. The Fourier coefficients of the first ten modes are larger than one percent for case Med, whereas only wavenumbers $n \leq 4$ have significant contributions for case Med-m. In the sideline direction, regardless of the modal excitation, less Fourier coefficients are larger than one percent. However, the magnitude of the coefficients is larger which further supports the previous observation that noise in the sideline direction is mostly connected with small turbulent scales, whereas large-scale structures seem to be most effective in radiating in downstream direction. As mentioned before the data compares favorably with experimental measurements for the unexcited jet studied by Juvé & Sunyach(1981).

From the findings presented in the two previous sections, we decide to choose case Med-m as the baseline configuration. From this flow case, we intend to round off the work by investigating SGS-model effects and the influence of the azimuthal resolution on the results.

3.5 Influence of the relaxation coefficient χ

In this section, we compare important quantities (mean flow and near-field acoustics) obtained for three different values of the relaxation coefficient χ , as introduced in the context of the relaxation regularization (see section 2.2). In the baseline configuration, the relaxation coefficient is set equal to the upper bound of the dynamic determination procedure (outlined for example in section III, of Stolz, Adams & Kleiser (2001*b*)). A more detailed description of the dynamic determination of the relaxation coefficient is given by Stolz (2000). This dynamic determination is based on the constraint that no kinetic energy should accumulate in the wavenumber range $\omega_c \leq \omega \leq \omega_N$ (i.e. above the cutoff wavenumber ω_c of the filter and below the resolved Nyquist wavenumber ω_N) during the time integration. In order to ensure stability of the time integration, the upper bound is set to the inverse of the time step. In our case, this results in a relaxation coefficient of $\chi = 50$. Two cases with reduced relaxation coefficients of $\chi = 42.5$ and $\chi = 30$ are investigated which correspond to $\chi = 0.85/\Delta t$ and $\chi = 0.7/\Delta t$, respectively.

3.5.1 Effect on the flow field

Figure 3.44 shows the streamwise development of the mean axial velocity at the centerline w_c and its RMS for the three different values of the relaxation coefficient χ . Note that the reference data is shifted as described at the beginning of section 3.4.1. The downstream development of the jet centerline velocity is almost unaffected by the changes of the relaxation coefficient as the profiles in Fig. 3.44 nearly collapse. Only

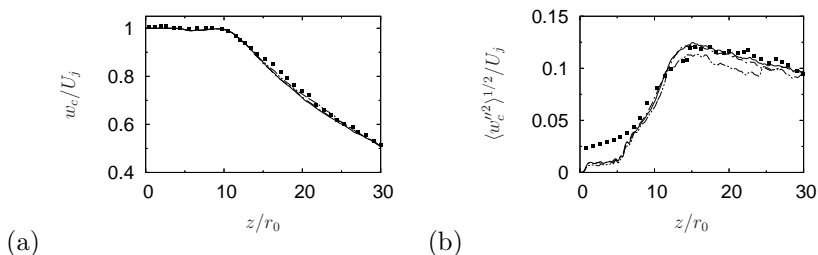


Figure 3.44: (a) Mean axial velocity w_c and (b) RMS of axial velocity fluctuations $\langle w'^2 \rangle^{1/2}$ along the jet centerline: \cdots L- χ , \cdots M- χ , — Med-m and \blacksquare Arakeri et al. (2003).

downstream of $z/r_0 \approx 18$ they deviate slightly from the baseline configuration. Again, the results are in very good agreement with the experimental reference data Arakeri *et al.* (2003). Case **Med-m**, the baseline configuration with the largest value of χ decays the strongest, whereas slightly higher axial velocities are observed with reduced values of the relaxation coefficient. But clearly, these differences are minute. The length of the potential core varies only little, i.e., with decreasing relaxation coefficient the length increases from $z/r_0 = 12.17$, to $z/r_0 = 12.23$ and $z/r_0 = 12.30$, respectively. The axial RMS velocities show almost no difference for the reduction to $\chi = 42.5$ (case **M- χ**). Close to the inflow case **L- χ** saturates at slightly lower values. The subsequent rise of RMS intensities during transition is similar for all cases, only downstream of the breakdown of the jet case **L- χ** has a reduced peak of $\langle w''^2 \rangle^{1/2} = 0.113$ at $z/r_0 = 15.8$. In addition, we note that for the strongly reduced relaxation coefficient the profiles are more spiky, in particular far downstream. There, the mean flow convection is small and thus results converge only slowly. For brevity the results for the RMS of the radial velocity along the jet centerline are not shown here since its distribution is similar to the axial velocity: Almost no differences are visible up to the closing of the potential core for all cases. Further downstream case **M- χ** remains almost indistinguishable from case **Med-m**, only for the large reduction of 30% we find again slightly reduced values. Overall, the large changes of χ seem not to have strong effects on the flow simulation, and therefore can be considered to be rather independent of the choice of χ as long as it stays within certain bounds.

Similar effects of the development can be observed along the nozzle lip line when altering the relaxation coefficient χ . The RMS of the axial and radial velocity versus downstream coordinate are given in Fig. 3.45. Consistent with the previous observation of the lower saturation levels, we find again reduced RMS intensities for both velocity components of case **L- χ** . The delayed onset of transition reported by Bogey & Bailly (2005*b*) might be related to the lower excitation level employed in their study. As noted before, we find better agreement with their data for the low amplitude case **Low-m** (see section 3.3.2 for details on the effect of the disturbance amplitude in combination with the removal of low azimuthal wavenumbers from the inflow forcing). Because of the strong correlation between the fluctuations along the lip line and the observed noise the reduced turbulent intensities might indicate also a reduced overall sound pressure level for case **L- χ** .

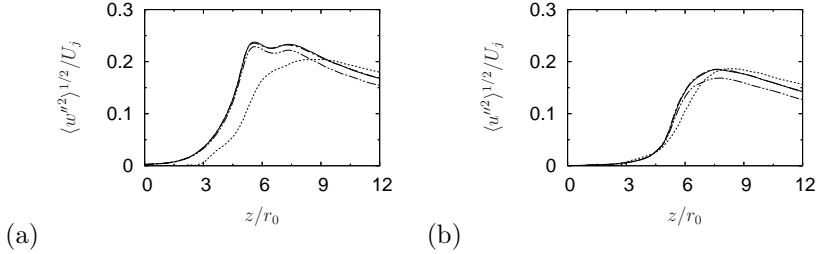


Figure 3.45: RMS of (a) axial velocity fluctuations $\langle w''^2 \rangle^{1/2}$ and (b) radial velocity fluctuations $\langle u''^2 \rangle^{1/2}$ along the nozzle lip line: - - - L- χ , - · - M- χ , — Med-m and ····· Bogey & Bailly (2005b).

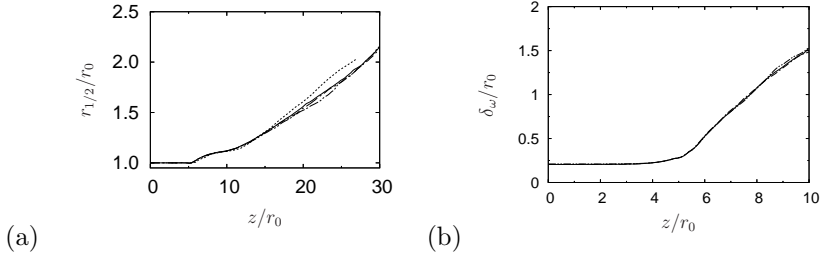


Figure 3.46: Streamwise development of (a) jet half-width $r_{1/2}$ and (b) vorticity thickness δ_ω : - - - L- χ , - · - M- χ and — Med-m. In (a) also ····· Bogey & Bailly (2005b) for comparison.

The jet half-width and thereby the jet's spreading is one of the key parameters investigated in the self-similar region. As noted before, the computational domain does not cover large parts of it, however, conclusion from the development of the jet half-width as well as the vorticity thickness help in assessing the sensitivity of the flow development when changing χ . The jet half-width in Fig. 3.46(a) shows that results scatter only slightly in a short region. Case L- χ exhibits the smallest spreading, whereas the baseline configuration spreads the most in a region downstream of $z/r_0 \approx 18$.

For the vorticity thickness shown in Fig. 3.46(b) we find an almost perfect match of the data. For the investigated range of changes to the relaxation coefficients the effect on the vorticity thickness shown in Fig. 3.46(b) seems to be small – besides the attenuation of RMS velocities

for significantly reduced relaxation coefficients.

The turbulent kinetic energy spectra (see equation (3.1)) allow a detailed view on the effect of the relaxation coefficient on the different azimuthal wavenumbers. Here, we provide graphs for the streamwise positions $z/r_0 = 0, 3, 6$ in Fig. 3.47(a) and for the positions $z/r_0 = 9, 12$ and 15 in Fig. 3.47(b). At the inflow all excited modes contain the same amount of disturbance energy. Only mild deviations can be observed in the other, initially unexcited, wavenumbers. This picture remains almost unchanged at the second downstream position $z/r_0 = 3$. At the last position in Fig. 3.47(a), low azimuthal wavenumbers n contain less energy when using large relaxation coefficients, however, differences are minute in this double-logarithmic representation. Further downstream (at $z/r_0 = 9, 12, 15$ shown in Fig. 3.47(b)), the distributions remain similar, only the upstream differences seem to alter transition and thereby, to redistribute the energy differently between the azimuthal wavenumbers.

In order to clarify the reason for the earlier saturation of RMS intensities for case L- χ (see Figures 3.44, 3.45), low and high wavenumbers are separated in the TKE representation of Fig. 3.48. As mentioned before, we find indistinguishable TKE distributions in the excited wavenumber range $n = 4, \dots, 8$ in Fig. 3.48(a). Only slightly higher levels are

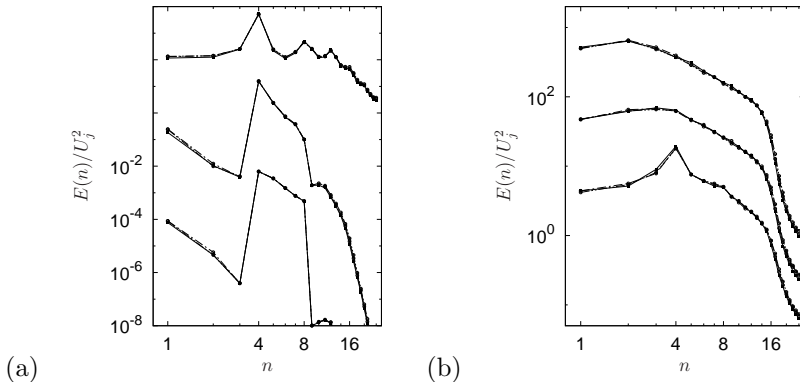


Figure 3.47: One-dimensional turbulence energy spectra E in θ -direction along the nozzle lip line at streamwise positions $z/r_0 = i \cdot 3$ (from bottom to top) (a) $i = 0, 1, 2$, (b) $i = 3, 4, 5$: \cdots L- χ , $-\cdots$ M- χ and — Med-m. The groups of spectra are shifted by a factor of 10 for clarity.

observed for cases L- χ and M- χ compared to Med-m, however, their alignment does not necessarily correspond to relaxation coefficient χ . In contrast, higher wavenumbers exhibit a correlation between the relaxation coefficient χ and the TKE. As can be expected from the functional form of the relaxation regularization, the lower the relaxation coefficient, the less energy we drain from the system which leads to a TKE increase at high wavenumbers. The energy sink models dissipating scales not resolved by the coarse LES grid, and its effect can be seen in Fig. 3.48(b). For wavenumbers $n \geq 17$, the TKE aligns inversely to χ , i.e., the relaxation term acts as an energy sink on the high wavenumbers as intended. As we artificially reduce the coefficient χ , less energy in the high wavenumber range is dissipated which results in higher energy levels. These small but noticeable differences caused at the inflow lead to different saturation levels upstream of $z/r_0 \leq 6$. The downstream differences, in particular between the baseline configuration (case Med-m) and case L- χ , are thus linked to the sensitivity of the jet flow which has been described in some detail in sections 1.2 and 2.5.3.

As said before, the observed changes are only very small taking into account that χ is reduced by 15% and 30%, respectively. Therefore, results in the flow field can be considered independent of the choice of χ . A reliable estimate for χ is the upper bound of the dynamic procedure (Stolz, Adams & Kleiser, 2001*a,b*).

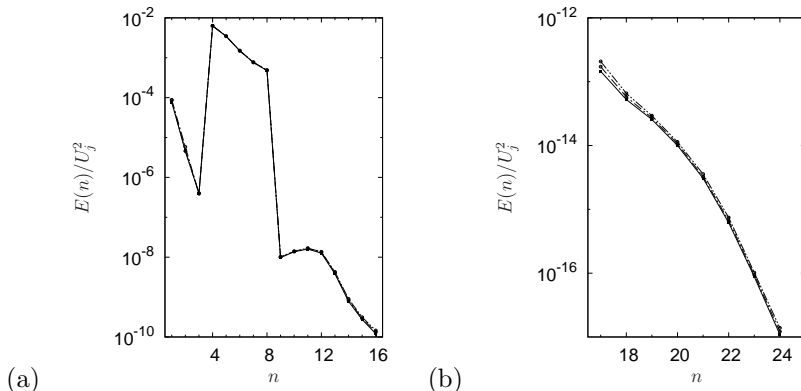


Figure 3.48: One-dimensional turbulence energy spectra E in θ -direction along the nozzle lip line at streamwise positions $z/r_0 = 0$ (a) $n = 1, \dots, 16$, (b) $n = 17, \dots, 24$: \cdots L- χ , \cdots M- χ and — Med-m.

3.5.2 Effect on the acoustic field

Within this subsection we briefly compare the results within the acoustic near field for the cases L- χ , M- χ and Med-m. As could be seen in the previous section, a 15% reduction of χ does not have any noticeable effect on the flow, however, reducing it by 30% alters the transition process such that the RMS along the jet centerline and along the lip line are slightly reduced.

Following the previous sequence, the acoustic pressure spectra in the near field are now compared. The same observation locations as before are presented in Fig. 3.49(a)–(f) (the difference in polar distances R between the reference data and the current results has been accounted for by assuming a $1/R$ -decay, see Tab. 3.4, page 69). For all observer locations we find almost perfect agreement among the three different cases. Only within the frequency range $0.5 \leq St \leq 1.2$ differences can be observed - most noticeable around the peak location of $St = 0.9$ (which is connected to the previously described “cut-and-connect” process, see section 3.3.4 for details). The differences in magnitude are well below 1 dB . The sampling times are not sufficient to adequately resolve low-frequency noise. This prevents any additional conclusions to be drawn (e.g., consistency of low-frequency data in the acoustic near field). Nevertheless, the effect of large changes of the relaxation coefficient χ on the noise is only small.

To conclude this sensitivity study, the overall sound pressure level for the three relaxation coefficients are plotted in Fig. 3.50. As could be expected from the distribution of the radial velocity fluctuations we find the lowest OASPL for case L- χ . The medium-valued case M- χ with $\chi = 42.5$, is virtually identical with the baseline configuration. All axial distributions are similar in shape, only the magnitude for case L- χ is approximately 2 dB lower. In Fig. 3.50(b) we also plot the difference in overall sound pressure level compared to the reference case. Around $z/r_0 = 6$, the smallest difference between case Med-m and L- χ of 1.5 dB occurs. With increasing distance the difference increases to roughly 2.2 dB as the pressure levels for L- χ further reduce.

3.5.3 Summary on the effects of the relaxation coefficient

From the previous comparison we find the simulation results of case Med-m to remain SGS-model independent in the sense that a reduction of the relaxation coefficient does not affect the results tremendously.

For an intentionally strong suppression of the energy drain in the inaccurately resolved wavenumber range above ω_c , a slight modification of the transition process is observed. This also has an effect on the directly computed acoustic field. For a reduction of 15% we find virtually no difference of the results and, hence, the independence of the results from the relaxation coefficient χ is concluded.

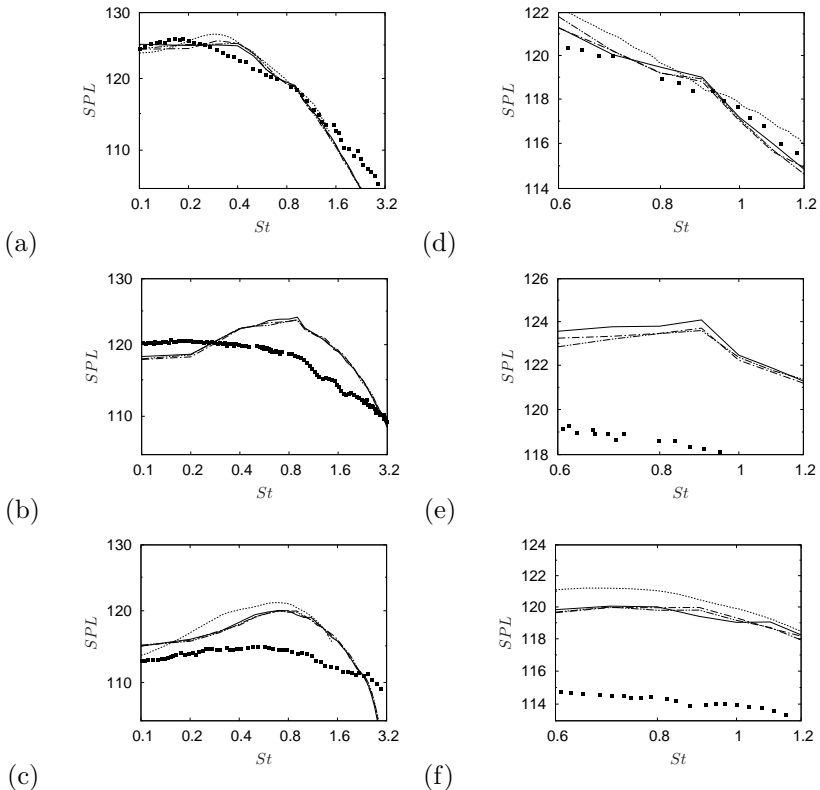


Figure 3.49: Near-field pressure spectra in dB at (a) $\phi = 30^\circ$, (b) $\phi = 60^\circ$ and (c) $\phi = 90^\circ$: \cdots L- χ , $---$ M- χ and $---$ Med-m. \blacksquare Bogey et al. (2007b) at (a) $r = 15r_0$, $z = 30r_0$, (b) $r = 15r_0$, $z = 20r_0$, (c) $r = 15r_0$, $z = 10r_0$. \cdots Bogey & Bailly (2005b) at (a) $r = 12r_0$, $z = 29r_0$, (c) $r = 15r_0$, $z = 11r_0$. Graphs (d), (e) and (f) show close-up of Strouhal $0.6 \leq St \leq 1.2$.

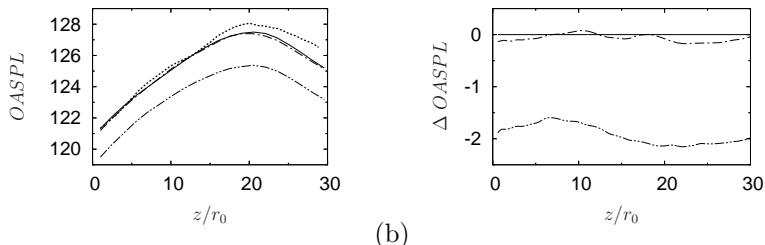


Figure 3.50: Axial distribution of (a) overall sound pressure levels and (b) the differences to the baseline configuration *Med-m* (OASPL in dB) along $r/r_0 = 15$: \cdots $L-\chi$, $-\cdot-$ $M-\chi$, — *Med-m*, (a) only $\cdots\cdots$ *Bogey & Bailly (2006a)*.

3.6 Effect of the deconvolution operator

The focus of this section is on the effect of the deconvolution operator on the simulation results. As in the previous section we restrict ourselves to some flow quantities and data in the acoustic near-field. The results are compared to the previously established baseline configuration, case *Med-m*. For case *ADM* we employ the same relaxation coefficient χ as in case *Med-m*. The only difference is now that during the evaluation of the nonlinear convective terms we do employ approximately deconvolved quantities. For details we refer to section 2.2 and in particular to the set of governing equations that are given by equations (2.17a) – (2.17c).

3.6.1 Effect on the flow field

The impact of the deconvolved nonlinear term on the mean axial velocity along the jet centerline is found to be small, as can be seen in Fig. 3.58(a). The results coincide almost completely with the baseline configuration *Med-m*. Only downstream of $z/r_0 \approx 12$ and within a length of roughly seven jet diameters the centerline distributions slightly deviate from each other. In this region we find that case *ADM* exhibits a slightly less pronounced decay compared to case *Med-m*. In both figures we provide again the experimental reference data (as described in more detail in section 3.4.1). The corresponding axial RMS velocities are given in Fig. 3.51(b). As observed previously, the decelerated decay of w_c comes along with reduced RMS intensities, i.e., we observe that downstream of the location where the potential core closes (*ADM*: $z_c = 12.23r_0$; compared to *Med-m*: $z_c = 12.17r_0$) the RMS of case

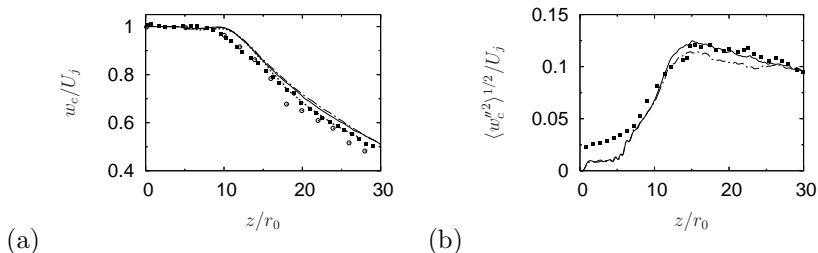


Figure 3.51: (a) Mean axial velocity w_c and (b) RMS of axial velocity fluctuations $\langle w''^2 \rangle^{1/2}$ along the jet centerline: --- ADM, — Med-m and ■ Arakeri et al. (2003).

ADM saturates at a lower peak levels and then stays almost constant in downstream direction. The same does also hold for the radial velocity fluctuations along the jet centerline which are not shown here. Thus, the mean quantities seem to be only weakly affected by the approximate deconvolution model.

This first impression is further substantiated by the results for the jet half-width and the vorticity thickness shown in Fig. 3.52. Similar to the mean-velocity decay, only minute differences between the half-widths for the two cases are noticed (Fig. 3.52(a)). Hence, their growth rates $d(r_{1/2}/r_0)/dz$ equal 0.056 (determined again by the linear fit in the range $15 \leq z/r_0 \leq 30$). Figure 3.52(b) shows the almost identical distributions of the vorticity thickness for the two cases. Up to the streamwise position of $z/r_0 \approx 8$ the distributions are identical, further downstream minute differences can be observed.

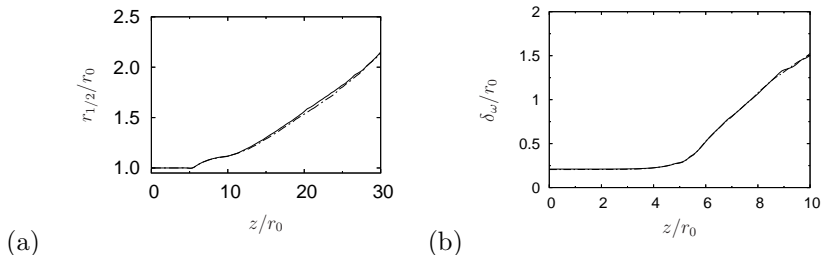


Figure 3.52: Streamwise development of (a) jet half-width $r_{1/2}$ and (b) vorticity thickness δ_ω : --- ADM and — Med-m.

For completeness, the axial and radial RMS along the jet lip line are shown in Fig. 3.53(a) and (b). In general, we observe a similar

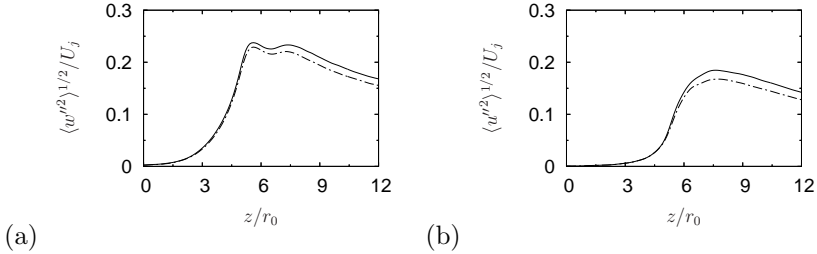


Figure 3.53: RMS of (a) axial velocity fluctuations $\langle w''^2 \rangle^{1/2}$ and (b) radial velocity fluctuations $\langle u''^2 \rangle^{1/2}$ along the nozzle lip line: --- ADM and — Med-m.

trend as for the RMS along the jet centerline only more pronounced: The application of the deconvolution operator on the velocity field and successive calculation of the convective term results in reduced RMS intensities. The radial velocity component $\langle u''^2 \rangle^{1/2}$ is stronger affected and clearly reduced compared to case Med-m. Qualitatively, the axial evolution seems to be almost unaffected by the deconvolution approach.

The TKE spectra along the nozzle lip line from the inflow plane to $z/r_0 = 6$, shown in in Fig. 3.54(a), and from $z/r_0 = 9$ to $z/r_0 = 15$ in Fig. 3.54(b). In the early transitional region, i.e. between $z/r_0 = 0$ and $z/r_0 = 6$, we observe no significant difference in the energy-containing low-order modes. Nevertheless, deconvolution (which is also applied to the imposed inflow sponge) has a more dissipative character compared to the baseline configuration Med-m at the inflow. Wavenumbers $n = 4, \dots, 8$ of case ADM have a slightly reduced turbulent kinetic energy. In this particular wavenumber range the differences are diminishing in the downstream direction, however, we clearly see the dissipative character of the deconvolution approach reflected by reduced energy in the high wavenumber range $n \geq 9$. In the region of strongest vortex interaction, i.e. between the streamwise locations $z/r_0 = 6$ and $z/r_0 = 9$ (top spectra in Fig. 3.54(a) and bottom spectra in Fig. 3.54(b)), differences between the cases ADM and Med-m start to appear also in the dominant large-scale wavenumber range $n \leq 8$. As noted before, this is a combined effect of SGS-model differences on the one hand and also of the jet's sensitivity to inflow modifications on the other.

The axial velocity spectra along the jet centerline and the lip line are given in Figures 3.55(a) and (b), respectively. For the physical interpretation of the findings we refer to sections 3.3.2 and 3.3.4 and at this point limit the discussion to the effects of ADM. For both radial locations we observe no striking difference between the relaxation term regularization used for case **Med-m** and the deconvolution employed for case **ADM**. The results, in particular for the dominant Strouhal numbers, are virtually identical. We observe no frequency shift due to ADM, but slightly smoother spectral shapes. The less spiky spectra in the velocity field are related to the previously noticed increase in dissipation when using ADM. For example this more dissipative character resulted in reduced turbulent kinetic energy levels for high wavenumbers which are associated with high frequency contributions to the spectra (see Fig. 3.54).

For completeness, we compare the Reynolds stresses for case **ADM** to the baseline configuration in Fig. 3.56. Here, we employ a different representation allowing for a more complete picture of the development within the whole LES domain. In Fig. 3.56 the radial profiles for the normal stress components and the shear stress component $\langle \rho u'' w'' \rangle$ are given (at ten equidistant streamwise locations ranging from the inflow at $z/r_0 = 0$ up to $z/r_0 = 27$; from left bottom to right top in each subplot). The radial extent of the profiles is from $r/r_0 \approx 0$ to $r/r_0 = 6$. Overall,

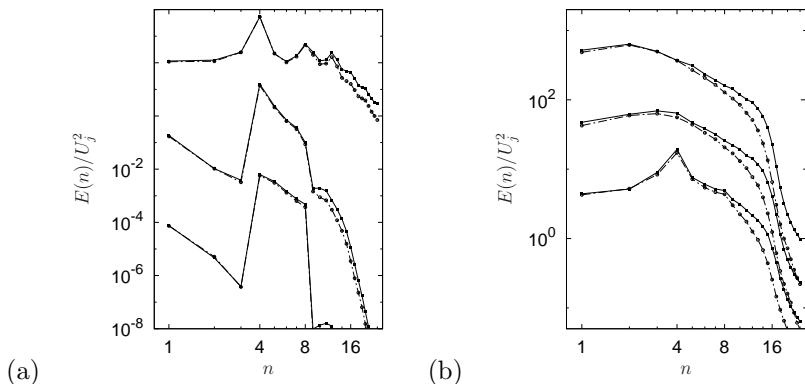


Figure 3.54: One-dimensional turbulence energy spectra E in θ -direction along the nozzle lip line at streamwise positions $z/r_0 = i \cdot 3$ (from bottom to top) (a) $i = 0, 1, 2$, (b) $i = 3, 4, 5$: --- **ADM** and — **Med-m**. The spectra are shifted by a factor of 10 for clarity.

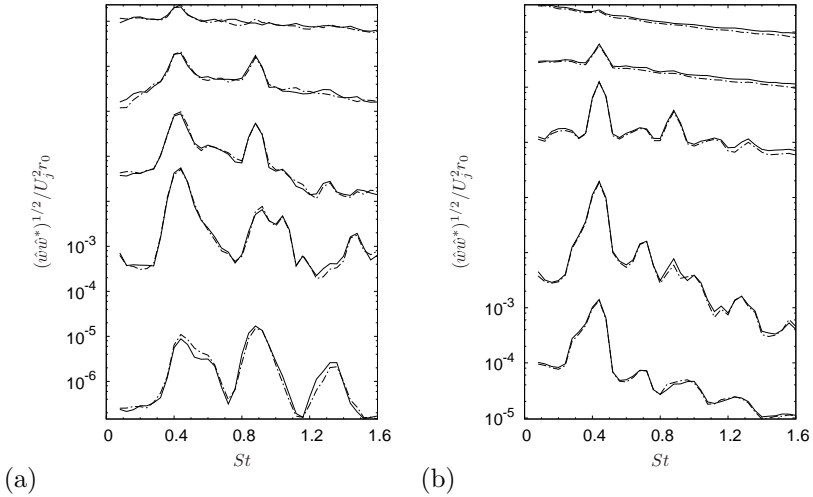


Figure 3.55: Axial velocity spectra at streamwise positions $z/r_0 = i \cdot 3$ ($i = 0, \dots, 4$ from bottom to top) along: (a) jet centerline, (b) jet lip line: --- ADM and — Med-m. The spectra are shifted by a factor of 10 for clarity.

we find similarly shaped profiles for all measurement locations. But consistent with the reduced turbulent fluctuations, reduced turbulent stresses for case ADM compared to Med-m are found. This difference is most noticeable in the region where strong vortex pairing and vortex interaction has been observed, i.e., around the streamwise location of $z/r_0 = 9$.

In summary, the ADM approach shows to be effective in the high wavenumber range only and not to alter energy-containing scales that are accurately represented on the employed grid. Compared to case Med we observe a slightly more dissipative character and thereby notice decreased levels of turbulent intensities.

3.6.2 Effect on the acoustic field

As could be seen before, ADM has a rather small influence on the flow results, and hence, large differences in the acoustic near field are not to be expected. Figure 3.57 shows again the previously investigated observer locations that correspond to angles of 30° , 60° and 90° measured from

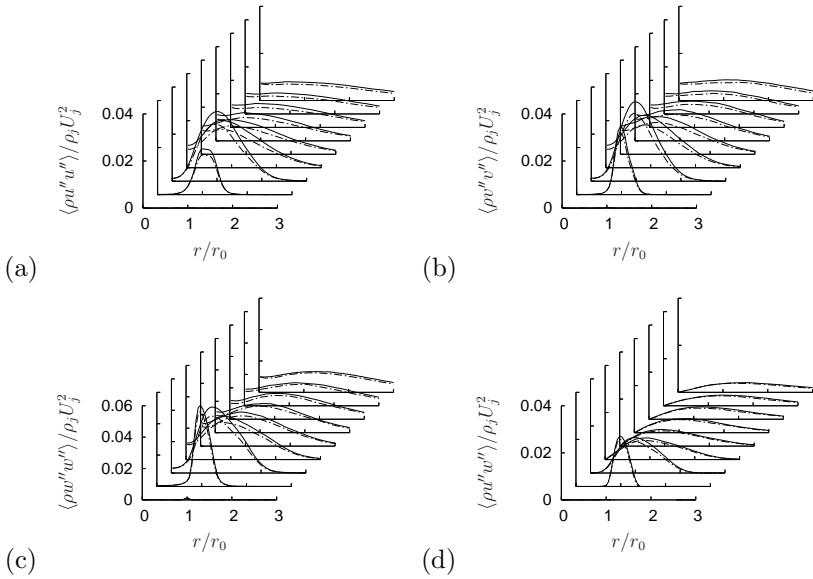


Figure 3.56: Spatial development of Reynolds stress profiles at streamwise positions $z/r_0 = i \cdot 3$ with $i = 0, \dots, 9$ (from left bottom to right top): \cdots ADM and — Med-m. (a) $\langle \rho u'' u'' \rangle$ (b) $\langle \rho v'' v'' \rangle$ (c) $\langle \rho w'' w'' \rangle$ (d) $\langle \rho u'' w'' \rangle$.

the downstream jet axis. Note again that the reference data has been shifted in amplitude assuming a $1/R$ -decay of the SPL (see Tab. 3.4, page 69). The differences between case Med-m and case ADM are very small. The lines almost collapse and only within the peak region of the spectra ($St \approx 0.9$) we observe smallest deviations. The sound pressure levels for case ADM are reduced for broad frequency bands compared to the baseline configuration except around the peaks shown in Fig. 3.57(d) and (f), which are amplified. We also notice that the spectra are slightly smoother when employing the deconvolution procedure. The smoother spectra are most likely a result of the slightly increased dissipation in the high wavenumber regime (observed in the previous section), which tends to damp high frequency noise. However, one has to mention that the overall sampling time and thereby the spectral resolution should be increased to obtain a more detailed picture of the effects.

Finally, the integral sound pressure contributions of all frequencies is

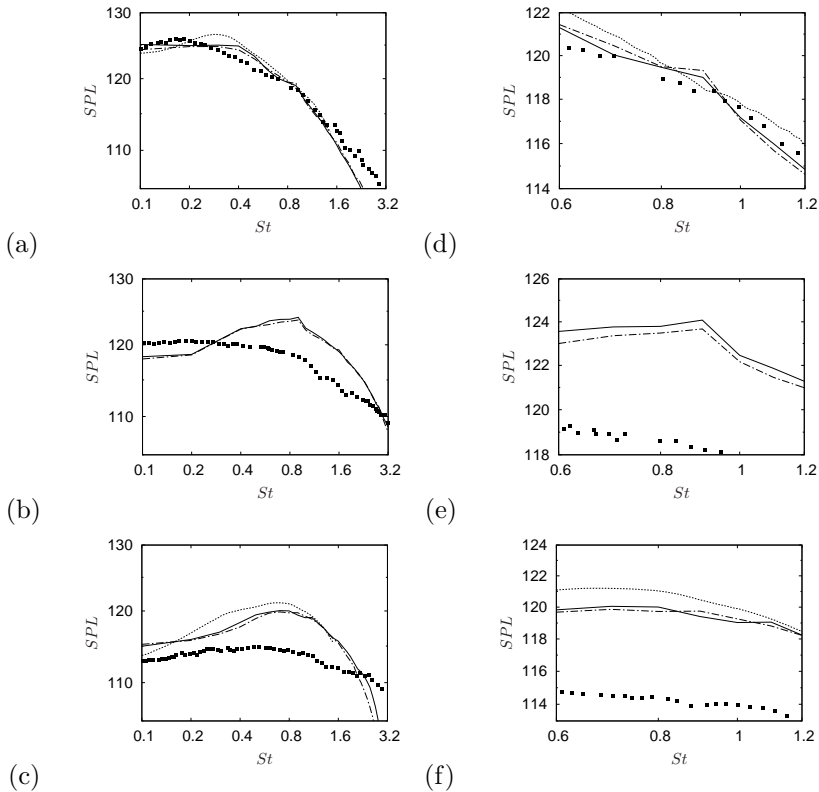


Figure 3.57: Near-field pressure spectra in dB at (a) $\phi = 30^\circ$, (b) $\phi = 60^\circ$ and (c) $\phi = 90^\circ$: --- ADM, and — Med-m. ■ Bogey et al. (2007b) at (a) $r = 15r_0$, $z = 30r_0$, (b) $r = 15r_0$, $z = 20r_0$, (c) $r = 15r_0$, $z = 10r_0$ Bogey & Bailly (2005b) at (a) $r = 12r_0$, $z = 29r_0$, (c) $r = 15r_0$, $z = 11r_0$. Graphs (d), (e) and (f) show close-up of Strouhal $0.6 \leq St \leq 1.2$.

again determined and shown along a line of constant radius $r/r_0 = 15$ in Fig. 3.58(a). Figure 3.58(b) shows the actual difference to the baseline configuration. The overall sound pressure levels are nearly identical up to the streamwise location $z/r_0 \approx 15$. Further downstream, we find slightly lower levels for case ADM which are linked to the reduced turbulent intensities (RMS velocities and velocity spectra). The differences are

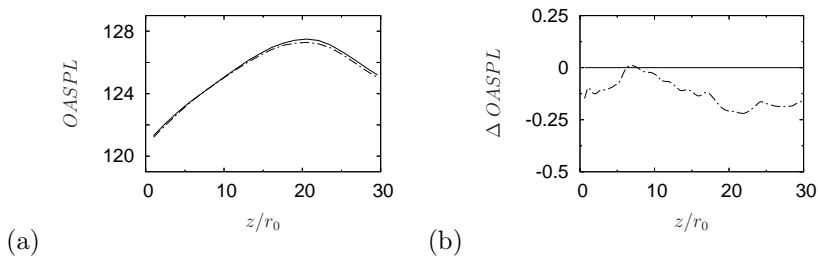


Figure 3.58: Axial distribution of (a) overall sound pressure levels and (b) the differences to the baseline configuration *Med-m* (OASPL in dB) along $r/r_0 = 15$: --- ADM and — *Med-m*.

minute, as shown in Fig. 3.58(b), and remains smaller than 0.25 dB at all times.

3.6.3 Summary on the effects of the deconvolution approach

The effect of ADM is restricted to the high-wavenumber regime and thus, no pronounced influence of the choice of the SGS model on the prediction results could be found (ADM-RT vs. ADM). Because the observed differences of the flow quantities in the transition region are minute the acoustic results are almost identical to the baseline configuration. For the current setup, predictions that use the relaxation regularization only show to provide accurate results at lower computational cost.

3.7 Resolution effects on the simulation results

As mentioned before, this relatively high Reynolds numbers come into reach only when using high-order schemes, optimized time-integration methods and effective subgrid-scale models. These simulations are still very costly and therefore grid-independence studies are rarely found in the literature. Rare exceptions, but again only for relatively low Reynolds numbers, are often simulations for which results from direct numerical simulations are available (such as the temporal mixing layer by Vreman *et al.* (1996), the turbulent channel flow investigation of Gullbrand & Chow (2003) or the case of decaying incompressible isotropic turbulence by Meyers *et al.* (2003)) such that informative conclusions can be drawn.

In contrast to the exceptions cited above, the results for the current

LES study are more complicated to compare because of the unavoidable lack of reference DNS data. In addition, one has to be aware that grid refinement may have different effects depending on the functional form of the filter definition in the governing equations. One has to distinguish between changes in resolution that only affect the discretization error or those which also affect the filter width Δ (introduced as length-scale parameter in the context of scale separation at the beginning of chapter 2). If the filter width is affected by the changes in resolution the effect of the discretization error of the numerical schemes and the SGS model contributions (and associated errors) are combined. For example, when the filter width Δ is kept constant and the computational resolution is successively refined we would expect convergence toward a solution of the filtered governing equations, i.e., effects of the subgrid-scale model can be assessed. In the limit of vanishing grid spacing, the solution converges to the grid-independent filtered solution of the governing equations and only the SGS errors remain. In contrast to this, when refining the grid and simultaneously shifting the filter cutoff to higher wavenumbers, one approaches a direct numerical simulation, i.e., an unfiltered solution of the governing equations. With the present SGS modeling approaches, namely ADM and the relaxation regularization of ADM (ADM-RT), we have to distinguish between these cases: For the deconvolution approach the additionally employed explicit filter (in the sense of explicitly applied in contrast to implicitly filtered by the grid) further decreases the discretization error in the high (represented but not accurately resolved) wavenumber range and thus SGS model effects could be separated. However, all simulations reported herein, except for case ADM, rely on the relaxation regularization only and thus the quantities are grid-filtered quantities. Consequently, when using the relaxation term and refining the resolution, the results eventually converge toward the unfiltered DNS result.

During this work the question arose whether the currently employed number of Fourier modes in the azimuthal direction is sufficient. Based on various jet-noise studies in the literature we considered $N_\theta = 50$ as sufficient for all LES (see, e.g., similar studies for slightly different jet flow parameters by Bodony ($N_\theta = 32$: Bodony, 2004; Bodony & Lele, 2005) or Barré ($N_\theta = 48$: Barré *et al.*, 2006; Barré, 2006). However, a reduction to $N_\theta = 32$ during tests showed effects on the mean flow field that were strikingly similar to exciting low azimuthal wavenumbers in the forcing procedure (see section 3.2 for details of this study), calling

for a more detailed investigation of the resolution effect.

In addition to the effect of grid refinement in combination with LES, a crucial point has to be kept in mind concerning the sensitivity of the jet flow: As we have seen from the previous findings (see sections 3.2 and 3.3) and also in the referenced literature jets are very sensitive to changes at the entrance region and thus to the physical inflow condition. In the case of a numerical investigation, this inflow conditions is inevitably coupled to the resolution employed through the disturbance triggering. Ideally, the effects of changing resolution should be investigated separately to distinguish inflow effects from resolution effects. However, this would have necessitated the costly time- and space-dependent interpolation of the reference solution during the whole simulation time which was considered infeasible. Instead, the spatial resolution in azimuthal direction was changed, accepting that this has several closely coupled but unfortunately inseparable effects. One effect is certainly the previously described mode-clipping. As this artificial truncation of the Fourier modes corresponds to a spectral cutoff filter different amounts of energy are extracted from the system. In addition, there is an effect of the change in effectiveness of the way of introducing the disturbances to the flow: With increasing resolution the sponge technique allows for smoother representations of the time-dependent reference solutions. Thereby, the inflow disturbances are more effectively imposed for a higher resolution although the overall amplitude is kept constant. And last, there is at least a mild effect by the shift of the filter transfer function to higher wavenumbers. Therefore, we cannot expect a grid-independent solution from this current setup. Rather, we hope to deduce further implications about the certainty of the predictive quality and thereby hope to obtain better confidence in the results and the observed mechanisms. From our point of view these different arguments render such an investigation appropriate.

In Fig. 3.59 we first show the number of the retained Fourier modes (determined according to equation (2.28), section 2.4.2) that correspond to the three different azimuthal resolutions. We see that the interior region $r/r_0 \leq 0.33$ is unaffected by the number of azimuthal grid points due to the artificial clipping of modes. For cases LR and Med-m the whole shear layer region is covered by the chosen resolution, i.e. $N_\theta = 32$ for case LR compared to the standard number of $N_\theta = 50$ employed in case Med-m. The highly resolved case HR further increases the number of retained modes and reaches the maximum number at $k = 19$ or $r_{19} \approx$

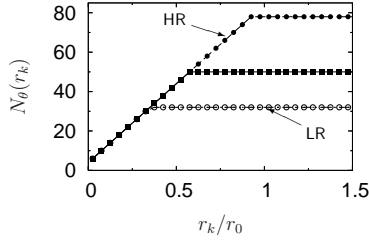


Figure 3.59: Visualization of linear dependence of number of retained Fourier modes N_θ^r on discrete radial coordinate r_k for different azimuthal resolution N_θ : $-\circ-$ LR, $-\blacksquare-$ Med-m and $-\blacklozenge-$ HR.

$0.93r_0$.

Because of the sensitivity of the jet flow to changes in the shear layer mentioned previously we compare the computational grid employed by Bogey & Bailly (2005b) to the grid of the present LES in the close vicinity of the nozzle lip line, i.e. at $r/r_0 \approx 1$. Bogey & Bailly (2005b) employ a Cartesian grid of $N_x \times N_y \times N_z = 255 \times 221 \times 221$ grid points. The discretization in the y and z directions are identical and thus symmetric about the jet centerline. The transverse mesh spacing is uniform for $y \leq 2r_0$ with $\Delta y_0 = r_0/15$, and then increases at a rate of 2% to reach $\Delta y = 0.4r_0$ well outside the jet flow. The axial mesh spacing is constant from the inflow for almost the whole domain, i.e. for $0 \leq x \leq 25r_0$ the spacing is $\Delta x = 2\Delta y_0$. Further downstream it is stretched to form a sponge zone. The comparison of cylindrical coordinates to Cartesian ones has two limiting cases in azimuthal direction: The first, with the smallest radial spacing Δr and thus also with azimuthal spacing $r_0\Delta\theta$, is perfectly aligned with y - and z -direction and equal to $\Delta y_0 = r_0/15$. The second, with the most disadvantageous grid spacing is found along the bisecting line, i.e. under 45° to one of the coordinate axis y or z . Because of the Cartesian formulation a factor of $\sqrt{2}$ enters the grid spacing, resulting in $\Delta r = r_0\Delta\theta = \sqrt{2}r_0/15$. In summary, the current cylindrical grid (described in more detail in section 3.1.1), has the following properties: The radial spacing in the shear layer is $\Delta r = 0.05r_0$, whereas the azimuthal spacing corresponding to the standard resolution of $N_\theta = 50$ is given by $r_0\Delta\theta = r_0(2\pi)/N_\theta = 0.126r_0$. The streamwise grid is almost constant with $\Delta z/r_0 \approx 0.10$ between $0 \leq z/r_0 \leq 32$ (where the combined grid stretching and outflow sponge region sets in). Thus, compared to the grid employed in the numerical reference data (Bogey & Bailly,

2005b), the radial grid size around the lip line correspond to roughly 75% of the spacing in the highest resolved direction and to 53% in the worst case. Because our streamwise grid spacing is similarly related to the radial grid as the one by Bogey ($\Delta z \approx 2\Delta r$), we find a smaller spacing corresponding to 75%. For a better comparison, the azimuthal spacings are given in Tab. 3.8.

Table 3.8: Comparison of grid spacings for different azimuthal resolutions N_θ for case LR, Med-m and HR. Reference data by Bogey & Bailly (2005b) for the aligned spacing Δy and the bisecting spacing $r_0\widetilde{\Delta\theta}$.

Case	N_θ	$\Delta = r_0\Delta\theta$	$\Delta/\Delta y$ [%]	$\Delta/r_0\widetilde{\Delta\theta}$ [%]
LR	32	0.196	294	208
Med-m	50	0.126	189	134
HR	78	0.080	120	85

3.7.1 Resolution effect on the flow field

In contrast to the previous sections we first draw the attention to the one-dimensional turbulent kinetic energy spectra at the inflow plane. The wavenumbers are represented from $n = 1$ to $n = 9$ in Fig. 3.60(a) and from $n = 9$ to the maximum number given by $N_\theta/2 - 1$ in Fig. 3.60(b). Thereby, the previously described effect of changes of inflow forcing due to resolution changes is best visualized. In Fig. 3.60(a) we find an alignment of the TKE spectra according to the number of employed Fourier modes. With increasing resolution, the spectra are shifted to higher energy levels as if the disturbance amplitude had been increased (see beginning of section 3.7). The unexcited modes $n \geq 9$ shown in Fig. 3.60(b) have significantly less energy but also exhibit a resolution effect. For the highly resolved case the accuracy limit of the computer is reached and thus wiggles appear in the highest represented wavenumbers. Based on this analysis of the energy spectra at the inflow, we point out that this and the subsequent section show combined effects of (i) changes in the azimuthal resolution, (ii) changes in excitation level associated with it and (iii) a shift of the filter cutoff to higher frequencies. In the following, we will refer to this combination as resolution effect. The effect of the relaxation regularization can also be noticed in the spectra shown

in Fig. 3.60(b): Depending on azimuthal resolution a discontinuity in the spectral decay at approximately two thirds of the maximum number N_θ occurs. This discontinuity correspond to the previously cutoff frequency of the filter. The cutoff should theoretically be effective around wavenumbers $n \approx 10$ for case LR, $n \approx 16$ for **Med-m** and $n \approx 25$ for the fine resolution in case **HR** (corresponding to $\omega_c \approx 0.63\pi$, see section 2.3). For LR we observe a kink around $n = 12$ and 13, whereas **Med-m** exhibits the effect of the filter cutoff at $n = 15$ and 16. For the high resolved case **HR** we find the cutoff to be at mode $n = 24, 25$. The slight shifts between the theoretical value of $2N_\theta/3$ is linked to the filter definition as we employ a graded filter without a clear spectral cutoff.

Figure 3.61 shows the resolution effect on the streamwise development of the mean axial velocity at the centerline w_c and its RMS. Again, we like to remark that the reference data is shifted in axial direction to account for the differences in the lengths of the potential cores. The data of Bogey & Bailly is shifted by $z_0/r_0 = -2$ in both graphs. For the experimental data, we chose to employ different shifts in Figures 3.61(a) and (b) in order to compare the spatial evolution of both profiles: For the centerline decay and the RMS the employed shifts are $z_0/r_0 = -3.1$ and $z_0/r_0 = -5.1$ for the data of Arakeri and coworkers and $z_0/r_0 = -2.4$ and $z_0/r_0 = -4.4$ for the data of Lau *et al.* We observe a dependence of the simulation results on the azimuthal resolution. For the different

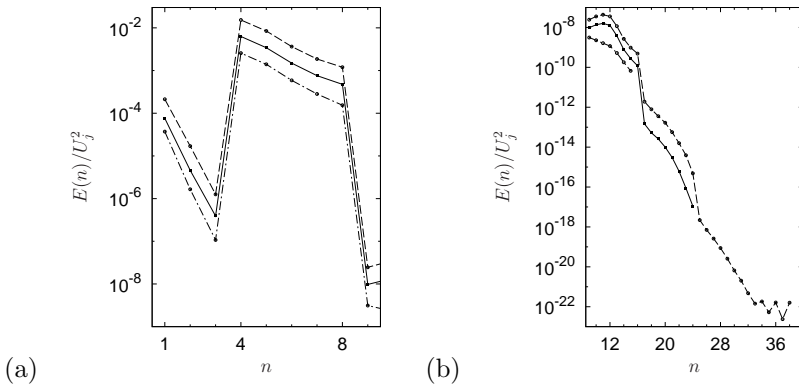


Figure 3.60: One-dimensional turbulence energy spectra E in θ -direction along the nozzle lip line at streamwise positions $z/r_0 = 0$ (a) $n = 1, \dots, 9$, (b) $n = 9, \dots, N_\theta/2 - 1$: --- LR, — **Med-m** and -.- HR.

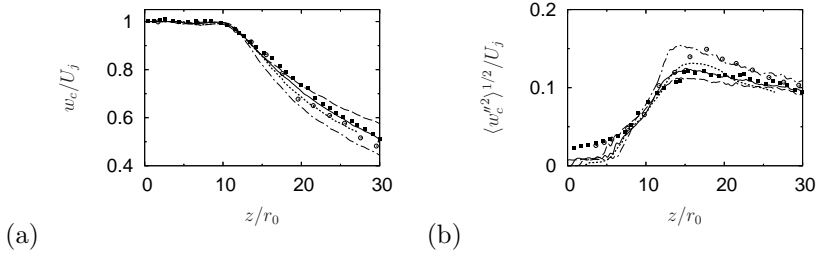


Figure 3.61: (a) Mean axial velocity w_c and (b) RMS of axial velocity fluctuations $\langle w''^2 \rangle^{1/2}$ along the jet centerline: --- LR, — Med-m, ···· HR, ······ Bogey & Bailly (2005b), \circ Lau et al. (1979), \blacksquare Arakeri et al. (2003).

resolutions two things can be noticed in Fig. 3.61(a): First, results for the coarsely resolved case LR exhibit the strongest decay of axial velocity whereas the results of the baseline configuration and the fine resolution case HR are found in closer agreement. Second, the mean centerline velocity of the medium resolved case Med-m and the fine azimuthal grid of case HR differ. These deviations are, however, restricted to a region downstream of $z/r_0 \approx 15$. As pointed out before, we cannot expect the results to converge perfectly as we (in the limit of infinitely small grid spacing) approach a DNS and not a grid independent LES result. Similar differences at the centerline are even observed for DNS investigations (Müller, 2007). Figure 3.61(b) compares the axial RMS and we find correspondingly large values for case LR which seems similar in its appearance to cases for which azimuthal wavenumbers $n = 1$ through 8 were excited (see section 3.2.2, Fig. 3.5(a)). The highly resolved case HR shows very similar behavior compared to the baseline configuration, and since the deviation between cases Med-m and HR compared to cases Med-m and LR is clearly less the results seem to converge.

The development of the jet half-width and the vorticity thickness, as shown in Fig. 3.62, depend quite strongly on the azimuthal resolution. Note that at $r = r_0$ where these quantities are analyzed the full azimuthal resolution is employed by the code and the mode-clipping is inactive. The jet spreading and thus the half-width $r_{1/2}$ is enhanced for the coarsely resolved case LR. The baseline resolution is found in fair agreement with the results by Bogey & Bailly (2006a). The fine resolved case HR exhibits a significantly reduced spreading. The same alignment is found for the vorticity thickness which is shown in Fig. 3.62(b). With

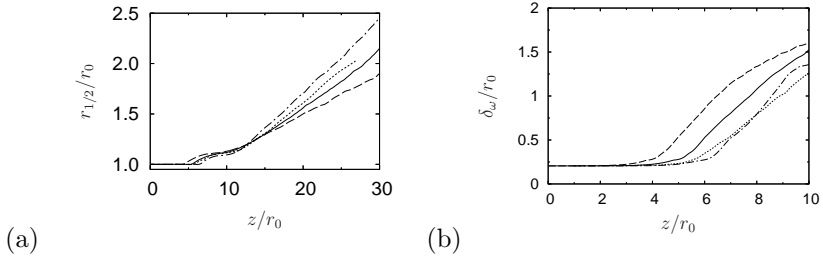


Figure 3.62: Streamwise development of (a) jet half-width $r_{1/2}$ and (b) vorticity thickness δ_ω : --- LR, — Med-m and -.- HR.

increasing resolution the vorticity thickness grows at earlier streamwise positions but visually the growth rates seem similar for the initial region.

The axial and radial RMS velocities along the nozzle lip line are shown in Fig. 3.63 together with the reference LES. Two interesting

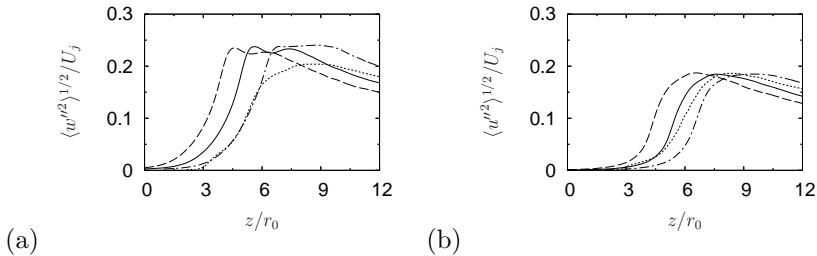


Figure 3.63: RMS of (a) axial velocity fluctuations $\langle w''^2 \rangle^{1/2}$ and (b) radial velocity fluctuations $\langle u''^2 \rangle^{1/2}$ along the nozzle lip line: --- LR, — Med-m, -.- HR and Bogey & Bailly (2005b).

things can be noted: First, cases Med-m and HR show similar distributions indicating a trend of convergence. We note that for the fine resolution the dual-peak structure is slightly less pronounced compared to the baseline configuration. However, it is clearly visible and its attenuation might be a combined effect of differences at the inflow. Second, and more important, is the fact that the dual-peak development of $\langle w''^2 \rangle^{1/2}$ disappears for the coarse resolution and the intensities level out at approximately 0.25. The onset of case LR is found in good agreement with the data from Bogey & Bailly (again the peak value observed in

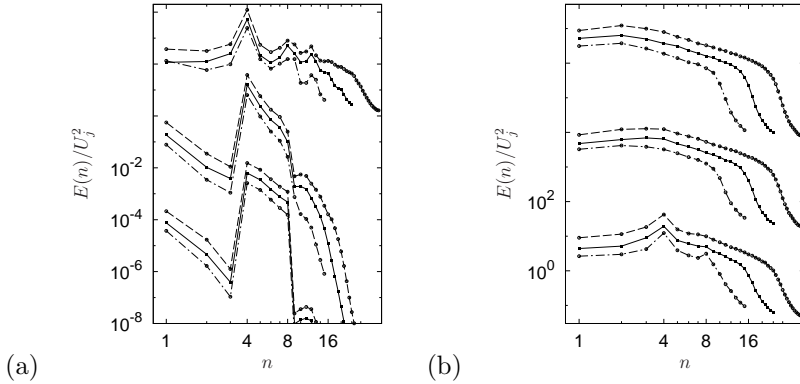


Figure 3.64: One-dimensional turbulence energy spectra E in θ -direction along the nozzle lip line at streamwise positions $z/r_0 = i \cdot 3$ (from bottom to top) (a) $i = 0, 1, 2$. The spectra are shifted by a factor of 10 for clarity. (b) $i = 3, 4, 5$. The groups of spectra are shifted by a factor of 1000 for clarity. --- LR, — Med-m and -.- HR.

their simulation is clearly lower which is most likely linked to the kind of disturbance generation discussed previously). For the radial direction we find a similar alignment as before. The reference data falls between case LR and the baseline configuration. The shapes of the distributions are similar, however, in the case of the fine resolution (case HR) a well defined maximum is observed, whereas the lower resolved cases exhibit a short plateau region. Again, we note that the shift in axial position accounts for the differences in potential core length and is directly linked to the changes in disturbance introduced at the inflow.

To investigate more precisely the effect of the vanishing dual-peak structure (see Fig. 3.63(a)), we determine again the one-dimensional turbulent kinetic energy spectra in the azimuthal direction. Figure 3.64(a) shows the spectra along the nozzle lip line for the first three axial positions $z/r_0 = 0, 3, 6$ using a shifting factor of ten, whereas Fig. 3.64(b) shows positions $z/r_0 = 9, 12, 15$ and employs a factor of one thousand to prevent an overlap of the spectra. The differences in disturbance energy at the inflow (as discussed above) have the expected effect on the downstream spectra. This is expressed by different levels of energy among the three cases. At $z/r_0 = 6$ the spectra still show similar results at different levels. Only further downstream, at $z/r_0 = 9$, we see the effect of the

resolution: Case LR shows a significant increase of energy in the first helical mode $n = 1$, again this is in very good agreement with what was found for low excitation amplitudes. For a detailed discussion we refer to sections 3.2 and 3.3. This increase of energy in $n = 1$ is accompanied by a significant reduction at high wavenumbers with $n \geq 8$. For the better resolved cases, we observe very similar spectra with a dominance of $n = 4$ and further dominance of azimuthal harmonics $n = 8$ and $n = 12$. Thus, it seems that the coarse resolution restricts the interaction of modes to low wavenumbers (that are represented on the azimuthal grid). Thereby, a transitional development is supported which is similar to a transition dominated by the helical mode $n = 1$. In contrast, cases Med-m and HR have again similar spectral contributions from the different azimuthal wavenumbers. The differences between these two cases are restricted to a TKE increase for case HR as well as a broader spectrum linked to the increased number of represented wavenumbers. As observed previously, the further development in axial direction is governed by the upstream influence, i.e., with increasing distance from the jet inflow more and more wavenumbers grow and thus can interact and the spectra are characterized by a broad-banded shape. In particular, the high resolution case HR exhibits a linear range between $4 \leq n \leq 18$. Thus, from Fig. 3.64(a) and (b) we find that within the transitional region the same physical results are obtained for the medium and fine resolution of $N_\theta = 50$ and $N_\theta = 78$. The magnitude difference is an effect that can be linked to the previously discussed problem of unequal excitation at the inflow. For the coarse resolution, we observe changes in the transitional behavior, i.e. the turbulent energy spectra are dominated by the helical mode $n = 1$, and hence to disregard high azimuthal wavenumbers may result in a numerically motivated preference of low azimuthal modes.

The azimuthal one-dimensional at the axial position $z/r_0 = 24$, are shown in Fig. 3.65 together with a straight line of slope $-5/3$. In Fig. 3.65(a) the spectra are evaluated at $r = r_0$ and in graph (b) the radial position corresponds to $r = 3r_0$. From these two graphs we see that further downstream (compared to the transitional region) the spectra develop similarities to the $-5/3$ inertial scaling. The azimuthal wavenumbers $n = 2, 3, 4$ are found slightly dominant and more energetic. In more detail and in particular in a narrow range of the logarithmic representation of the ordinate, we plot the spectra at a radially shifted position in Fig. 3.65(b) and note that the overshoot for $n \leq 4$ is lost.

For completeness, we provide the axial velocity spectra at several

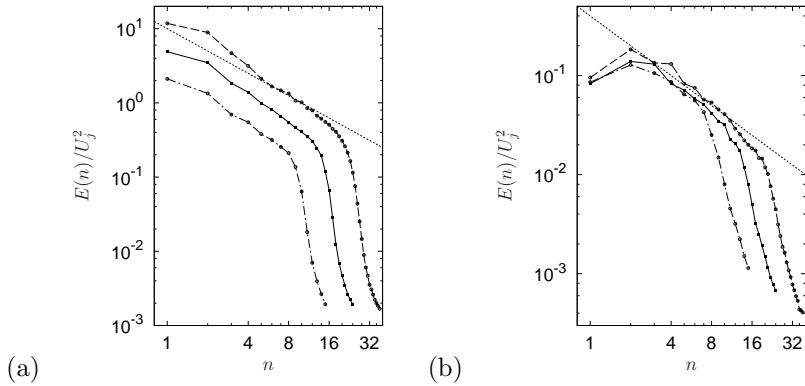


Figure 3.65: One-dimensional turbulence energy spectra E in θ -direction at streamwise position $z/r_0 = 24$: (a) at nozzle lip line $r/r_0 = 1$ (b) at $r/r_0 = 3$: $---$ LR, $—$ Med-m and $- \cdot -$ HR. The dotted line correspond to slope $-5/3$.

downstream positions in Fig. 3.66(a) and (b). Here, we do not repeat the physical interpretation of the results and only refer to sections 3.2 and 3.3 for details. In the vicinity of the inflow (and as could be expected from the previously discussed energy spectra) the velocity spectra remain uninfluenced by the azimuthal resolution besides the amplitude effect. The spectra develop similarly along the jet centerline (see Fig. 3.66(a)) and the nozzle lip line (see Fig. 3.66(b)). Only within the high frequencies, i.e. for Strouhal numbers $St \geq 1$ deviations of the results are observed. At the third streamwise profile, corresponding to $z/r_0 = 6$, the most noticeable resolution effect is found to occur along the nozzle lip line: As the helical mode $n = 1$ dominates the energy spectra of case LR we also see the advent of a dominant frequency that corresponds to the fundamental frequency of $n = 1$ (the peak at $St \approx 0.68$ is discussed in quite some detail in sections 3.2 and 3.3 in the context of the velocity spectra for case Low and Low-m). In contrast, the results of the higher resolved cases Med-m and HR are virtually identical for both evaluated radial positions. Only next to the dominant peaks in the spectra minor deviations emerge. Further downstream, these effects from the change in transition further consolidate and the results can be grouped as follows: The coarse resolution of case LR modifies the transition and artificially shifts the dominance to low azimuthal wavenumbers and frequencies. The baseline configuration Med-m and the fine resolved case

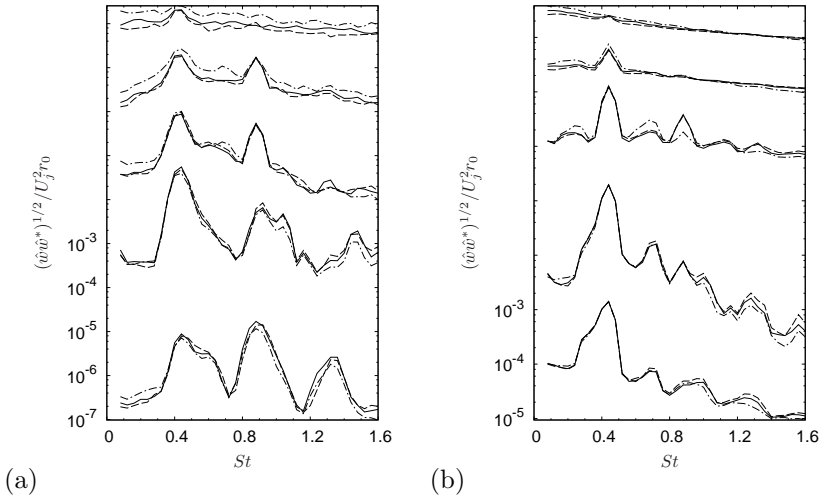


Figure 3.66: Axial velocity spectra at streamwise positions $z/r_0 = i \cdot 3$ ($i = 0, \dots, 4$ from bottom to top) along: (a) jet centerline, (b) jet lip line: --- LR, — Med-m and -.- HR. The groups of spectra are shifted by a factor of 10 for clarity.

HR are found in very good agreement and the differences are restricted to a less noisy signal for the high resolution. Recall that this better signal-to-noise ratio can be related to the increased resolution but also the increased number of samples used for the statistics.

From the findings within the fluid dynamic region we conclude that the chosen resolution of $N_\theta = 50$ seems to be sufficient to capture all relevant physical interactions. One has to act with caution when employing only a low number of Fourier modes in the periodic direction as this has a substantial effect on the transition process and most likely this will also carry over to the directly computed noise which is addressed in the following.

3.7.2 Effect on the acoustic field

The flow-field results suggest that the azimuthal resolution effect is most significant for case LR. The spectra of case HR compared to the standard resolution of case Med-m are not expected to deviate strongly. Because

of the minute differences in magnitude of the axial and radial RMS (see Fig. 3.63(a) and (b)) we expect differences in overall sound pressure level to be directly linked to the resolution effect on the initial condition and on the grid filter in azimuthal direction.

Figure 3.67 shows the frequency dependent pressure spectra at the previously investigated three polar angles of $\phi = 30^\circ, 60^\circ$ and 90° . For the details of the physical interpretation and the employed scaling, we again refer to the discussion in sections 3.2.3, 3.3.3 and 3.4.2. The spectra shown in Fig. 3.67(a) are as if different types of modal compositions were used in the respective excitations. For small observation angles from the downstream jet axis case LR shows a broad and dominant frequency band below $St \approx 0.5$. The peak levels are increased by approximately 5 dB for the coarsely resolved case. This band of frequencies is most likely directly related to the implicit grid filtering of the coarse azimuthal grid employed in case LR. Case HR is again in close agreement to the baseline configuration. The resolution effects on the acoustic spectra and the resulting differences between the two groups are comparable to effects caused by the removal of lower order modes from the forcing (which are investigated separately, see section 3.4.2 for details). For increasing angles ϕ we find similar results for the medium and fine resolution, however, case LR (the case where the transition is strongly affected by the coarse azimuthal resolution) has a broad dominant frequency band below $St \leq 0.8$ and deviates clearly from cases Med-m and HR. Finally, in directions perpendicular to the jet axis this trend continues and results for case LR are comparable to a different modal excitation, as for example employed in section 3.2. The previously noticed bi-tonal dominance, as for example seen in Fig. 3.42(c) is smeared out, which might be related to the coarse grid. In passing, we note that for all observer locations the finer resolution results in a less pronounced decay of high frequencies compared to the baseline configuration. The presented results for the directly computed pressure spectra in the acoustic near field suggest that the azimuthal resolution has a pronounced effect on the predicted transition scenario and thereby on the emitted noise. For sufficient resolution, i.e. in our case $N_\theta = 50$, we observe almost identical results compared to a highly resolved case. The minor deviations are a combined effect of resolution associated modifications of the jet inflow condition and grid-filter effects on the results. The physical results are substantiated by the fine resolved case HR.

The overall sound pressure levels are given in Fig. 3.68(a) (again along

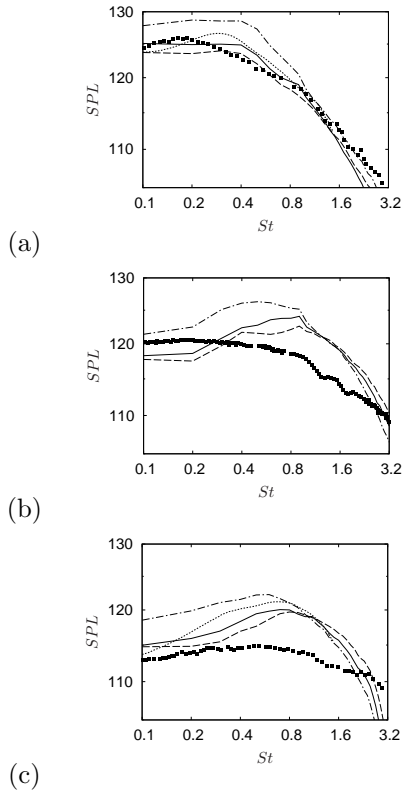


Figure 3.67: Near-field pressure spectra in dB at (a) $\phi = 30^\circ$, (b) $\phi = 60^\circ$ and (c) $\phi = 90^\circ$: $-\cdot-$ LR, $—$ Med-m and $---$ HR. \blacksquare Bogey et al. (2007b) at (a) $r = 15r_0$, $z = 30r_0$, (b) $r = 15r_0$, $z = 20r_0$, (c) $r = 15r_0$, $z = 10r_0$. \cdots Bogey & Bailly (2005b) at (a) $r = 12r_0$, $z = 29r_0$, (c) $r = 15r_0$, $z = 11r_0$.

the line $r/r_0 = 15$) and Fig. 3.68(b) gives the differences compared to the standard resolution case Med-m. As mentioned previously, for the current numerical setup the azimuthal resolution directly affects the disturbance energy transferred to the flow. Therefore, the increased OASPL for case HR are again a combined effect of a more effective excitation, and the shift of the grid cutoff to higher frequencies for finer resolu-

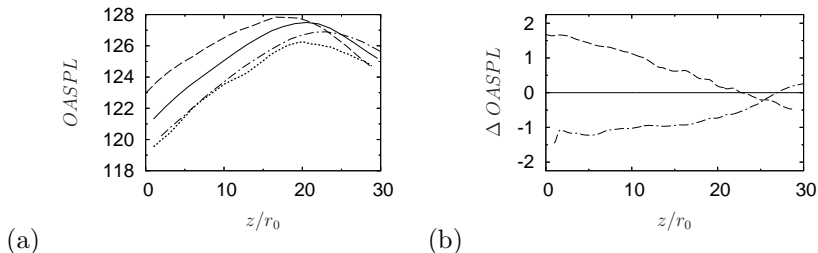


Figure 3.68: Axial distribution of (a) overall sound pressure levels and (b) the differences to the baseline configuration *Med-m* (OASPL in dB) along $r/r_0 = 15$: --- LR, — *Med-m*, -.- HR, (a) only *Bogey & Bailly (2006a)*.

tions (as found in the TKE spectra shown in Fig. 3.60). In Fig. 3.68(b), the data orders according to the azimuthal resolution: the coarser the grid the lower the overall sound pressure level. The large differences between the baseline configuration and the well resolved case HR are counter-intuitive as flow field and near-field spectra were found in very good agreement. However, since we found no drastic influence of the azimuthal resolution on the pressure spectra within the frequency range of $0.1 \leq St \leq 3.2$ we link the differences between case *Med-m* and HR mostly to grid-filtering effects inherently tied to the azimuthal resolution at these radial distances.

3.7.3 Summary of azimuthal resolution effects

The study of azimuthal resolution effects shows that one has to be cautious when interpreting simulation results for one single computational setup. In this study, the azimuthal resolution is directly tied to the inflow forcing and thereby modifies the physically very important inflow condition. This could partially be compensated by a separate investigation focusing on disturbance amplitude effects on the flow and its noise. Thereby, the following conclusions most likely hold for a more general setup: A coarse azimuthal resolution results in a jet transition in which low azimuthal wavenumbers dominate – although modes $n = 4$ through $n = 8$ are excited. For the coarsely resolved case LR this results in a helically ($n = 1$) dominated transition which alters the noise generating mechanism from the excited “cut-and-connect” process observed previously to one which is dominated by stable vortex pairings. In addition, as we approach the near-field the azimuthal grid spacing

becomes too coarse. This effectively acts as a grid filter on short wavelengths associated with the smallest scales and yields a steeper decay in the pressure spectra and a loss of spectral accuracy. The increase of resolution to $N_\theta = 78$ exhibits no fundamental differences compared to the results of the standard resolution. In general, the results of the two cases **Med-m** and **HR** fall close together, and all three investigated resolution cases consistently align in the same order. We conclude from this that convergence can be expected but clearly has not yet been reached and re-emphasize that a grid-independent result is not to be expected with the currently employed SGS-modeling approach.

Chapter 4

Summary, conclusions and recommendations

4.1 Summary and conclusions

In order to reveal some of the physics that underlie the noise generation of a turbulent subsonic jet a series of direct noise computations were performed. A Mach 0.9 jet at a Reynolds number of $Re = 4.5 \cdot 10^5$ was investigated by means of large-eddy simulations, in which the focus was on the effect of inflow disturbances obtained by superimposing linearly unstable eigenmodes. By forcing unstable modes their role, the particularity of their nonlinear interaction and its contribution to transition to turbulence and thus to the noise generation mechanism was studied in detail. First, two physical parameters, the disturbance amplitude and the composition of the disturbances, were varied such that each set of inflow disturbances was tested at three different excitation amplitudes. Based on the agreement with reference data a baseline configuration was identified among the six investigated cases (case **Med-m**, 3% disturbance amplitude, excitation of wavenumbers $|n| = \pm 4, \dots, \pm 8$). Subsequently, the effect of computational parameters on the flow and the noise field was studied. This sensitivity study of the computational approach comprised five additional simulations. Three of them focused on effects of the employed subgrid-scale model and the remaining two on effects associated with the numerical resolution.

In order to perform the investigations mentioned above the following steps were taken

- A highly accurate DNS/LES code solving the compressible Navier-Stokes equations has been developed that allows to simulate round jet flows in cylindrical geometries in a wide range of Mach and Reynolds numbers. The spatial discretization is based on compact-finite differences of tenth order and a Fourier spectral method. The time integration scheme uses a six-stage Runge-Kutta scheme (Berland *et al.*, 2006) of fourth-order accuracy which is optimized with respect to its dispersion and dissipation properties. The coordinate singularity $r = 0$ of the cylindrical coordinate system is accounted for following Mohseni & Colonius (2000).

- Appropriate boundary conditions have been set up to physically model a jet issuing into quiescent surrounding fluid. The combination of so-called sponge layers (Israeli & Orszag, 1981; Bodony, 2006) and nonreflecting boundary conditions (Thompson, 1987; Kim & Lee, 2000) allows (i) to impose the inflow profile without causing artificial noise (ii) to enable the entrainment of surrounding fluid into the jet stream and (iii) to truncate the computational domain while letting the generated noise leave the domain without causing reflections. Using this approach, the flow develops naturally and surrounding fluid is entrained at a rate which depends on the vortex interaction and not on the imposed boundary conditions.
- A numerical code solving the global eigenvalue problem established by the linearized compressible Navier-Stokes equations in cylindrical coordinates has been developed. This code allows to investigate the spatial and temporal stability properties of locally parallel base flows.
- The spatial stability properties of a velocity profile described by a hyperbolic-tangent function have been studied. In addition, the effect of the initial momentum thickness on the growth rates has been quantified. These unstable modes provide the basis for the functional form of the inflow excitation used in the present study.
- The nonlinear disturbance evolution of two different modal compositions and its effect on the emitted noise has been investigated for a high Reynolds number high subsonic jet flow using LES. The first type consists of all helical wavenumbers that are spatially amplified according to linear theory. The second type of excitation is restricted to higher azimuthal wavenumbers in order to initially decrease the azimuthal coherence of the disturbances and to investigate its effect on the flow and on the noise. For both types of excitation three disturbance amplitudes are investigated. The jet flow parameters were chosen to compare with the experiments by Maestrello (1976), Juvé *et al.* (1979), Lau *et al.* (1979), Arakeri *et al.* (2003) and Bogey *et al.* (2007*b*). Also several LES investigations by Bogey & Bailly focus on a jet at comparable operating conditions (see e.g. 2005*b*; 2006*c*; 2007).
- In order to assess the predictive capabilities of the chosen SGS

model an LES has been performed which employs an approximately deconvolved velocity field in the evaluation of the nonlinear terms (approximate deconvolution model ADM).

- A resolution study of the azimuthal grid has been performed to investigate its effect on the flow and noise field. Thereby, we have pointed out the possible misinterpretation of the coarse-grid LES results.

4.1.1 Effect of physical parameters

The sensitivity of the simulation results to the physical disturbance generation was investigated by varying first the collection of instabilities that are excited at the inflow and second the disturbance amplitude. Two types of modal compositions were set up: The first consisted of all helical wavenumbers n that are spatially amplified according to linear stability theory, i.e. unstable eigenmodes of wavenumbers $|n| = 1, \dots, 8$. The second type excluded low wavenumbers $|n| \leq 3$ from the inflow excitation. For both types the disturbance amplitude was varied from 1.5% to 4.5% of the jet exit velocity. In general, the effect of the forcing amplitude was found to follow consistently the expectations. The effects of changes in composition of the unstable eigenmodes on the development of the flow field as well as on the directly computed near-field sound were large.

When exciting all unstable helical waves ($1 \leq |n| \leq 8$) transition is characterized by large dominant and stable vortical structures that scale with the jet nozzle diameter. With increasing forcing amplitude the transition process is initiated closer to the inflow, but the dominant structures are only weakly affected and maintain their strong azimuthal coherence. They are predominantly two-dimensional until their sudden breakdown into much smaller scales. The analysis of the azimuthal turbulent kinetic energy spectra reveals that in the case of a low amplitude excitation the helical mode $n = 1$ is dominant slightly upstream of the closing of the potential core. Further downstream, where effects can no longer be considered linear the wavenumber $n = 2$ is dominant regardless of the disturbance amplitude. Compared to experimental and numerical reference data a faster decay of the axial velocity together with enhanced RMS intensities is observed along the jet centerline. Because of strong vortex pairings the RMS distribution of the axial velocity exhibits a

very pronounced dual-peak structure along the jet nozzle lip line. These distributions are similarly observed in tonally-excited jet experiments.

In particular for observer locations at polar angles of $\phi = 30^\circ$ measured from the downstream axis, the near-field pressure spectra exhibit a dominance around $St \approx 0.2$ and are in good agreement with the reference data. The previously mentioned vortex pairings leave an imprint on the acoustic near field and tonal contributions occur in the otherwise broad-banded spectra. With increasing angle ϕ the dominant low-frequency band shifts to higher frequencies and the tonal contributions exceed the broad-band noise by approximately 9 dB . At a shallow angle to the jet axis, the azimuthal pressure correlations are significantly lower than reported in the literature, indicating less contributions by large coherent structures. This might be related to the exclusion of the varicose mode $n = 0$ from the inflow excitation. In the sideline direction the acoustic pressure is uncorrelated and matches the data from literature, supporting the established concept of noise emission associated with small-scale turbulence.

When low azimuthal wavenumbers $n \leq 3$ are excluded from the inflow excitation, we observe a pronounced streamwise delay of the transition process. Also, an enhanced effect of the forcing amplitude is found. With increasing forcing amplitude the transition process is again shifted upstream as expected. As the forcing amplitude is increased the roll-up process of the shear layers is modified. The analysis of the azimuthal mode dynamics shows that the large azimuthally coherent structures generated by low-amplitude excitation are dominated by the varicose and first helical mode $n = 0$ and $n = 1$. In contrast, the roll-up process for high forcing amplitudes involves distorted three-dimensional streamwise elongated vortices dominated by the varicose mode $n = 0$ and even modes $n = 4$ and $n = 8$. On the one hand, this amplitude-dependent modification of the roll-up leads to a significant reduction of turbulence intensities along the jet centerline. The downstream development of the RMS fluctuations are in good agreement with experimental as well as numerical data reported in the literature. On the other hand, the eigenmode forcing results in localized structures which again cause a dual-peak RMS distributions along the jet lip line (similarly observed in tonally forced jet experiments).

This modification of the transition process and the turbulence levels directly affects the acoustic near field. As expected, the acoustic spectra significantly depend on the observer location. With increasing

angle from the downstream jet axis, the dominance of a low-frequency band shifts from $St \approx 0.4$ to higher frequencies around $St \approx 0.9$. The strong emissions at Strouhal numbers $St \leq 0.4$, in particular for low (1.5%) amplitude excitation, are linked to vortices that randomly undergo vortex pairings that most efficiently radiate in the downstream direction. These pairings are caused by the initially unexcited, naturally least stable helical mode $n = 1$. For medium (3%) and especially for high (4.5%) disturbance amplitudes the pressure spectra contain a tonal component outside the initially excited frequency band. This frequency is close to the higher harmonic of one of the forced fundamental frequencies as well as the frequency of the preferred (column) mode of the jet. The azimuthal correlation coefficient of the pressure fluctuations at polar angles $\phi = 30^\circ$ and $\phi = 90^\circ$ support the established links. At small angles from the jet axis, the observed correlations are slightly lower than the reference data which again might be related to exclusion of the varicose mode. However, experimental investigations of tonally excited jets report similar distributions. At $\phi = 90^\circ$, the noise is dominated by small-scale turbulence and the uncorrelated pressure signals match the reference data.

The analysis of Fourier mode amplitudes at the tone frequency and harmonics thereof shows that the tone observed in the near-field spectra can be linked to the rise, saturation and breakdown of structures that are generated during the early transition process. As a result of the excitation close to the preferred mode, the helical modes $n = \pm 4$ reach appreciable disturbance levels allowing its azimuthal higher harmonic $n = 8$ as well as mode $n = 0$ to rise with enhanced growth rates. These modes significantly contribute to noise emitted from a location slightly upstream of the collapse of the potential core which is perceived dominantly at intermediate observer locations. Supported by weakly nonlinear theory this frequency is explained as a mode interaction of initially excited modes. The growth rates observed in the LES are found in very good agreement with estimates based on weakly nonlinear interactions of linearly unstable eigenmodes of the inflow profile.

4.1.2 Effect of numerical parameters

The sensitivity of the results to numerical simulation parameters was tested by modifying details of the subgrid-scale model and changing the azimuthal resolution.

Starting out from the previously identified baseline configuration, the relaxation coefficient was gradually reduced (χ was set constant in space and time for all LES, see section 3.5). The overall effect of the investigated reduction is insignificant. Even for a 30% reduction of the coefficient the LES results do not exhibit substantial differences and only a reduction of turbulence intensities along the jet centerline and the nozzle lip line by less than 9% are observed. This reduction in turbulence intensity transfers to a 1.5 dB reduction of overall sound pressure level, however, the effect of the drastic reduction is small in the relevant frequency range. From this we conclude that using the chosen ad-hoc value reasonable and reliable LES results are obtained (this values corresponds to the upper limit of the determination procedure outlined by Stolz *et al.* (2001b)).

The application of the approximate deconvolution to the nonlinear terms had almost no effect on the investigated mean flow quantities. In comparison to the baseline case the deconvolution resulted in slightly reduced turbulent fluctuations and Reynolds stresses. From the comparison of the turbulent kinetic energy spectra this reduction can be linked to damping that comes into effect in the nonlinear development of the flow and is restricted mostly to the high azimuthal wavenumber range. The acoustic near-field prediction is nearly unaffected.

Resolution and inflow excitation are tightly coupled in the current setup and hence, the results of our study of the azimuthal resolution effect are difficult to assess. Nevertheless, the variation shows two main trends: First, when reducing the azimuthal resolution by a factor of approximately 3/2 ($N_\theta = 32$) the whole transition process is delayed and dominated by low azimuthal wavenumbers due to the reduced excitation amplitude and the non-represented higher wavenumbers. This allows for the naturally least stable helical mode to grow dominantly and to alter transition to turbulence which also influences the emitted sound field. Second, the finer-resolved case for which the number of azimuthal grid points was increased by approximately the same factor ($N_\theta = 78$) showed that the differences compared to the standard resolution $N_\theta = 50$ are small, being mostly restricted to the high-frequency range as a result of the shift of the cutoff frequency. As expected, the highly resolved case exhibits a less significant decay of sound pressure level in this frequency range. Overall, the resolution of $N_\theta = 50$ employed in all but two cases is considered sufficient to accurately resolve the triggered transition mechanism and the noise generated thereby.

4.2 Recommendations

During this work certain aspects were identified that could be further improved after the simulation environment has now been successfully established and tested. Also recommendations for future investigations are made. The overlap region in the vicinity of the inflow sponge causes a small wake-like flow that has been identified for some cases. This could be prevented easily by reducing the amplitude of the ambient sponge. Within this investigation we preferred not to change any parameter other than the ones mentioned.

If one abandons the option of storing the simulated data for post-processing the computational cost could be significantly reduced. Observer locations within the acoustic near-field would need to be identified in advance. Pressure or density signals would then be analyzed during the simulations evaluated and reduce the costly I/O (input-output) of data. Of course this limits the possibility for post-processing of data. Fundamental research, however, can often not know in advance what analysis might shed light on unknown aspects and thus renders this saving measure not always feasible.

The following recommendations for future investigations can be made. First, the effect of the inclusion of a generic nozzle into the simulation domain should be investigated in detail. The question that should be addressed is whether simulations need to account for details of a nozzle (resolution of oncoming turbulent boundary layer, wake-like region behind nozzle lip, level of oncoming turbulence contained in the boundary layer, etc.) in order to obtain a better overall agreement with experimental findings. The computational cost of such simulations are significantly higher if details of the turbulent boundary layer need to be captured accurately. By addressing this question one could clarify if a simple model proves to be sufficient to trigger the underlying and dominant noise mechanisms (for example, a combination of instability modes as employed in this work, or an algebraically growing combination of modes, see, e.g. Schmid (2007)). Thereby, the computational effort could be devoted to the turbulence of the jet flow.

Second, several physical parameters could be investigated which would further increase the complexity of the problem. In this work, only isothermal jet flows are investigated. As the effect of entropy fluctuations generated by a heated core flow on the emitted noise is still subject of a controversial debate (Viswanathan, 2004a) an investigation

of a heated core might be of interest. Also a heated jet is a more realistic model of the flow behind a jet engine. Thus, among the parameters to be investigated, temperature is definitely a key factor but numerical issues concerning stabilization of the outflow region might occur (Bogey *et al.*, 2007a). Also Reynolds number effects should be investigated to obtain a picture of the range of applicability of the current numerical tool. The significant reduction of the initial momentum thickness towards experimentally observed values could answer questions related to the over-predicted sideline pressure spectra.

Third, if more modeling expertise has been established to successfully simulate the problems mentioned above, physical complexity can be further increased by turning to coaxial jet configurations. As in a realistic flow behind a state-of-the-art jet engine a heated core flow with very high flow velocities would be surrounded by a secondary isothermal flow with lower velocities. The mean flow profile would exhibit two shear layers, one between the core and the by-pass flow and a second shear layer that develops outside of the secondary flow towards the atmospheric surrounding. Thereby, information of the complex flow pattern of a more and more realistic jet model could become accessible and insight into the underlying noise generation mechanisms might help to reach the ultimate goal of further jet-noise reduction.

Appendix A

Linear stability theory

As pointed out in chapter 2 (section 2.5.5) we choose to trigger the transition of the jet using linearly unstable eigenmodes. In this chapter the derivation of the linearized compressible Navier-Stokes equations is given, followed by the discretization and the numerical methods employed to solve the eigenvalue problem that results from the procedure. Thereafter the sensitivity of an inflow profile to the initial momentum thickness is investigated.

A.1 Linearized governing equations

A.1.1 Compressible Navier-Stokes equations in cylindrical coordinates

For the linear stability investigation the governing equations are the unsteady, three dimensional compressible Navier-Stokes equations. Here, we use the enthalpy form of the energy equation and employ a cylindrical coordinate system. For brevity we start out from the nondimensional form which is obtained by normalizing the dependent variables as follows

$$\begin{aligned} u &= \frac{u^*}{u_\infty} & v &= \frac{v^*}{u_\infty} & w &= \frac{w^*}{u_\infty} \\ \rho &= \frac{\rho^*}{\rho_\infty} & p &= \frac{p^*}{\rho_\infty u_\infty^2} & T &= \frac{c_p^* T^*}{a^{*2}}, \end{aligned} \tag{A.1}$$

where the superscript asterisk $(\cdot)^*$ denotes a dimensional quantity and the subscript $(\cdot)_\infty$ denotes some reference quantity. The variables u^* , v^* , w^* , ρ^* , p^* and T^* represent the cylindrical velocity components in (r, θ, z) -direction, density, pressure and temperature. The speed of sound is given by a^* and c_p denotes the specific heat at constant pressure. The independent variables in space are nondimensionalized by some reference length L_∞ ,

$$r = \frac{r^*}{L_\infty} \quad z = \frac{z^*}{L_\infty}, \tag{A.2}$$

the angular coordinate θ is in radians, whereas time is normalized by

$$t = \frac{t^* u^*}{L_\infty^*} . \quad (\text{A.3})$$

Restricting ourselves to a Newtonian fluid and assuming Fourier's law of heat transfer by conduction to be valid the nondimensionalized parameters known as Reynolds, Mach and Prandtl number,

$$Re = \frac{\rho_\infty^* u_\infty^* L_\infty^*}{\mu_\infty^*} \quad (\text{A.4a})$$

$$Ma = \frac{u_\infty^*}{a_\infty^*} \quad (\text{A.4b})$$

$$Pr = \frac{c_p^* \mu_\infty^*}{k_\infty^*} \quad (\text{A.4c})$$

are introduced, where μ_∞ is the dynamic viscosity and k_∞ the coefficient of thermal conductivity. In cylindrical coordinates the governing equations are the continuity equation,

$$\frac{\partial \rho}{\partial t} + \frac{1}{r} \frac{\partial}{\partial r} (r \rho u) + \frac{1}{r} \frac{\partial}{\partial \theta} (\rho v) + \frac{\partial}{\partial z} (\rho w) = 0 , \quad (\text{A.5})$$

the radial, azimuthal and streamwise momentum equation,

$$\frac{\partial(\rho u)}{\partial t} + \frac{1}{r} \frac{\partial}{\partial r} (r \rho u^2) + \frac{1}{r} \frac{\partial}{\partial \theta} (\rho u v) \quad (\text{A.6a})$$

$$+ \frac{\partial}{\partial z} (\rho u w) - \frac{\rho v^2}{r} = -\frac{\partial p}{\partial r} + S_r ,$$

$$\frac{\partial(\rho v)}{\partial t} + \frac{1}{r} \frac{\partial}{\partial r} (r \rho u v) + \frac{1}{r} \frac{\partial}{\partial \theta} (\rho v^2) \quad (\text{A.6b})$$

$$+ \frac{\partial}{\partial z} (\rho v w) + \frac{\rho u v}{r} = -\frac{1}{r} \frac{\partial p}{\partial \theta} + S_\theta ,$$

$$\frac{\partial(\rho w)}{\partial t} + \frac{1}{r} \frac{\partial}{\partial r} (r \rho u w) + \frac{1}{r} \frac{\partial}{\partial \theta} (\rho v w) \quad (\text{A.6c})$$

$$+ \frac{\partial}{\partial z} (\rho w^2) = -\frac{\partial p}{\partial z} + S_z ,$$

and the energy equation,

$$\begin{aligned} \rho \frac{\partial T}{\partial t} + \rho \left(u \frac{\partial T}{\partial r} + \frac{v}{r} \frac{\partial T}{\partial \theta} + w \frac{\partial T}{\partial z} \right) & \quad (A.7) \\ &= \frac{1}{Re Pr} \left(\frac{1}{r} \frac{\partial}{\partial r} \left(kr \frac{\partial T}{\partial r} \right) + \frac{1}{r} \frac{\partial}{\partial \theta} \left(k \frac{1}{r} \frac{\partial T}{\partial \theta} \right) + \frac{\partial}{\partial z} \left(k \frac{\partial T}{\partial y} \right) \right) \\ &+ (\gamma - 1) Ma^2 \left(\frac{\partial p}{\partial t} + \left(u \frac{\partial p}{\partial r} + \frac{v}{r} \frac{\partial p}{\partial \theta} + w \frac{\partial p}{\partial z} \right) + \frac{1}{Re} \Phi \right). \end{aligned}$$

Please note that within the derivation Stokes hypothesis is not yet employed. All results however do rely on the relation between the dynamic viscosity μ and the second coefficient of viscosity, i.e., $\lambda = -2/3\mu$. To close the system of equations the equation of state for an ideal gas is assumed to be valid, i.e.

$$p = \rho RT = \rho \frac{1}{\gamma Ma^2} T, \quad (A.8)$$

where R is the specific gas constant. γ is the ratio of the specific heat at constant pressure c_p^* and the specific heat at constant volume c_v^*

$$\gamma = \frac{c_p^*}{c_v^*}$$

and is set to $\gamma = 1.4$.

The terms S_i in equations (A.6a)–(A.6c) refer to the viscous fluxes in radial, azimuthal and streamwise direction and are defined as

$$S_r = \frac{\partial \tau_{rz}}{\partial z} + \frac{1}{r} \frac{\partial (r \tau_{rr})}{\partial r} + \frac{1}{r} \frac{\partial \tau_{r\theta}}{\partial \theta} - \frac{1}{r} \tau_{\theta\theta} \quad (A.9a)$$

$$S_\theta = \frac{1}{r^2} \frac{\partial (r^2 \tau_{r\theta})}{\partial r} + \frac{1}{r} \frac{\partial \tau_{\theta\theta}}{\partial \theta} + \frac{\partial \tau_{\theta z}}{\partial z} \quad (A.9b)$$

$$S_z = \frac{1}{r} \frac{\partial (r \tau_{rz})}{\partial r} + \frac{1}{r} \frac{\partial \tau_{\theta z}}{\partial \theta} + \frac{\partial \tau_{zz}}{\partial z}, \quad (A.9c)$$

with the viscous stress tensor components τ_{ij} being defined as

$$\tau_{rr} = 2 \frac{\mu}{Re} \frac{\partial u}{\partial r} + \frac{\lambda}{Re} \operatorname{div} \mathbf{u} \quad (\text{A.10a})$$

$$\tau_{\theta\theta} = 2 \frac{\mu}{Re} \left(\frac{1}{r} \frac{\partial v}{\partial \theta} + \frac{u}{r} \right) + \frac{\lambda}{Re} \operatorname{div} \mathbf{u} \quad (\text{A.10b})$$

$$\tau_{zz} = 2 \frac{\mu}{Re} \frac{\partial w}{\partial z} + \frac{\lambda}{Re} \operatorname{div} \mathbf{u} \quad (\text{A.10c})$$

$$\tau_{r\theta} = \frac{\mu}{Re} \left(r \frac{\partial}{\partial r} \left(\frac{v}{r} \right) + \frac{1}{r} \frac{\partial u}{\partial \theta} \right) \quad (\text{A.10d})$$

$$\tau_{rz} = \frac{\mu}{Re} \left(\frac{\partial u}{\partial z} + \frac{\partial w}{\partial r} \right) \quad (\text{A.10e})$$

$$\tau_{\theta z} = \frac{\mu}{Re} \left(\frac{1}{r} \frac{\partial w}{\partial \theta} + \frac{\partial v}{\partial z} \right). \quad (\text{A.10f})$$

The divergence of $\mathbf{u} = [u, v, w]^T$ in cylindrical coordinates is given by

$$\operatorname{div} \mathbf{u} = \frac{1}{r} \frac{\partial(ru)}{\partial r} + \frac{1}{r} \frac{\partial v}{\partial \theta} + \frac{\partial w}{\partial z}. \quad (\text{A.11})$$

In equation (A.7) Φ is the nondimensional dissipation given as

$$\begin{aligned} \Phi = & 2\mu \left(\left(\frac{\partial u}{\partial r} \right)^2 + \left(\frac{1}{r} \frac{\partial v}{\partial \theta} + \frac{u}{r} \right)^2 + \left(\frac{\partial w}{\partial z} \right)^2 \right) \\ & + \mu \left(r \frac{\partial}{\partial r} \left(\frac{v}{r} \right) + \frac{1}{r} \frac{\partial u}{\partial \theta} \right)^2 + \mu \left(\frac{1}{r} \frac{\partial w}{\partial \theta} + \frac{\partial v}{\partial z} \right)^2 \\ & + \mu \left(\frac{\partial u}{\partial z} + \frac{\partial w}{\partial r} \right)^2 + \lambda (\operatorname{div} \mathbf{u})^2. \end{aligned} \quad (\text{A.12})$$

When compressibility effects are of importance the dependence of the viscosity μ on the temperature T has to be taken into account. As for the nonlinear simulations we here rely on Sutherland's law of viscosity (see equation (2.10)).

A.1.2 Linearization

The instantaneous values of the velocities u , v , w , the density ρ , the pressure p and the temperature T are decomposed into a stationary mean

or so-called base flow and a time-dependent fluctuating disturbance, i.e.,

$$\begin{aligned} u &= \bar{U} + \tilde{u} & v &= \bar{V} + \tilde{v} & w &= \bar{W} + \tilde{w} \\ \rho &= \bar{\rho} + \tilde{\rho} & p &= \bar{p} + \tilde{p} & T &= \bar{T} + \tilde{T} . \end{aligned} \quad (\text{A.13})$$

Please note that in the context of the linearization of flow quantities tilde denotes a infinitesimal disturbance and should not to be mistaken for Favre-averaged quantities (see equation (2.3) in section 2.1). Employing this decomposition and neglecting quadratic terms of fluctuating quantities the linearized equation of state reads

$$\tilde{p} = \bar{\rho} R \tilde{T} + \tilde{\rho} R \bar{T} = \frac{1}{\gamma Ma^2} \left(\bar{\rho} \tilde{T} + \tilde{\rho} \bar{T} \right) , \quad (\text{A.14})$$

which is employed for eliminating expressions in disturbance fluctuations in the following. Employing Sutherland's law the amplitude function of the fluctuating viscosity $\tilde{\mu}$ is represented as first order expansion in temperature \tilde{T} . Similarly, the second coefficient of viscosity $\tilde{\lambda}$ and the coefficient of thermal conductivity \tilde{k} (using Fourier's law) are expanded to obtain the following relations:

$$\tilde{\mu} = \frac{d\bar{\mu}}{d\bar{T}} \tilde{T} ; \quad \tilde{\lambda} = \frac{d\bar{\lambda}}{d\bar{T}} \tilde{T} ; \quad \tilde{k} = \frac{d\bar{k}}{d\bar{T}} \tilde{T} . \quad (\text{A.15})$$

Substituting equations (A.13)–(A.15) into the nondimensional governing equations (A.5)–(A.7), subtracting the governing equations of the base flow and neglecting again terms of second and higher order in fluctuations yields the linearized perturbation equations given below by equations (A.16)–(A.18).

Continuity:

$$\frac{\partial \bar{\rho}}{\partial t} + \frac{1}{r} \frac{\partial}{\partial r} (r \bar{\rho} \tilde{u} + r \bar{\rho} \bar{U}) + \frac{1}{r} \frac{\partial}{\partial \theta} (\bar{\rho} \tilde{v} + \bar{\rho} \bar{V}) + \frac{\partial}{\partial z} (\bar{\rho} \tilde{w} + \bar{\rho} \bar{W}) = 0 \quad (\text{A.16})$$

r -momentum:

$$\begin{aligned} \bar{\rho} \left[\frac{\partial \tilde{u}}{\partial t} + \bar{U} \frac{\partial \tilde{u}}{\partial r} + \tilde{u} \frac{\partial \bar{U}}{\partial r} + \frac{\bar{V}}{r} \frac{\partial \tilde{u}}{\partial \theta} + \frac{\tilde{v}}{r} \frac{\partial \bar{U}}{\partial \theta} + \bar{W} \frac{\partial \tilde{u}}{\partial z} + \tilde{w} \frac{\partial \bar{U}}{\partial z} - \frac{2\bar{V}\tilde{v}}{r} \right] \\ + \bar{\rho} \left[\bar{U} \frac{\partial \bar{U}}{\partial r} + \frac{\bar{V}}{r} \frac{\partial \bar{U}}{\partial \theta} + \bar{W} \frac{\partial \bar{U}}{\partial z} - \frac{\bar{V}^2}{r} \right] = -\frac{\partial \bar{p}}{\partial r} + S_r^{\text{lin}} \end{aligned} \quad (\text{A.17a})$$

θ -momentum:

$$\begin{aligned} \bar{\rho} \left[\frac{\partial \tilde{v}}{\partial t} + \bar{U} \frac{\partial \tilde{v}}{\partial r} + \tilde{u} \frac{\partial \bar{V}}{\partial r} + \frac{\bar{V}}{r} \frac{\partial \tilde{v}}{\partial \theta} + \frac{\tilde{v}}{r} \frac{\partial \bar{V}}{\partial \theta} + \bar{W} \frac{\partial \tilde{v}}{\partial z} + \tilde{w} \frac{\partial \bar{V}}{\partial z} + \frac{\bar{U}\tilde{v} + \bar{V}\tilde{u}}{r} \right] \\ + \bar{\rho} \left[\bar{U} \frac{\partial \bar{V}}{\partial r} + \frac{\bar{V}}{r} \frac{\partial \bar{V}}{\partial \theta} + \bar{W} \frac{\partial \bar{V}}{\partial z} - \frac{\bar{U}\bar{V}}{r} \right] = -\frac{\partial \bar{p}}{\partial \theta} + S_\theta^{\text{lin}} \end{aligned} \quad (\text{A.17b})$$

z -momentum:

$$\begin{aligned} \bar{\rho} \left[\frac{\partial \tilde{w}}{\partial t} + \bar{U} \frac{\partial \tilde{w}}{\partial r} + \tilde{u} \frac{\partial \bar{W}}{\partial r} + \frac{\bar{V}}{r} \frac{\partial \tilde{w}}{\partial \theta} + \frac{\tilde{v}}{r} \frac{\partial \bar{W}}{\partial \theta} + \bar{W} \frac{\partial \tilde{w}}{\partial z} + \tilde{w} \frac{\partial \bar{W}}{\partial z} \right] \\ + \bar{\rho} \left[\bar{U} \frac{\partial \bar{W}}{\partial r} + \frac{\bar{V}}{r} \frac{\partial \bar{W}}{\partial \theta} + \bar{W} \frac{\partial \bar{W}}{\partial z} \right] = -\frac{\partial \bar{p}}{\partial z} + S_z^{\text{lin}} \end{aligned} \quad (\text{A.17c})$$

Energy equation:

$$\begin{aligned}
 & \bar{\rho} \left[\frac{\partial \tilde{T}}{\partial t} + \bar{U} \frac{\partial \tilde{T}}{\partial r} + \tilde{u} \frac{\partial \bar{T}}{\partial r} + \frac{\bar{V}}{r} \frac{\partial \tilde{T}}{\partial \theta} + \frac{\tilde{v}}{r} \frac{\partial \bar{T}}{\partial \theta} + \bar{W} \frac{\partial \tilde{T}}{\partial z} + \tilde{w} \frac{\partial \bar{T}}{\partial z} \right] + \tilde{\rho} \left[\bar{U} \frac{\partial \bar{T}}{\partial r} + \frac{\bar{V}}{r} \frac{\partial \bar{T}}{\partial \theta} + \bar{W} \frac{\partial \bar{T}}{\partial z} \right] \\
 &= \frac{1}{RePr} \left(\frac{1}{r} \frac{\partial}{\partial r} \left(r \bar{k} \frac{\partial \tilde{T}}{\partial r} + r \tilde{k} \frac{\partial \bar{T}}{\partial r} \right) + \frac{1}{r^2} \frac{\partial}{\partial \theta} \left(\bar{k} \frac{\partial \tilde{T}}{\partial \theta} + \tilde{k} \frac{\partial \bar{T}}{\partial \theta} \right) + \frac{\partial}{\partial z} \left(\bar{k} \frac{\partial \tilde{T}}{\partial z} + \tilde{k} \frac{\partial \bar{T}}{\partial z} \right) \right) \\
 &\quad + (\gamma - 1) Ma^2 \left(\frac{\partial \tilde{p}}{\partial t} + \bar{U} \frac{\partial \tilde{p}}{\partial r} + \tilde{u} \frac{\partial \bar{p}}{\partial r} + \frac{\bar{V}}{r} \frac{\partial \tilde{p}}{\partial \theta} + \frac{\tilde{v}}{r} \frac{\partial \bar{p}}{\partial \theta} + \bar{W} \frac{\partial \tilde{p}}{\partial z} + \tilde{w} \frac{\partial \bar{p}}{\partial z} + \frac{1}{Re} \Phi^{\text{lin}} \right)
 \end{aligned} \tag{A.18}$$

Within equation (A.17) S_i^{lin} denote the linearized viscous fluxes found by linearizing equations (A.9a)–(A.9c). For brevity only the viscous term in radial direction is given here:

$$\begin{aligned}
 S_r^{\text{lin}} = \frac{1}{Re} & \left[\bar{\mu} \left(\frac{\partial^2 \tilde{u}}{\partial z^2} + \frac{\partial^2 \tilde{w}}{\partial r \partial z} \right) + \left(\frac{\partial^2 \bar{U}}{\partial z^2} + \frac{\partial^2 \bar{W}}{\partial r \partial z} \right) \tilde{\mu} + \frac{d\bar{\mu}}{d\bar{T}} \frac{\partial \bar{T}}{\partial z} \left(\frac{\partial \tilde{u}}{\partial z} + \frac{\partial \tilde{w}}{\partial r} \right) + \left(\frac{\partial \bar{U}}{\partial z} + \frac{d\bar{W}}{dr} \right) \frac{\partial \tilde{\mu}}{\partial z} \right. \\
 & + \frac{2\bar{\mu}}{r} \left(\frac{\partial \tilde{u}}{\partial r} - \frac{\tilde{u}}{r} - \frac{1}{r} \frac{\partial \tilde{v}}{\partial \theta} \right) + \frac{2}{r} \frac{d\bar{\mu}}{d\bar{T}} \left(\frac{\partial \bar{U}}{\partial r} - \frac{\bar{U}}{r} - \frac{1}{r} \frac{\partial \bar{V}}{\partial \theta} \right) \tilde{T} + 2\bar{\mu} \frac{\partial^2 \tilde{u}}{\partial r^2} \\
 & + 2 \frac{d\bar{\mu}}{d\bar{T}} \left(\frac{\partial^2 \bar{U}}{\partial r^2} \tilde{T} + \frac{\partial \bar{T}}{\partial r} \frac{\partial \tilde{u}}{\partial r} \right) + 2 \frac{\partial \bar{U}}{\partial r} \frac{\partial \tilde{\mu}}{\partial r} + \frac{\bar{\mu}}{r} \left(\frac{\partial^2 \tilde{v}}{\partial r \partial \theta} - \frac{1}{r} \frac{\partial \tilde{v}}{\partial \theta} + \frac{1}{r} \frac{\partial^2 \tilde{u}}{\partial \theta^2} \right) \\
 & + \frac{1}{r} \frac{d\bar{\mu}}{d\bar{T}} \left(\frac{\partial^2 \bar{V}}{\partial r \partial \theta} - \frac{1}{r} \frac{\partial \bar{V}}{\partial \theta} + \frac{1}{r} \frac{\partial^2 \bar{U}}{\partial \theta^2} \right) \tilde{T} + \frac{1}{r} \frac{d\bar{\mu}}{d\bar{T}} \frac{\partial \bar{T}}{\partial \theta} \left(\frac{\partial \tilde{v}}{\partial r} - \frac{\tilde{v}}{r} + \frac{1}{r} \frac{\partial \tilde{u}}{\partial \theta} \right) \\
 & + \frac{1}{r} \left(\frac{\partial \bar{V}}{\partial r} - \frac{\bar{V}}{r} + \frac{1}{r} \frac{\partial \bar{U}}{\partial \theta} \right) \frac{\partial \tilde{\mu}}{\partial \theta} + \bar{\lambda} \left(\frac{1}{r} \frac{\partial \tilde{u}}{\partial r} - \frac{\tilde{u}}{r^2} + \frac{\partial^2 \tilde{u}}{\partial r^2} + \frac{1}{r} \frac{\partial^2 \tilde{v}}{\partial r \partial \theta} - \frac{1}{r^2} \frac{\partial \tilde{v}}{\partial \theta} + \frac{\partial^2 \tilde{w}}{\partial r \partial z} \right) \\
 & + \left(\frac{1}{r} \frac{\partial \bar{U}}{\partial r} - \frac{\bar{U}}{r^2} + \frac{\partial^2 \bar{U}}{\partial r^2} + \frac{1}{r} \frac{\partial^2 \bar{V}}{\partial r \partial \theta} - \frac{1}{r^2} \frac{\partial \bar{V}}{\partial \theta} + \frac{\partial^2 \bar{W}}{\partial r \partial z} \right) \tilde{\lambda} \\
 & \left. + \frac{\partial \bar{\lambda}}{\partial r} \left(\frac{\tilde{u}}{r} + \frac{\partial \tilde{u}}{\partial r} + \frac{1}{r} \frac{\partial \tilde{v}}{\partial \theta} + \frac{\partial \tilde{w}}{\partial z} \right) + \left(\frac{\bar{U}}{r} + \frac{\partial \bar{U}}{\partial r} + \frac{1}{r} \frac{\partial \bar{V}}{\partial \theta} + \frac{\partial \bar{W}}{\partial z} \right) \frac{\partial \tilde{\lambda}}{\partial r} \right].
 \end{aligned}
 \tag{A.19a}$$

Similarly, the viscous terms S_θ^{lin} and S_z^{lin} are derived. The linearized dissipation function Φ^{lin} is

$$\begin{aligned}
\Phi^{\text{lin}} = & 2\bar{\mu} \left[2 \frac{\partial \bar{U}}{\partial r} \frac{\partial \tilde{u}}{\partial r} + \frac{2}{r^2} \frac{\partial \bar{V}}{\partial \theta} \frac{\partial \tilde{v}}{\partial \theta} + \frac{2}{r^2} \frac{\partial \bar{V}}{\partial \theta} \tilde{u} + \frac{2}{r^2} \frac{\partial \tilde{v}}{\partial \theta} \bar{U} + \frac{2}{r^2} \bar{U} \tilde{u} + 2 \frac{\partial \bar{W}}{\partial z} \frac{\partial \tilde{w}}{\partial z} \right] \\
& + \bar{\mu} \left[2 \frac{\partial \bar{V}}{\partial r} \frac{\partial \tilde{v}}{\partial r} - \frac{2}{r} \frac{\partial \bar{V}}{\partial r} \tilde{v} - \frac{2}{r} \frac{\partial \tilde{v}}{\partial r} \bar{V} + \frac{2}{r^2} \bar{V} \tilde{v} + \frac{2}{r} \frac{\partial V b}{\partial r} \frac{\partial \tilde{u}}{\partial \theta} + \frac{2}{r} \frac{\partial \tilde{v}}{\partial r} \frac{\partial \bar{U}}{\partial \theta} - \frac{2}{r^2} \tilde{v} \frac{\partial \bar{U}}{\partial \theta} - \frac{2}{r^2} \bar{V} \frac{\partial \tilde{u}}{\partial \theta} + 2 \frac{\partial \bar{U}}{\partial \theta} \frac{\partial \tilde{u}}{\partial \theta} \right. \\
& \quad \left. + 2 \frac{\partial \bar{W}}{\partial z} \frac{\partial \tilde{w}}{\partial z} + \frac{2}{r} \frac{\partial \bar{W}}{\partial \theta} \frac{\partial \tilde{v}}{\partial z} + \frac{2}{r} \frac{\partial \tilde{w}}{\partial \theta} \frac{\partial \bar{V}}{\partial z} + 2 \frac{\partial \bar{V}}{\partial z} \frac{\partial \tilde{v}}{\partial z} + 2 \frac{\partial \bar{U}}{\partial z} \frac{\partial \tilde{u}}{\partial z} + 2 \frac{\partial \bar{U}}{\partial z} \frac{\partial \tilde{w}}{\partial r} + 2 \frac{\partial \tilde{u}}{\partial z} \frac{\partial \bar{W}}{\partial r} + 2 \frac{\partial \bar{W}}{\partial r} \frac{\partial \tilde{w}}{\partial r} \right] \\
& + \bar{\lambda} \left[\frac{\tilde{u}}{r} \frac{\partial \tilde{u}}{\partial r} + \frac{1}{r} \frac{\partial \tilde{v}}{\partial \theta} + \frac{\partial \tilde{w}}{\partial z} \right] \\
& + 2 \left[\left(\frac{\partial \bar{U}}{\partial r} \right)^2 + \frac{1}{r^2} \left(\frac{\partial \bar{V}}{\partial \theta} \right)^2 + 2 \frac{\partial \bar{V}}{\partial \theta} \frac{\bar{U}}{r} + \left(\frac{\bar{U}}{r} \right)^2 + \left(\frac{\partial \bar{W}}{\partial z} \right)^2 \right] \bar{\mu} \\
& + \left[\left(\frac{\partial \bar{V}}{\partial r} \right)^2 - \frac{2}{r} \frac{\partial \bar{V}}{\partial r} \bar{V} + \frac{1}{r^2} \bar{V}^2 + \frac{2}{r} \frac{\partial \bar{V}}{\partial r} \frac{\partial \bar{U}}{\partial \theta} - \frac{2}{r^2} \bar{V} \frac{\partial \bar{U}}{\partial \theta} + \frac{1}{r^2} \left(\frac{\partial \bar{U}}{\partial \theta} \right)^2 + \frac{1}{r^2} \left(\frac{\partial \bar{W}}{\partial \theta} \right)^2 + \frac{2}{r} \frac{\partial \bar{W}}{\partial \theta} \frac{\partial \bar{V}}{\partial z} \right. \\
& \quad \left. + \left(\frac{\partial \bar{V}}{\partial z} \right)^2 + \left(\frac{\partial \bar{U}}{\partial z} \right)^2 + 2 \frac{\partial \bar{U}}{\partial z} \frac{\partial \bar{W}}{\partial z} + \left(\frac{\partial \bar{W}}{\partial r} \right)^2 \right] \bar{\mu} \\
& + \left[\frac{\bar{U}}{r} \frac{\partial \bar{U}}{\partial r} + \frac{1}{r} \frac{\partial \bar{V}}{\partial \theta} + \frac{\partial \bar{W}}{\partial z} \right] \bar{\lambda}
\end{aligned} \tag{A.20}$$

A.1.3 Wave ansatz for disturbances

For clarity, bars from the base-flow quantities will be omitted in the remainder. To further simplify the linearized equations we restrict ourselves to a locally parallel flow, i.e., all base-flow quantities depend only on the independent variable r . In addition, the disturbances are thought of as traveling waves and thus a normal-mode ansatz for the perturbations the flow variables in equation (A.13) of the form

$$q = \bar{q}(r) + \tilde{q}(r, \theta, z, t) = Q(r) + \hat{q}(r)e^{i(\alpha z + n\theta - \omega t)} \quad (\text{A.21})$$

is made, where q or Q denote a component of the velocity vector or a scalar quantity (disturbance or base-flow quantity), α and n denote the axial and the azimuthal wavenumber, respectively and ω is the angular frequency. The complex amplitudes of the eigenfunctions of q are denoted by hats. Under these restrictions and assumptions the following local linear perturbation equations for a compressible, parallel flow in a cylindrical coordinate frame of reference are obtained, where, as mentioned before, density fluctuations are eliminated using the linearized equations of state for an ideal gas. In detail these are the continuity equation

$$\begin{aligned} \frac{d\hat{u}}{dr} + \left[\frac{1}{p} \frac{dp}{dr} - \frac{1}{T} \frac{dT}{dr} + \frac{1}{r} \right] \hat{u} & \quad (\text{A.22}) \\ + \left[\frac{in}{r} \right] \hat{v} & \\ + [i\alpha] \hat{w} & \\ + \left[\frac{U}{p} \right] \frac{d\hat{p}}{dr} & \\ + \left[\frac{1}{p} \left\{ -\frac{U}{T} \frac{dT}{dr} + \frac{dU}{dr} + \frac{U}{r} + i \left(\alpha W + n \frac{V}{r} - \omega \right) \right\} \right] \hat{p} & \\ - \left[\frac{U}{T} \right] \frac{d\hat{T}}{dr} & \\ + \left[\frac{1}{T} \left\{ \frac{2U}{T} \frac{dT}{dr} - \frac{dU}{dr} - \frac{U}{r} - \frac{U}{p} \frac{dp}{dr} \right. \right. & \\ \left. \left. - i \left(\alpha W + n \frac{V}{r} - \omega \right) \right\} \right] \hat{T} = 0, & \end{aligned}$$

the momentum equation in radial direction

$$\begin{aligned}
 & [Re^{-1} (2\mu + \lambda)] \frac{d^2 \hat{u}}{dr^2} \tag{A.23a} \\
 & + \left[-\rho U + Re^{-1} \left(\frac{1}{r} (2\mu + \lambda) + \frac{dT}{dr} \left(2 \frac{d\mu}{dT} + \frac{d\lambda}{dT} \right) \right) \right] \frac{d\hat{u}}{dr} \\
 & + \left[-\rho \left(\frac{dU}{dr} + i \left(\alpha W + n \frac{V}{r} - \omega \right) \right) \right. \\
 & \quad \left. + Re^{-1} \left(-\frac{1}{r^2} (2\mu + \lambda) - \mu \left(\alpha^2 + \frac{n^2}{r^2} \right) + \frac{1}{r} \frac{d\lambda}{dT} \frac{dT}{dr} \right) \right] \hat{u} \\
 & + \left[i Re^{-1} \frac{n}{r} (\mu + \lambda) \right] \frac{d\hat{v}}{dr} \\
 & + \left[\rho \frac{2V}{r} + i Re^{-1} \left(-\frac{n}{r^2} (3\mu + \lambda) + \frac{n}{r} \frac{d\lambda}{dT} \frac{dT}{dr} \right) \right] \hat{v} \\
 & + \left[i Re^{-1} \alpha (\mu + \lambda) \right] \frac{d\hat{w}}{dr} + \left[i Re^{-1} \alpha \frac{d\lambda}{dT} \frac{dT}{dr} \right] \hat{w} \\
 & - \frac{d\hat{p}}{dr} - \left[\frac{\rho}{p} \left(U \frac{dU}{dr} - \frac{V^2}{r} \right) \right] \hat{p} \\
 & + \left[2 \frac{dU}{dr} \frac{d\mu}{dT} + \frac{d\lambda}{dT} \left(\frac{U}{r} + \frac{dU}{dr} \right) \right] \frac{d\hat{T}}{dr} \\
 & + \left[\frac{\rho}{T} \left(U \frac{dU}{dr} - \frac{V^2}{r} \right) + Re^{-1} \left(\frac{d^2 \lambda}{dT^2} \frac{dT}{dr} \left(\frac{dU}{dr} + \frac{U}{r} \right) \right. \right. \\
 & \quad \left. \left. + \frac{d^2 \mu}{dT^2} \frac{dT}{dr} \frac{dU}{dr} + 2 \frac{d\mu}{dT} \left(\frac{d^2 U}{dr^2} + \frac{1}{r} \left(\frac{dU}{dr} - \frac{U}{r} \right) \right) \right) \right. \\
 & \quad \left. + \frac{d\lambda}{dT} \left(\frac{1}{r} \frac{dU}{dr} - \frac{U}{r^2} + \frac{d^2 U}{dr^2} \right) \right. \\
 & \quad \left. + i \frac{d\mu}{dT} \left(\alpha \frac{dW}{dr} + n \left(\frac{dV}{dr} - \frac{V}{r} \right) \right) \right] \hat{T} = 0
 \end{aligned}$$

the momentum equation in azimuthal direction

$$\begin{aligned}
 & \left[iRe^{-1} \frac{n}{r} (\mu + \lambda) \right] \frac{d\hat{u}}{dr} & (A.23b) \\
 & + \left[iRe^{-1} \left(\frac{n}{r^2} (3\mu + \lambda) + \frac{n}{r} \frac{d\mu}{dT} \frac{dT}{dr} \right) - \rho \left(\frac{dV}{dr} + \frac{V}{r} \right) \right] \hat{u} \\
 & + \left[Re^{-1} \mu \right] \frac{d^2 \hat{v}}{dr^2} + \left[Re^{-1} \left(\frac{d\mu}{dT} \frac{dT}{dr} + \frac{\mu}{r} \right) - \rho U \right] \frac{d\hat{v}}{dr} \\
 & + \left[Re^{-1} \left(-\frac{n^2}{r^2} (2\mu + \lambda) - \frac{1}{r} \frac{d\mu}{dT} \frac{dT}{dr} - \mu \left(\alpha^2 + \frac{1}{r^2} \right) \right) \right. \\
 & \quad \left. - \rho \left(\frac{U}{r} + i \left(\alpha W + n \frac{V}{r} - \omega \right) \right) \right] \hat{v} \\
 & - \left[Re^{-1} \frac{\alpha n}{r} (\mu + \lambda) \right] \hat{w} \\
 & + \left[-\frac{\rho}{p} \left(U \frac{dV}{dr} + \frac{UV}{r} \right) - i \frac{n}{r} \right] \hat{p} \\
 & + \left[Re^{-1} \frac{d\mu}{dT} \left(\frac{dV}{dr} - \frac{V}{r} \right) \right] \frac{d\hat{T}}{dr} \\
 & + \left[\frac{d^2 \mu}{dT^2} \frac{dT}{dr} \left(\frac{dV}{dr} - \frac{V}{r} \right) + \frac{d\mu}{dT} \left(\frac{d^2 V}{dr^2} - \frac{V}{r^2} \right) \right. \\
 & \quad \left. + in \left(\frac{2n}{r^2} U \frac{d\mu}{dT} + \frac{d\lambda}{dT} \left(\frac{1}{r} \frac{dU}{dr} + \frac{U}{r^2} \right) \right) \right. \\
 & \quad \left. + \frac{\rho}{T} \left(U \frac{dV}{dr} + \frac{UV}{r} \right) \right] \hat{T} = 0
 \end{aligned}$$

the momentum equation in axial direction

$$\begin{aligned}
 & [iRe^{-1}\alpha(\mu + \lambda)] \frac{d\hat{u}}{dr} && \text{(A.23c)} \\
 & + \left[iRe^{-1}\alpha \left(\frac{1}{r}(\mu + \lambda) + \frac{d\mu}{dT} \frac{dT}{dr} \right) - \rho \frac{dW}{dr} \right] \hat{u} \\
 & + \left[-Re^{-1} \frac{\alpha n}{r} (\mu + \lambda) \right] \hat{v} \\
 & + [Re^{-1}\mu] \frac{d^2\hat{w}}{dr^2} + \left[Re^{-1} \left(\frac{\mu}{r} + \frac{d\mu}{dT} \frac{dT}{dr} \right) - \rho U \right] \frac{d\hat{w}}{dr} \\
 & - \left[Re^{-1} \left(\alpha^2 (\mu + \lambda) + \frac{\mu n^2}{r^2} \right) + i\rho \left(\alpha W + n \frac{V}{r} - \omega \right) \right] \hat{w} \\
 & - \left[\frac{\rho}{p} U \frac{dW}{dr} + i\alpha \right] \hat{p} \\
 & + \left[Re^{-1} \frac{d\mu}{dT} \frac{dW}{dr} \right] \frac{d\hat{T}}{dr} \\
 & + \left[Re^{-1} \left(\frac{d^2\mu}{dT^2} \frac{dW}{dr} + \frac{d\mu}{dT} \left(\frac{dW}{dr} + \frac{1}{r} \frac{dW}{dr} \right) \right. \right. \\
 & \quad \left. \left. + i \left(\alpha \frac{d\lambda}{dT} \left(\frac{dU}{dr} + \frac{U}{r} \right) \right) + \frac{\rho}{T} U \frac{dW}{dr} \right] \hat{T} = 0
 \end{aligned}$$

and the energy equation

$$\begin{aligned}
& \left[-2(\gamma - 1) Ma^2 Re^{-1} \left(2\mu \frac{dU}{dr} + \frac{U}{r} \right) \right] \frac{d\hat{u}}{dr} \tag{A.24} \\
& + \left[-(\gamma - 1) Ma^2 Re^{-1} \left(4\mu \frac{U}{r^2} + \frac{2\lambda}{r} \left(\frac{dU}{dr} + \frac{U}{r} \right) \right. \right. \\
& \quad \left. \left. + i2\mu \left(\alpha \frac{dW}{dr} + \frac{n}{r} \left(\frac{dV}{dr} - \frac{V}{r} \right) \right) \right) + \rho \frac{dT}{dr} - (\gamma - 1) Ma^2 \frac{dp}{dr} \right] \hat{u} \\
& - \left[2(\gamma - 1) Ma^2 Re^{-1} \mu \left(\frac{dV}{dr} - \frac{V}{r} \right) \right] \frac{d\hat{v}}{dr} \\
& + \left[\frac{2}{r} (\gamma - 1) Ma^2 Re^{-1} \left(\mu \left(\frac{dV}{dr} - \frac{V}{r} \right) \right. \right. \\
& \quad \left. \left. - i n \left(\frac{2\mu}{r} U + \lambda \left(\frac{dU}{dr} + \frac{U}{r} \right) \right) \right) \right] \hat{v} \\
& - \left[2(\gamma - 1) Ma^2 Re^{-1} \mu \frac{dW}{dr} \right] \frac{d\hat{w}}{dr} \\
& - \left[i2\alpha(\gamma - 1) Ma^2 Re^{-1} \lambda \left(\frac{dU}{dr} + \frac{U}{r} \right) \right] \hat{w} \\
& - [(\gamma - 1) Ma^2 U] \frac{d\hat{p}}{dr} \\
& + \left[\frac{\rho U}{p} \frac{dT}{dr} - i(\gamma - 1) Ma^2 \left(\alpha W + n \frac{V}{r} - \omega \right) \right] \hat{p} \\
& - \left[(RePr)^{-1} k \right] \frac{d^2 \hat{T}}{dr^2} - \left[(RePr)^{-1} \left(2 \frac{dk}{dT} \frac{dT}{dr} + \frac{k}{r} \right) - \rho U \right] \frac{d\hat{T}}{dr} \\
& + \left[-\frac{\rho U}{T} \frac{dT}{dr} + i\rho \left(\alpha W + n \frac{V}{r} - \omega \right) + (RePr)^{-1} k \left(\frac{n^2}{r^2} + \alpha^2 \right) \right. \\
& \quad \left. - (RePr)^{-1} \left(\frac{d^2 k}{dT^2} \left(\frac{dT}{dr} \right) + \frac{dk}{dT} \left(\frac{d^2 T}{dr^2} + \frac{1}{r} \frac{dT}{dr} \right) \right) \right. \\
& \quad \left. - (\gamma - 1) Ma^2 Re^{-1} \frac{d\mu}{dT} \left(2 \frac{U^2}{r^2} + 2 \left(\frac{dU}{dr} \right)^2 + \left(\frac{dV}{dr} - \frac{V}{r} \right)^2 \right. \right. \\
& \quad \left. \left. + \left(\frac{dW}{dr} \right)^2 \right) - (\gamma - 1) Ma^2 Re^{-1} \frac{d\lambda}{dT} \left(\frac{dU}{dr} + \frac{U}{r} \right)^2 \right] \hat{T} = 0.
\end{aligned}$$

A.1.4 Boundary conditions

In order to solve the system of linearized equations established in equations (A.22) through (A.24) appropriate boundary conditions are to be imposed. In order to avoid to impose artificial pressure boundary conditions we rely on a staggered grid to discretize the equations. As we will see in the following section in more detail we only impose boundary conditions on the velocities and the temperature which are represented on a grid employing the boundary points. The pressure boundary condition is only implicitly fulfilled through the linearized continuity equation which is solved on a set of staggered grid points which does not include the two boundary points.

For a well-posed problem the staggered representation of the system of linearized equations (i.e. (A.22) through (A.24)) is subject to eight boundary conditions. We follow Khorrami (1995) and impose decaying disturbances at the far-field boundary. In other words, as $r \rightarrow \infty$ all disturbance amplitudes are required to vanish

$$r \rightarrow \infty : \quad \hat{u} = \hat{v} = \hat{w} = \hat{T} = 0 . \quad (\text{A.25})$$

Due to the symmetry constraints around the pole $r = 0$ the boundary conditions depend on the azimuthal wavenumber $|n|$ (where the magnitude of the wavenumber denotes again the right- and left-turning mode $|n| = \pm n$). For $n = 0$ we impose

$$\begin{aligned} \frac{d\hat{w}}{dr} = \frac{d\hat{T}}{dr} = 0 \\ \hat{u} = \hat{v} = 0 \end{aligned} \quad (\text{A.26a})$$

for $n = 1$

$$\begin{aligned} \hat{w} = \hat{T} = 0 \\ \frac{d\hat{u}}{dr} = 0 \\ \hat{u} \pm i\hat{v} = 0 \end{aligned} \quad (\text{A.26b})$$

and for modes $|n| > 1$

$$\hat{u} = \hat{v} = \hat{w} = \hat{T} = 0 . \quad (\text{A.26c})$$

A.1.5 Matrix notation of equations

If the temporal stability problem is to be investigated the spatial and azimuthal wavenumber α and n in equation (A.21) are real whereas ω is the complex angular frequency

$$\omega = \omega_r + i\omega_i,$$

which we wish to isolate. Equations (A.22) through (A.24) can be written in the following matrix notation for the temporal problem (superscript t)

$$[\mathbf{A}^t \mathbf{D}^2 + \mathbf{B}^t \mathbf{D} + \mathbf{C}^t] \hat{\mathbf{u}} = \omega \mathbf{E}^t \hat{\mathbf{u}}. \quad (\text{A.27})$$

Here, \mathbf{D} denotes the differential operator $\mathbf{D} = \frac{d}{dr}$, $\mathbf{D}^2 = \frac{d^2}{dr^2}$ the second derivative and $\hat{\mathbf{u}}$ is given as

$$\hat{\mathbf{u}} = [\hat{u}, \hat{v}, \hat{w}, \hat{p}, \hat{T}]^T. \quad (\text{A.28})$$

The non-zero coefficients of matrices \mathbf{A}^t , \mathbf{B}^t , \mathbf{C}^t and \mathbf{E}^t can readily be extracted from the above equations and for brevity is only exemplified for the vectors of the first rows ($i = 1$; $j = 1, \dots, 5$) of the matrices (the first rows correspond to the linearized continuity equation):

$$\begin{aligned} A_{1j}^t &= (0, 0, 0, 0, 0) \\ B_{1j}^t &= \left(1, 0, 0, \frac{U}{p}, -\frac{U}{T}\right) \\ C_{11}^t &= \frac{1}{p} \frac{dp}{dr} - \frac{1}{T} \frac{dT}{dr} + \frac{1}{r} \\ C_{12}^t &= \frac{in}{r} \\ C_{13}^t &= i\alpha \\ C_{14}^t &= \frac{1}{p} \left\{ -\frac{U}{T} \frac{dT}{dr} + \frac{dU}{dr} + \frac{U}{r} + i \left(\alpha W + n \frac{V}{r} \right) \right\} \\ C_{15}^t &= \frac{1}{T} \left\{ \frac{2U}{T} \frac{dT}{dr} - \frac{dU}{dr} - \frac{U}{r} - \frac{U}{p} \frac{dp}{dr} - i \left(\alpha W + n \frac{V}{r} \right) \right\} \\ E_{1j}^t &= \left(0, 0, 0, \frac{i}{p}, -\frac{i}{T}\right) \end{aligned} \quad (\text{A.29})$$

In contrast to this, when investigating base flows with respect to their spatial stability properties, the angular frequency ω and the azimuthal

wavenumber n are real whereas the axial wavenumber is now complex

$$\alpha = \alpha_r + i\alpha_i .$$

However, in order to arrive at a similar matrix notation of the spatial eigenvalue problem a more elaborate way has to be taken. Due to the viscous terms the momentum and energy equations contain quadratic expressions of the axial wavenumber α we wish to isolate. We therefore introduce a transformation of the form

$$\bar{q} = \alpha \hat{q} , \tag{A.30}$$

where q is used for the three velocities (u, v, w) and the temperature. Note that the overbar denotes here the transformed variable and not a base-flow quantity. For details concerning the motivation and the validity we refer to the work of Khorrami & Malik (1993). Using this transformation we can now establish the global spatial eigenvalue problem (superscript s)

$$[\mathbf{A}^s \mathbf{D}^2 + \mathbf{B}^s \mathbf{D} + \mathbf{C}^s] \hat{\mathbf{u}} = \alpha \mathbf{E}^s \hat{\mathbf{u}} \tag{A.31}$$

for the modified eigenvector

$$\hat{\mathbf{u}} = \left[\hat{u}, \hat{v}, \hat{w}, \hat{p}, \hat{T}, \bar{u}, \bar{v}, \bar{w}, \bar{T} \right]^T . \tag{A.32}$$

The transformation given by equation (A.30) can be applied in a straightforward manner. Thus we again restrict this documentation to the vectors of the first rows of each coefficient matrix of the spatial eigenvalue problem, i.e., $(i = 1; j = 1, \dots, 9)$, corresponding to the continuity

equation for which no nonlinear wavenumber α occurs:

$$\begin{aligned}
 A_{1j}^s &= (0, 0, 0, 0, 0, 0, 0, 0, 0) \\
 B_{1j}^s &= (1, 0, 0, \frac{U}{p}, -\frac{U}{T}, 0, 0, 0, 0) \\
 C_{11}^s &= \frac{1}{p} \frac{dp}{dr} - \frac{1}{T} \frac{dT}{dr} + \frac{1}{r} \\
 C_{12}^s &= \frac{in}{r} \\
 C_{13}^s &= 0 \\
 C_{14}^s &= \frac{1}{p} \left\{ -\frac{U}{T} \frac{dT}{dr} + \frac{dU}{dr} + \frac{U}{r} + i \left(n \frac{V}{r} - \omega \right) \right\} \\
 C_{15}^s &= \frac{1}{T} \left\{ \frac{2U}{T} \frac{dT}{dr} - \frac{dU}{dr} - \frac{U}{r} - \frac{U}{p} \frac{dp}{dr} - i \left(n \frac{V}{r} \right) - \omega \right\} \\
 C_{16}^s &= C_{17}^s = C_{18}^s = C_{19}^s = 0 \\
 E_{1j}^s &= (0, 0, -i\alpha, -\frac{i\alpha W}{p}, \frac{i\alpha W}{T}, 0, 0, 0, 0) .
 \end{aligned} \tag{A.33}$$

Note that the same number of boundary conditions (corresponding to equations (A.25) through (A.26c)) are sufficient to solve the spatial eigenvalue problem.

A.2 Discretization on Gauss-Lobatto and Gauss points

The discretization used for the solution of the linearized system of equations is based on a Chebyshev collocation method. The velocities and the temperature are represented on Gauss-Lobatto points given by

$$\xi_j = \cos \left(\frac{j\pi}{N} \right), \quad j = 0, \dots, N, \tag{A.34}$$

whereas pressure is defined on a staggered grid of Gauss points defined by

$$\xi_{j+1/2} = \cos \left(\frac{(2j+1)\pi}{2N} \right), \quad j = 0, \dots, N-1. \tag{A.35}$$

Following Canuto *et al.* (1988) or Peyret (2002) the derivatives at any Chebyshev collocation point can be represented in matrix form, however, due to the representation of the momentum and energy equations

on Gauss-Lobatto points and the continuity equation on Gauss points different differential operators need to be defined. In addition, interpolating matrices become necessary to interpolate between the two sets of grid points.

For a variable q at the collocation points defined by equation (A.34) we have $q^{(p)}(\xi_j) = \Sigma_j D_{ij}^{(p)} q(\xi_j)$. The coefficients of the first-order derivative matrix $D_{ij}^{(1)}$ are given by

$$\begin{aligned} D_{ij}^{(1)} &= \frac{c_i (-1)^{i+j}}{c_j \xi_i - \xi_j}, & 0 \leq i, j \leq N, i \neq j \\ D_{ii}^{(1)} &= -\frac{\xi_i}{2(1 - \xi_i^2)}, & 1 \leq i \leq N - 1 \\ D_{00}^{(1)} &= -D_{NN}^{(1)} = \frac{2N^2 + 1}{6}, \end{aligned} \tag{A.36}$$

where $c_0 = c_N = 2$, $c_i = 1$ for $1 \leq i \leq N - 1$. We note that Peyret (2002) also gives an explicit expression for the second-order derivative matrix, however, within the current work we employ the matrix multiplication of D to obtain $D_{ij}^{(2)} = \Sigma_{k=0}^N D_{ik}^{(1)} D_{ik}^{(1)}$.

The derivatives $q^{(p)}(\xi_{j+1/2})$ on the staggered Gauss points are calculated in the following manner: First the function values are interpolated with a interpolation matrix (to be defined), successively differentiated on the Gauss-Lobatto points by the operator defined in equation (A.36) and afterwards extrapolated back onto the Gauss points.

As in the work of Khorrami (1991) we employ two interpolating matrices to alternate between the staggered Gauss and the non-staggered Gauss-Lobatto points which for completeness are given here. The interpolation matrix from non-staggered to staggered grid the takes the form

$$M_{ij} = \frac{(-1)^{i+j} \left(1 - \xi_{j+1/2}^2\right)^{1/2}}{N (\xi_i - \xi_{j+1/2})}, \quad \begin{array}{l} i = 0, \dots, N; \\ j = 0, \dots, N - 1 \end{array} \tag{A.37}$$

The inverse interpolation is given by

$$M_{ij}^* = \frac{(-1)^{i+j+1} \left(1 - \xi_{i+1/2}^2\right)^{1/2}}{c_j N (\xi_{i+1/2} - \xi_j)}, \quad \begin{array}{l} i = 0, \dots, N - 1; \\ j = 0, \dots, N \end{array} \tag{A.38}$$

where c_j is again defined as $c_0 = c_N = 2$, $c_j = 1$ for $1 \leq j \leq N - 1$. In order for \mathbf{M} and \mathbf{M}^* to be square matrices an extra row ($i = N$) and an extra column ($j = N$) of zero elements is added.

In order to satisfy the boundary conditions at infinity a mapping from the Chebyshev interval $[-1, 1]$ to the physical domain $[0, r_{\max}]$ is necessary. In addition, steep gradients of the base-flow profile and the corresponding eigenfunctions are to be accurately resolved. Bayliss & Turkel (1992) propose a two-parameter mapping which has been adapted for the current problem

$$r(\xi) = \left(1 - \xi_c - \frac{\tan((\xi - \tau_1)\tau_2)}{s_1} \right) \frac{r_{\max}}{2}, \quad (\text{A.39})$$

where $\xi_c = 1 - 2r_c/r_{\max}$ and

$$\begin{aligned} \tau_1 &= \frac{\tau_0 - 1}{\tau_0 + 1} \\ \tau_2 &= \frac{\tan^{-1}(s_1(1 - \xi_c))}{1 - \tau_1} \\ \tau_0 &= \frac{\tan^{-1}(s_1(1 + \xi_c))}{\tan^{-1}(s_1(1 - \xi_c))}. \end{aligned} \quad (\text{A.40})$$

The parameter r_c determines the radial location where the grid is to be refined and s_1 controls the degree of grid refinement.

Case	N	r_c/r_0	r_{\max}/r_0	s_1
A	150	0.9	20	5.0
B	350	1.0	5	18.0
LES	292	1.0	20	45.0

Table A.1: Number of Chebyshev collocation points N and grid stretching parameters for validation cases A, B and eigenfunctions employed for all LES cases.

A.3 Determination of disturbances in conservative variables

The linear disturbances are given in primitive variables, i.e., the cylindrical velocities u , v , w , pressure p and temperature T . In contrast,

the LES code solves for the vector of conservative variables given by $\mathbf{Q} = (\rho, \rho u_1, \rho u_2, \rho u_3, E)^T$ (in case of ADM-RT, see section 2.2). Hence, the corresponding conservative variables need to be calculated in order to impose these linear disturbances at the inflow.

The vector of the disturbances \mathbf{Q}' , as introduced in equation (2.35), is determined as follows

$$\mathbf{Q}' = (\tilde{\rho}, \tilde{\rho}\tilde{u}_1 + \tilde{\rho}\bar{U}_1, \tilde{\rho}\tilde{u}_2 + \tilde{\rho}\bar{U}_2, \tilde{\rho}\tilde{u}_3 + \tilde{\rho}\bar{U}_3, \tilde{E})^T, \quad (\text{A.41})$$

where for clarity the notation introduced in equation (A.13) is employed. The density perturbation is determined using the linearized equation of state introduced in equation (A.14). Note that equation (A.41) employs the Cartesian velocity components which are related to the cylindrical components employed in the stability solver (for both disturbances and base-flow components) through the rotation matrix

$$\begin{bmatrix} u_1 \\ u_2 \\ u_3 \end{bmatrix} = \begin{bmatrix} \cos \theta & -\sin \theta & 0 \\ 0 & 0 & 1 \\ -\sin \theta & -\cos \theta & 0 \end{bmatrix} \begin{bmatrix} u \\ v \\ w \end{bmatrix}. \quad (\text{A.42})$$

The linear disturbance of the total energy \tilde{E} is determined according to

$$\begin{aligned} \tilde{E} &= \frac{\tilde{p}}{\gamma - 1} + \frac{1}{2}\tilde{\rho}(\bar{U}_1\tilde{u}_1 + \bar{U}_2\tilde{u}_2 + \bar{U}_3\tilde{u}_3) \\ &\quad + \frac{1}{2}\tilde{\rho}(\bar{U}_1^2 + \bar{U}_2^2 + \bar{U}_3^2). \end{aligned} \quad (\text{A.43})$$

Appendix B

Implementation details of sponge technique

For completeness, the details of the implementation of the sponge which imposes the inflow profile together with the excited disturbances and the sponges which maintain the quiescent surrounding of the computational domain are given here.

B.1 Inflow sponge

As pointed out in section 2.5.2 (also see Fig. 2.6) the disturbances introduced at the inflow are locally confined to the so-called *inflow sponge*. Its spatial extent is given by a combination of an exponential decay in radial direction combined with a Gaussian-shaped profile in downstream direction. This local confinement enables entrainment of the surrounding fluid. The functional form of this inflow sponge is given by

$$\sigma_{\text{infl}}(r, z) = \begin{cases} A_{\text{spg, infl}} [f(r) \cdot g(z)] & : z > z_{0, \text{infl}} \\ A_{\text{spg, infl}} [f(r) \cdot g(z_{0, \text{infl}})] & : 0 \leq z \leq z_{0, \text{infl}} \end{cases}, \quad (\text{B.1})$$

where the inflow-sponge amplitude $A_{\text{spg, infl}} = 1.0$ and $f(r)$ and $g(z)$ are the radial and streamwise distribution given by

$$f(r) = (1 + (\exp\{r^2 \log(r_c/r_0)\} - 1)^{n_r})^{-1} \quad (\text{B.2})$$

$$g(z) = \exp\left\{-\left(\frac{z - z_{c, \text{infl}}}{d_{z_{\text{infl}}}}\right)^2\right\}. \quad (\text{B.3})$$

In equation (B.1) we set $z_{0, \text{infl}} = 0.6r_0$ which shifts the starting point of the one-sided Gaussian decay into the domain to have a short entrance region of constant sponge amplitude. Thus, for $z \leq z_{0, \text{infl}}$, the sponge strength is set to $\sigma_{\text{infl}}(r, z) = \sigma_{\text{infl}}(r, z_{0, \text{infl}})$. The parameters determining the radial decay in equation (B.2) are chosen as $r_c = 1.3r_0$ and $n_r = 7.0$. The parameters of the Gaussian profile in equation (B.3) are set to $z_{c, \text{infl}} = 0.3r_0$ and $d_{z_{\text{infl}}} = 0.4r_0$. In Fig. B.1(a) the radial dependence for this set of parameters is shown, whereas in Fig. B.1 (b) the streamwise profile is plotted. In Fig. B.2 the sponge amplitude for the inflow plane is visualized as a three-dimensional surface in the r - z -plane.

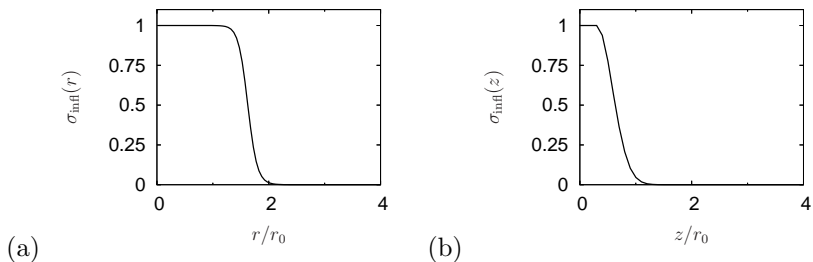


Figure B.1: Inflow sponge strength distribution represented on discrete computational grid: (a) $\sigma_{\text{infl}}(r, z = 0)$ in radial direction for $z = 0$ and (b) $\sigma_{\text{infl}}(r \approx 0, z)$ in streamwise direction for first radial grid line $r = r_{\text{min}}$.

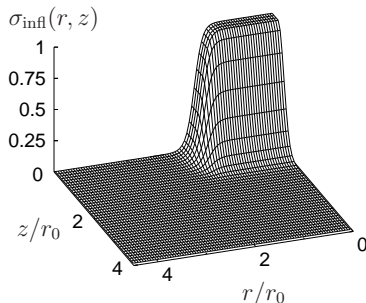


Figure B.2: Inflow sponge strength distribution represented on discrete computational grid in perspective view upstream: $\sigma_{\text{infl}}(r, z)$ within vicinity of inflow region.

In the inflow region this sponge is active, i.e., before the time advancement the conservative vector \mathbf{Q} is driven to the reference state \mathbf{Q}_{infl} . As described before (see section 2.5.5), \mathbf{Q}_{infl} is based on a collection of instability waves that are superimposed on the laminar inflow profile (see equation (2.35)). At each sub-step of the Runge-Kutta integration the amplitude A_n and phase ϕ_n of each azimuthal modes n is modified. We employ a similar random walk process as described by Lui (2003) but here, in addition to the phase, also modify the forcing amplitude. Therefore, random numbers rnd_1 and rnd_2 in the interval $\text{rnd} \in (0, 1)$ are determined (using the random number generator described by Press *et al.* (1992), p. 272). Depending on the value of rnd_i , the amplitude and

Table B.1: Description of random walk process with parameter bounds for rnd_1 and rnd_2 .

Change by Δ	range for A_n	range for ϕ_n
increase	$0.00 < rnd_1 < 0.55$	$0.00 < rnd_2 < 0.65$
no change	–	$0.65 \leq rnd_2 \leq 0.85$
decrease	$0.55 \leq rnd_1 < 1.0$	$0.85 < rnd_2 < 1.0$

Table B.2: Amount of change Δ used for inflow randomization of amplitude A_n and phase ϕ_n and lower and upper bounds of amplitude A_n .

Quantity	Δ per time step	min	max
A_n	0.005	0.03	0.10
ϕ_n	$0.1\omega_n\Delta t$	–	–

the phase are varied in a random walk process described in Table B.1, i.e. increased or decreased by certain amounts Δ which are tabulated in Table B.2. The combination of the chosen parameters results in a random distribution within the defined amplitude bounds, whereas the phase relations between various modes is continuously varied and according to the chosen values mostly increasing. Note that the amplitude of each mode n is nonzero at all times as $A_n \in [0.03; 0.10]$ and that the maximum change per integration sub-step is restricted to $\Delta = 0.005$ (see Table B.2). For clarity this is exemplified by looking at the azimuthal wavenumber $n = \pm 4$ only. In Fig. B.3(a) the temporal randomization of the disturbance amplitude A_n for azimuthal wavenumbers $n = \pm 4$ is shown along with the corresponding development of the phase shift ϕ_n in Fig. B.3(b). The amplitude values for the full Runge-Kutta time steps (six-stage Runge-Kutta scheme) are marked by symbols. All modal excitation amplitudes A_n are initialized using $A_n = \min(A_n) + \Delta A_n = 0.035$ before starting the random walk process, but from thereon are independent of each other, as can be seen in Fig. B.3(a).

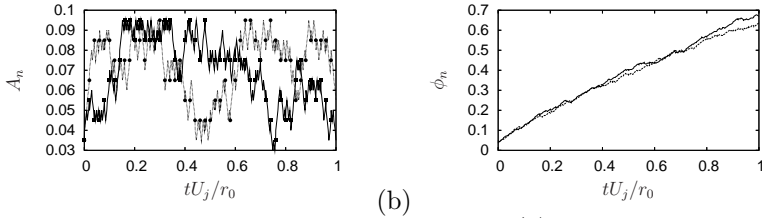


Figure B.3: Randomization of inflow disturbances: (a) disturbance amplitude A_n and (b) phase shift ϕ_n for azimuthal wavenumbers $n = \pm 4$. $n = 4$: — and \blacksquare ; $n = -4$ - - - - and \bullet .

B.2 Sponge preserving ambient-state and outflow damping

As described in section 2.5.2, a drift of the mean pressure is prevented by employing a surrounding sponge layer that we refer to as *ambient sponge*. Similarly, to the inflow, the sponge drives the conservative state vector \mathbf{Q} to a state that corresponds to ambient fluid at rest. However, in order not to prevent surrounding fluid from being entrained, only the density and energy (and thereby pressure) are acted on. The spatial extent of the sponge layer is given by a combination of two error functions described by

$$\sigma_{\text{spg,amb}} = A_{\text{spg,amb}} [\sigma_r (1 - \sigma_z) + \sigma_z \cdot (1 - f(r))], \quad (\text{B.4})$$

where $A_{\text{spg,amb}}$ is set to $A_{\text{spg,amb}} = 0.25$. The functions σ for the radial and axial direction, respectively, are given by the expressions

$$\sigma_r = \frac{1}{2} \left[1 - \text{erf} \left\{ \beta_r \left(-r + \left(r_{\text{max}} - \frac{W_r}{2} \right) \right) \right\} \right] \quad (\text{B.5})$$

$$\sigma_z = \frac{1}{2} \left[1 - \text{erf} \left\{ \beta_z \left(z - \frac{W_z}{2} \right) \right\} \right]. \quad (\text{B.6})$$

Here β_i denote the coefficients to adapt the steepness of the profile and W_i the corresponding spatial extents of the sponge layer, where the subscripts r and z denote the radial and axial direction and the index 1 is used for the inflow region in z -direction. The algebraic formulation is as proposed by Bodony *et al.* (Bodony & Lele, 2005; Bodony, 2006). Similarly as the inflow sponge region is radially confined by $f(r)$ defined in equation (B.2), the ambient sponge sets in outside the inflow sponge by using again $f(r)$. The spatial distribution of the ambient sponge in the vicinity of the inflow region can be seen in Fig. B.4. Fig. B.5 shows

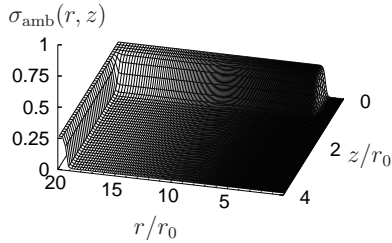


Figure B.4: Ambient sponge strength distribution in a perspective view upstream: $\sigma_{amb}(r, z)$ in the inflow region.

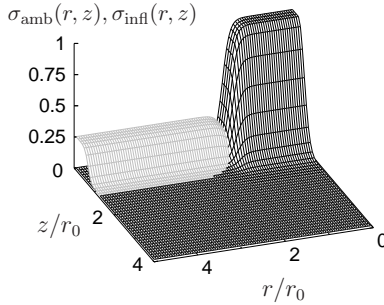


Figure B.5: Sponge amplitude distributions in vicinity of jet entrance: inflow sponge given in black, ambient sponge given in grey.

the *inflow sponge* and the *ambient sponge* in the jet entrance region.

The *outflow sponge* is defined similarly to the streamwise part of the *ambient sponge*:

$$\sigma_{out} = \frac{A_{spg,out}}{2} \left[1 - \operatorname{erf} \left\{ \beta_{out} \left(-z + \left(z_{max} - \frac{W_{out}}{2} \right) \right) \right\} \right] \quad (\text{B.7})$$

Here, $A_{spg,out} = 1$ and denotes the amplitude at the outflow, β_{out} again is the coefficient to adapt the steepness of the profile and W_{out} the corresponding spatial extent of the sponge layer. All parameters employed within the sponges are listed in table B.3.

Table B.3: Parameters for inflow, ambient and outflow sponge.

	inflow _{infl}	ambient _{amb}	outflow _{out}
A_i	1.0	0.25	1.0
β_i		$\beta_r = \beta_z = 5.5$	0.5
W_i		$W_r = 1.2; W_z = 1.25$	8.0
r_{\max}		L_r/r_0	
z_{\max}			L_z/r_0

Appendix C

Phase-speed and grid anisotropy effects

The effect of the phase speed anisotropy of the employed compact schemes is briefly discussed. Also, the effect of the different mesh spacings in different coordinate directions is taken into account.

The grid Strouhal numbers quoted in the section 2.9 are estimates since the determination is based on the assumption of perfectly aligned waves. Determining the exact obtainable frequency for the system (discretization, order-reduction due to boundary closure, effect of sponges on propagating waves, etc) is very complex and the given values are to serve as estimates only. Oblique waves have a less restrictive grid Strouhal number St^g due to anisotropy. For instance, we restrict the discussion to a r - θ plane and find in figure C.1 the polar plot of the two-dimensional phase speed anisotropy for the first derivative approximation using tenth-order compact finite differences (for further details see Lele, 1992). Note that the phase speed is plotted for different nondimensional wavenumbers $k\Delta s/\pi = 1/10, 2/10, \dots, 10/10$ assuming equidistant mesh spacings in radial and axial directions (r and z) and α is the angle between the propagation direction and the downstream positive z axis. From this figure we find that small wavenumbers are well resolved and the phase speed is very close to unity, whereas the innermost curves are the shortest waves that are resolved on the mesh. Note in particular that least errors are found along angles of 45 degrees.

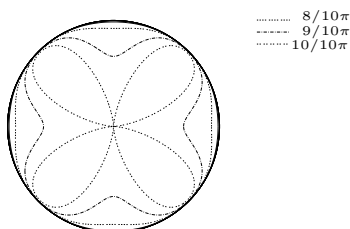


Figure C.1: Polar plot of phase speed anisotropy for first derivative approximation using tenth-order compact scheme (Lele, 1992). Phase speeds are plotted for wavenumbers $k\Delta s/\pi = 1/10, 2/10, \dots, 10/10$.

The above arguments hold for equidistant grid spacings. As shown in sections 2.6 and 3.1.1, we employ a grid with different spacings in the radial and axial directions (as our azimuthal discretization employs

a Fourier spectral method we restrict ourselves again to a r - z plane). The unequal grid spacing in the different coordinate directions obviously influences the phase speed at propagation angles near $\pm\pi/2$ (here measured from the downstream z axis or radial r axis) and does not affect perfectly aligned waves. The phase speed anisotropy for unequal grid spacing (Colonius & Lele, 2004) is given by

$$c_{\text{ph,num}} = \frac{\cos(\alpha)k_{\text{mod}}(k \cos(\alpha)) + \rho \sin(\alpha)k_{\text{mod}}(k \sin(\alpha)/\rho)}{k}, \quad (\text{C.1})$$

where $c_{\text{ph,num}} = c_{\text{ph,num}}(k, \alpha, \rho)$ is the computed phase speed and k_{mod} is the modified wavenumber of the tenth-order compact finite-difference scheme. For the moment, let ρ be the ratio of the grid spacing along the grid line to the grid spacing in perpendicular direction. For differentiation with respect to z we set $\rho = \tilde{\rho} = \Delta z / \Delta r$, for differentiation with respect to r we set $\rho = \tilde{\tilde{\rho}} = \Delta r / \Delta z$. For grid ratios smaller than unity (i.e. a relative increase of the perpendicular grid spacing) the anisotropy for waves perpendicular to the grid line becomes worse.

For the three observer locations in the acoustic near-field at $\phi = 30^\circ, 60^\circ$ and 90° the grid ratios are $\tilde{\rho} = 1.25, 0.59, 0.42$ and $\tilde{\tilde{\rho}} = 0.8, 1.7, 2.4$, respectively. Using equation (C.1) the polar plots of the phase speed for the three observer locations are determined and shown in figures C.2 - C.4.

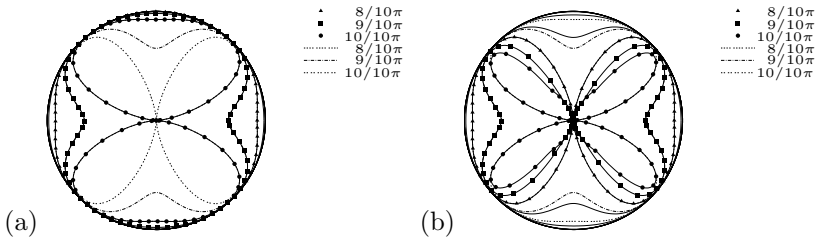


Figure C.2: Polar plot of phase speed anisotropy for first derivative approximation at observer location $\phi = 30^\circ$ using tenth-order compact scheme (Lele, 1992). Phase speeds are plotted for wavenumbers $k\Delta s/\pi = 1/10, 2/10, \dots, 10/10$ for a non-equidistant grid with ratio (a) $\tilde{\rho} = 1.25$ and (b) $\tilde{\tilde{\rho}} = 0.8$. The isovales $k\Delta s/\pi = 8/10, 9/10, 10/10$ are highlighted by symbols (dashed lines of equidistant grid spacing for comparison).

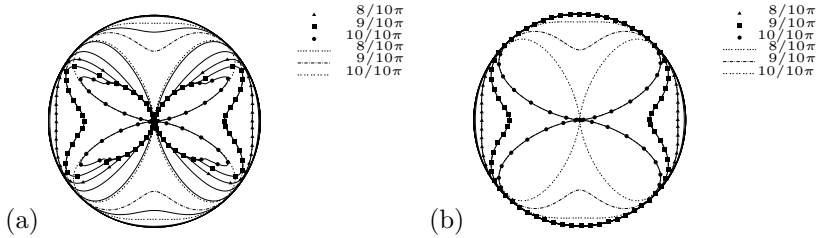


Figure C.3: Polar plot of phase speed anisotropy for first derivative approximation at observer location $\phi = 60^\circ$ using tenth-order compact scheme (Lele, 1992). Phase speeds are plotted for wavenumbers $k\Delta s/\pi = 1/10, 2/10, \dots, 10/10$ for a non-equidistant grid with ratio (a) $\tilde{\rho} = 0.59$ and (b) $\tilde{\rho} = 1.7$. The isovalues $k\Delta s/\pi = 8/10, 9/10, 10/10$ are highlighted by symbols (dashed lines of equidistant grid spacing for comparison).

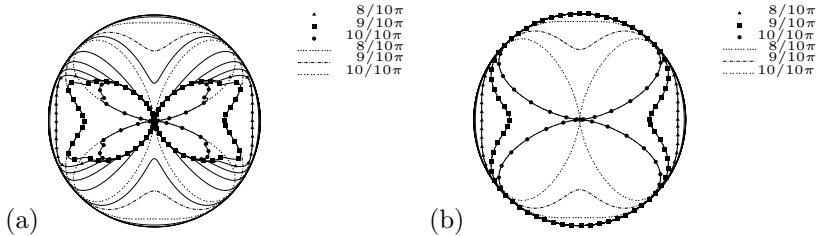


Figure C.4: Polar plot of phase speed anisotropy for first derivative approximation at observer location $\phi = 90^\circ$ using tenth-order compact scheme (Lele, 1992). Phase speeds are plotted for wavenumbers $k\Delta s/\pi = 1/10, 2/10, \dots, 10/10$ for a non-equidistant grid with ratio (a) $\tilde{\rho} = 0.42$ and (b) $\tilde{\rho} = 2.4$. The isovalues $k\Delta s/\pi = 8/10, 9/10, 10/10$ are highlighted by symbols and for comparison are given in dashed lines for a equidistant grid spacing.

From this we find three relevant locations with $\rho < 1$ shown in figures C.2 (b) ($\partial/\partial r$, down-/upstream propagating) and C.3 (a) and C.4 (a) ($\partial/\partial z$, radially propagating). Significant phase speed anisotropy is found for the radially most distant location only ($\phi = 90^\circ$, $r = 18r_0$). Here, (see figure C.4 (a)) waves at $\alpha = \pi/2$ to the downstream axis z are propagated anisotropically and only wavenumbers $k\Delta s < 4/10\pi$

are propagated isotropically. Hence, the effective cutoff frequency of the grid is lower compared to the estimate. Note that the relaxation-term subgrid model is employed and hence the anisotropic phase propagation of high wavenumbers is of minor relevance for the LES.

Bibliography

- ADAMS, N. A. 1993 Numerische Simulation von Transitionsmechanismen in kompressiblen Grenzschichten. PhD thesis, Technische Universität München.
- ADAMS, N. A. 2000 Direct simulation of the turbulent boundary layer along a compression ramp at $M = 3$ and $Re_\theta = 1685$. *J. Fluid Mech.* **420**, 47–83.
- AIRBUS S.A.S. 2007 *Global Market Forecast 2007–2026*. http://www.airbus.com/fileadmin/documents/gmf/PDF_dl/00-all-gmf_2007.pdf.
- ANDERSON, J. L., PREISER, S. & RUBIN, E. L. 1968 Conservation form of the equations of hydrodynamics in curvilinear coordinate systems. *J. Comput. Phys.* **2**, 279–287.
- ANDERSSON, N., ERIKSSON, L.-E. & DAVIDSON, L. 2005a Effects of inflow conditions and subgrid model on LES for turbulent jets. In *11th AIAA/CEAS Aeroacoustics Conference & Exhibit, AIAA Paper 2005-2925*. Monterey, CA.
- ANDERSSON, N., ERIKSSON, L.-E. & DAVIDSON, L. 2005b Investigation of an isothermal Mach 0.75 jet and its radiated sound using large-eddy simulation and Kirchhoff surface integration. *Int. J. Heat Fluid Flow* **26**, 393–410.
- ARAKERI, V. H., KROTHAPALLI, A., SIDDAVARAM, V., ALKISLAR, M. B. & LOURENCOA, L. M. 2003 On the use of microjets to suppress turbulence in a Mach 0.9 axisymmetric jet. *J. Fluid Mech.* **490**, 75–98.
- ARNDT, R. E. A., LONG, D. F. & GLAUSER, M. N. 1997 The proper orthogonal decomposition of pressure fluctuations surrounding a turbulent jet. *J. Fluid Mech.* **340**, 1–33.
- BAILLY, C. & BOGEY, C. 2006 Current understanding of jet noise-generation mechanisms from compressible large-eddy-simulations. In *Direct and Large-Eddy Simulation VI*, pp. 1–10.

- BARRÉ, S. 2006 Étude numérique et expérimentale du bruit aérodynamique avec application aux jets ronds subsoniques. PhD thesis, École Centrale de Lyon.
- BARRÉ, S., BOGEY, C. & BAILLY, C. 2006 Computation of the noise radiated by jets with laminar/turbulent nozzle-exit conditions. In *12th AIAA/CEAS Aeroacoustics Conference and Exhibit, AIAA Paper 2006-2443*. Cambridge, MA.
- BAYLISS, A., CLASS, A. & MATKOWSKY, B. J. 1995 Adaptive approximation of solutions to problems with multiple layers by Chebyshev pseudo-spectral methods. *J. Comput. Phys.* **116**, 160–172.
- BAYLISS, A. & TURKEL, E. 1992 Mappings and accuracy for Chebyshev pseudo-spectral approximations. *J. Comput. Phys.* **102**, 349–359.
- BECHERT, D. & PFIZENMAIER, E. 1975 On the amplification of broad band jet noise by a pure tone excitation. *J. Sound Vibration* **43** (3), 581–587.
- BERLAND, J., BOGEY, C. & BAILLY, C. 2006 Low-dissipation and low-dispersion fourth-order Runge–Kutta algorithm. *Comput. Fluids* **35**, 1459–1463.
- BODONY, D. J. 2004 Aeroacoustic prediction of turbulent free shear flows. PhD thesis, Stanford University.
- BODONY, D. J. 2006 Analysis of sponge zones for computational fluid mechanics. *J. Comput. Phys.* **212**, 681–702.
- BODONY, D. J. & LELE, S. K. 2002 Large eddy simulation of turbulent jets and progress towards a subgrid scale noise model. In *Proceedings of International Workshop on “LES for Acoustics”* (ed. T. Hüttl, C. Wagner & J. Delfs). DLR, Göttingen, Germany.
- BODONY, D. J. & LELE, S. K. 2004 Jet noise prediction of cold and hot subsonic jets using large-eddy simulation. In *10th AIAA/CEAS Aeroacoustics Conference & Exhibit, AIAA Paper 2004-3022*. Manchester.
- BODONY, D. J. & LELE, S. K. 2005 On using large-eddy simulation for the prediction of noise from cold and heated turbulent jets. *Phys. Fluids* **17** (085103).

- BODONY, D. J. & LELE, S. K. 2008 Current status of jet noise predictions using large-eddy simulation. *AIAA J.* **46** (2), 364–380.
- BOERSMA, B. J. & LELE, S. K. 1999 Large eddy simulation of compressible turbulent jets. In *Annual Research Briefs*. Center for Turbulence Research, Stanford University and NASA - Ames Research Center.
- BOGEY, C. & BAILLY, C. 2005*a* Decrease of the effective Reynolds number with eddy-viscosity subgrid-scale modeling. *AIAA J.* **43**, 437–439.
- BOGEY, C. & BAILLY, C. 2005*b* Effects of inflow conditions and forcing on subsonic jet flows and noise. *AIAA J.* **43** (5), 1000–1007.
- BOGEY, C. & BAILLY, C. 2006*a* Computation of a high Reynolds number jet and its radiated noise using large eddy simulation based on explicit filtering. *Comput. Fluids* **35**, 1344–1358.
- BOGEY, C. & BAILLY, C. 2006*b* Investigation of downstream and sideline subsonic jet noise using Large Eddy Simulation. *Theoret. Comput. Fluid Dynamics* **20** (1), 23–40.
- BOGEY, C. & BAILLY, C. 2006*c* Large eddy simulations of transitional round jets: Influence of the Reynolds number on flow development and energy dissipation. *Phys. Fluids* **18** (065101).
- BOGEY, C. & BAILLY, C. 2007 An analysis of the correlations between the turbulent flow and the sound pressure fields of subsonic jets. *J. Fluid Mech.* **583**, 71–97.
- BOGEY, C., BAILLY, C. & JUVÉ, D. 2000 Numerical simulation of sound generated by vortex pairing in a mixing layer. *AIAA J.* **38** (12), 2210–2218.
- BOGEY, C., BAILLY, C. & JUVÉ, D. 2003 Noise investigation of a high subsonic, moderate Reynolds number jet using a compressible large eddy simulation. *Theoret. Comput. Fluid Dynamics* **16**, 273–297.
- BOGEY, C., BARRÉ, S. & BAILLY, C. 2007*a* Direct computation of the noise generated by a hot coaxial jet. In *13th AIAA/CEAS Aeroacoustics Conference and Exhibit, AIAA Paper 2007-3587*. Rome.

- BOGEY, C., BARRÉ, S., FLEURY, V., BAILLY, C. & JUVÉ, D. 2007b Experimental study of the spectral properties of near-field and far-field jet noise. *Int. J. of Aeroacoustics* **6** (2), 73–92.
- BROWN, C. A. 2005 Acoustics of excited jets - a historical perspective. Technical Memorandum 213889. NASA - Glenn Research Center.
- BROWN, G. L. & ROSHKO, A. 1974 On density effects and large structure in turbulent mixing layers. *J. Fluid Mech.* **64**, 775–816.
- CANUTO, C., HUSSANI, M. Y., QUARTERONI, A. & ZANG, T. A. 1988 *Spectral Methods in Fluid Dynamics*. Springer-Verlag.
- CASTELAIN, T. 2006 Contrôle de jet par microjets impactants. mesure de bruit rayonné et analyse aérodynamique. PhD thesis, École Centrale de Lyon.
- CHEUNG, L. C., BODONY, D. J. & LELE, S. K. 2007 Noise radiation predictions from jet instability waves using a hybrid nonlinear PSE-acoustic analogy approach. In *13th AIAA/CEAS Aeroacoustics Conference and Exhibit, AIAA Paper 2007-3638*. Rome.
- CHEUNG, L. C. & LELE, S. K. 2007 Aeroacoustic noise prediction and the dynamics of shear layers and jets using the nonlinear parabolized stability equations. *Tech. Rep.* TF-103. Flow Physics and Computation Division, Stanford University.
- COHEN, J. & WYGNANSKI, I. 1987 The evolution of instabilities in the axisymmetric jet. Part 2. The flow resulting from the interaction between two waves. *J. Fluid Mech.* **176**, 221–235.
- COLONIUS, T. 2004 Modeling artificial boundary conditions for compressible flow. *Annu. Rev. Fluid Mech.* **36**, 315–345.
- COLONIUS, T. & LELE, S. K. 2004 Computational aeroacoustics: progress on nonlinear problems of sound generation. *Prog. Aerospace Sci.* **40**, 345–416.
- COLONIUS, T., LELE, S. K. & MOIN, P. 1997 Sound generation in a mixing layer. *J. Fluid Mech.* **330**, 375–409.
- CONSTANTINESCU, G. S. & LELE, S. K. 2003 A highly accurate technique for the treatment of flow equations at the polar axis in cylindrical coordinates using series expansions. *J. Comput. Phys.* **184**, 165–186.

- CRIGHTON, D. G. 1981 Acoustics as a branch of fluid mechanics. *J. Fluid Mech.* **106**, 261–298.
- CROW, S. C. & CHAMPAGNE, F. H. 1971 Orderly structure in jet turbulence. *J. Fluid Mech.* **48**, 547–591.
- DARRIGOL, O. 2002 Between hydrodynamics and elasticity theory: the first five births of the Navier-Stokes Equations. *Arch. Hist. Exact Sci.* **56** (2), 95–150.
- FFOWCS WILLIAMS, J. E. 1963 The noise from turbulence convected at high speed. *Phil. Trans. R. Soc. A* **255** (1061), 469–503.
- FFOWCS WILLIAMS, J. E. & HAWKINGS, D. L. 1969 Sound generation by turbulence and surfaces in arbitrary motion. *Phil. Trans. R. Soc. A* **264** (1151), 321–342.
- FREUND, J. B. 2001 Noise sources in a low-Reynolds-number turbulent jet at Mach 0.9. *J. Fluid Mech.* **438**, 277–305.
- FREUND, J. B., MOIN, P. & LELE, S. K. 1997 Compressibility effects in a turbulent annular mixing layer. *Tech. Rep.* TF-72. Flow Physics and Computation Division, Stanford University.
- GOLDSTEIN, M. E. 1984 Aeroacoustics of turbulent shear flows. *Annu. Rev. Fluid Mech.* **16**, 263–285.
- GULLBRAND, J. & CHOW, F. K. 2003 The effect of numerical errors and turbulence models in large-eddy simulations of channel flow, with and without explicit filtering. *J. Fluid Mech.* **495**, 323–341.
- GUTMARK, E. & HO, C.-M. 1983 Preferred modes and the spreading rates of jets. *Phys. Fluids* **26** (10), 2932–2938.
- HANIFI, A., SCHMID, P. J. & HENNINGSON, D. S. 1996 Transient growth in compressible boundary layer flow. *Phys. Fluids* **8** (3), 826–837.
- HU, F. Q., HUSSAINI, M. Y. & MANTHEY, J. L. 1996 Low-dissipation and low-dispersion Runge-Kutta schemes for computational acoustics. *J. Comput. Phys.* **124**, 177–191.
- HUERRE, P. & MONKEWITZ, P. A. 1990 Local and global instabilities in spatially developing flows. *Annu. Rev. Fluid Mech.* **22**, 473–537.

- HUSSAIN, A. K. M. F. 1986 Coherent structures and turbulence. *J. Fluid Mech.* **173**, 303–356.
- HUSSAIN, A. K. M. F. & HASAN, M. A. Z. 1985 Turbulence suppression in free turbulent shear flows under controlled excitation. Part 2. Jet-noise reduction. *J. Fluid Mech.* **150**, 159–168.
- ISRAELI, M. & ORSZAG, S. A. 1981 Approximation of radiation boundary conditions. *J. Comput. Phys.* **41**, 115–135.
- JEONG, J. & HUSSAIN, F. 1995 On the identification of a vortex. *J. Fluid Mech.* **285**, 69–94.
- JORDAN, P. & GERVAIS, Y. 2007 Subsonic jet aeroacoustics: associating experiment, modelling and simulation. *Experiments in Fluids* **44** (1), 1–21.
- JUVÉ, D. & SUNYACH, M. 1981 Near and far field azimuthal correlations for excited jets. In *7th AIAA Aeroacoustics Conference, AIAA Paper 1981-2011*. Palo Alto, CA.
- JUVÉ, D., SUNYACH, M. & COMTE-BELLOT, G. 1979 Filtered azimuthal correlations in the acoustic far field of a subsonic jet. *AIAA J.* **17** (1), 112–113.
- KEIDERLING, F. & KLEISER, L. 2007 Influence of inflow forcing on jet flow and jet noise predicted by LES. In *13th AIAA/CEAS Aeroacoustics Conference and Exhibit, AIAA Paper 2007-3618*. Rome.
- KEIDERLING, F., MÜLLER, S. B. & KLEISER, L. 2004 A high-fidelity numerical method for the simulation of compressible flows in cylindrical geometries. *Proc. Appl. Math. Mech.* **4**, 572–573.
- KHORRAMI, M. R. 1991 A Chebyshev spectral collocation method using a staggered grid for the stability of cylindrical flows. *Int. J. Numer. Methods Fluids* **12**, 825–833.
- KHORRAMI, M. R. 1995 Stability of a compressible axisymmetric swirling jet. *AIAA J.* **33** (4), 650–658.
- KHORRAMI, M. R. & MALIK, M. R. 1993 Efficient computation of spatial eigenvalues for hydrodynamic stability analysis. *J. Comput. Phys.* **104**, 267–272.

- KIM, J. W. & LEE, D. J. 2000 Generalized characteristic boundary conditions for computational aeroacoustics. *AIAA J.* **38** (11), 2040–2049.
- LAU, J. C. 1981 Effects of exit Mach number and temperature on mean-flow and turbulence characteristics in round jets. *J. Fluid Mech.* **105**, 193–218.
- LAU, J. C., MORRIS, P. J. & FISHER, M. J. 1979 Measurements in subsonic and supersonic free jets using a laser velocimeter. *J. Fluid Mech.* **93**, 1–27.
- LAUFER, J. & YEN, T.-C. 1983 Noise generation by a low-Mach-number jet. *J. Fluid Mech.* **134**, 1–31.
- LELE, S. K. 1992 Compact finite difference schemes with spectral-like resolution. *J. Comput. Phys.* **103**, 16–42.
- LELE, S. K. 1997 Computational aeroacoustics: A review. In *35th AIAA Aerospace Sciences Meeting & Exhibit, AIAA Paper 97-0018*. Reno, NV.
- LIGHTHILL, M. J. 1952 On sound generated aerodynamically. I. General theory. In *Proceedings of the Royal Society of London, Series A*, , vol. 211, pp. 564–587.
- LIGHTHILL, M. J. 1954 On sound generated aerodynamically. II. Turbulence as a source of sound. In *Proceedings of the Royal Society of London, Series A*, , vol. 222, pp. 1–32.
- LILLEY, G. M. 1974 On the noise from jets. Noise mechanisms. In *AGARD-CP-131*, pp. 13.1–13.12.
- LILLEY, G. M. 1995 Jet noise classical theory and experiments. In *Aeroacoustics of Flight Vehicles - Theory and Practice, Volume I: Noise Sources* (ed. H. H. Hubbard). NASA - Langley Research Center, Hampton VA.
- LUI, C. & LELE, S. K. 2003 Sound generation mechanism of shock-associated noise. In *9th AIAA/CEAS Aeroacoustics Conference and Exhibit, AIAA Paper 2003-3315*. Hilton Head, SC.
- LUI, C. C. M. 2003 A numerical investigation of shock-associated noise. PhD thesis, Stanford University.

- MAESTRELLO, L. 1976 Two-point correlations of sound pressure in the far field of a jet: experiment. *Tech. Rep.* 72835. NASA - Langley Research Center, Hampton Virginia.
- MEYERS, J., GEURTS, B. J. & BAELMANS, M. 2003 Database analysis of errors in large-eddy simulation. *Phys. Fluids* **15** (9), 2740–2755.
- MICHALKE, A. 1984 Survey on jet instability theory. *Prog. Aerospace Sci.* **21**, 159–199.
- MICHALKE, A. & FUCHS, H. V. 1975 On turbulence and noise of an axisymmetric shear flow. *J. Fluid Mech.* **70**, 179–205.
- MICHALKE, A. & HERMANN, G. 1982 On the inviscid instability of a circular jet with external flow. *J. Fluid Mech.* **114**, 343–359.
- MITCHELL, B. E., LELE, S. K. & MOIN, P. 1999 Direct computation of the sound generated by vortex pairing in an axisymmetric jet. *J. Fluid Mech.* **383**, 113–142.
- MOHSENI, K. & COLONIUS, T. 2000 Numerical treatment of polar coordinate singularities. *J. Comput. Phys.* **157**, 787–795.
- MOLLO-CHRISTENSEN, E., KOLPIN, M. A. & MARTUCELLI, J. R. 1964 Experiments on jet flows and jet noise far-field spectra and directivity patterns. *J. Fluid Mech.* **18**, 285–301.
- MÜLLER, S. 2007 Numerical investigations of compressible turbulent swirling jet flows. PhD thesis, ETH Zürich, Diss. ETH No. 17375.
- MÜLLER, S. B., KEIDERLING, F. & KLEISER, L. 2004 Viscous compressible stability investigations in cylindrical coordinates. *Proc. Appl. Math. Mech.* **4**, 468–469.
- MÜLLER, S. B. & KLEISER, L. 2008 Viscous and inviscid spatial stability analysis of compressible swirling mixing layers. *Phys. Fluids* **20**, 114103.
- PANCHAPAKESAN, N. R. & LUMLEY, J. L. 1993 Turbulence measurements in axisymmetric jets of air and helium. Part 1. Air jet. *J. Fluid Mech.* **246**, 197–223.
- PEYRET, R. 2002 *Spectral Methods for Incompressible Viscous Flow*. Springer.

- PIROZZOLI, S. & BERNARDINI, M. 2007 Space- and time-optimized schemes for computational aeroacoustics. In *13th AIAA/CEAS Aeroacoustics Conference and Exhibit, AIAA Paper 2007-3481*. Rome.
- PRESS, W. H., TEUKOLSKY, S., VETTERLING, T. M. & FLANNERY, B. P. 1992 *Numerical Recipes in Fortran 77*, 2nd edn. Cambridge University Press.
- SAGAUT, P. 2001 *Large eddy simulation for incompressible flows: an introduction*, 1st edn. Berlin Heidelberg New York: Springer-Verlag.
- SANDHAM, N. D., MORFEY, C. L. & HU, Z. W. 2006 Nonlinear mechanisms of sound generation in a perturbed parallel jet flow. *J. Fluid Mech.* **565**, 1–23.
- SANDHAM, N. D. & SALGADO, A. M. 2008 Nonlinear interaction model of subsonic jet noise. *Phil. Trans. R. Soc. A* **366** (1876), 2745–2760.
- SCHLATTER, P., STOLZ, S. & KLEISER, L. 2004 Relaxation-term models for LES of transitional/turbulent flows and the effect of aliasing errors. In *Direct and Large-Eddy Simulation V*, pp. 65–72. Kluwer, Dordrecht, The Netherlands.
- SCHLICHTING, H. 1979 *Boundary-Layer Theory*, 7th edn. McGraw-Hill Book Company.
- SCHMID, P. J. 2007 Nonmodal stability theory. *Annu. Rev. Fluid Mech.* **39**, 129–162.
- SEROR, C., SAGAUT, P., BAILLY, C. & JUVÉ, D. 2001 On the radiated noise computed by large-eddy simulation. *Phys. Fluids* **13** (2), 476–487.
- SHUR, M. L., SPALART, P. R., STRELETS, M. K. & GARBARUK, A. V. 2006 Further steps in LES-based noise prediction for complex jets. In *44th AIAA Aerospace Sciences Meeting & Exhibit, AIAA Paper 2006-0485*. Reno, NV.
- STANLEY, S. A. & SARKAR, S. 2000 Influence of nozzle conditions and discrete forcing on turbulent planar jets. *AIAA J.* **38** (6).
- STOLZ, S. 2000 Large-eddy simulation of complex shear flows using an approximate deconvolution model. PhD thesis, ETH Zürich, Zürich, Switzerland, Diss. ETH No. 13681.

- STOLZ, S. & ADAMS, N. A. 1999 An approximate deconvolution procedure for large-eddy simulation. *Phys. Fluids* **11** (7), 1699–1701.
- STOLZ, S., ADAMS, N. A. & KLEISER, L. 2001*a* An approximate deconvolution model for large-eddy simulation with application to incompressible wall-bounded flows. *Phys. Fluids* **13** (4), 997–1015.
- STOLZ, S., ADAMS, N. A. & KLEISER, L. 2001*b* The approximate deconvolution model for large-eddy simulations of compressible flows and its application to shock-turbulent-boundary-layer interaction. *Phys. Fluids* **13** (10), 2985–3001.
- STROMBERG, J. L., McLAUGHLIN, D. K. & TROUTT, T. R. 1980 Flow field and acoustic properties of a Mach number 0.9 jet at a low Reynolds number. *J. Sound Vibration* **72** (2), 159–176.
- SUZUKI, T. & COLONIUS, T. 2006 Instability waves in a subsonic round jet detected using a near-field phased microphone array. *J. Fluid Mech.* **565**, 197–226.
- TAM, C. K. W. 1971 Directional acoustic radiation from a supersonic jet generated by shear layer instability. *J. Fluid Mech.* **46**, 757–768.
- TAM, C. K. W. 1995*a* Jet noise generated by large-scale coherent motion. In *Aeroacoustics of Flight Vehicles - Theory and Practice, Volume I: Noise Sources* (ed. H. H. Hubbard). NASA - Langley Research Center, Hampton VA.
- TAM, C. K. W. 1995*b* Supersonic jet noise. *Annu. Rev. Fluid Mech.* **27**, 17–43.
- TAM, C. K. W. 1998 Jet Noise: Since 1952. *Theoret. Comput. Fluid Dynamics* **10**, 393–405.
- TAM, C. K. W., PASTOUCHENKO, N. N. & SCHLINKER, R. H. 2003 On the two sources of supersonic jet noise. In *9th AIAA/CEAS Aeroacoustics Conference and Exhibit, AIAA Paper 2003-3163*. Hilton Head, SC.
- TAM, C. K. W., PASTOUCHENKO, N. N. & VISWANATHAN, K. 2005 Fine-scale turbulence noise from hot jets. *AIAA J.* **43** (8), 1675–1683.
- TANNA, H. K. 1977*a* An experimental study of jet noise part I: Turbulent mixing noise. *J. Sound Vibration* **50** (3), 405–428.

- TANNA, H. K. 1977*b* An experimental study of jet noise part II: Shock associated noise. *J. Sound Vibration* **50** (3), 429–444.
- TANNEHILL, J. C., ANDERSON, D. A. & PLETCHER, R. H. 1997 *Computational Fluid Mechanics and Heat Transfer*, 2nd edn. Taylor & Francis.
- THOMPSON, K. W. 1987 Time dependent boundary conditions for hyperbolic systems. *J. Comput. Phys.* **68**, 1–24.
- TINNEY, C. E. & JORDAN, P. 2008 The near pressure field of co-axial subsonic jets. *J. Fluid Mech.* **611**, 175–204.
- UZUN, A., LYRINTZIS, A. S. & BLAISDELL, G. A. 2004 Coupling of integral acoustics methods with LES for jet noise prediction. *Int. J. of Aeroacoustics* **3** (4), 297–346.
- VINOKUR, M. 1974 Conservation equations of gasdynamics in curvilinear coordinate systems. *J. Comput. Phys.* **14**, 105–125.
- VISWANATHAN, K. 2004*a* Aeroacoustics of hot jets. *J. Fluid Mech.* **516**, 39–82.
- VISWANATHAN, K. 2004*b* Parametric study of noise from dual-stream nozzles. *J. Fluid Mech.* **521**, 35–68.
- VREMAN, B. 1995 Direct and large-eddy simulation of the compressible turbulent mixing layer. PhD thesis, Universiteit Twente.
- VREMAN, B., GEURTS, B. & KUERTEN, H. 1996 Comparison of numerical schemes in large-eddy simulation of the temporal mixing layer. *Int. J. Numer. Meth. Fluids* **22**, 297–311.
- WANG, M., FREUND, J. B. & LELE, S. K. 2006 Computational prediction of flow-generated sound. *Annu. Rev. Fluid Mech.* **38**, 483–512.
- WILLIAMSON, J. H. 1980 Low-storage Runge-Kutta schemes. *J. Comput. Phys.* **35**, 48–56.
- WINANT, C. D. & BROWAND, F. K. 1974 Vortex pairing: the mechanism of turbulent mixing-layer growth at moderate Reynolds number. *J. Fluid Mech.* **63**, 273–255.

- ZAMAN, K. B. M. Q. 1985 Far-field noise of a subsonic jet under controlled excitation. *J. Fluid Mech.* **152**, 83–111.
- ZAMAN, K. B. M. Q. & HUSSAIN, A. K. M. F. 1980 Vortex pairing in a circular jet under controlled excitation. Part 1. General jet response. *J. Fluid Mech.* **101**, 449–491.
- ZAMAN, K. B. M. Q. & HUSSAIN, A. K. M. F. 1981 Turbulence suppression in free shear flows by controlled excitation. *J. Fluid Mech.* **103**, 133–159.

Curriculum vitae

Name	Felix Keiderling
Date of birth	July 8, 1975
Place of birth	Karlsruhe, Germany
Nationality	German
Oct. 2002 - Sept. 2008	PhD student and research assistant under supervision of Prof. L. Kleiser, Institute of Fluid Dynamics, ETH Zürich
May - June 2007 Oct. - Dec. 2007	Recipient of HPC EUROPA scholarship: Visiting Researcher University of Stuttgart, Germany
Mar. - Apr. 2006	Visiting Research Scientist École Centrale de Lyon, France
July 2002	Diploma (Dipl.-Ing.) in Aerospace Engi- neering, University of Stuttgart, Germany
Dec. 2000	Master of Science (MS) in Aerospace Engi- neering, University of Arizona, Tucson AZ, USA
Aug. 1998 - Dec. 2000	DAAD scholarship for graduate studies in Aerospace Engineering, University of Ari- zona, Tucson AZ, USA
Jan. - Mar. 1998	BMW Rolls-Royce, Dahlewitz, Germany
Oct. - Dec. 1997	Lufthansa Technik, Hamburg, Germany
Sept. 1995 - July 2002	Undergraduate and graduate studies in Aerospace Engineering, University of Stuttgart, Germany
July 1995	Abitur (graduation from high-school), Max-Planck-Gymnasium, Lahr, Germany

Abstract

The effect of nonlinear interaction of instability eigenmodes on jet flow transition and its noise for a round jet at a Mach number of $Ma = 0.9$ and a Reynolds number of $Re = 4.5 \cdot 10^5$ based on jet exit conditions is investigated by large-eddy simulations. At the inflow, helical perturbations determined from linear stability theory are superimposed on a laminar base flow in order to initiate transition to turbulence. Two different ranges of azimuthal wavenumbers n are excited. The first type of simulations excites modes $|n| = 1, \dots, 8$ while the second excludes $|n| < 3$ from the inflow forcing. For both modal compositions we investigate the effect of the disturbance amplitude and vary it in the range from 1.5% to 4.5% of the jet inlet velocity. Thereby, we aim to characterize sources of noise generation and, in particular, underlying mode interactions.

For the first type of excitation the changes in forcing amplitude mostly affect the streamwise position of the transition process which is shifted upstream for larger excitation levels. The transition process is similar for the three amplitudes and is characterized by strong vortex pairings that directly place an imprint on the emitted noise. The simulation results are in fair agreement with experimental and numerical reference data.

For the second type of excitation we observe changes in the transition of the jet with increasing forcing amplitude. As the shear layer roll up, pronounced vortex pairings are more and more weakened and vortex rings are distorted to form three-dimensional structures. This change in transitional behavior affects the acoustic near field which exhibits features of both, natural and tonally-excited jets. In particular for high forcing amplitudes, a tonal component outside the initially excited frequency range is observed. This tone can be linked to fluid-dynamic events in the early transitional region as well as at the end of the potential core. Furthermore, its frequency can be explained by a weakly nonlinear interaction of initially excited eigenmodes.

To substantiate the soundness of the predictions, insensitivity against the choice of certain numerical parameters is demonstrated. The relaxation-term coefficient of the ADM subgrid-scale model is reduced and effects are found to be small. Subgrid-scale model effects are further investigated by simulating a baseline configuration using approximately deconvolved information. Finally, we address the effect of the azimuthal resolution on our simulation results.